Design, construction and operation of an A.C. side excited machine

Al-Akayshee, Qasim Hamood

Award date:
1996

Awarding institution:
University of Bath

DESIGN, CONSTRUCTION AND OPERATION OF AN A.C SIDE EXCITED MACHINE

by Qasim Hamood Al-Akayshee

Submitted for the Degree of Doctor of Philosophy

of the University of Bath

1996

ProQuest LLC
789 East Eisenhower Parkway
P.O. Box 1346
Ann Arbor, MI 48106-1346

ACKNOWLEDGMENTS

I would like to express my sincere gratitude to Professor J.F.Eastham for his most valuable supervision as well as for his guidance, keen interest and tireless support during the whole course of this project. Working with him has been an experience to witness his humility, patience and perfection in the practice of electrical engineering. I am indebted to him for all the help and advice that I have received.

I am also grateful to Professor D.Roger and his group of Applied Electromagnetic Research Centre. In this respect I am particularly grateful to Dr.H.C.Lai, Mr.R.J.Hill-Cottingham, and Dr.P.Leonard for their unfailing advice, comments, and help throughout this project.

I would like to thank all the academic and technical staff of the School of Electronic and Electrical Engineering at Bath University, and all former and present friends for their support.

Finally, but not least, I wish to express my deep and special thanks to my entire family for all their encouragement, endurance and forbearance which provided the strength and derive to see this work to its successful conclusion.

ABSTRACT

This thesis presents the design, construction and operation of AC side excited machines. These are brushless machines, the rotor is passive and carries neither permanent magnets or winding. The applications of such machines are outlined. AC side exited machines are presented in two forms, heteropolar and homopolar. The principle of operation of both machines is described and a full explanation for the magnetic field in both machines is given.

The differences between them are presented by using three dimensional finite element modelling. It was found that a homopolar machine has some advantages over the heteropolar machine and hence this form of machine was constructed as a prototype.

The practical results of the machine are presented and compared with the three dimensional finite element modelling and good agreement has been achieved. A simple theory of the synchronous machine is also employed for this homopolar machine and compared with the prototype results.

An improved machine design is presented, using three dimensional finite element modelling and compared with a conventional machine.

Contents

LIST OF SYMBOLS

$\mathbf{A}$	Magnetic vector potential (Wb/m)
$\mathbf{A}_z$	Z component of $\mathbf{A}$
B	Magnetic flux density (Tesla)
B_{amp}	Amplitude of flux density
B_g	Air-gap flux density
B_p	Longitudinal blocks flux density
B_r	Rotor flux density
B_s	Stator flux density
$C_{R1}...C_{R4}$	Phase R armature coils
$C_{Y1}...C_{Y4}$	Phase Y armature coils
$C_{B1}...C_{B4}$	Phase B armature coils
D	Mean diameter
D_g	Mean diameter at the air-gap
D_p	Mean diameter at the longitudinal path
D_r	Mean diameter at the rotor
D_s	Mean diameter at the stator
E_{af}	Armature voltage due to field current
E_{ag}	Net air-gap voltage

E_A	Armature reaction drop voltage
emf	Induced voltage (Volt)
e_s	Voltage source (Volt)
F	Force
FE	Finite Element
FEM	Finite Element Modelling
g	Air gap length
g_{eff}	Effective air gap
$\mathbf{H}$	Magnetic field strength (Ampere-turn/meter)
I, i	Current
I_d	Direct axis armature current component
I_q	Quadrature axis armature current component
I_{ph}	Phase current
I_s	Slot current
i_a, i_b, i_c	Machine phase currents
$[i]$	Column vector of phase currents
$\mathbf{J}_s$	Current density (A/m^2)
K_d	Distribution factor
K_p	Pich factor
L	Effective axial length (metre)
L_{ad}	Armature reaction inductance
L_l	Leakage inductance

L_s	Synchronous inductance
mmf	Magnetomotive force
N_{coil}	Number of turns in the coil
$\hat{\mathbf{n}}$	Normal unit vector
P	Number of pairs of poles
P_f	Packing factor
p	$\frac{d}{dt}$
R	Electric resistance (Ω)
R_{arm}	Armature phase resistance
R_{field}	Field resistance
r_a	Armature phase resistance (Ω)
t_p	Pole pitch
t_s	Slot pitch
t_t	Tooth width
$[V]$	Column vector of phase to neutral emf
V_{an}	Load voltage (Volt)
X	Inductive reactance (Ω)
X_{ad}	Armature reaction reactance (Ω)

X_l	Leakage reactance (Ω)
X_s	Synchronous reactance (Ω)
α	Tooth width to slot pitch ratio
∇	Curl
θ	Rotor excitation displacement
λ	Flux linkage
λ_{coil}	Armature coil flux linkage
$\lambda_{phase-R}$	Flux linkage phase R
$\lambda_{phase-Y}$	Flux linkage phase Y
$\lambda_{phase-B}$	Flux linkage phase B
$\lambda_{CR1}...\lambda_{CR4}$	Flux linkage coil 1 ...coil 4 phase R
$\lambda_{CY1}...\lambda_{CY4}$	Flux linkage coil 1 ...coil 4 phase Y
$\lambda_{CB1}...\lambda_{CB4}$	Flux linkage coil 1 ...coil 4 phase B
μ_o	Permeability of free space (H/m)
μ_r	Relative permeability
ϕ	Magnetic flux

ϕ_{arm}	Magnetic flux due to armature current
ϕ_{field}	Magnetic flux due to field current
Φ	Reduced scalar potential
ω	Angular speed (rad/sec)
σ	Conductivity
δ	Load angle
$3D$	Three Dimensional
$2D$	Two Dimensional

Chapter 1

A.C. Side Excited Machine Topologies

1.1 Introduction

A.C. side excited synchronous machines have both excitation and armature windings on the stator side of the air-gap, the machines are robust and have been used for high speed applications [1].

The machine has also been suggested for use in alternative energy schemes [2], especially in small hydro and wind power applications where advantage can be taken of their easy and comparatively low-skilled maintenance requirements, where standardization, simplicity and reliability are more important than so-

phistication.

The rotors carry no windings and are brushless but the generated voltage can be regulated by varying the stator-side excitation.

The competing technologies are permanent magnet machines or brushless alternatives in which the field current is provided by rotating rectifiers. The second of these alternatives carries rotor windings which are not possible at high speeds. Permanent magnet machines however can be constructed for high speeds but do not provide means of simple voltage control. They do however have a superior power/mass ratio and if used with a relatively expensive power electronic controller form an expensive, complex rival to the A.C. side excited machine.

1.2 High speed applications

Since the early sixties, A.C. side excited machines have been given considerable attention for use in aircraft applications.

Wharton [3] has given an interesting review. This included many different configurations and gave examples of their use.

The machines have also been used for A.C. high frequency generation from several hundred Hz to 100 kHz. The higher frequency machines are used for supplying power at radio frequencies [4].

A new promising application for these machines is concerned with the power supply for the manned base of NASA's Space Station Freedom. This will be supplied initially from two Solar Power Element modules (SPE's), yielding a total of 75 KW of electric power. As Freedom evolves and grows, increased power needs will be met by the addition of Solar Dynamic(SD) power modules. In a solar dynamic power module, a large reflector concentrates solar energy into a receiver with integral thermal energy storage. The working gas of a Brayton thermodynamic heat engine circulates through the receiver picking up energy and thereby drives a turbine-driven alternator to produce electric power. The thermal energy storage allows continuous production of power throughout the orbit(sun and shade). For optimum operation, the turbine in the Brayton turbine-alternator-compressor component will rotate at high speed. Electric power will be produced at a frequency between 1 and 2 KHz. At these speeds, it is essential that the alternator be very rugged to provide the needed long life [5]. The alternator which has been constructed for this application is a modified Lundell alternator (an A.C. side excited heteropolar machine), it has the following specifications [6]: 36,000 rpm, 1200 Hz 4 poles, 36 stator slots, rated at 14.3 KVA, 0.75 PF, 120 $Volts$ Line-Neutral.

1.3 Superconductivity applications

The topology is well adapted for use with superconducting field coils, due to the stationary nature of excitation coils the cryostat is considerably simplified.

Superconductivity is a phenomenon whereby certain metals, when cooled to very low temperatures (below the critical temperature) become perfect conductors of electricity (resistance is not just very small, it is absolutely zero). Critical temperatures are a few degrees Kelvin, demanding the use of liquid helium as a refrigerant. The Dutch physist H.Kammerlingh Onnes [7] discovery of superconductivity in 1911, was a direct consequence of his development of helium liquefaction techniques. *Onnes* discovered that, in addition to their critical temperatures, superconductors also have a critical field, above which they revert from the superconductivity state to a normal resistive state, for the metals which *Onnes* investigated (i.e mercury, lead, and tin), the critical field is smaller than $\frac{1}{20}$ $Tesla$.

However in the late 1950s and early 1960s a new class of high field superconducting alloys was discovered by the workers in the USA, notably *Matthias* and *Kunzler*. Unlike the pure metals which *Onnes* had worked with, these materials were able to remain superconducting up to very high fields and were also able to carry extremely high currents densities. These superconducting alloys are type II superconductor (i.e Niobium Titanium $NbTi$ and Niobium Tin $Nb3Sn$), in practice the usual operating temperature is 4.2K of liquid helium under atmospheric pressure (Low Temperature Superconductor LTc).

The practical applications in power engineering began only when type II LTc was developed [8], and these have been used in conventional machines. In particular the use of air-cored synchronous machines using superconducting field coils has been extensively considered, an early development is shown in

Fig. 1.1. This is the MIT [9], 3600 rpm, three phase, 80 KVA alternator with a rotating superconducting field winding and an air-cooled copper armature.

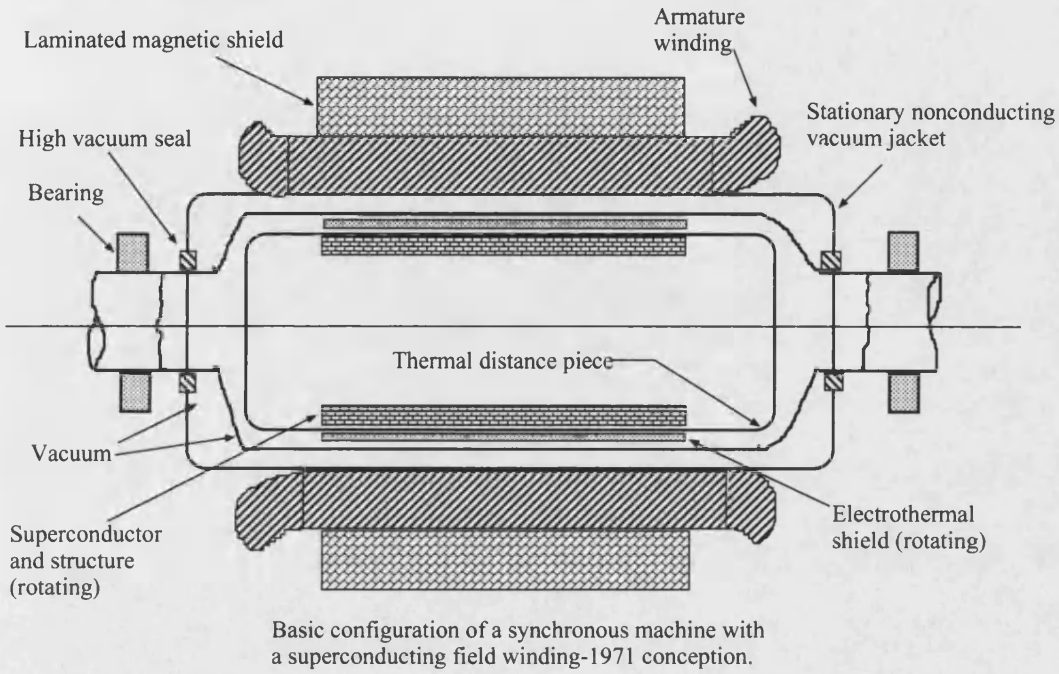

Figure 1.1: $80KVA$ alternator with a rotating superconducting field winding

A design concept for large superconducting machines has been considered later [10], and high power superconducting generators have been designed to produce power $\geq 3MVA$ [11, 12, 13, 14, 15, 16], generally the development of these large superconducting generators have been considered worldwide [17, 18].

All these machines have suffered from the use of rotating field windings which in turn demand rotating cryostats. In contrast if the A.C. side excited configuration is employed the excitation winding is stationary. This considerably simplifies the cryostat, so several experiments have been performed using the superconductor field coils on the A.C. side of the machine and a double sided disc alternator has been constructed [19]. The alternator topology for this de-

velopment is shown in Fig. 1.2. The stationary superconductor field winding is located in the centre of a toroidally wound three phase armature. A ferromagnetic shaft passes through the field coil and carries flux, via the rotor paddles, to the air gaps either side of the armature winding. A heteropolar field pattern is set up within the stator core, and when the shaft is rotated by a prime mover the armature windings have voltages induced in them by the alternating flux they experience. The cryostats in this design, illustrated in Fig. 1.3, used High Temperature Superconducting (HTc) [20], material with high transition temperature (*Yttrium Barium Copper Oxide* $YBa_2CU_3O_7$). These materials were announced in 1987, they have advantages over LTc superconductors because of a higher transition temperatures.

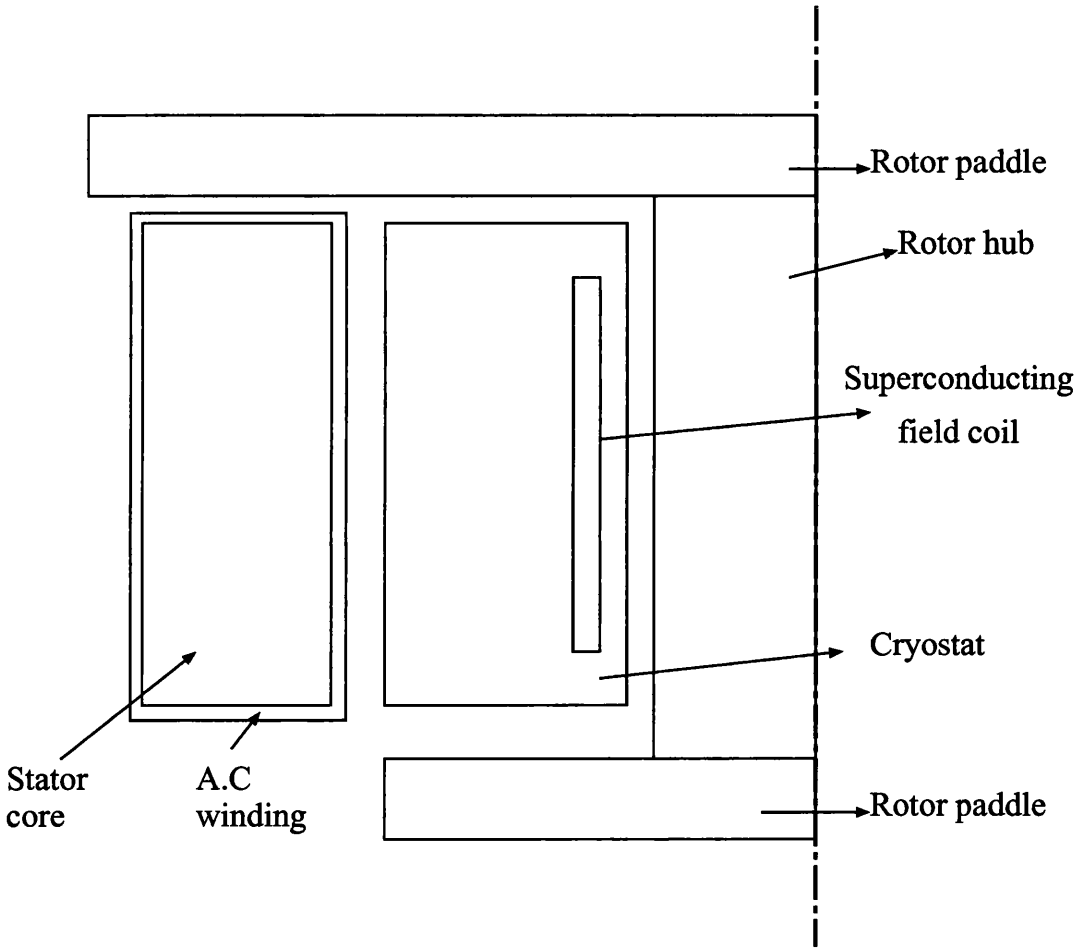

Figure 1.2: Sketch of alternator

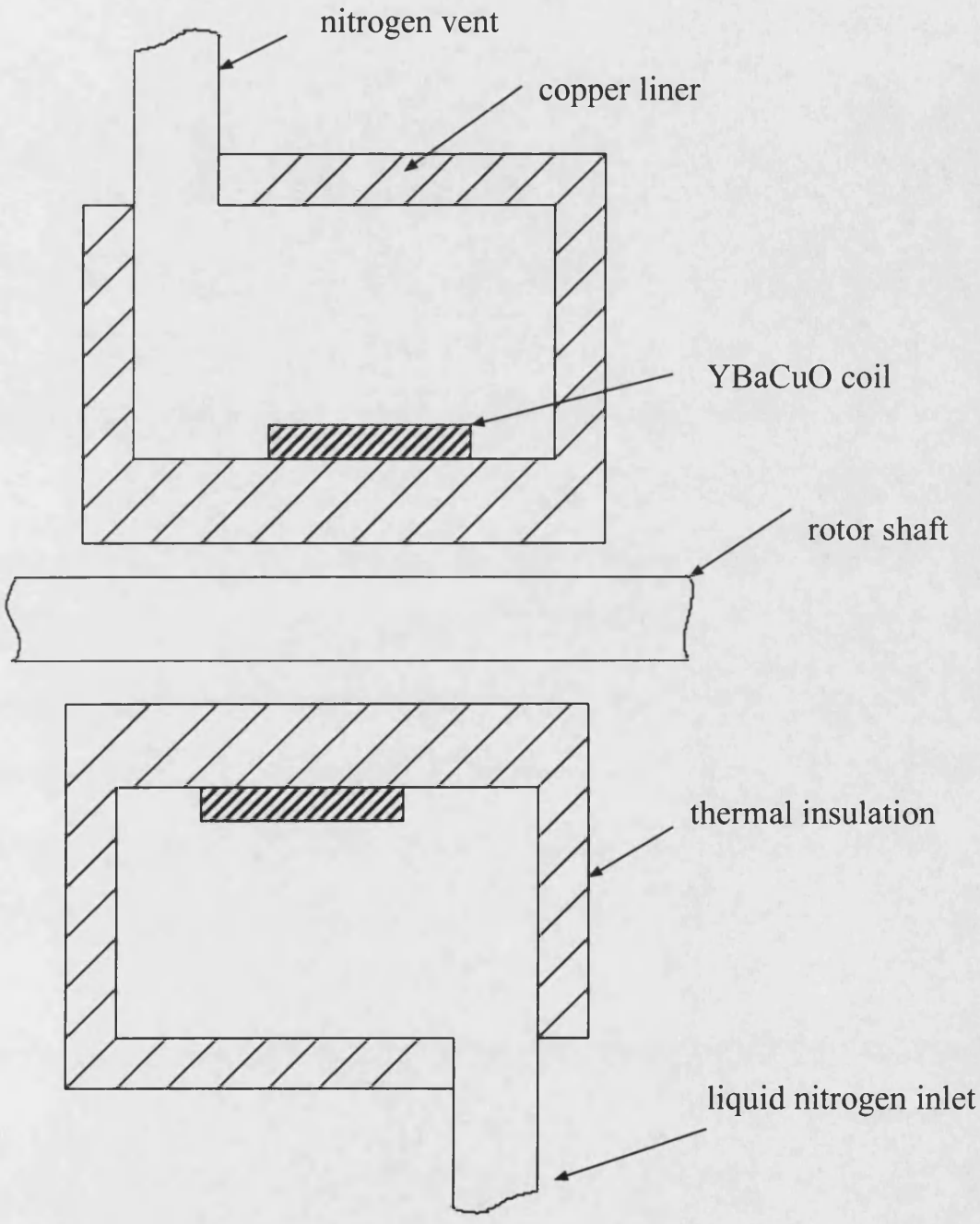

Figure 1.3: Sketch of cryostat

1.4 A.C. side excited linear machine topologies

It is possible to make a linear version of any rotating electrical machine. Linear versions of A.C. side excited machines are shown at Fig. 1.4 for the heteropolar and Fig. 1.5 the homopolar versions. These are known as Linear Synchronous Machines (LSMs). These have been considered as an alternative to the Linear Induction Machines (LIMs) in applications for high speed ground transportation.

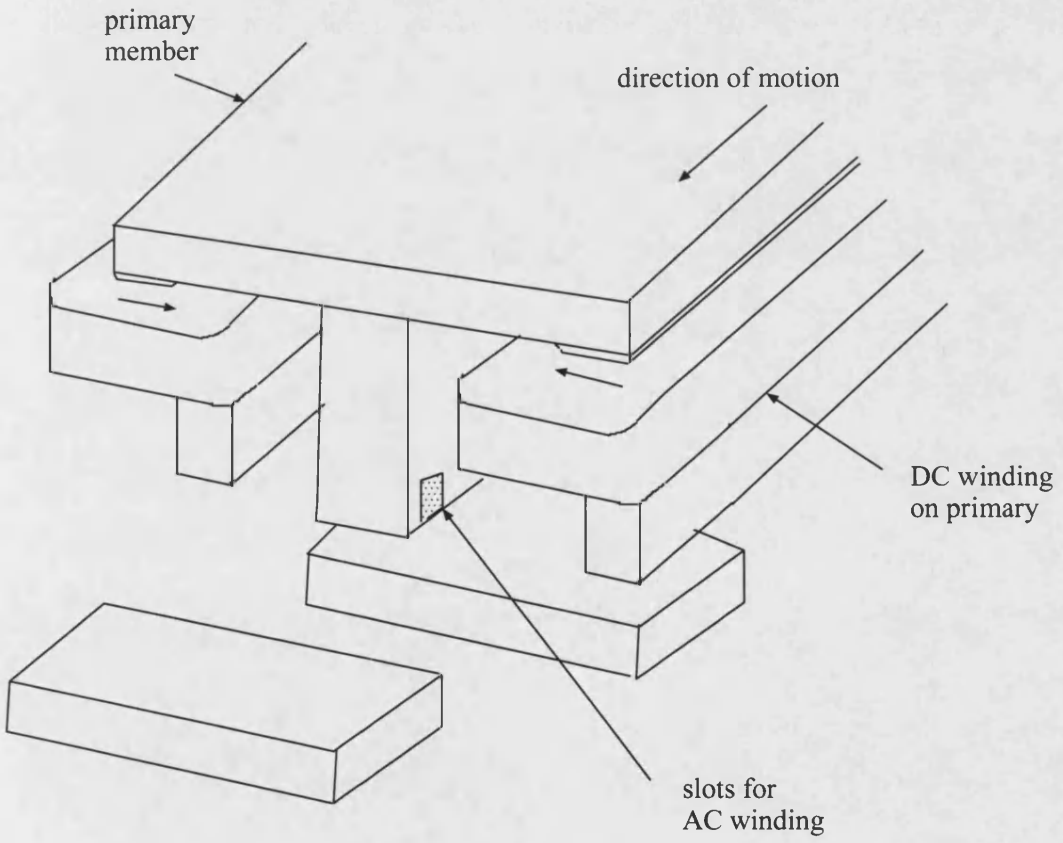

Figure 1.4: Heteropolar linear synchronous machine

A paper [21], compares LIM's and LSM's, there are a number of salient differ-

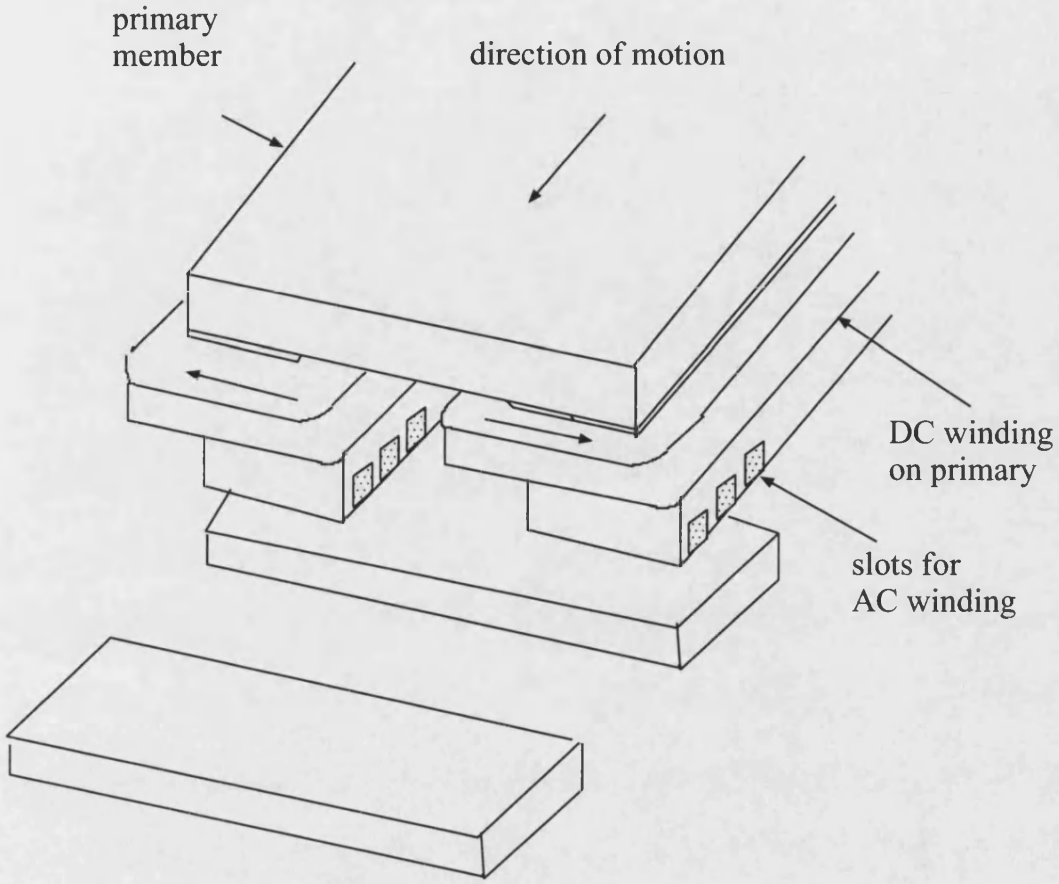

Figure 1.5: Homopolar linear synchronous machine

ences between them and summarized in the following:

Rotor construction: The synchronous machine requires a linear array of D.C. excitation poles. The induction machine requires a ladder of conductors formed from 'unrolling' the squirrel-cage, however, with some reduction in performance, the ladder can be replaced by a simple plate of a conductor backed by solid core-iron. This leads to an inexpensive and effective system which can not be rivalled by the linear synchronous machine. This requires either excitation coils, permanent magnets or arrangements a kin to homopolar machines in which the excitation coils are on the armature side of the gap.

Power supplies: The speed of the stator wave produced by the A.C. winding (the synchronous speed) of either machine is proportional to the supply frequency. A linear induction machine produces force so long as its rotor speed is different from the synchronous speed. Hence, a simple fixed frequency supply will suffice. However, a synchronous machine produces time-average force only if its rotor is traveling at synchronous speed. This means that, for variable speed working, the stator must be supplied from a variable frequency supply (commonly an inverter) and the frequency of the inverter must be carefully locked to the rotor speed.

Eddy current end effects: In a linear induction motor, transient eddy currents are induced in the rotor at the entry edge. This reduces the machine flux to zero at entry. The transient currents decay as a section of the rotor moves along the machine. Further eddy currents are induced as a section of the rotor leaves the excited region. The effect of these currents is to generally reduce the performance of the linear induction motor with respect to its rotary counterpart.

Linear synchronous machines potentially also have 'entry' and 'exit' edge losses. For example, if the excitation poles are made from solid iron then pole-face eddy currents will be driven at the stator edges. However, there is a crucial difference between synchronous and asynchronous linear motors. In the induction case the rotor must have conducting paths because the rotor induced currents provide the force. It is therefore not possible to modify the unwanted edge-effect forces without also changing the wanted propulsion force. The situation is different

in the synchronous case. Eddy currents are not involved in the basic force producing mechanism. It is therefore possible to minimise the transient edge eddy currents by, using laminated steel in the excitation pole construction.

Normal forces: The normal force produced by a linear induction motor is a function of the rotor speed. It commonly reverses sign; a force repelling the rotor from the stator at standstill may reverse to become an attractive force as the machine accelerates. The normal force produced by a synchronous machine is dependent on pole angle and the excitation and supply levels rather than speed. It is therefore easier to control so as, say, to provide a constant attractive force at all speeds.

A.C. side excited linear machines can be shown to have much higher efficiencies and power factors than LIMs [22, 23]. Linear synchronous machines, heteropolar and homopolar have been constructed and shown to be capable of providing both thrust and lift force at relatively high efficiencies force and power factors [24], together with ease of control [25, 26].

1.5 Outline of the thesis

This thesis presents two forms of A.C. side excited machines 'homopolar and heteropolar'. One homopolar machine has been constructed and the practical results have been compared with results from both forms of machines predicted from the finite element modelling.

In Chapter 2, the principle of operation for both machines is described. The field of both machines is fully described.

The construction of the homopolar machine and its specification are given in Chapter 3. Due account was taken of the nature of the magnetic field in each part of the machine in order to decide which section should be made from laminations.

In Chapter 4 the two machines are modelled in 2D and 3D finite element by using the 'MEGA' package [27]. It will be observed that 3D FEM has advantages in the analysis of electrical machines.

A comparison between the homopolar and heteropolar machines is detailed in Chapter 5.

The calculated parameters for the homopolar machine are presented in Chapter 6. The results from the measurements obtained from the prototype machine are also presented in this chapter to compare with the results obtained from FEM.

The analytical design approach is based on the theory of a 3 phase synchronous machine which can be applicable to this homopolar machine and this is illustrated in Chapter 7.

The machine has some penalties, for example, it has a high synchronous reactance and high saturation level. In Chapter 8, the improved machine design, it will be noticed that the amount of saturation as well as the machine reactance can be reduced.

Chapter 2

The principle of operation of Homopolar and Heteropolar machines

2.1 Introduction

The principle of operation of both homopolar and hetropolar machines is discussed in this chapter. It will be shown that the differences between the machines is that the flux crosses from stator to rotor radially and has the same direction at all points round the periphery for the homopolar version, conversely in the heteropolar case the flux crosses the air gap in both directions.

2.2 Principle of operation of a heteropolar machine

The rotor and the stator of a 2 pole heteropolar machine are shown in the Fig. 2.1 and Fig. 2.2 respectively.

The operation of this machine can be best explained by looking at the longitudinal section in Fig. 2.3 at particular position.

The two connected excitation coils are shown in the stator figure but the A.C. winding, carried in the slots of the centre core, is omitted for clarity (only one coil is shown). It will be observed that the excitation coils drive flux so that a pair of poles are induced in the rotor a 'north' pole at the left of the diagram and a 'south' at the right. If the rotor is turned by 180° as shown in Fig. 2.4, again two poles are induced but of opposite polarity. It follows therefore, that a 3 phase emf will be induced in a two pole winding inserted in the slots of the centre core. This form of machine is called heteropolar because of the formation of the 'north-south' pattern on the rotor.

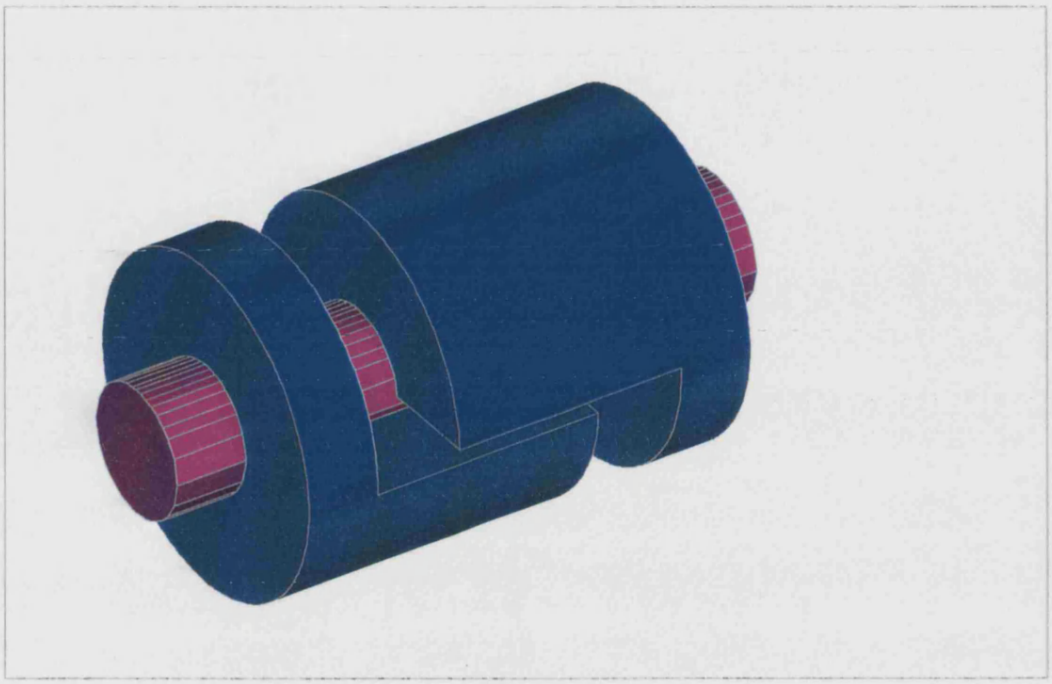

Figure 2.1: Heteropolar machine Rotor

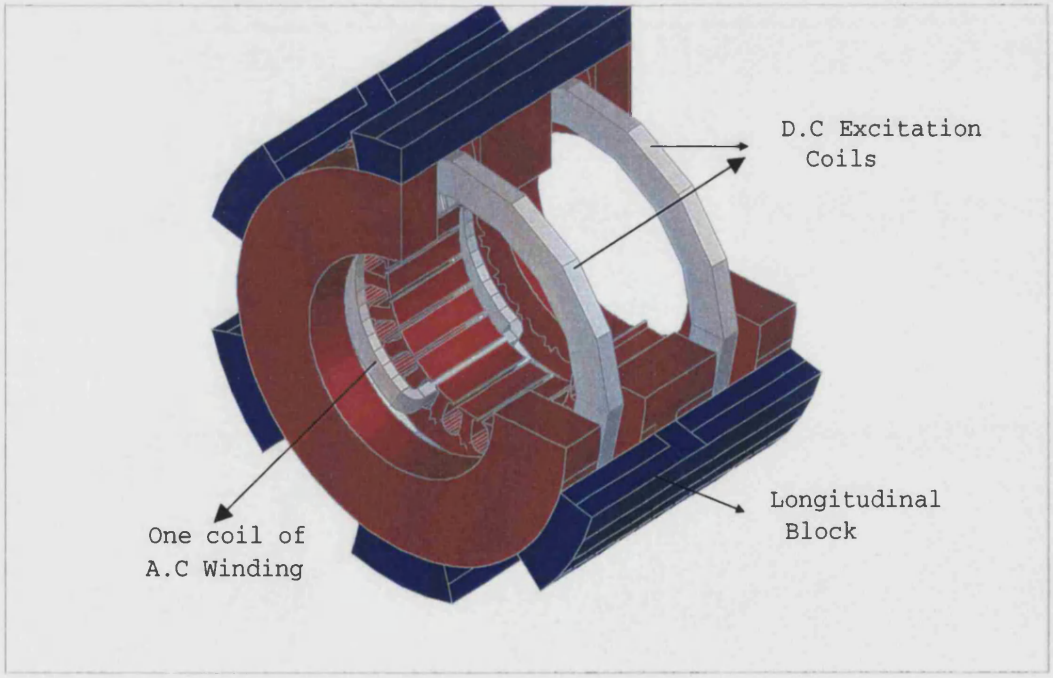

Figure 2.2: Heteropolar machine Stator

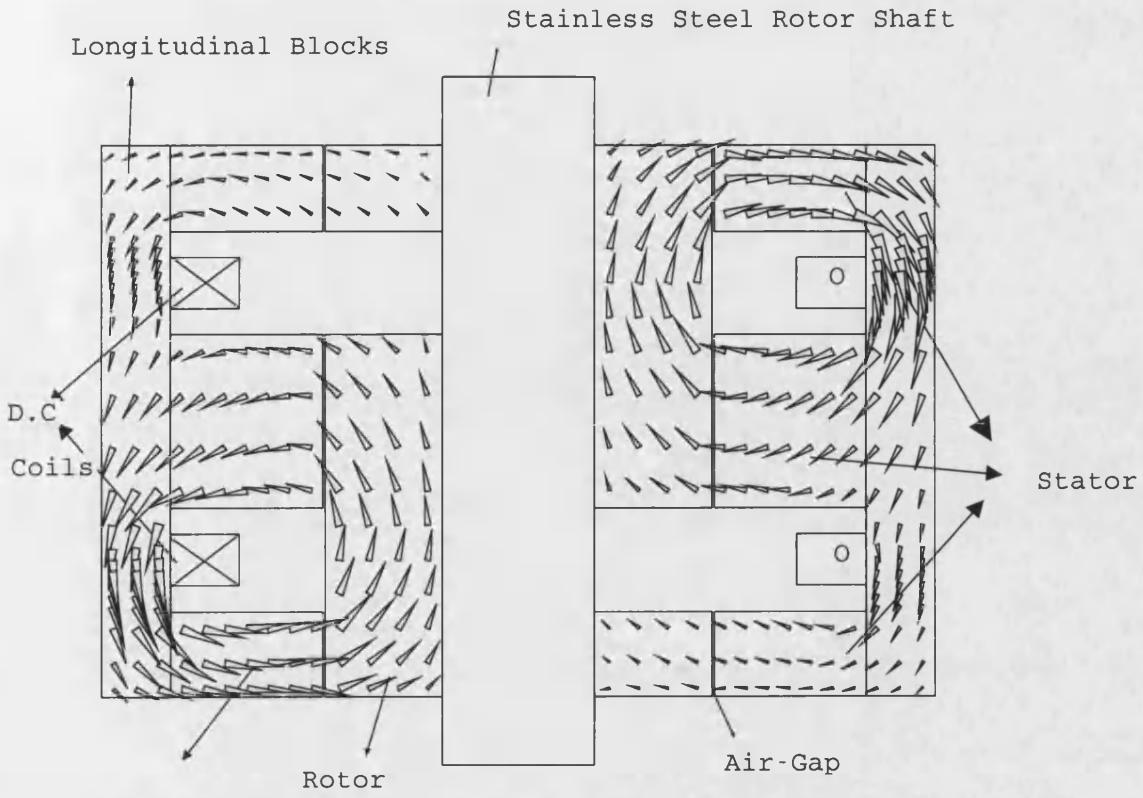

Figure 2.3: Longitudinal Section at 0° Position

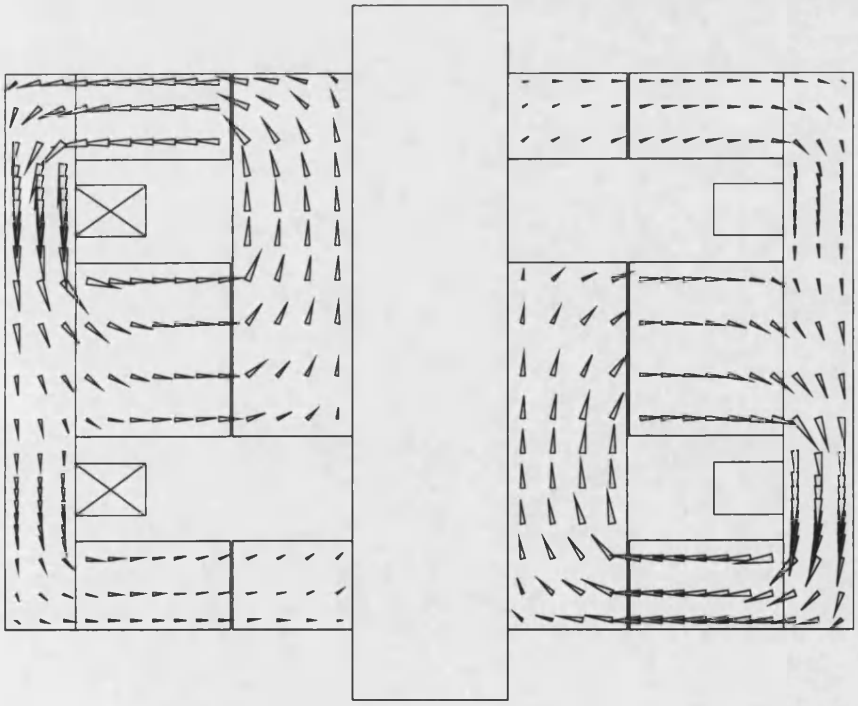

Figure 2.4: Longitudinal Section at 180° Position

2.3 Principle of operation of a homopolar machine

The rotor and stator of a 2-pole machine are shown in Fig. 2.5 and Fig. 2.6 respectively.

Only one excitation coil is used in this machine. The A.C. winding passes through the slots of both cores. Fig. 2.7 is a longitudinal section of the machine shown at one particular position, if the left hand stator is considered it will be seen that the rotor presents a 'north' pole at the top since flux passes from the rotor to the stator. However there is no flux driven from the rotor at the bottom. If now the rotor is turned by 180° as shown in Fig. 2.8 then it will be seen that flux still passes from the rotor to the stator at the left hand core with the rotor still presenting a 'north' pole.

Consideration of the figures shows that a similar situation occurs on the right hand side core but this time a 'south' pole is always presented by the stator. Since the flux is only modulated from one direction to zero in one core the machine is termed homopolar. However because of the two cores the flux linking a stator coil is first in one direction from one core and then in the reversed direction from the other [28].

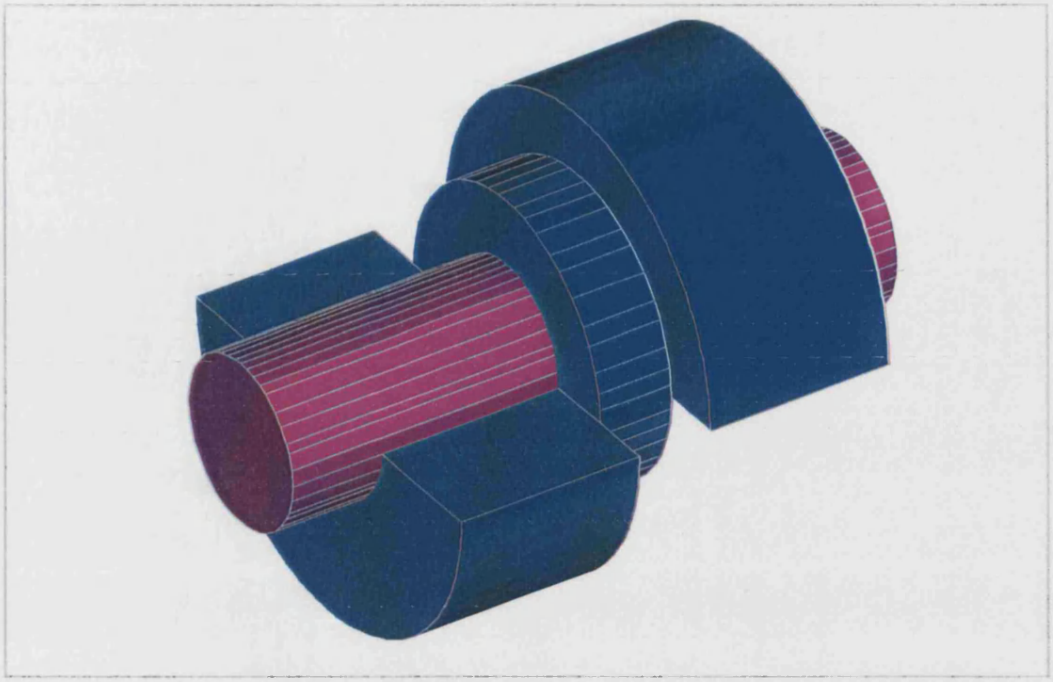

Figure 2.5: Homopolar machine Rotor

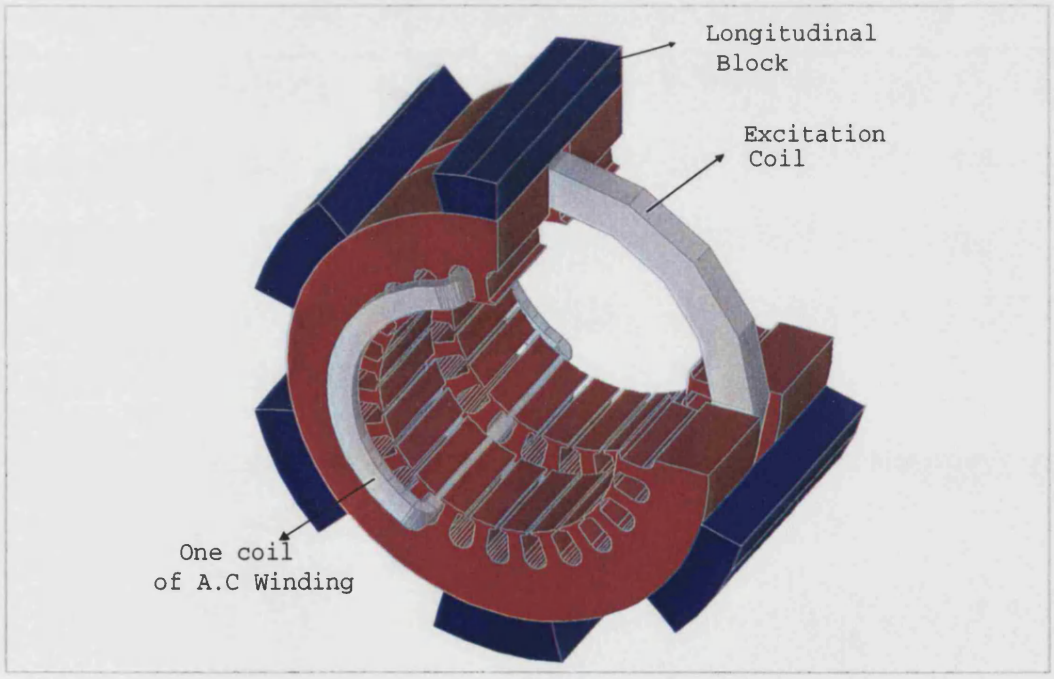

Figure 2.6: Homopolar machine Stator

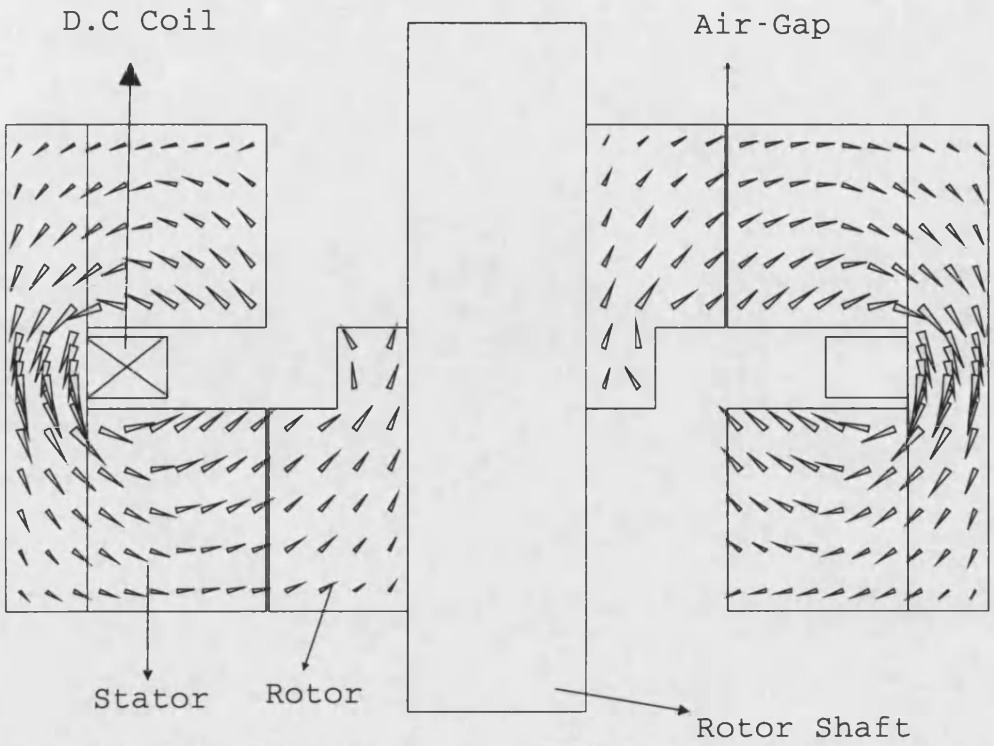

Figure 2.7: Longitudinal Section at 0° Position

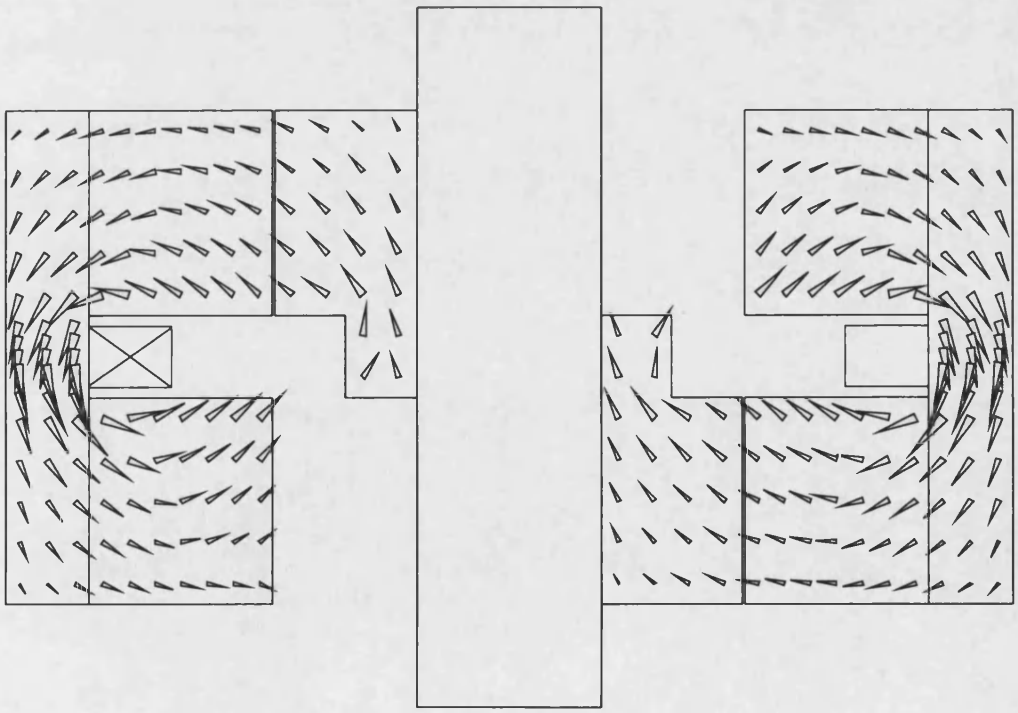

Figure 2.8: Longitudinal Section at 180° Position

Chapter 3

The practical construction of A Homopolar machine

3.1 Introduction

In order to provide practical validation of some of the finite element calculations performed in this thesis, a working model of a homopolar machine was constructed, this is shown in Fig. 3.1.

Fig. 3.1 A homopolar working model

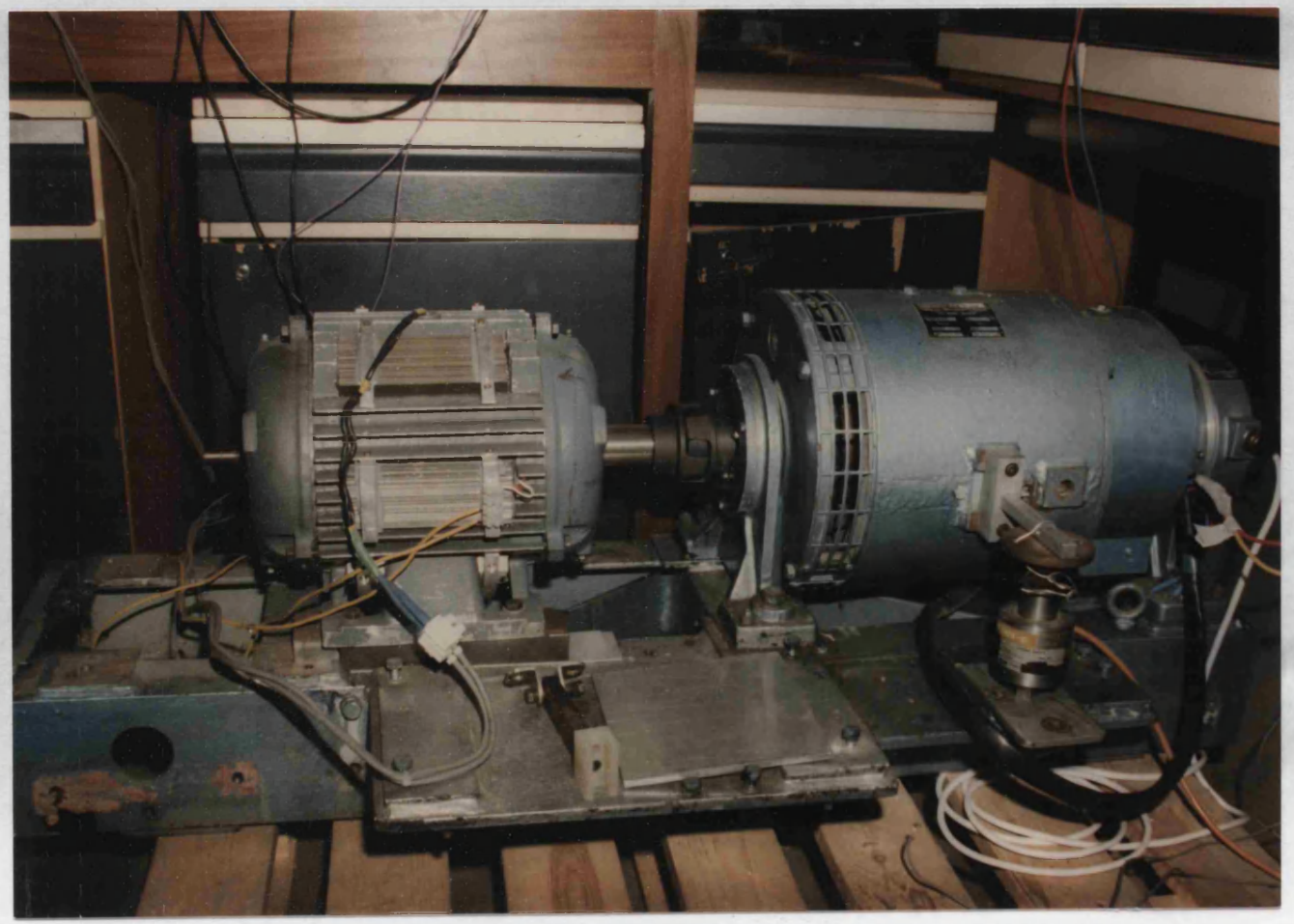

3.2 Principles of construction

In constructing the homopolar prototype machine due account was taken of the nature of the field traversing each part of the machine in order to decide which section should be made from either laminated or solid steel.

In the case of the D.C. field Fig. 3.2, the rotor sides at sections $A-A$ and $B-B$ see no change of flux as the machine rotates since one rotor side always experiences an outgoing field (section $A-A$) while the other rotor side (section $B-B$) sees a constant entering field. In principle therefore the rotor could be made of solid steel as far as the D.C. field concerned.

The rotor outgoing field enters the longitudinal blocks as shown in Fig. 3.2 (section $A-A$) . It predominantly enters the top three blocks but flux also traverses the other three. A similar sketch of the field at the other end of the machine is shown at Fig. 3.2 section $B-B$.

As the machine rotates the direction of the field in the longitudinal blocks remains constant however it is modulated in a particular block from a value which is close to zero to its full value. It follows therefore that the longitudinal blocks must be laminated.

This D.C. field also does not change direction in the longitudinal blocks, since the rotor outgoing field will enter the top longitudinal blocks in section $A-A$ as an entering path, and vice-versa in section $B-B$.

The only part in the machine which experiences change in the magnitude of

the D.C. field is the stator. This change is from a maximum in section $A-A$ (top part of the stator) to a minimum in section $B-B$, and vice-versa in the bottom part of the stator.

In Fig. 3.3, which shows the $A.C$ field, again both rotor sides in section $A-A$ and section $B-B$ experience this field as a constant field and section $A-A$ shows that, this field is outgoing from the rotor. Conversely in section $B-B$ this field enters the rotor. It follows therefore that the body of the rotor sees a field which is unidirectional.

The $A.C$ field is also unidirectional in the longitudinal blocks, since the rotor outgoing field enters the top longitudinal blocks in section $A-A$ as an entering path, and vice-versa in section $B-B$.

It can be concluded from above that the rotor could have been a solid rather than laminated since it sees a constant field from both the $A.C$ and D.C. excitation. However fluctuations in this field occur as a result of first the slots in the stator and secondly due to space harmonic fields produced by the $A.C$ winding which do not travel at rotor speed. To reduce the effect of the eddy currents which might be produced from these field fluctuations it would be preferable to laminate the rotor, however at high speeds this may not be possible.

The stator has to be laminated to reduce the eddy current effect produced by the $A.C$ field.

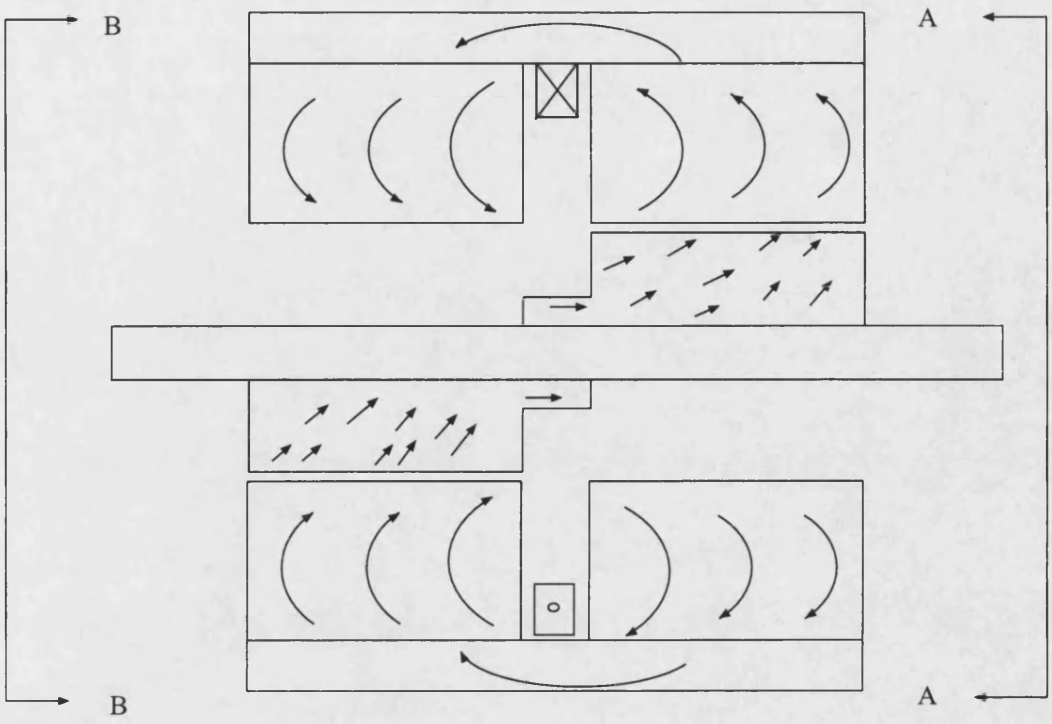

Figure 3.2: D.C. flux sections $A - A$ and $B - B$

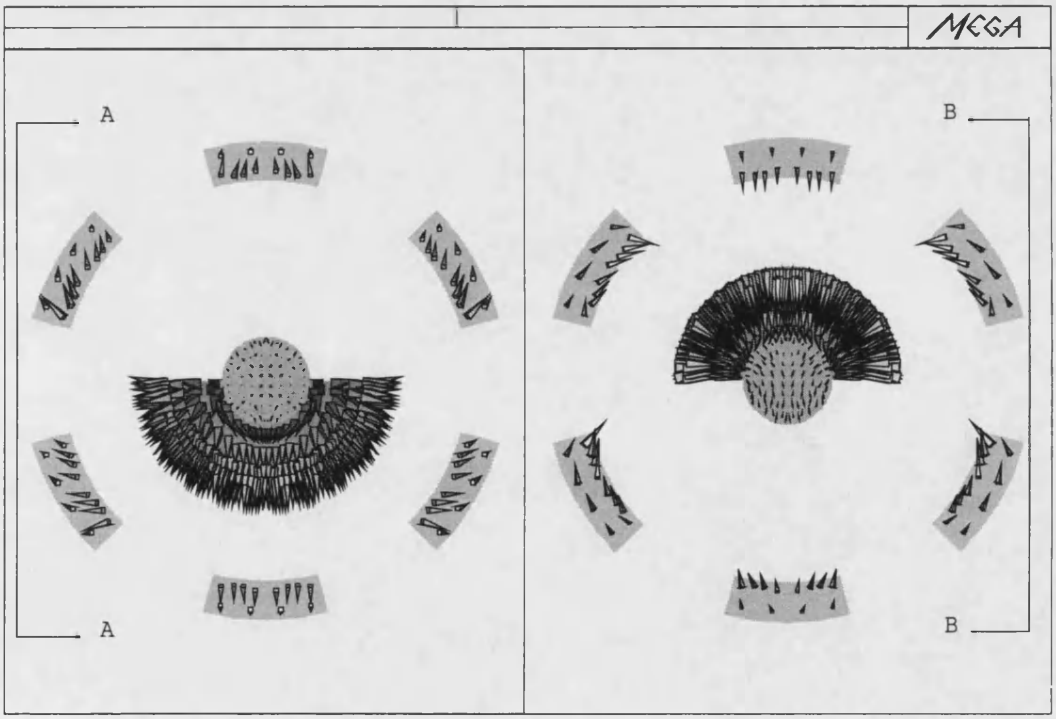

Figure 3.3: A.C. flux sections $A - A$ and $B - B$

3.3 Stator Design

The stator construction is shown in Fig. 3.4. It will be observed that two annular slotted stators are formed by laminated blocks to provide the necessary flux paths. A separate view of the two stators is shown in Fig. 3.5.

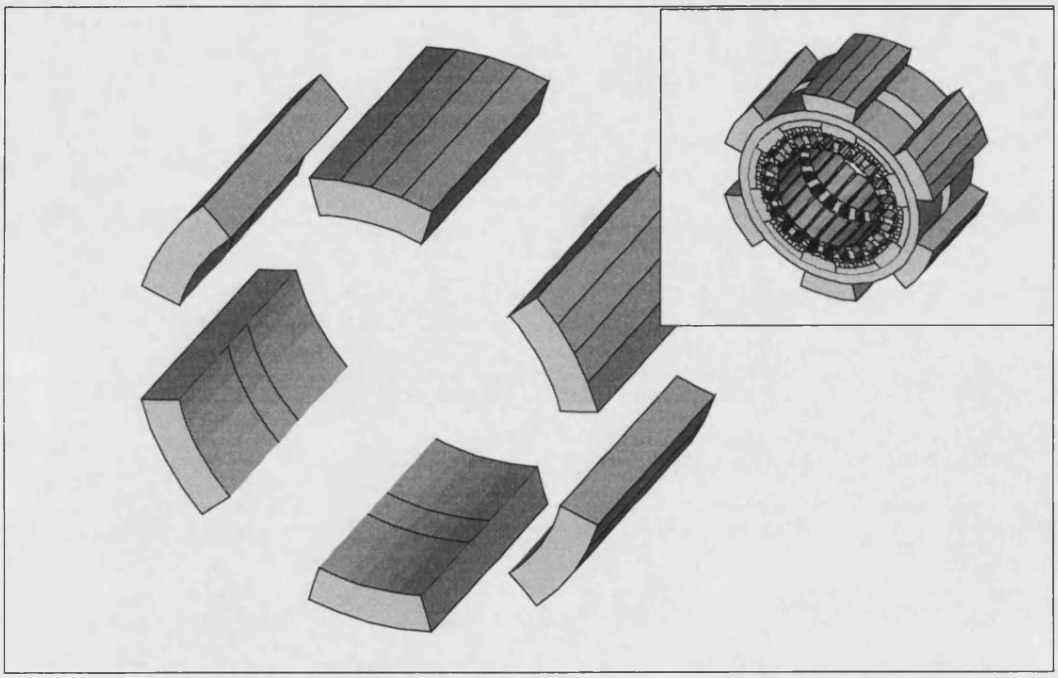

Figure 3.4: Two stator core with the longitudinal bars

Fig. 3.5 Two stator core, Homopolar machine

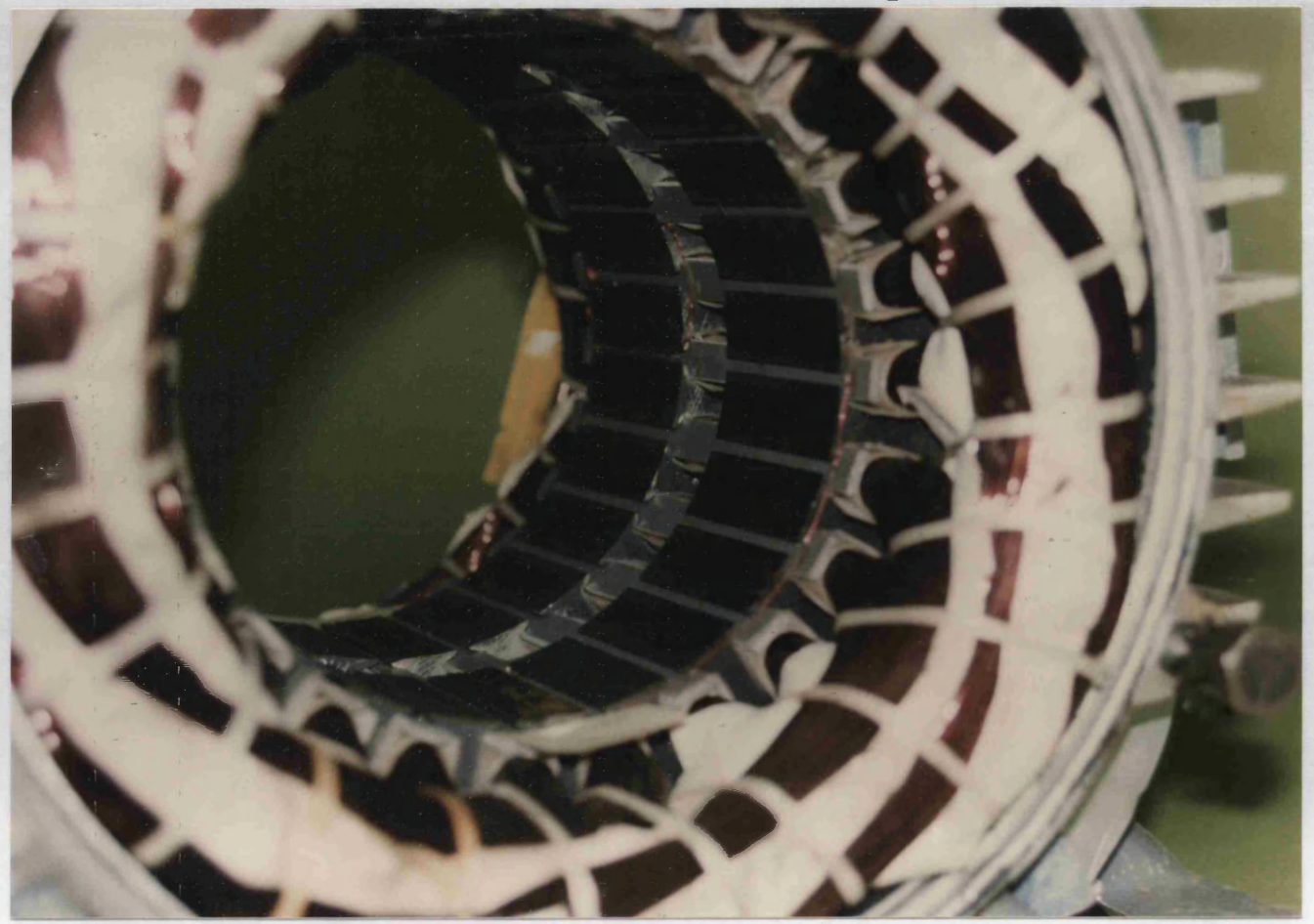

3.4 Rotor design

The rotor has been assembled from two different shapes of laminations. Half and full circular laminations were used, of 0.35 mm thickness. These were used to produce the shaped rotor shown in Fig. 2.5. A photograph of the rotor is shown at Fig. 3.6 during its construction.

3.5 Field and armature windings arrangement

The field coil is a solenoid type and was wound on a bobbin. Copper conductor was used. The bobbin is placed equi-distance from the stator cores. The leads are brought out from the hole in the outer case. The field coil is taped with a heavy duty insulation.

Each coil of the armature winding is in the form of a saddle occupying the slots of both cylindrical stators.

A single layer construction is employed following its common use in machines of this size. Fig. 3.7 shows the field and the A.C. winding (only two A.C. coils are shown for clarity).

Fi.g 3.6 Rotor laminations assembly

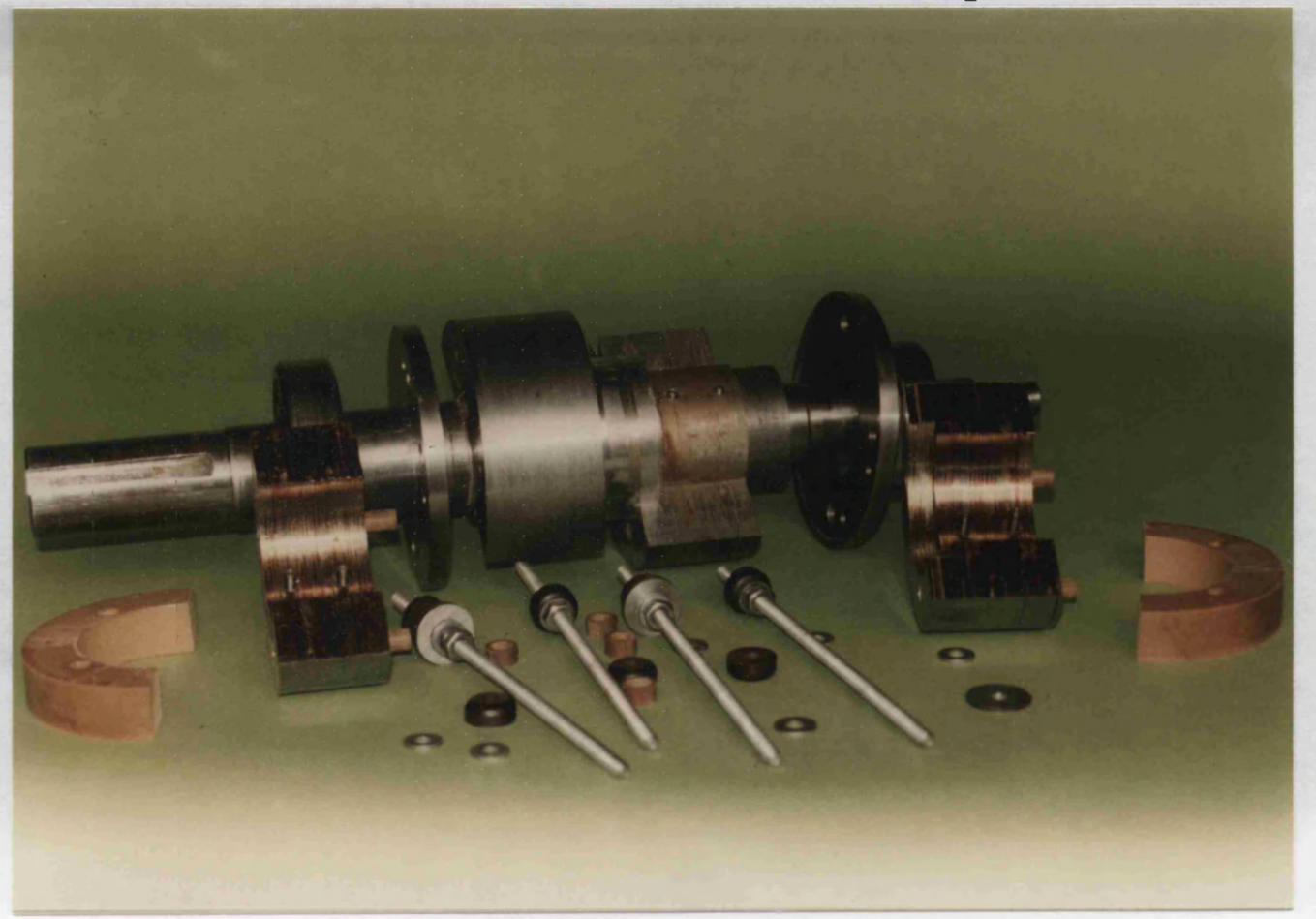

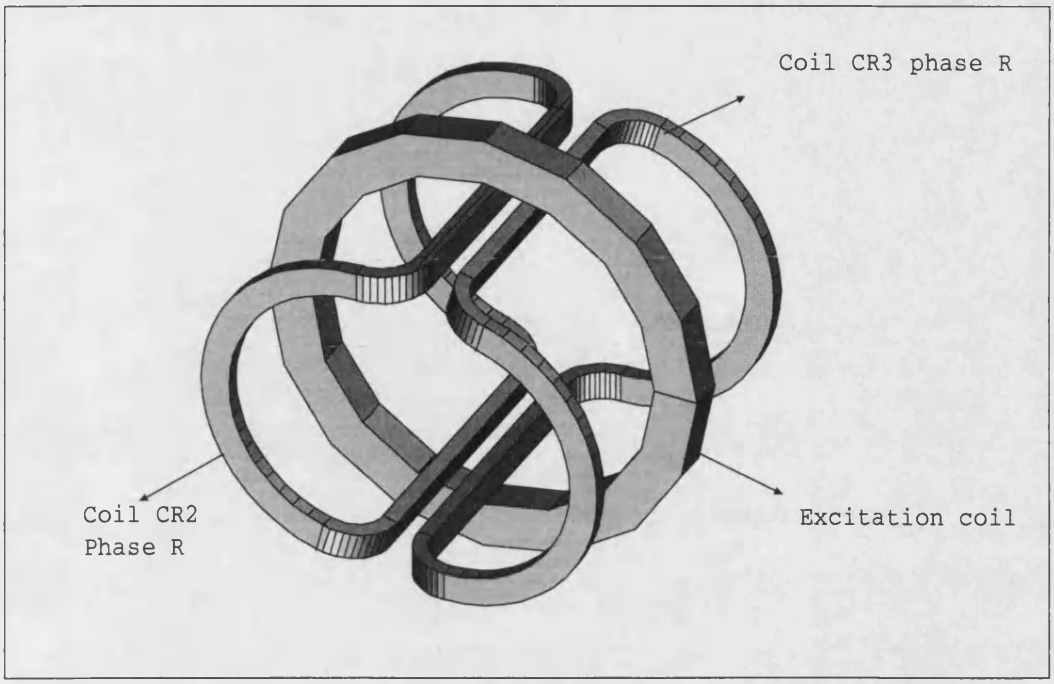

Figure 3.7: field and armature windings arrangement

3.6 Machine specifications

Using the above considerations the machine has been constructed in order to have all the specifications listed in the table(3.1). It has a two pole winding on the stator. The stator winding has two coils per phase and pole as shown in Fig. 3.8.

The nonlinear characteristics for the materials used for the rotor, stator and the six longitudinal blocks was found experimentally using the B-H testing machine (*MAGNET-PHYSIC REMAGRAPH*). These curves are presented in the *appendix – A.*

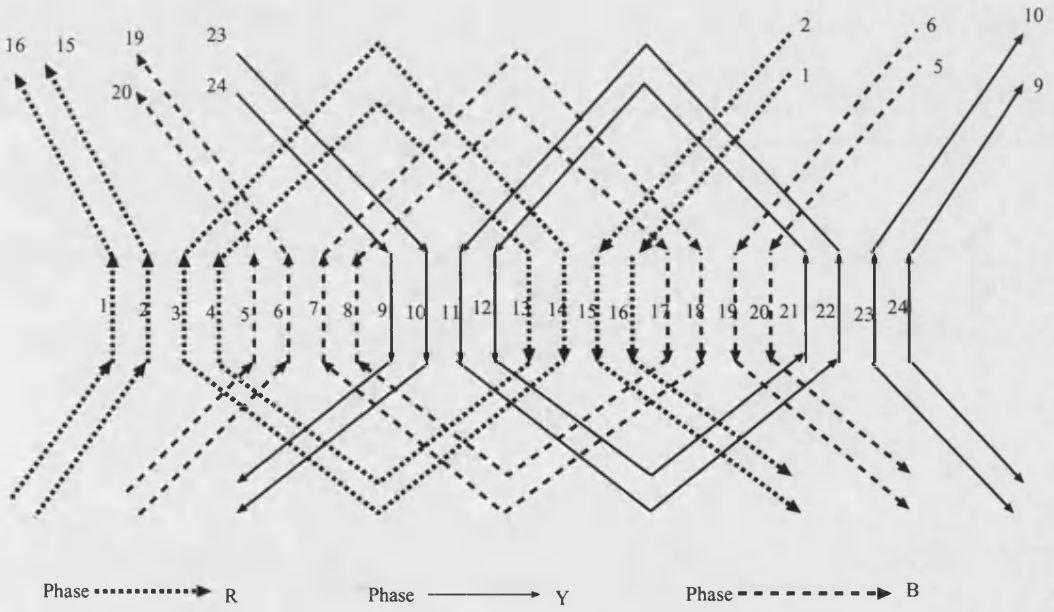

Figure 3.8: Two coils per phase and pole

Stator	
Pole-pitch	139.0154 mm
Slot-pitch	18.1 mm
Slot-width	12 mm
Tooth-width	6.6 mm
Number of slots	24
Material type	Laminated steel
Number of poles	2
Wire diameter of windings	0.8 mm
Number of turns in a coil	45
Lamination inner diameter	114.5 mm
Lamination outer diameter	203 mm
Number of blocked bars	6
Lamination blocked bar thickness	0.35 mm
Lamination blocked bar depth	20 mm
Blocked bar axial length	120 mm
Air-gap	
Length	0.675 mm
effective length	1.32 mm
Air gap flux density	0.3 T
Rotor	
Half circle lamination inner diameter	44.45 mm
Half circle lamination outer diameter	113.157 mm
Full circle lamination inner diameter	44.45 mm
Full circle lamination outer diameter	80 mm
Half circle lamination axial length	100 mm
Full circle lamination axial length	20 mm
Rotor shaft axial length	170 mm

Table 3.1: Machine specification

Chapter 4

Machine Modelling by means of Finite Element Methods

4.1 Introduction

To perform the analysis of electrical machines, an electromagnetic model is required. This can be used to find the characteristics of the machine, for example flux linkage, inductances etc (These are presented in the following chapter).

Finite Element methods have been used previously for the solution of various machines. Examples are given for A.C. machines in references [29, 30, 31, 32], and for D.C. machines in references [33, 34, 35]. In this thesis the finite element

'MEGA Package' [27], has been used to model the heteropolar and homopolar machines discussed in this thesis.

The MEGA package uses finite element techniques for modelling 2D and 3D problems. In the 2D case a vector potential formulation is used for all regions. In the 3D case magnetic scalar potential is used for all regions except those which contain the conducting material or excitation coils. In these latter two cases vector potential and reduced scalar potential are used respectively.

The MEGA package structure consists of two programs. The first program is MEGA-view which consistutes the pre-and post processor. This provides the user with a consistent interactive environment to define, post process, and edit the electromagnetic model. The second program is the solver 'MEGA solve', and once the problem has been set up using MEGA-view, the solver typically works out the problem non-interactively and can produce an answer file which is read back into MEGA-view for interactive post-processing. The MEGA Package solves 2D and 3D problems using the same viewer and solver.

4.2 2D FE theory

In a device which is very long so that its field can be assumed constant in one direction, a 2D model can be used for analysis. In rotating machine analysis, a 2D cartesian vector potential model is commonly used taking a plane of the machine which is at right angles to the shaft[36]. This ignores the effects due to the ends such as fields due to the end turns. The current is in the shaft direction with two magnetic flux density components in the modelling plane.

The formulation used solves for a single component of the magnetic vector potential, $\mathbf{A} = A_z\hat{\mathbf{Z}}$ where the field quantities are derived from $\mathbf{A}$. The induced electro-motive force emf is:

$$\mathbf{E}_z = -\frac{\partial A_z}{\partial t} \tag{4.1}$$

and the magnetic flux density is:

$$\mathbf{B} = \nabla \times A_z\hat{\mathbf{Z}} \tag{4.2}$$

The governing Partial Differential Equation (PDE) is deduced from Maxwell's equations, substituting into $\nabla \times \mathbf{H} = \mathbf{J}$ gives:

$$\nabla \times \frac{1}{\mu} \nabla \times \mathbf{A} + \sigma \frac{\partial \mathbf{A}}{\partial t} = \mathbf{J}_s \tag{4.3}$$

which reduces to:

$$-\nabla \cdot \frac{1}{\mu} \nabla A_z + \sigma \frac{\partial A_z}{\partial t} = \mathbf{J}_s \tag{4.4}$$

Note that the current is described by two terms, the first is due to the prescribed current source and the second to the induced eddy currents. If the model has coils with known current density, then J_s is prescribed and σ is zero in the region. It is also possible to model coils with unknown current allowing voltage forced or external circuits to be modelled. If a massive conductor has a prescribed voltage then $\mathbf{J}_s$ can be assigned the D.C. value of current that would flow if no eddy current effects were present, i.e:

$$\mathbf{J}_s = \sigma \mathbf{E}_a \tag{4.5}$$

where $\mathbf{E}_a$ is the applied voltage gradient. In this case the eddy current distribution will modify the final current distribution.

4.3 Machine modelling using 2D FE technique

The two machines were modelled using the 2D method described above during the first preliminary stages of these investigations unusually for electrical machines a plane along the axis of the machine (the shaft direction) was chosen and the model is given in Fig. 4.1 and Fig. 4.2 for heteropolar and homopolar machines respectively.

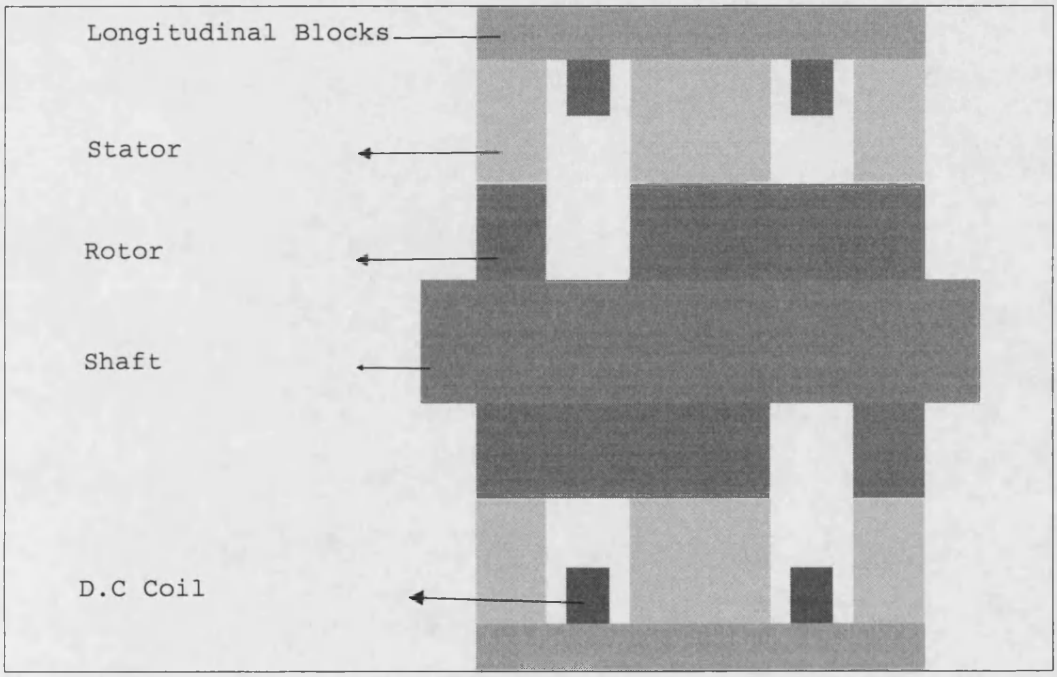

Figure 4.1: 2D FE Model, Heteropolar machine

A typical mesh used for the 2-pole machine is shown in Fig. 4.3 and Fig. 4.4 for heteropolar and homopolar machines respectively. 2D Cartesian magnetic vector potential was used to solve the model the geometry assumed to stay fixed and the field coil has been meshed as unique region with a known current density (J_s is prescribed). The other regions for stator , rotor, used the

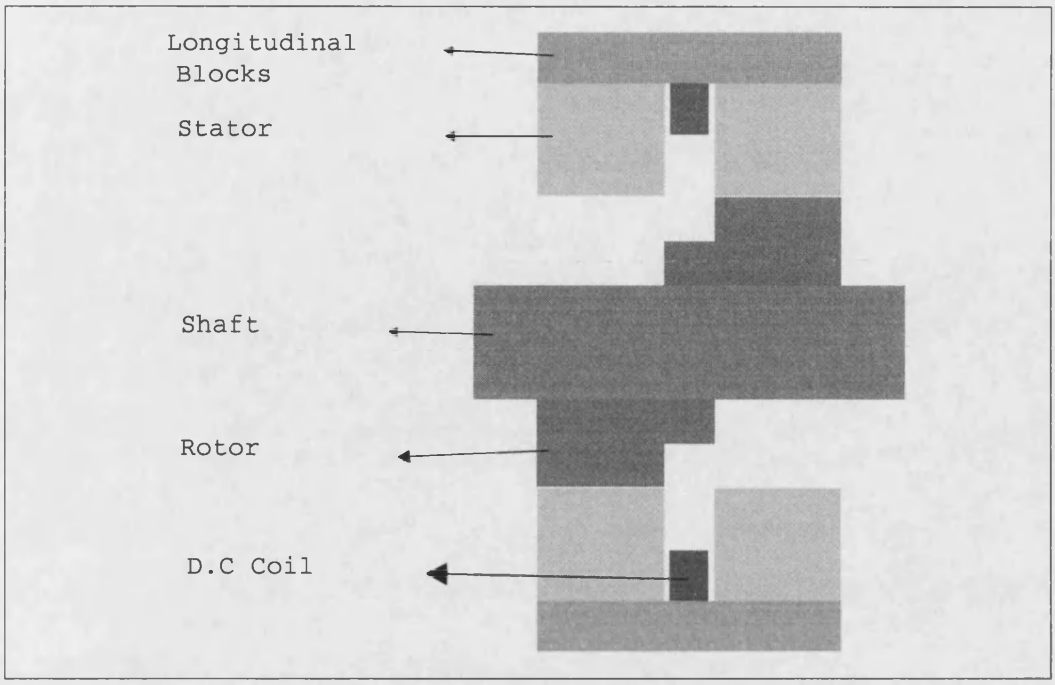

Figure 4.2: 2D FE Model, Homopolar machine

corresponding $B - H$ curves, these are given in appendix[A].

The field distribution as contours of nodal average are shown in Fig. 4.5 and Fig. 4.6 for heteropolar and homopolar machines respectively.

These results are of interest for preliminary design but it is apparent that the machines must be modelled in 3D because of the changes in geometry along plane cut at the right angles to the axis. In particular the field does not change in the Z-direction in the 2D model and the rotor shape is not symmetrical.

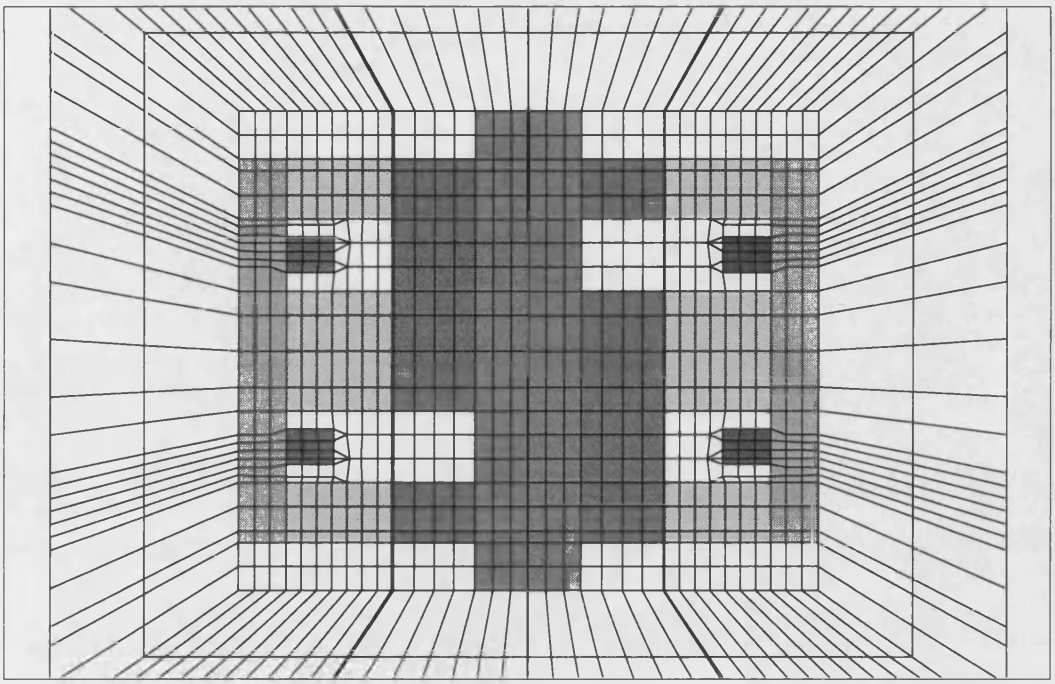

Figure 4.3: Typical Mesh used for 2D FE Model, Heteropolar machine

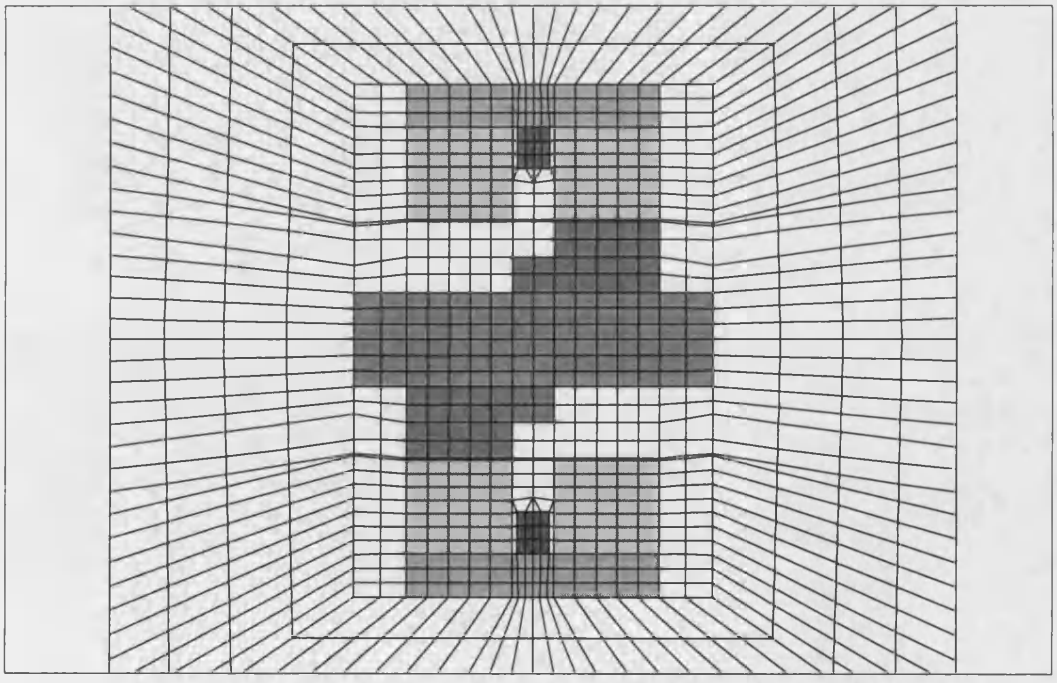

Figure 4.4: Typical Mesh used for 2D FE Model, Homopolar machine

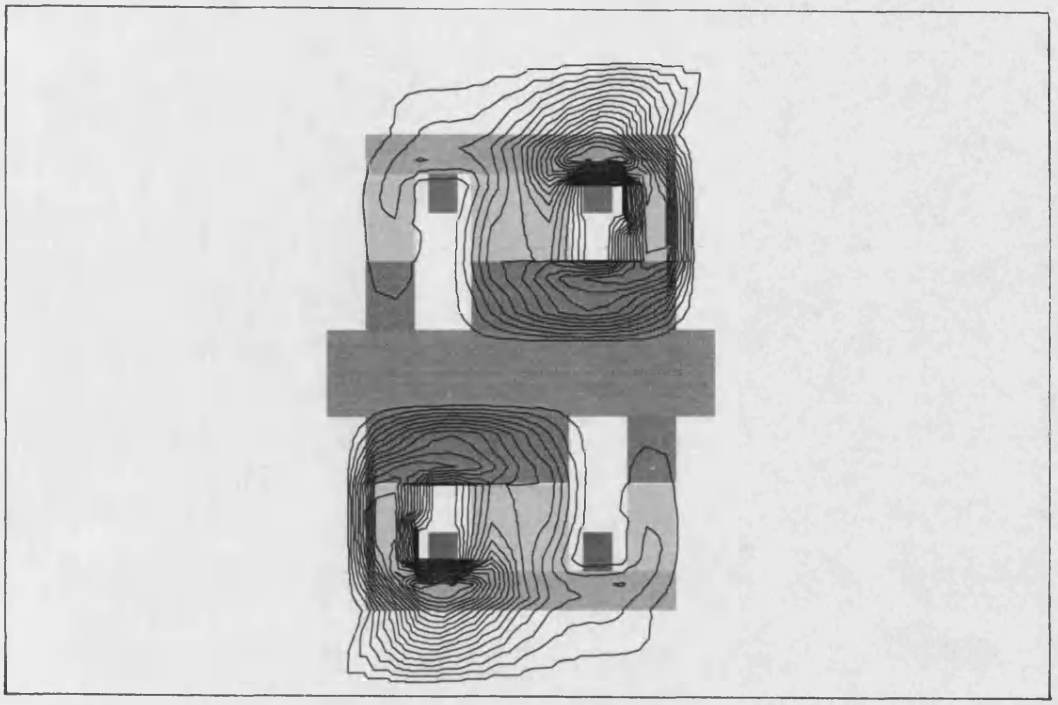

Figure 4.5: Contours of B in the heteropolar machine

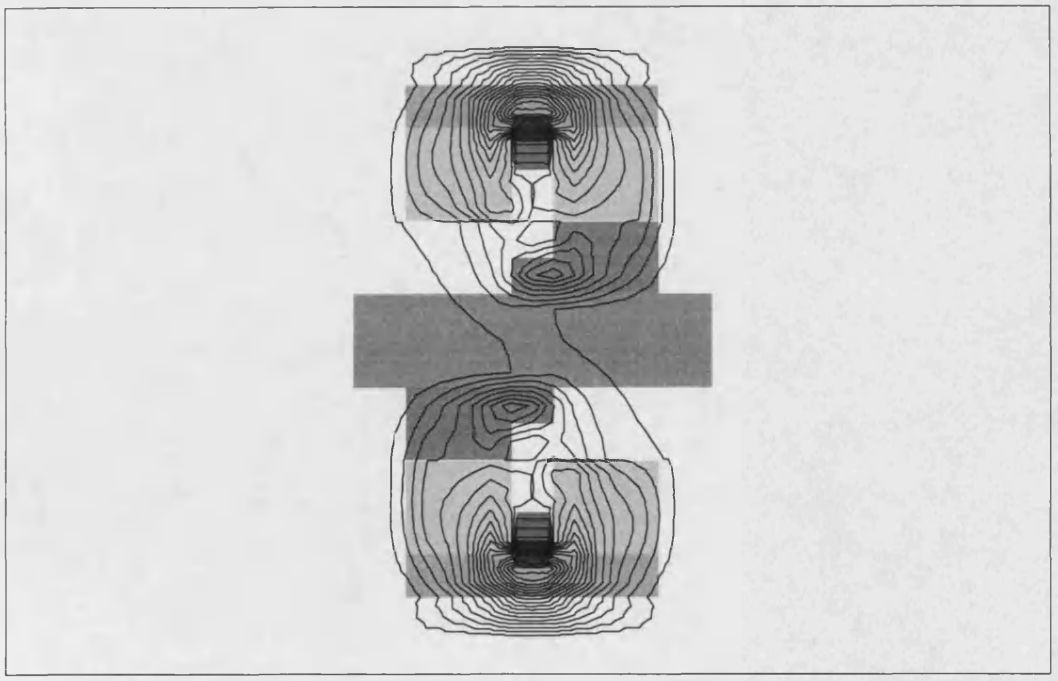

Figure 4.6: Contours of B in the homopolar machine

4.4 The 3D FE Modelling

The 3D mesh can be created by extruding a 2D base plane built from quadrilateral and triangle elements.The process of creating a 2D mesh is subset of the full 3D program.

This modelling method means that the base plane must contain the whole network topology of the entire model. The 3D FE Models are outlined in the following sections.

4.4.1 3D theory

In extending an electromagnetic field computation model from 2D to 3D, additional complexities arise, not only because of the 3D geometry, but also from the physical nature of the field itself which is a vector quantity [37]. The vector nature of the electromagnetic field implies that at each node there will be at least three unknown quantities to compute, which means that there will be a three fold increase in the size of the system matrix over that required for scalar unknowns. This in turn means a considerable escalation in computer cost. Using the magnetic vector potential $\mathbf{A}$ and an electric scalar potential V is the classical method of representing electromagnetic fields. The magnetic vector potential is used to represent the magnetic flux density:

$$\mathbf{B} = \nabla \times \mathbf{A} \tag{4.6}$$

When $\mathbf{A}$ and V are used then the electric field has two contributions:

$$\mathbf{E} = -\frac{\partial \mathbf{A}}{\partial t} - \nabla V \tag{4.7}$$

The $\frac{\partial \mathbf{A}}{\partial t}$ term is normally associated with the induced emf around a closed loop due to the changing field. The voltage term is useful for introducing sources into massive circuits and in allowing jumps in conductivity to be modelled correctly.

Substituting the above representations into Maxwell's equations, the partial differential equations are derived for the solution of:

$$\nabla \times \mathbf{H} = \mathbf{J} \tag{4.8}$$

Yielding,

$$\nabla \times \frac{1}{\mu} \nabla \times \mathbf{A} + \sigma \left(\frac{\partial \mathbf{A}}{\partial t} + \nabla V \right) = 0 \tag{4.9}$$

This equation leaves **A** without a gauge and leads to more unknowns than equations. To remedy this situation an augmented set of equations can be solved:

$$\nabla \times \frac{1}{\mu} \nabla \times \mathbf{A} - \left\{ \frac{1}{\mu} \nabla \nabla \cdot \mathbf{A} \right\} + \sigma \left(\frac{\partial \mathbf{A}}{\partial t} + \nabla V \right) = 0 \tag{4.10}$$

$$\nabla \cdot \sigma \left(\frac{\partial \mathbf{A}}{\partial t} + \nabla V \right) = 0 \tag{4.11}$$

The middle term of equation 4.10 is optionally added as a penalty term constraining the divergence of **A** to be *zero*. To ensure that the solution is unique the additional constraint:

$$\mathbf{A} \cdot \hat{\mathbf{n}} = 0 \tag{4.12}$$

on the boundary of **A** regions may be added.

4.5 Stator mesh

The first task was to construct a base plane normal to the machine shaft which can be thought of as a 2D slice through the model.

This base plane was constructed from quadrilaterals and triangles, each edge of which is defined by two nodes as shown in Fig. 4.7.

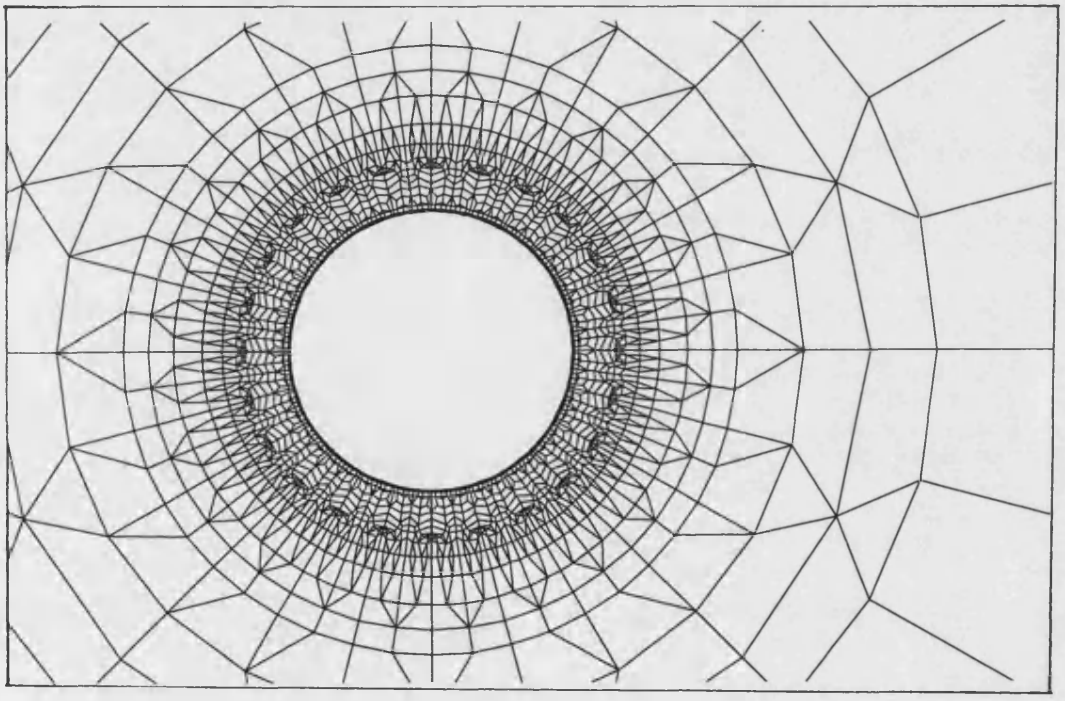

Figure 4.7: Stator base plane used for both machines

In this plane it will be noticed that the six longitudinally directed blocks have been meshed with the stators, and a half of the air gap is included in this mesh. The other half of the air gap is part of the rotor mesh (described in the following section). The problem has been defined as two meshes that can move relative to each other. This is described in section 4.9.

After creation of these elements, they must be labeled in such a way that will define the materials, for example; air, iron, conductor, and etc.

This is achieved by giving elements region identification numbers which defines their associated material properties as shown in Fig. 4.8.

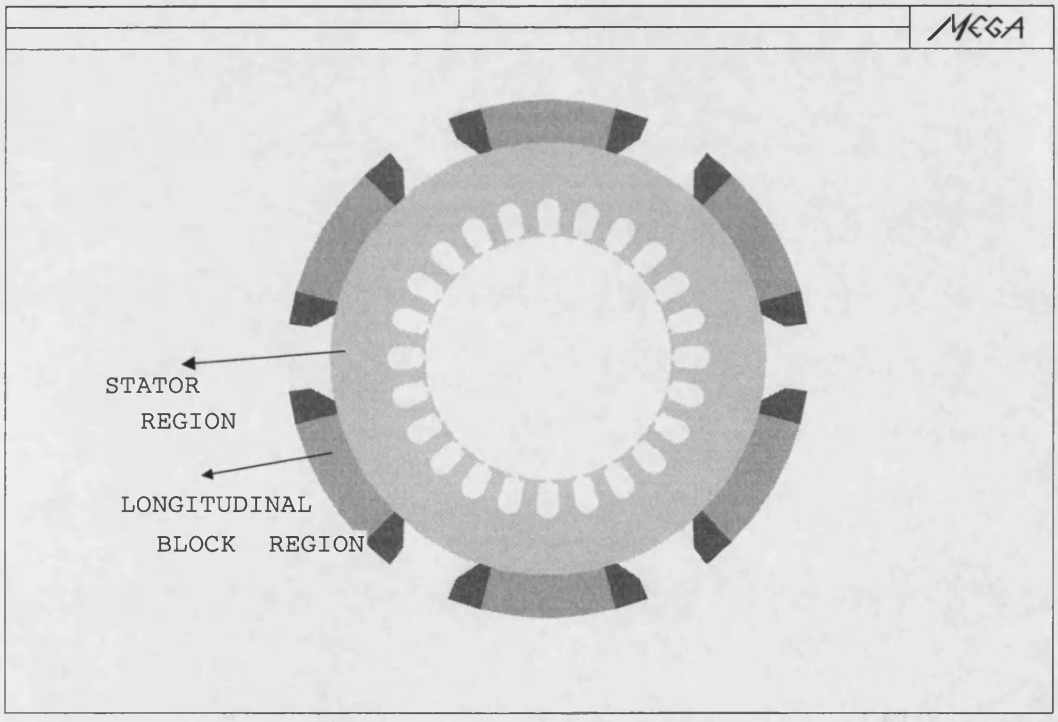

Figure 4.8: Stator base material identifications

The stator base plane mesh has about (2498) elements and (2198) nodes.

A full 3D framework of elements can be formed by extruding the base plane on

a given display level in the Z-direction and it is shown in Fig. 4.9 and Fig. 4.10 for the heteropolar and homopolar machines respectively.

Fig. 4.9 3D Stator, Heteropolar Machine

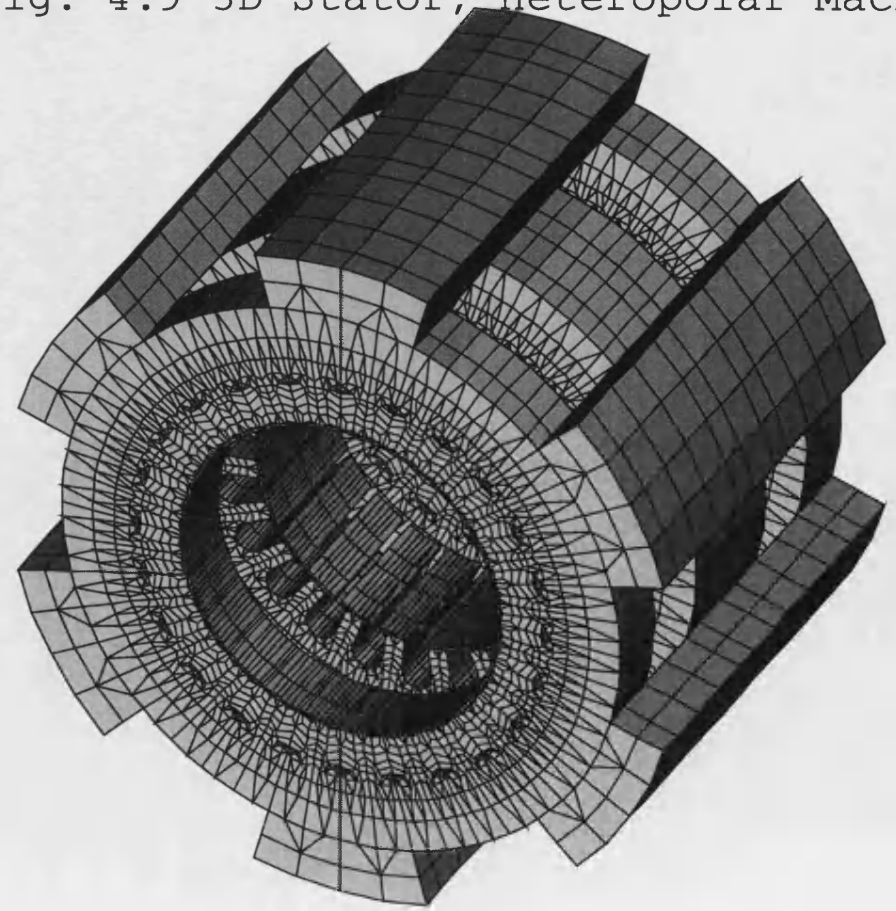

Fig. 4.10 3D Stator, Homopolar machine

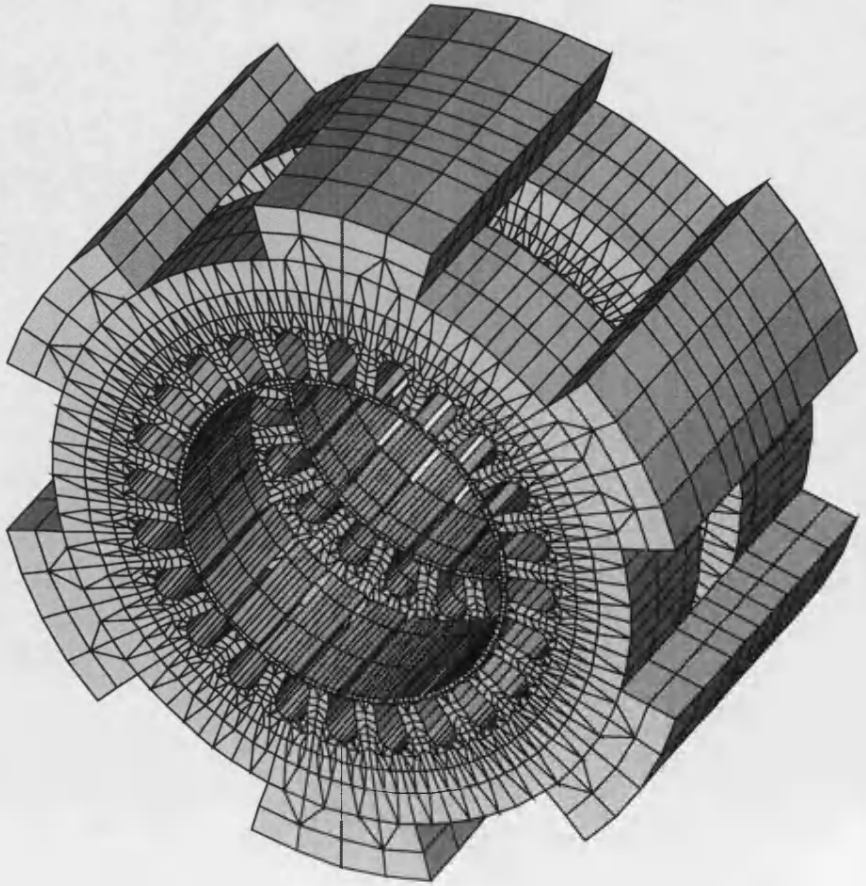

4.6 Rotor mesh

As it has been described in the previous section, a 2D slice rotor base plane has been constructed from quadrilateral and triangles elements and they are clear in Fig. 4.11. The rotor base plane has about (795) nodes and (806) elements, these numbers included the other half of the air-gap nodes and elements.

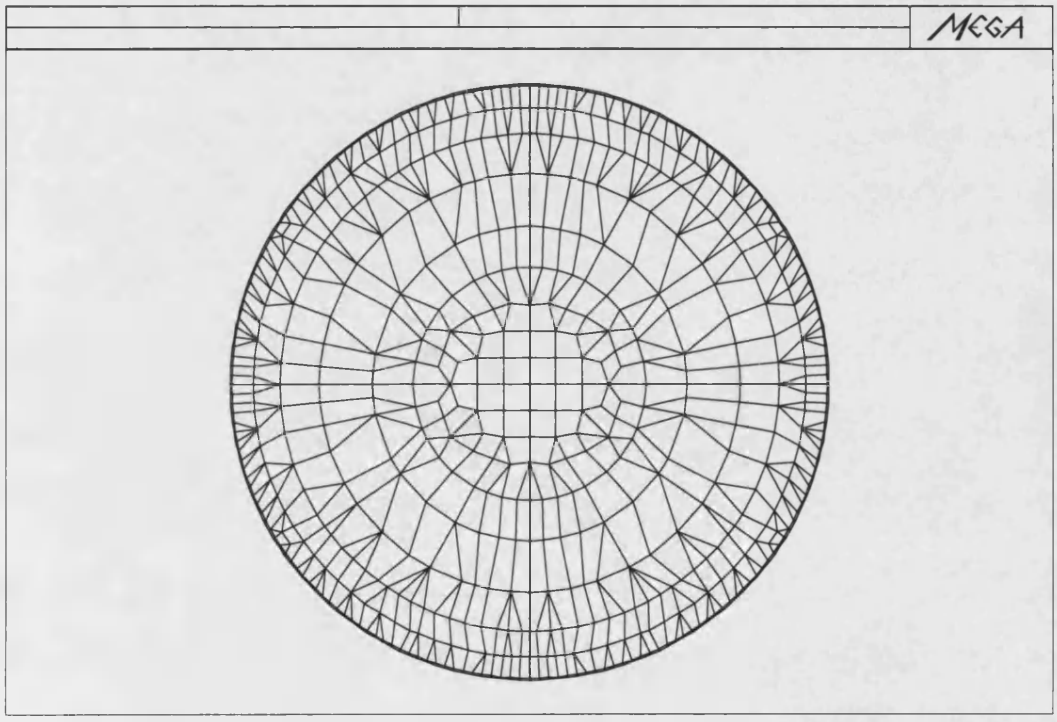

Figure 4.11: Rotor Base Plane Mesh

These elements have been characterized by given element region identification and may be observed in Fig. 4.12 and Fig. 4.13 for the heteropolar and homopolar machines.

A full 3D framework of elements has been formed by extruding the base plane on the same given display level (as it was in the stator case). Fig. 4.14 and Fig. 4.15 show the two rotors in 3D for heteropolar and homopolar machines

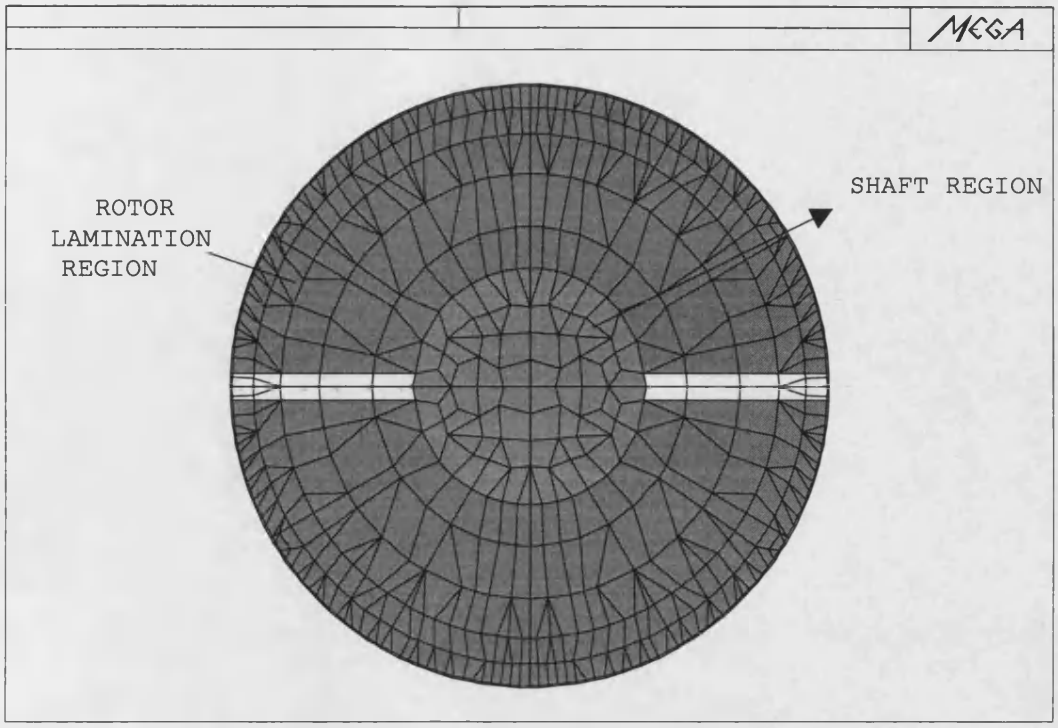

Figure 4.12: Rotor region identification, heteropolar machine

respectively and the changes in form as the plane moves in the Z-direction will be observed.

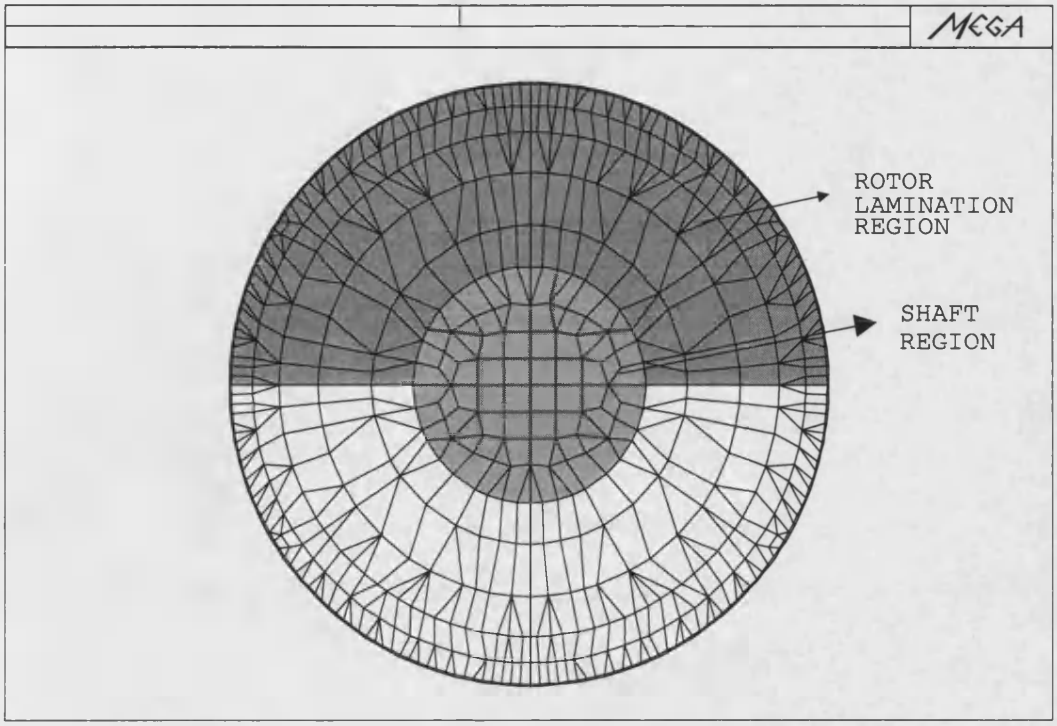

Figure 4.13: Rotor region identification, homopolar machine

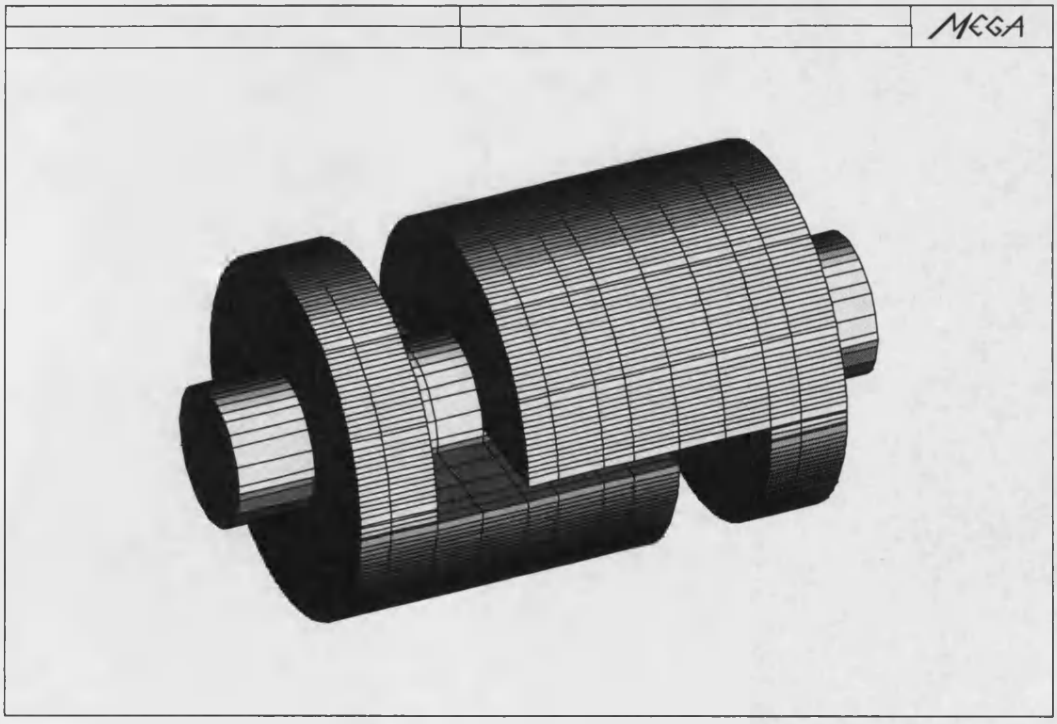

Figure 4.14: Rotor in 3D view, heteropolar machine

Fig. 4.15 3D Rotor, Homopolar machine

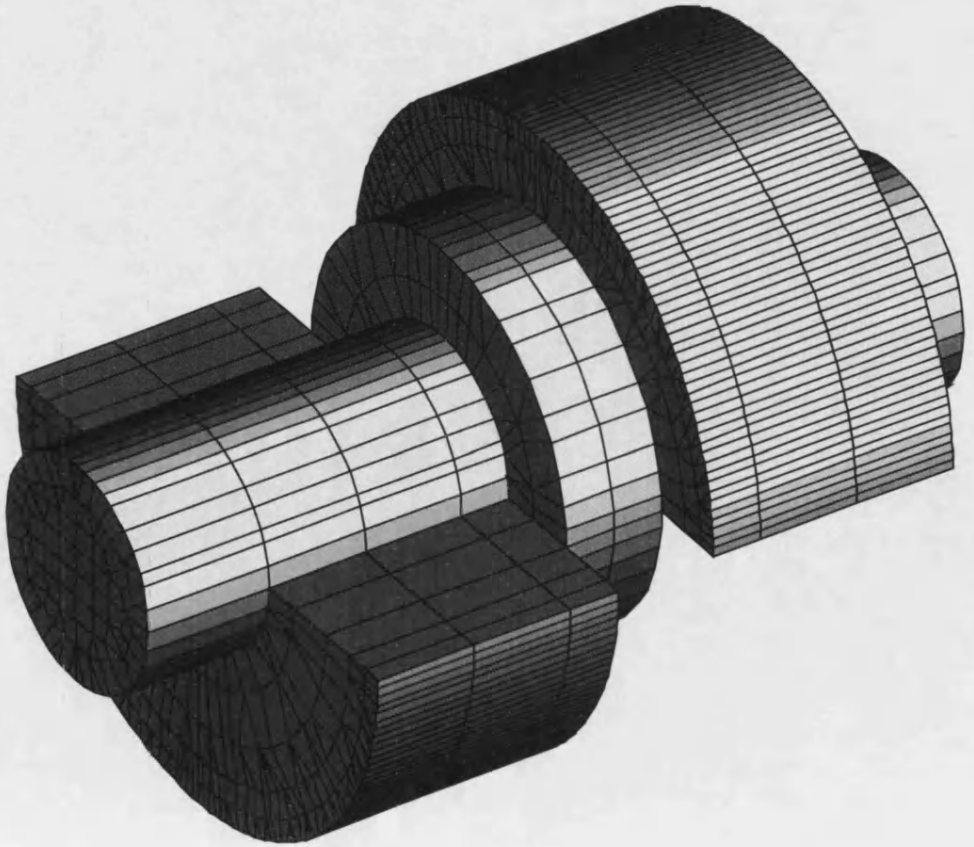

4.7 Coils representation

The MEGA program models 3D coils using a mesh (coil fragments) that is distinct from the finite element discretisation, and variety of coils can be created [27]. In this model two shapes of coils have been selected, solenoidal and saddle representing the excitation and armature coils respectively and are shown in Fig. 4.16. The full 3-phase armature winding with the excitation coil are shown in Fig. 4.17 and Fig. 4.18 for both machines heteropolar and homopolar respectively.

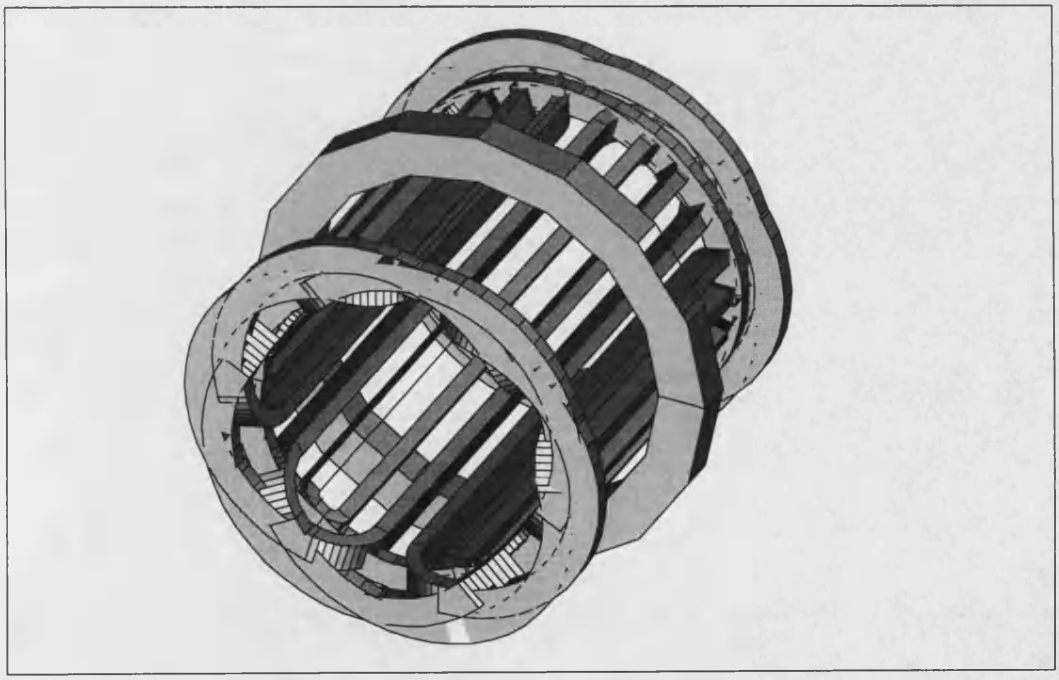

Figure 4.16: Coils used in 3D model

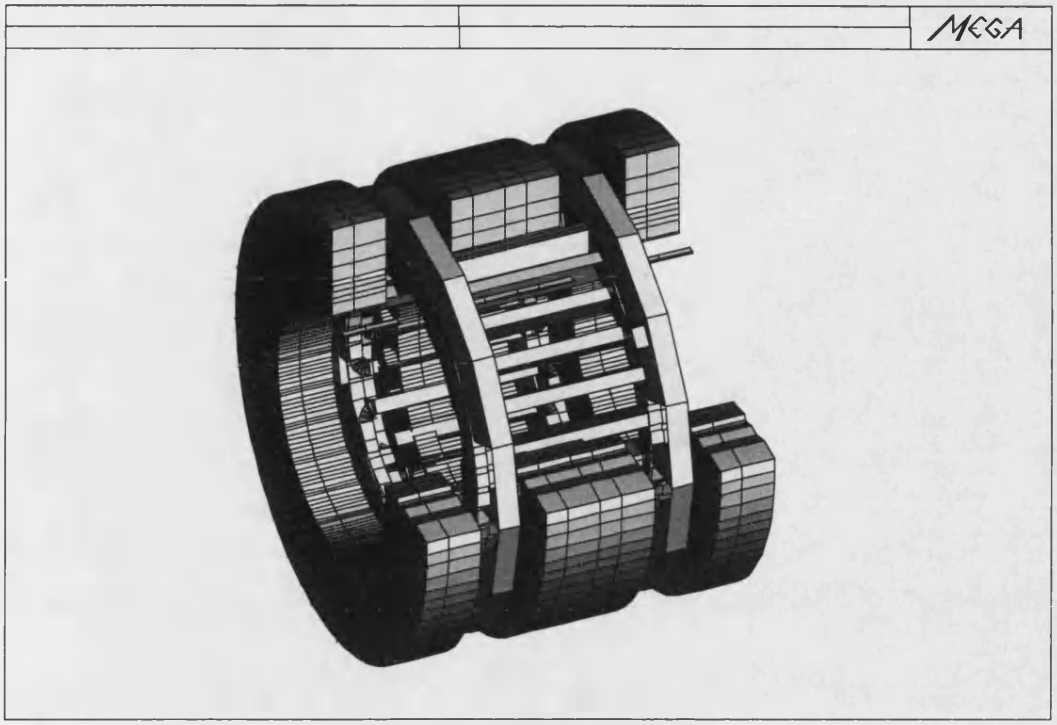

Figure 4.17: The 3 phase armature winding with the excitation coil, heteropolar machine

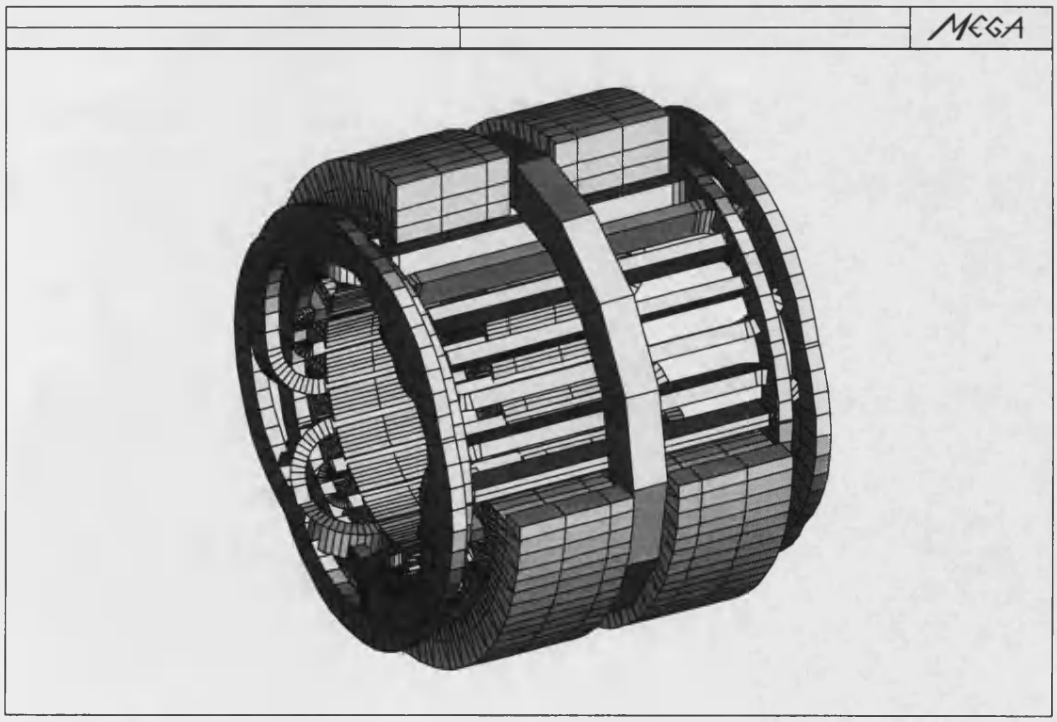

Figure 4.18: The 3 phase armature winding with the excitation coil, homopolar machine

4.8 Set-up for the reduced scalar region used for the coils

The coils must only exist in air regions of the model and the actual element in which a coil is embedded must be modelled using a reduced scalar potential of a unique region identity which is required to completely enclose the coils [38]. In this reduced scalar region shown in Fig. 4.19 and Fig. 4.20 for both machines which contain known source currents, *curl H* is no longer zero. However, since the form of the current is known, the magnetic field can be split into two parts.

The field due to the source current can be calculated using Biot-Savart:

$$\mathbf{H}_s = -\frac{1}{4\pi}\int_v \mathbf{J} \times \nabla\left(\frac{1}{r}\right) \mathrm{d}v \tag{4.13}$$

The actual field is given by the sum of the source field, H_s, and the gradient of a reduced scalar potential, Φ.

$$\mathbf{H} = -\nabla\Phi + \mathbf{H}_s \tag{4.14}$$

The volume in which this calculation is performed is called the reduced scalar region.

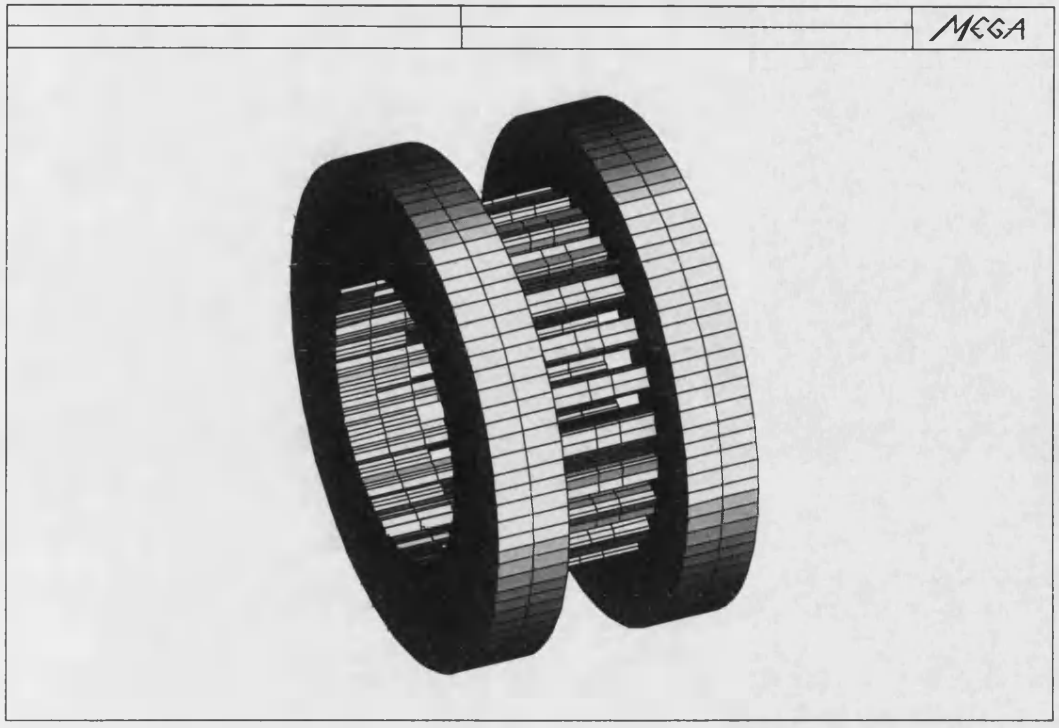

Figure 4.19: Reduced scalar region for the heteropolar machine winding

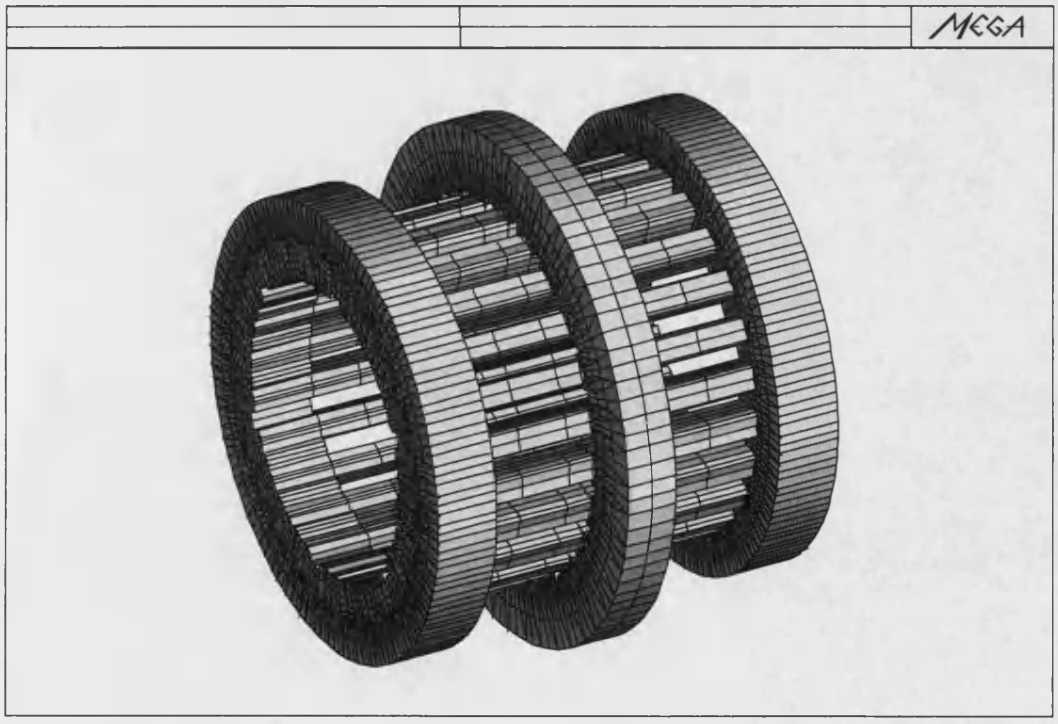

Figure 4.20: Reduced scalar region for the homopolar machine winding

4.9 Rotor Movement

It is required to model this machine with its rotor moving relative to the stator so that the characteristics of interest such as flux linkages, inductances (They are presented in chapter 5), which vary with the position can be evaluated. To carry out this kind of analysis, several meshes have to be created, one for each position and then each solved in turn. But the MEGA program has a facility of a coupling meshes using Lagrange multipliers[39].

The technique involves the use of Lagrange multipliers to couple independent meshes at a suitable interface plane. It is important that the two meshes must be created with the same reference point. Each mesh contributes half of the air gap elements (as it was explained in the previous sections 4.5 and 4.6). The nodes of the two meshes at the interface do not need to match and the number can be different and as in Fig. 4.21 which is shown for a $x - y$ plane.

The Lagrange surface is cylindrical in this problem and therefore the cylinders of the rotor and stator meshes must be coincident. Movement between the two meshes is a rotation in the given direction from the base position; and Fig. 4.22, for example, shows the rotor in the $x - y$ plane at angle of plus 45° degrees from the position base. A 3D view is shown in the following Section.

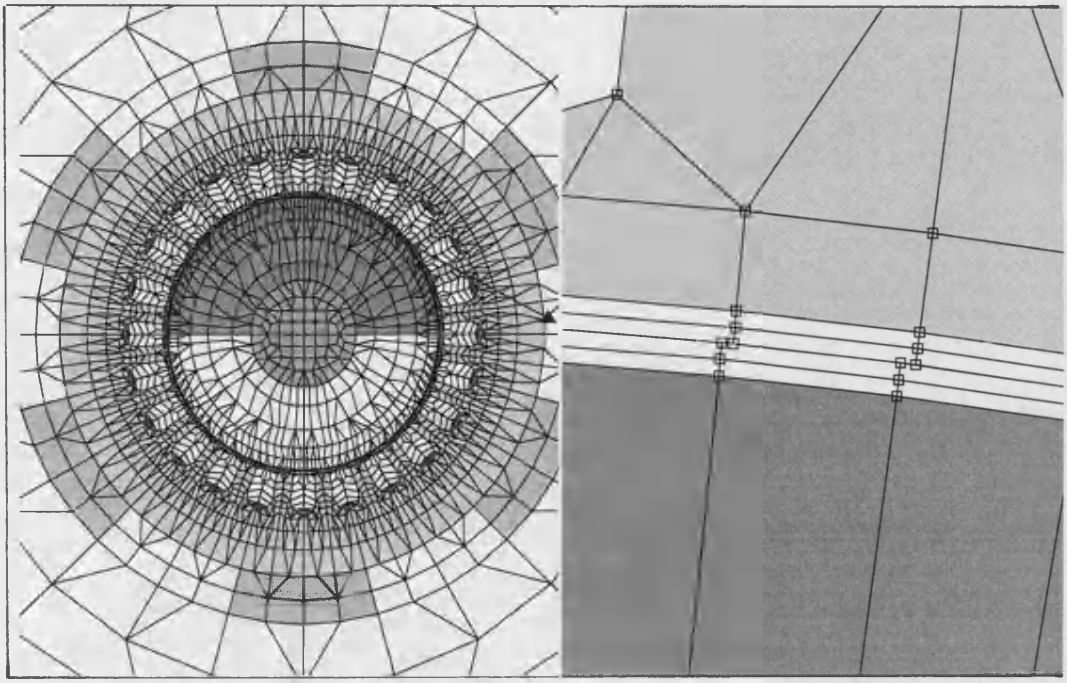

Figure 4.21: The coupling meshes

4.10 Whole machine 3D model

The full 3D mesh is shown in Fig. 4.23 and Fig. 4.24 for heteropolar and homopolar machine respectively.

The level structure of the mesh is illustrated by Fig. 4.25, Fig. 4.26, and Fig. 4.27 which show the machine cross section at three different positions in the Z direction.

Level number 4 (Fig. 4.25) has only the first half rotor slice, while the opposite side is shown in level 10 (Fig. 4.26). Level number 7 (Fig. 4.27) shows only the middle of the rotor.

The whole machine can be viewed as a 3D solid model which can be manip-

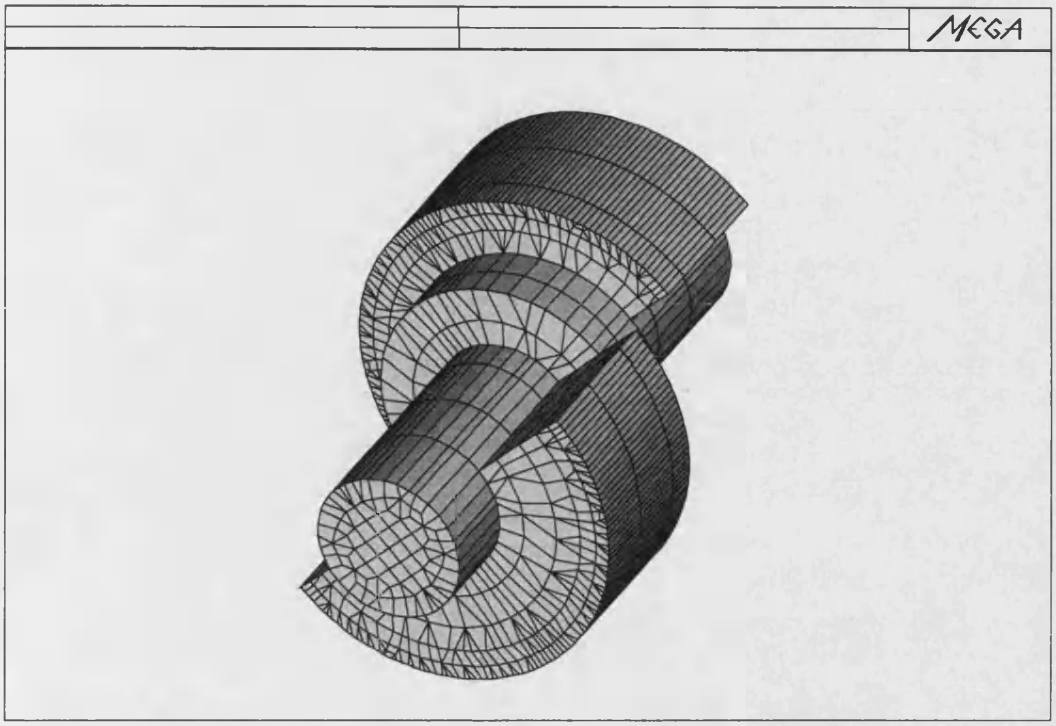

Figure 4.22: The rotor at 45° degree from base

ulated after the data of the whole mesh has been generated and is shown in Fig. 4.28 and Fig. 4.29 for heteropolar and homopolar machines respectively.

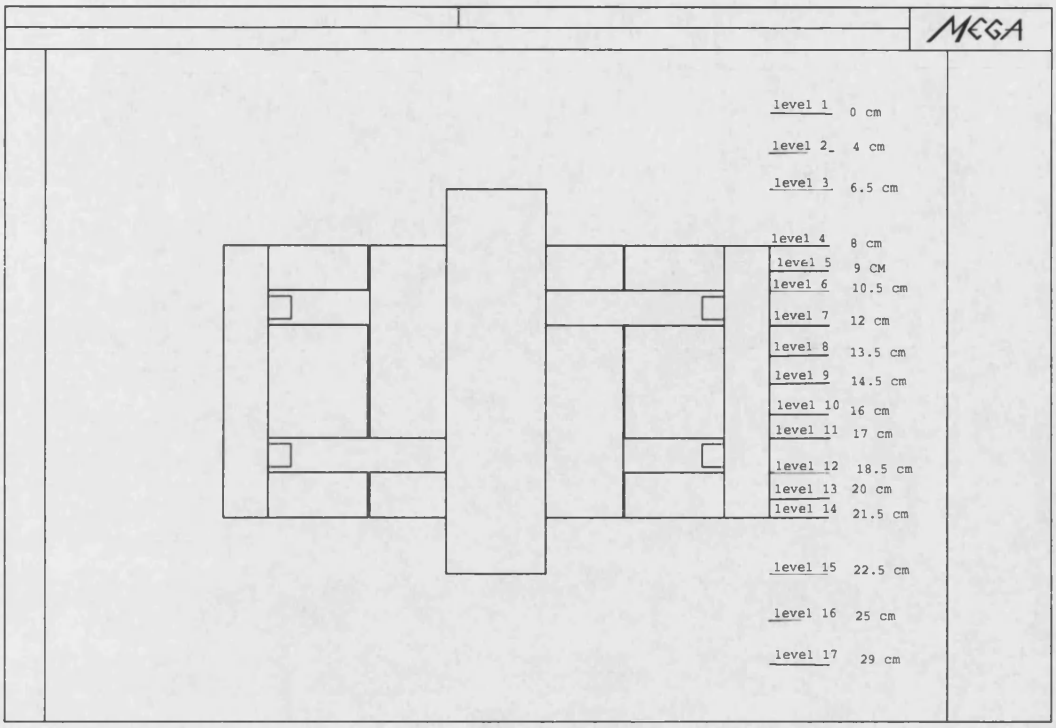

Figure 4.23: Heteropolar machine 3D extrusion

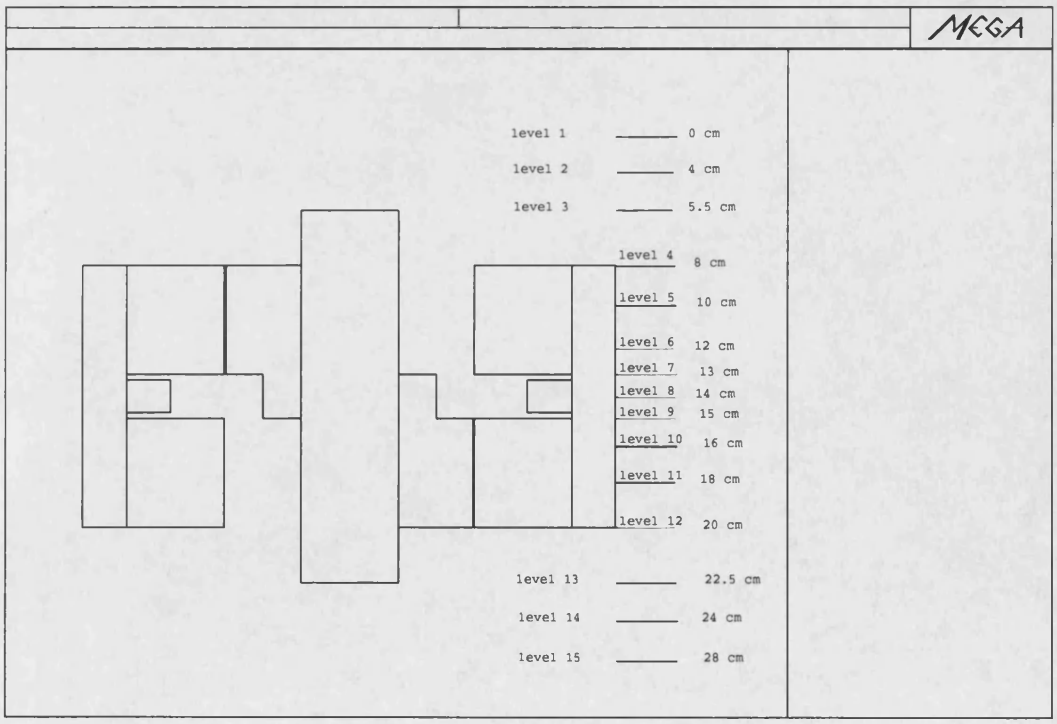

Figure 4.24: Homopolar machine 3D extrusion

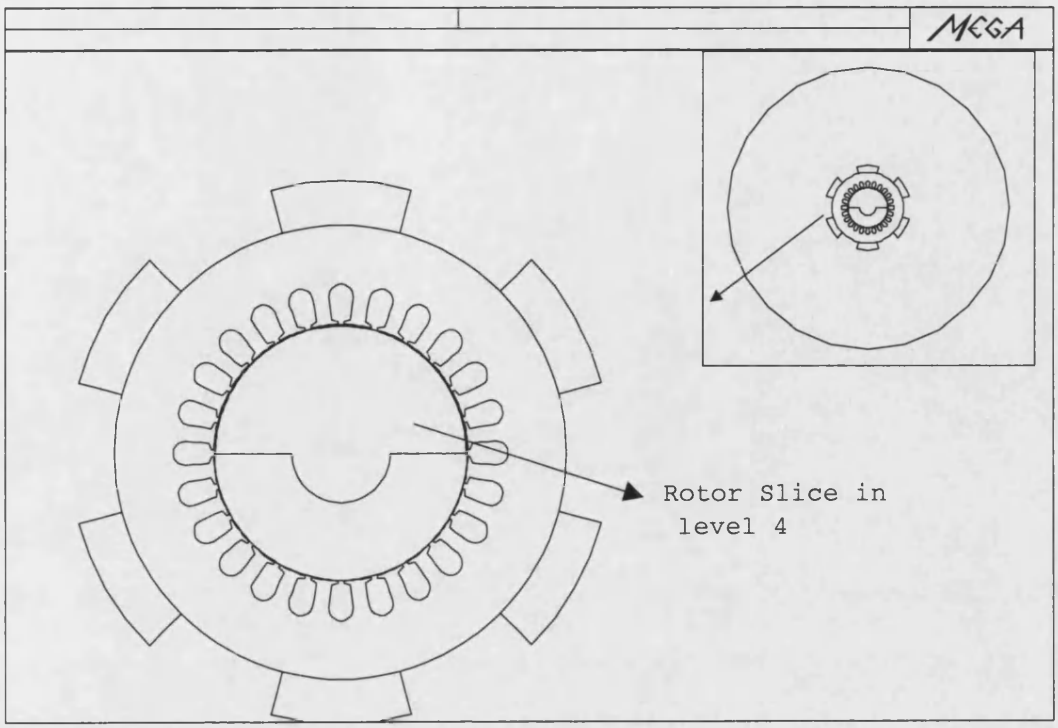

Figure 4.25: Level number 4

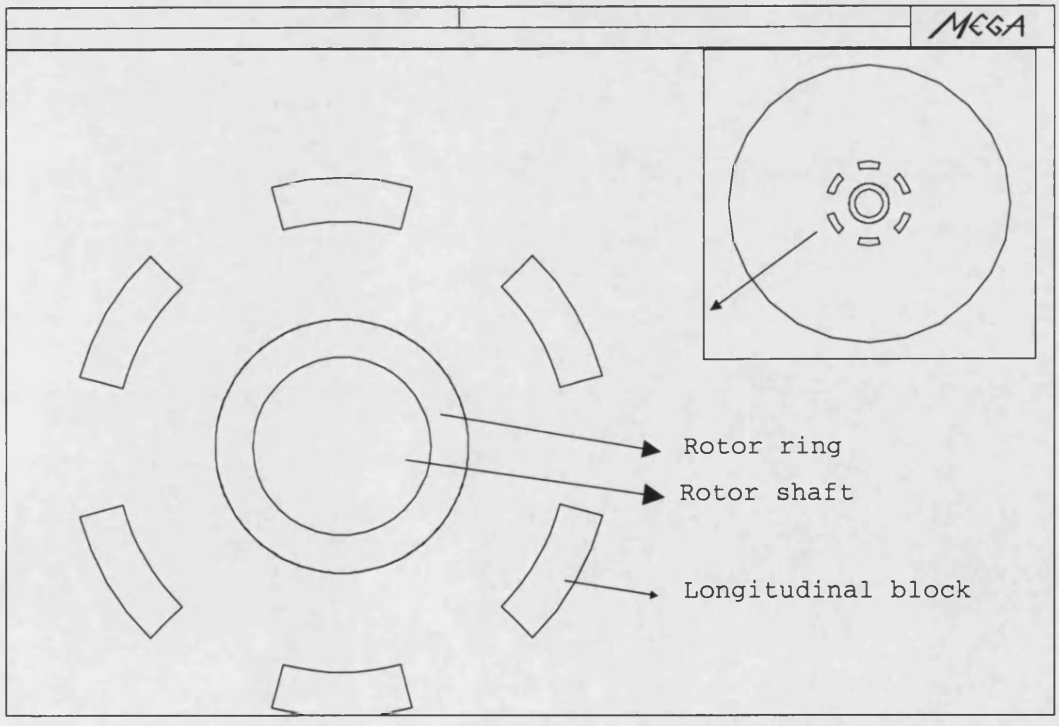

Figure 4.26: Level number 10

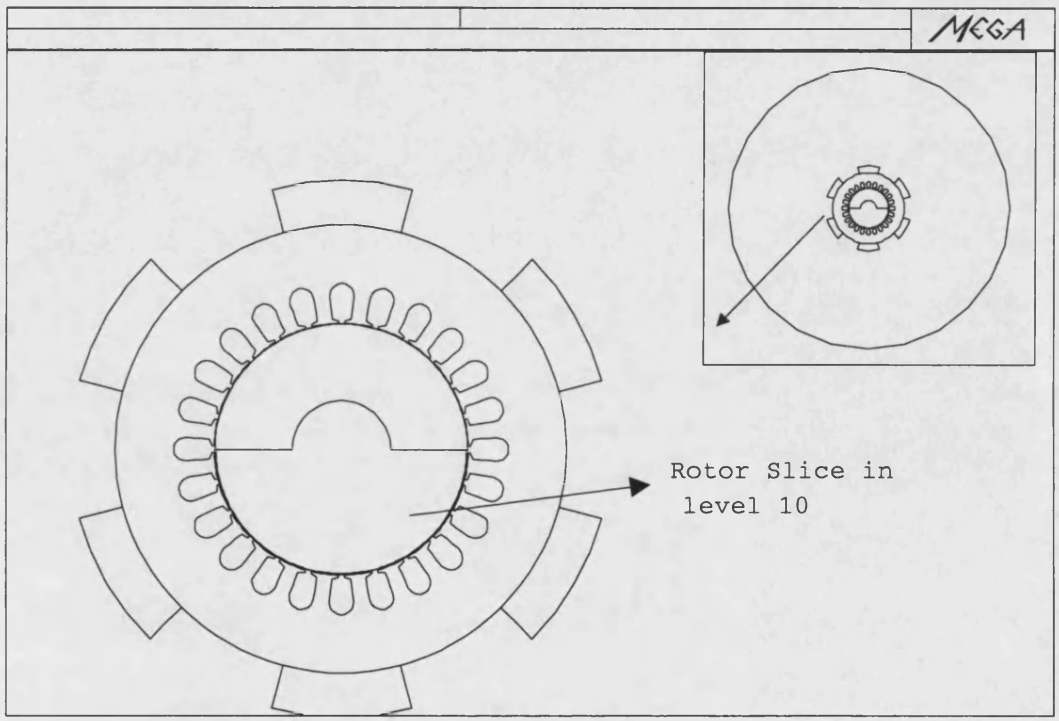

Figure 4.27: Level number 7

Fig. 4.28 Whole structure in 3D, Heteropolar machine

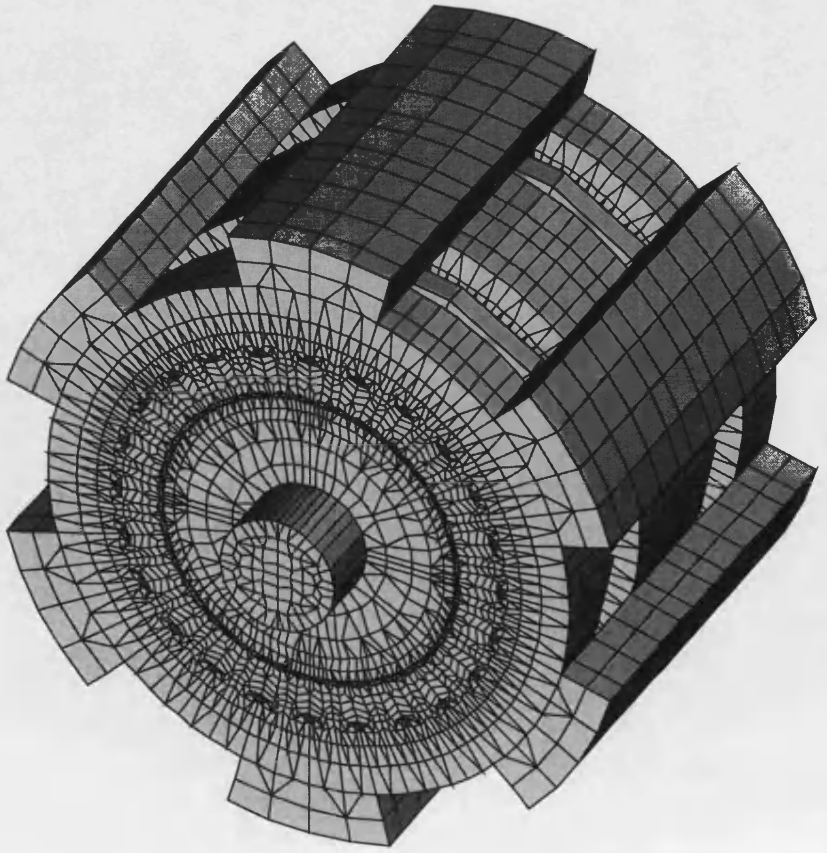

Fig. 4.29 Whole structure in 3D, Homopolar machine

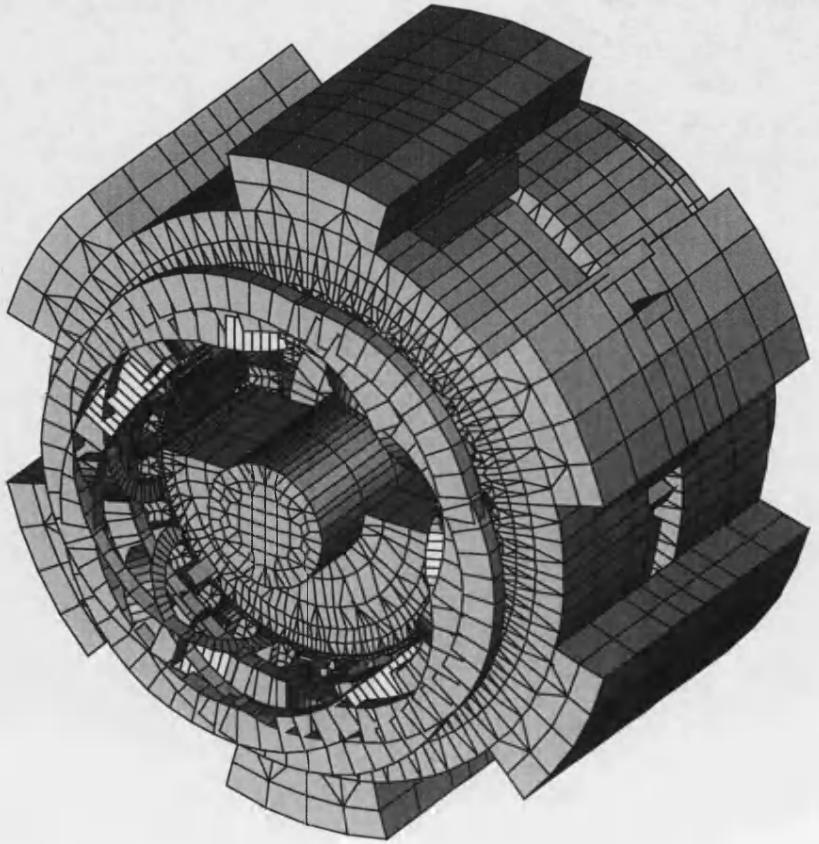

Chapter 5

A comparison between heteropolar and homopolar machines

5.1 Introduction

In this chapter designs for the two machines are presented and compared. The same armature winding and current densities are used for both machines. The field coils used are identical, one of them is needed in the homopolar case and two in the heteropolar case.

The homopolar machine was first designed in 3D FE with dimensions as shown

in Fig. 5.1. To meet the requirement that the induced voltage in the stator windings of the heteropolar design is the same as the homopolar, the dimensions shown in Fig. 5.2 were used. It will be noticed from the magnetic circuit of this machine that the middle stator is the same as one side of the homopolar stator. The other two outside cores are each one half the width of the centre core, since the flux density B_t in the slotted middle stator of a width d as shown in the sketch diagram in Fig. 5.3(A) is the same flux density of the other outside unslotted cores of a width $d/2$ as shown in the sketch diagram in Fig. 5.3(B). The $30mm$ space between the middle stator and the side cores has been left for the end turns of the AC winding. This is the same distance that has been used for the AC winding of the homopolar machine.

5.2 Excitation losses:

For the same excitation current, the total excitation losses in both machines are:

In the homopolar machine (one coil):

$$= I_{fho}^2 \times R$$

Where R is the field coil resistance, and I_{fho} is the homopolar machine field current.

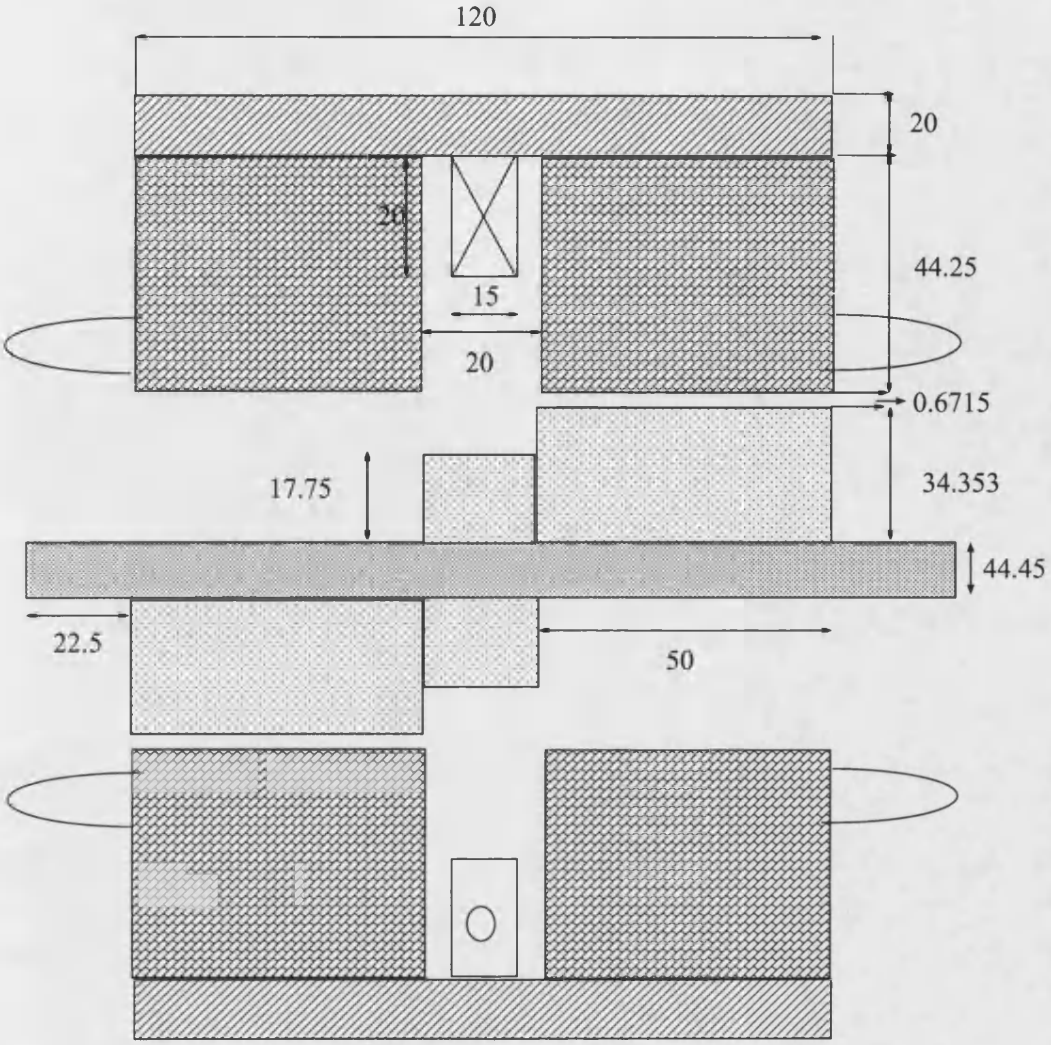

Figure 5.1: Homopolar Machine Dimensions

and for the heteropolar machine (two coils):

$$= 2 \times I_{fht}^2 \times R$$

I_{fht} is the heteropolar machine field current.

but for the same induced voltage in both machines, only 90% of the field current is needed as it is shown in Fig. 5.4.

Therefore the excitation loss in *heteropolar machine is:*

$$= 2 \times (0.9 I_{fho})^2 \times R = 1.62 \times I_{fho}^2 \times R$$

Therefore the loss in the heteropolar case is only 62% more than the loss in the homopolar machine, even though twice might be expected because there are two coils. For equal induced emf the losses are 32.8 *watts* in the heteropolar and 20.2 *watts* in the homopolar machine at $I_{fho} = 4.5$ *amperes* and $R = 1\Omega$.

5.3 Armature losses

In the homopolar machine the length of mean turn of the AC winding is about 55.6 *cm*. In the heteropolar machine, it is 41.6 *cm*, so that the armature resistance of the homopolar machine is 1.34 times the heteropolar.

In the heteropolar machine:

$$Armature \;\; losses = 3 \times I_{arm.}^2 R_{arm.} = 21.6 \;\; (watts)$$

at $I_{arm.} = 3$ *amperes* and $R_{arm.} = 0.8\ \Omega$.

In the homopolar machine:

$$Armature\ \ losses = 3 \times I^2_{arm.} \times 1.34 R_{arm.} = 4 I^2_{arm.} \times R_{arm.} = 28.8\ \ (watts)$$

again at at $I_{arm.} = 3$ *amperes* and $R_{arm.} = 0.8\ \Omega$.

5.4 Iron losses:

The total loss has been calculated in each part of the stator of each machine, in the teeth, back iron, and in the longitudinal blocks. The method was to first find value of the peak flux density and then corresponding value of specific loss in $watt/kg$ was found from steel manufacturers curves and they are presented in appendix [E].

Fig. 5.5, shows the flux around the longitudinal and stator parts for both machines (top picture for the homopolar and the other one for the hetropolar machine).

For the heteropolar machine: The peak flux density in the teeth is 0.72 *tesla* and, the specific total loss is 1.28 $watt/kg$. Meanwhile the peak flux density in the back iron is 0.5 *tesla* and the corresponding specific total loss value is 0.74

$watt/kg$.

The total specific loss in the teeth and the back iron is $1.28+0.74 = 2\ watts/kg$.

In the longitudinal blocks the peak flux density is 0.22 *tesla* which gives the corresponding specific loss of 0.22 $watts/kg$.

The volume of the stator is 2.013×10^{-3} and the volume density is 7690 kg/m^3 which gives the total weight of 15.5 kg.

Therefore the losses in the teeth and back iron is $15.5kg \times 2.02watts/kg = 31.31watts$.

The volume of the longitudinal blocks is 1.112×10^{-3} and for the same volume density above the losses is $0.22watts/kg \times 8.55kg = 1.88watts$.

Therefore the total iron loss in the stator in the heteropolar machine is $31.31 + 1.88 = 33.19$ $watts$.

For the homopolar machine: The peak flux density in the teeth is 0.77 *tesla* and from the curve in the appendix [E], the specific-total loss is $1.5watt/kg$. Meanwhile the peak flux density in the back iron is 0.4847 *tesla* and the corresponding specific total loss value is 0.71 $watt/kg$.

The total specific loss in the teeth and the back iron is $1.5 + 0.71 = 2.21$ $watt/kg$.

In the longitudinal blocks the peak flux density is 0.2 *tesla* which gives the corresponding specific loss of 0.18 $watts/kg$.

The volume of the stator is 1.8×10^{-3} and the volume density is 7690 kg/m^3 which gives the total weight of 14 kg.

Therefore the losses in the teeth and back iron is $14kg \times 2.2watt/kg = 31$ $watts$.

The volume of the longitudinal blocks is 0.834×10^{-3} and for the same volume density above the losses is $0.18watts/kg \times 6.42kg = 1.2$ $watts$.

Therefore the total iron loss in the stator of the homopolar machine is $30.9 + 1.2 = 32.1$ $watts$.

5.5 Weight comparison

The weight of the two machines was calculated and found to be homopolar 26.22 kg, and heteropolar 32.35 kg.

5.6 Comparison of the two machines

Table 5.1 compares the two machines. For equal induced emf and armature current the loss in the heteropolar is 10% greater than the loss in the homopolar machine. In addition the mass of the heteropolar is about 19% greater than the homopolar. On this simple basis therefore the homopolar machine has the advantages of both loss and weight and is to be preferred.

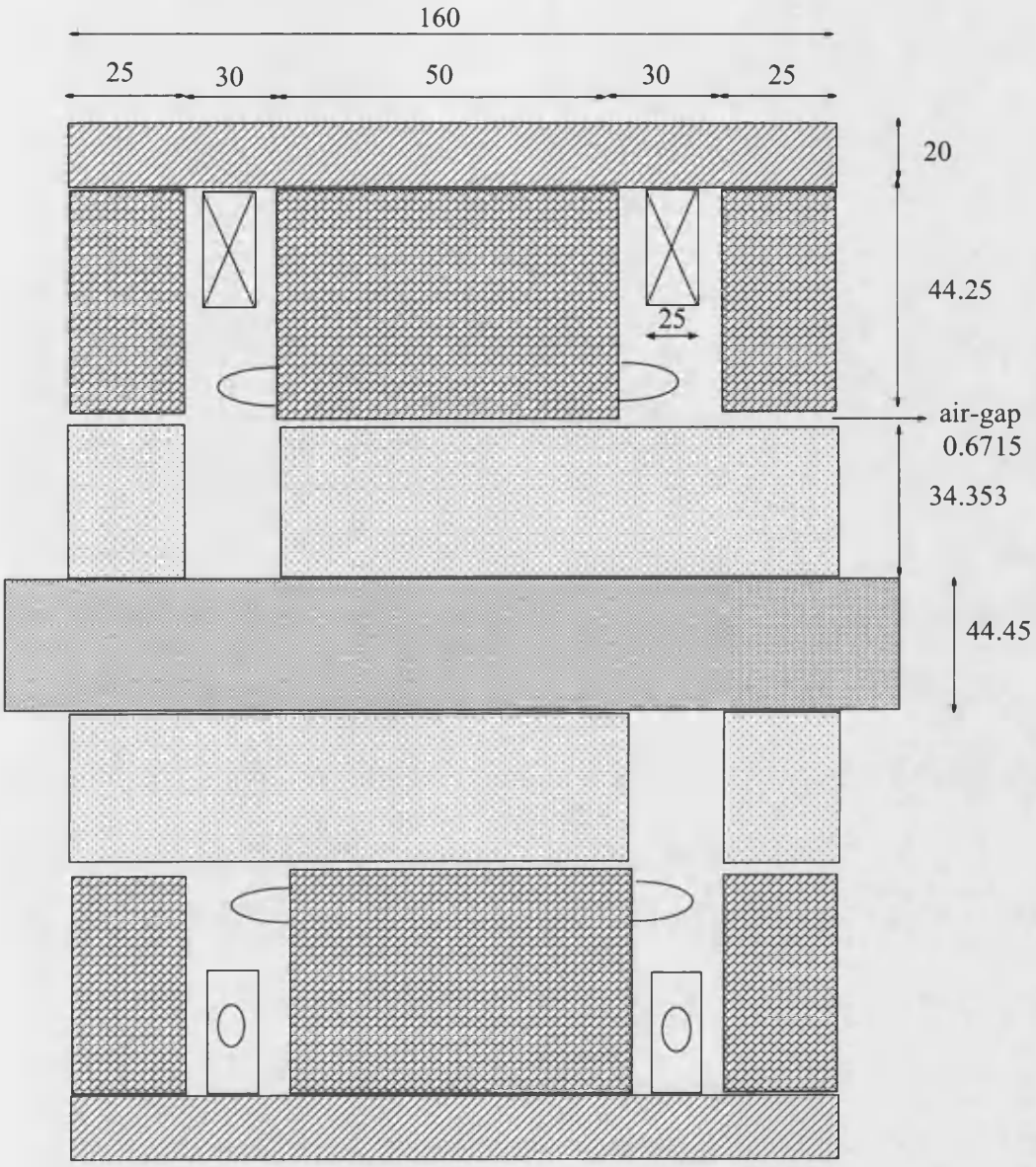

Figure 5.2: Heteropolar Machine Dimensions

Weight(kg) and loss($watt$)	**Heteropolar**	**Homopolar**
field loss	32.8	20.2
Armature loss	21.6	28.8
Total loss	54.4	49
Stator weight	24.05	20.42
Rotor weight	8.3	5.8
Total weight	32.35	26.22

Table 5.1: Comparison in weight and loss for both machines

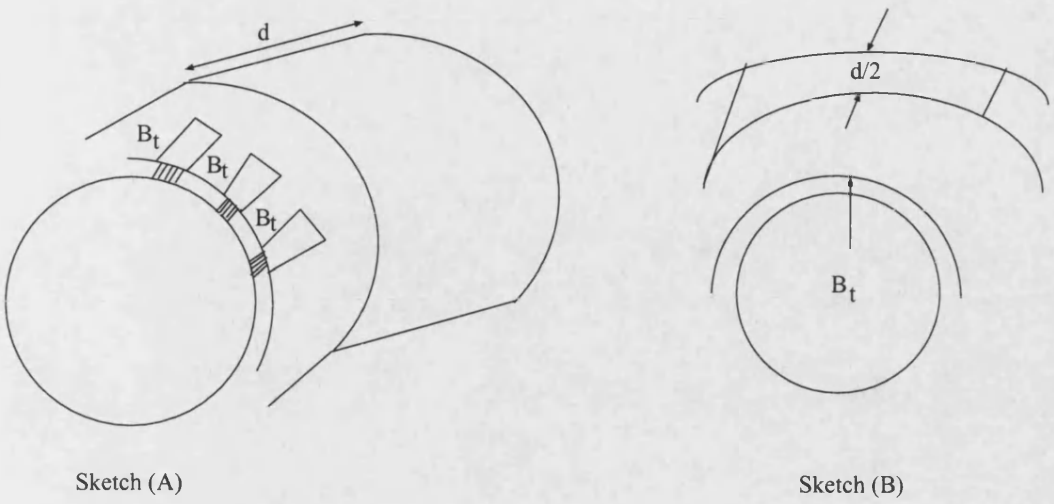

Figure 5.3: Sketch diagrams of d and $0.5d$ core width

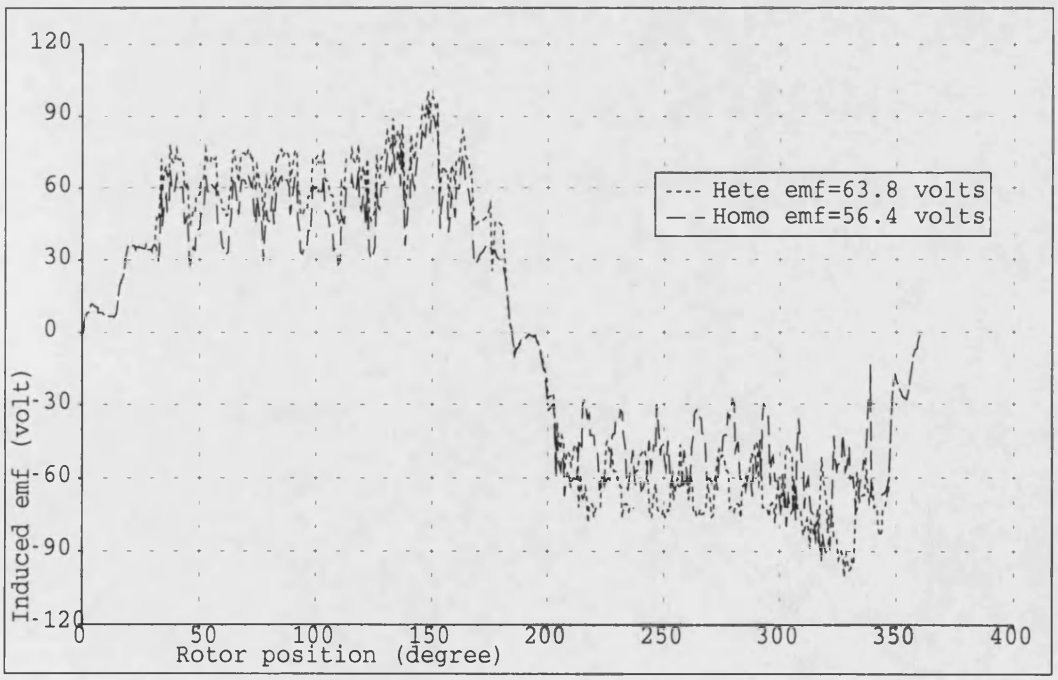

Figure 5.4: Phase-R only in both machines

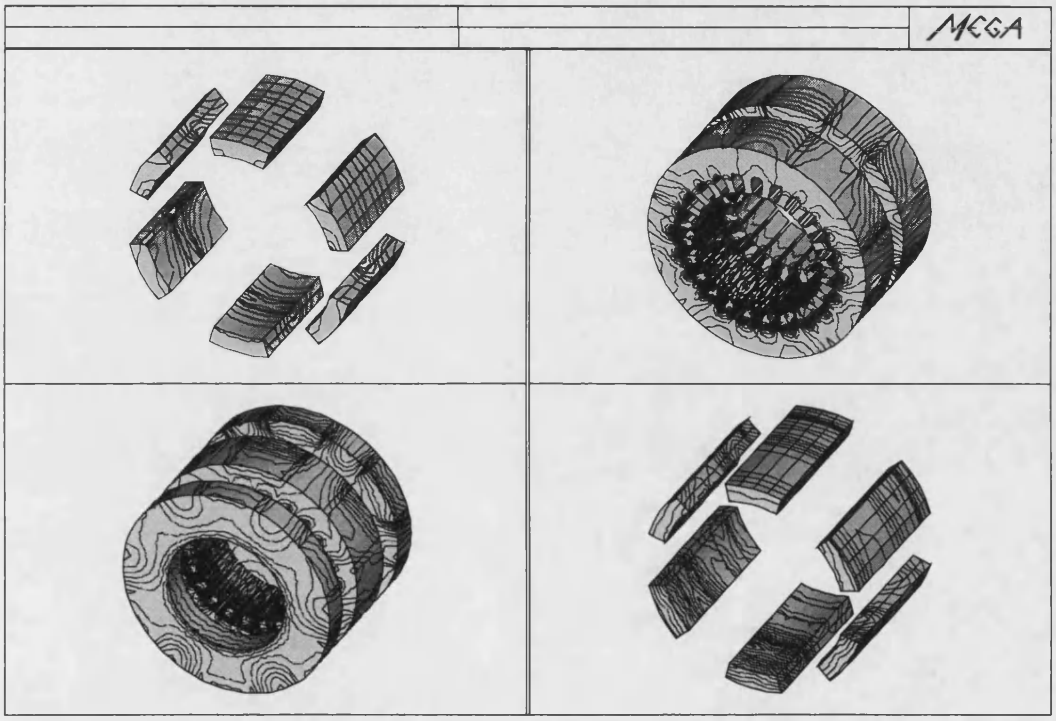

Figure 5.5: flux around the longitudinal blocks and stator

Chapter 6

Calculation by FE of machine parameters and performance. Verification with practical tests

6.1 Introduction

In this chapter calculation of the machine parameters and its performance by FE are presented together with the practical tests results.

The first exercise performed in these calculations was to check the induced emf at no load for both heteropolar and homopolar machines, by working out individual coil voltages and assessing the effect of the pole shape. The induced

emf was calculated from the rate of change of the flux linkages, and these in turn were found from the 3D FE machine model(the 3D FE models were described in chapter 4). Calculated emf phase voltages have already been used in the previous chapter for comparison purposes of the two machines.

In the second exercise, the coils in the armature were connected together to represent a $3-phase$ star connection, for example, $phase-R$ consists of four coils. To join them in series, the automatic port connection [27] facility in the FE package was used (please see Fig.3.8. for more details). Other coils belonging to other phases are also connected in the same way to represent $phase-Y$ and $phase-B$ and these phases were star connected.

A time stepped solution using FEM was used in different conditions:

1- When the field coil was the only excited coil. Here a wide range of current values were used and the emf on open circuit was calculated.

2- When the armature coils only were excited to find the unsaturated synchronous reactance and the ratio of X_d and X_q from the slip test.

3- When both field and armature windings are excited to represent the case of load performance. The field coil was connected to an external current source while the armature winding was connected to variable resistive and variable inductive loads.

4- The calculated parameters found in 1 and 2 above were used in the phasor diagram shown in Fig. 6.1 to find the load performance as a quick solution.

This is not as accurate as FE , however FE takes a long time to implement, for example one step of the 3D time-stepped solution takes about one hour shown on a HP 9000/720 $96MB\ RAM\ Workstation$, and about 120 steps are required per cycle.

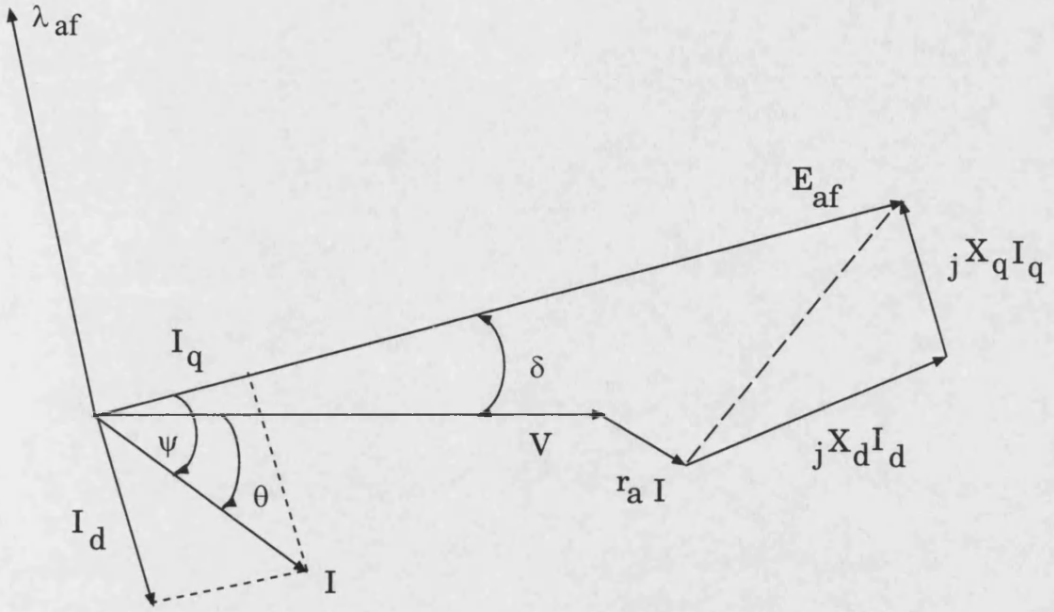

Figure 6.1: Synchronous machine phasor diagram

6.2 Calculation of armature phase flux linkage on no-load for the induced emf calculation.

The generated voltage of the machine appears at the terminals when there is no armature current flowing hence putting $i = 0$ in equation (6.1) we find:

$$\left[V \right] = -\left[R \right]\left[i \right] - \frac{\mathrm{d}}{\mathrm{d}t}\left\{ \left[L \right]\left[i \right] \right\} - \frac{\mathrm{d}}{\mathrm{d}t}\left[\lambda \right] \tag{6.1}$$

$$\left[V \right] = -\frac{\mathrm{d}}{\mathrm{d}t}\left[\lambda \right] \tag{6.2}$$

Where λ is the phase flux linkage.

Hence once the λ is known the phase emf can be calculated .

$$e = -\frac{d\lambda}{dx} \times \frac{dx}{dt} \tag{6.3}$$

In order to calculate λ the flux linking the separate armature coils is first calculated. This can be obtained from the 3D finite element plot as illustrated on Fig. 6.2 by defining 3, 3D surfaces and taking the average surface integral obtained from them.

Phase flux linkage can then be formed by adding the coil flux linkage from the coils of a phase (Fig. 6.3 gives the coil numbering used in the calculation) as described below.

The phase flux linkage can be expressed in terms of coil linkages as shown below:

$$\lambda_{phase-R} = \lambda_{CR1} + \lambda_{CR2} - \lambda_{CR3} - \lambda_{CR4} \tag{6.4}$$

$$\lambda_{phase-Y} = \lambda_{CY1} + \lambda_{CY2} - \lambda_{CY3} - \lambda_{CY4} \tag{6.5}$$

$$\lambda_{phase-B} = \lambda_{CB1} + \lambda_{CB2} - \lambda_{CB3} - \lambda_{CB4} \tag{6.6}$$

Where $-ve$ sign represents the winding direction of the coil.

The armature coil flux linkages were calculated using 3D field plots. The field distribution in Fig. 6.4 and Fig. 6.5 for heteropolar and homopolar machines respectively are used in this calculation. The normal component of the mid air-gap flux density with the rotor at standstill is plotted on Fig. 6.6 and Fig. 6.7 for both machines.

Calculated flux linkages of the coils at different rotor positions are given in Fig. 6.8 for the small central coils of the concentric group and in Fig. 6.9 for the large coils of the heteropolar machine. Similar results are shown in Fig. 6.10 and Fig. 6.11 for the homopolar machine. It will be observed that there is the expected 60° space shift between consecutive coil groups. The linkages of coils

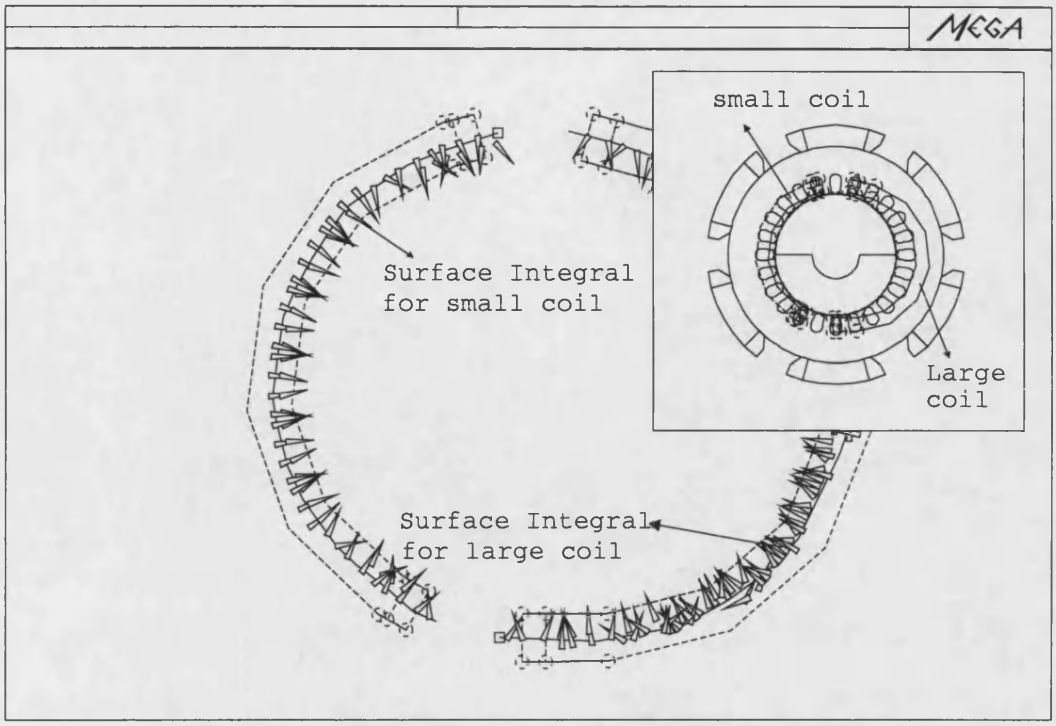

Figure 6.2: Surface integral along the coil

from a 3 phase set $C_{B1} + C_{B2}$ and $C_{Y4} + C_{Y3}$, $C_{R1} + C_{R2}$ are the same as those from coil groups $C_{R3} + C_{R4}$, $C_{B3} + C_{B4}$ and $C_{Y1} + C_{Y2}$ due to their symmetrical placement. Fig. 6.12 and Fig. 6.13 illustrate the flux linkage for the coil group of $phase - R$ for both heteropolar and homopolar machines respectively. From the above graphs, it can be seen that there are harmonics due to the slotting present, these can be minimised by skewing.

The general shape of the wave form is not sinusoidal but can be improved by shaping the poles so that the air-gap at the longitudinal pole edges is increased with respect to that in the pole centre. This is discussed in section 6.3 below.

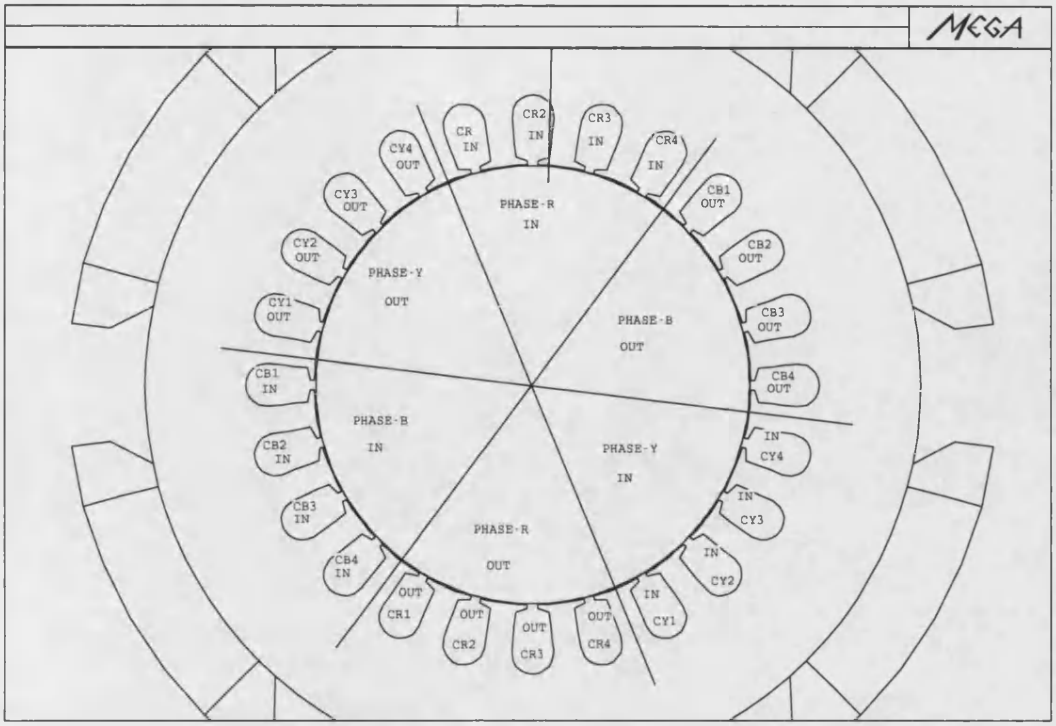

Figure 6.3: Coil numbering system

6.3 Coil flux linkage with modified rotor profile.

A more sinusoidal waveform can be obtained if the rotor is re-profiled as shown in Fig. 6.14 in 2D and Fig. 6.15 in 3D. It will be observed that the new profile has reduced the flux linkage as shown in Fig. 6.16 and reduced the harmonic content as shown in table 6.1, for coil C_{R2} of $phase - R$.

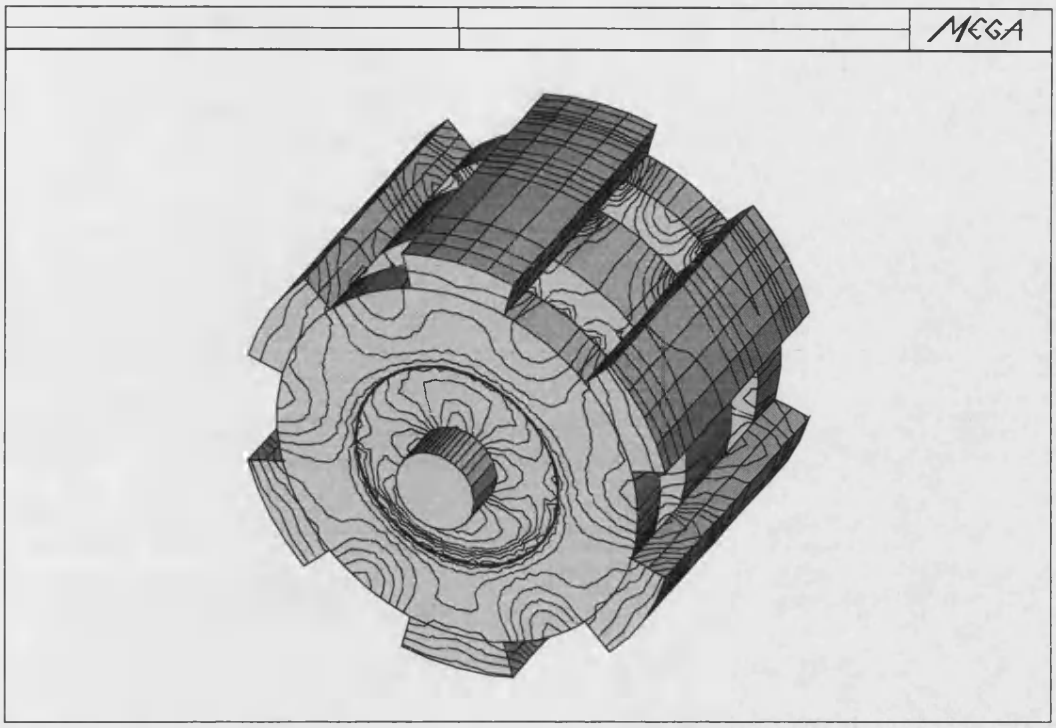

Figure 6.4: Field Distribution, heteropolar machine

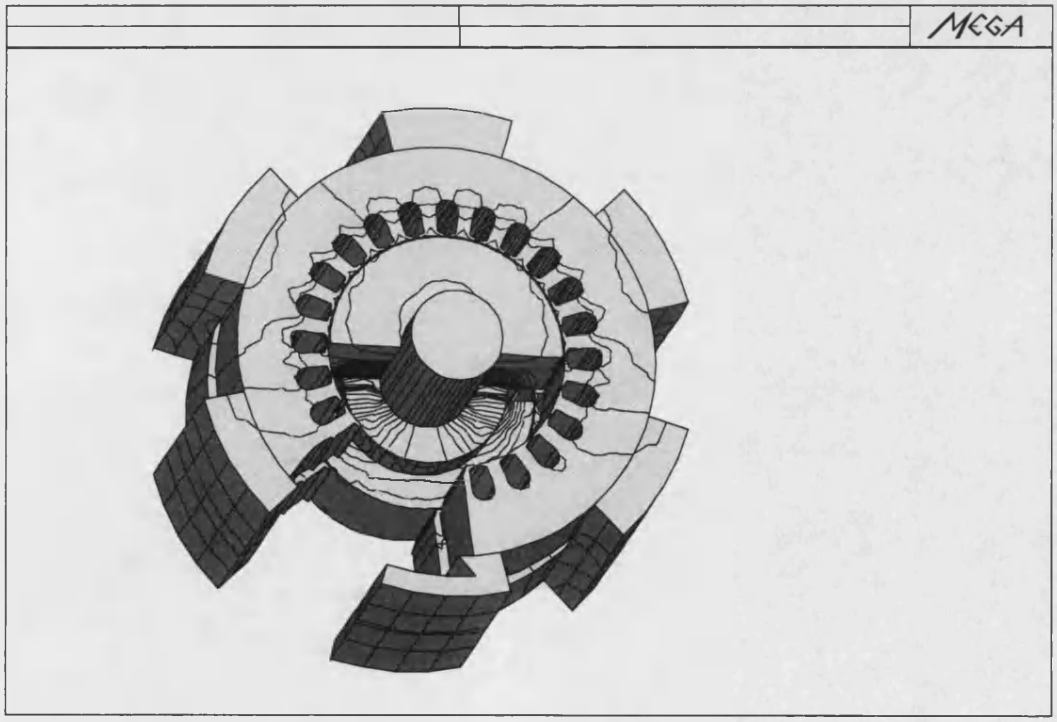

Figure 6.5: Field Distribution, homopolar machine

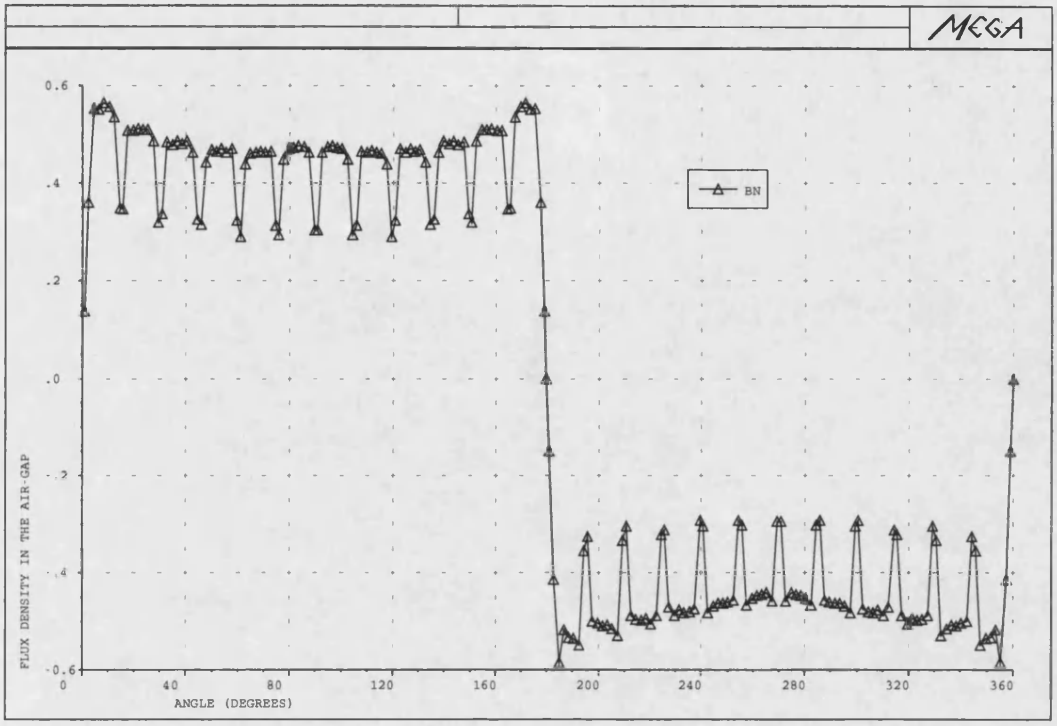

Figure 6.6: Air-gap flux density, heteropolar machine

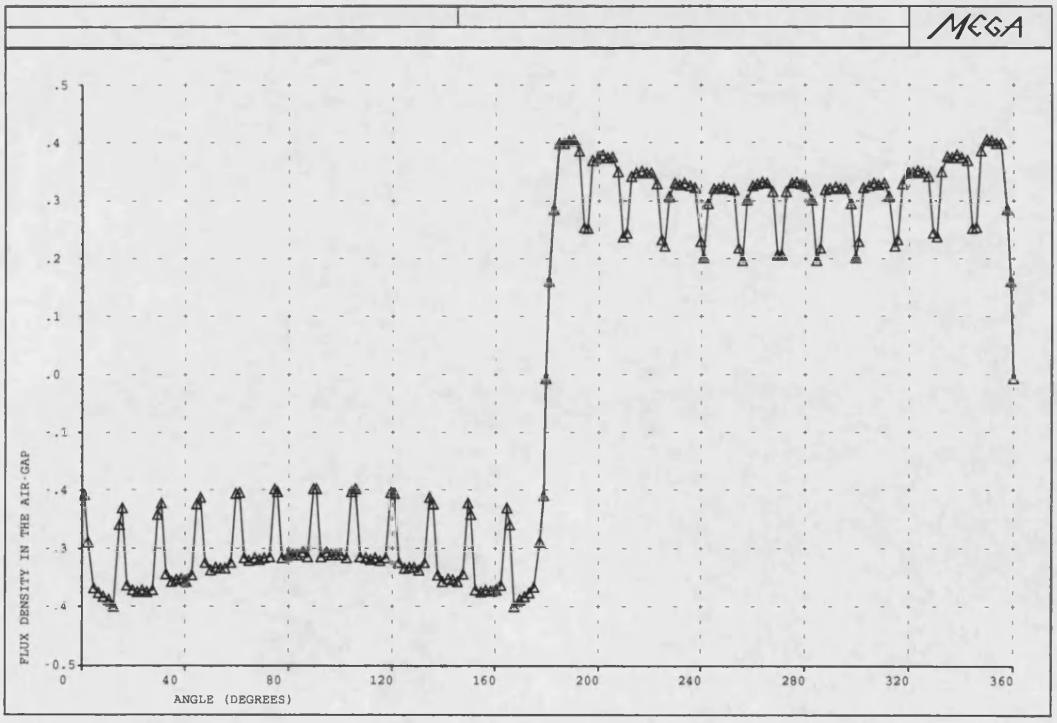

Figure 6.7: Air-gap flux density, homopolar machine

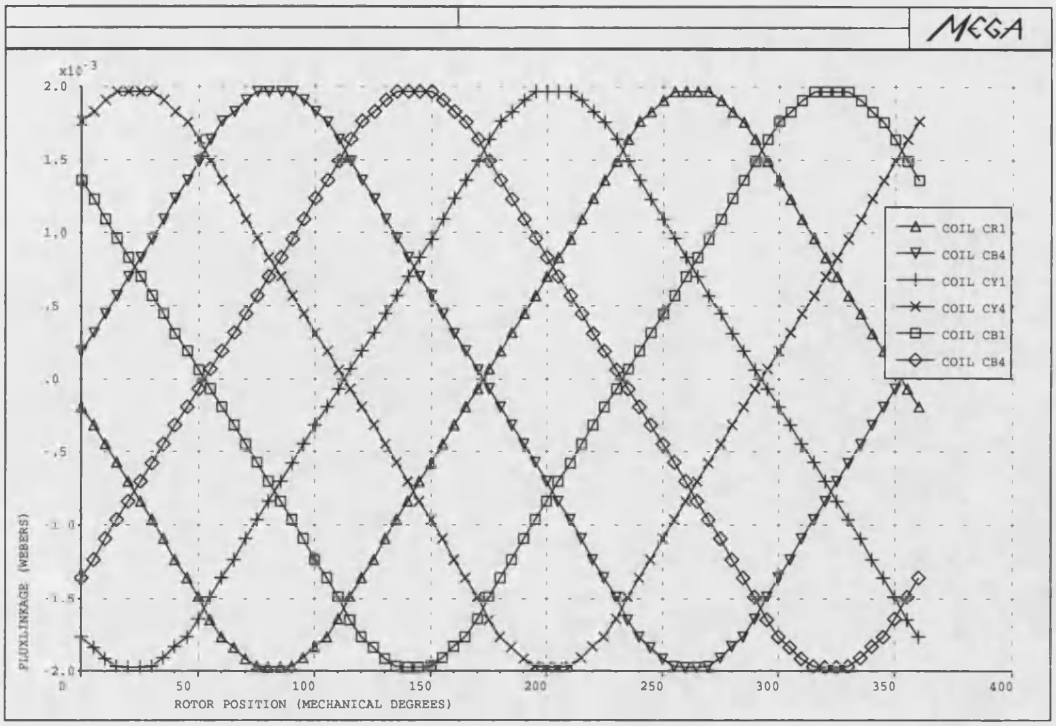

Figure 6.8: Flux-linkage of the inner coils in the concentric group in the heteropolar machine.

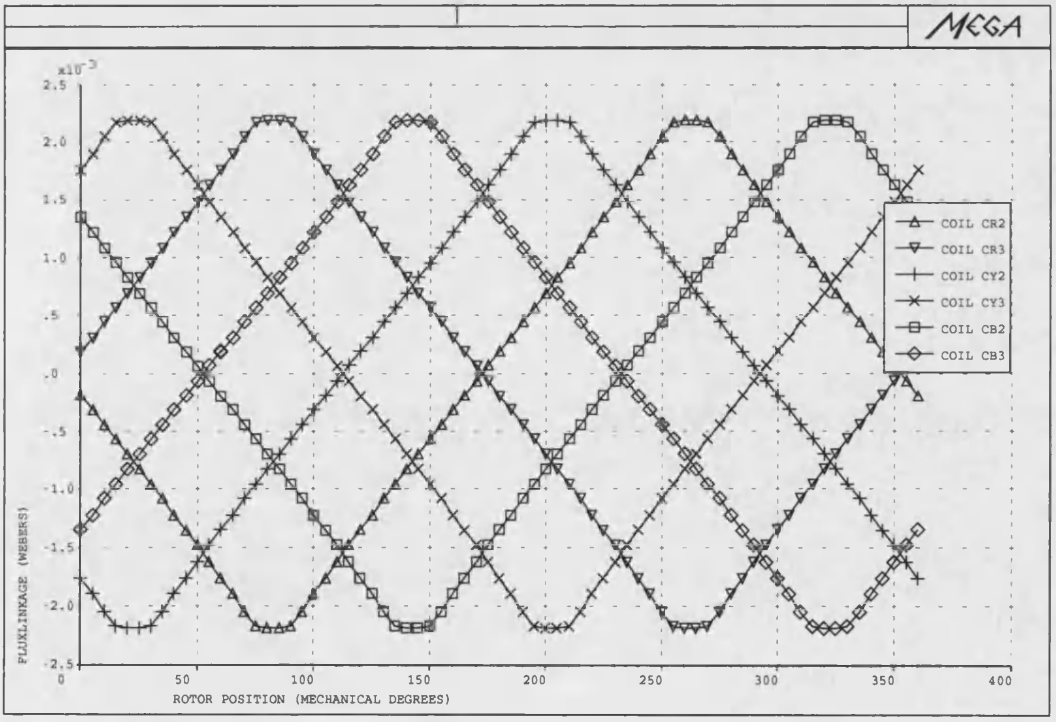

Figure 6.9: Flux-linkage of the outer coils in the concentric group in the heteropolar machine

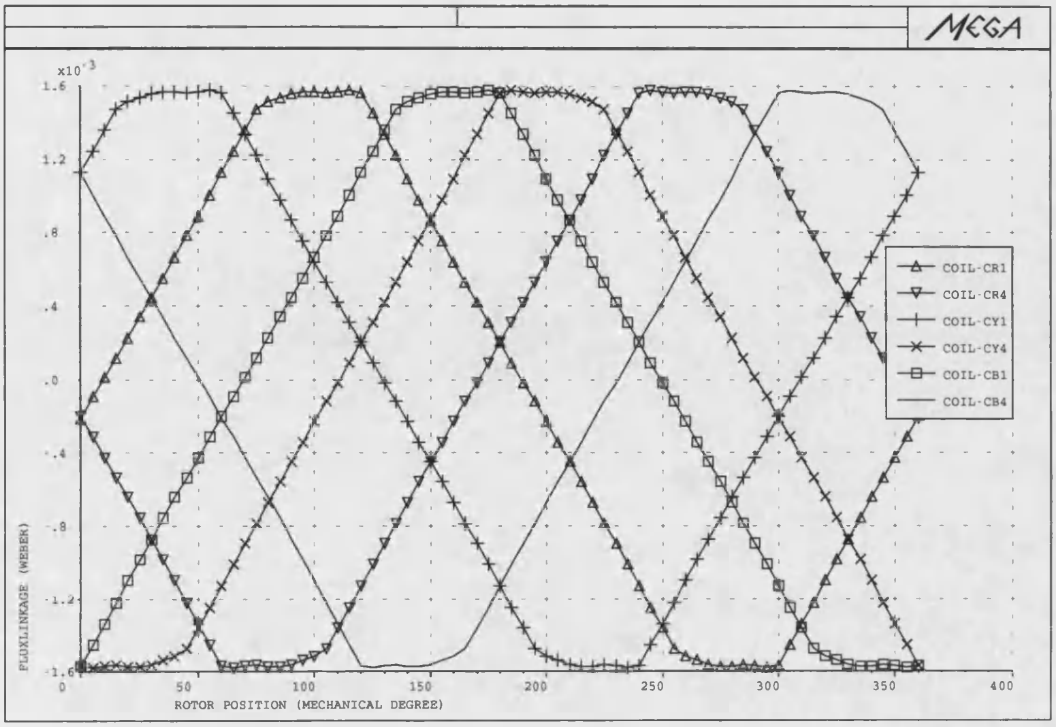

Figure 6.10: Flux-linkage of the inner coils in the concentric group in homopolar machine

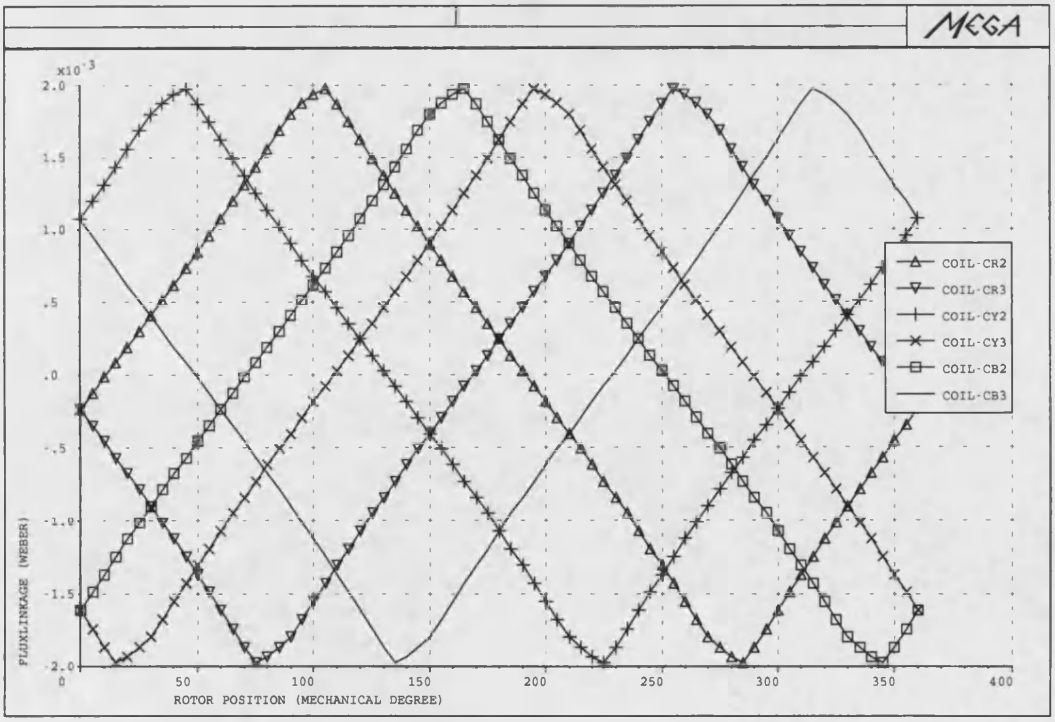

Figure 6.11: Flux-linkage of the outer coils in the concentric group in homopolar machine

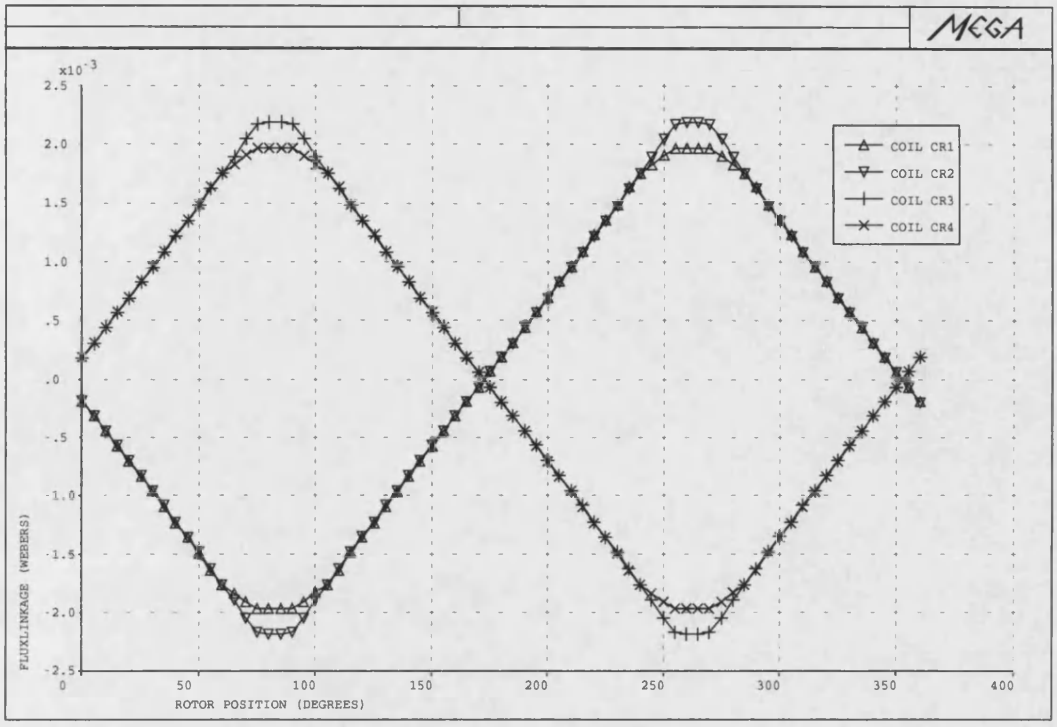

Figure 6.12: Phase-R coil group flux-linkage in heteropolar machine

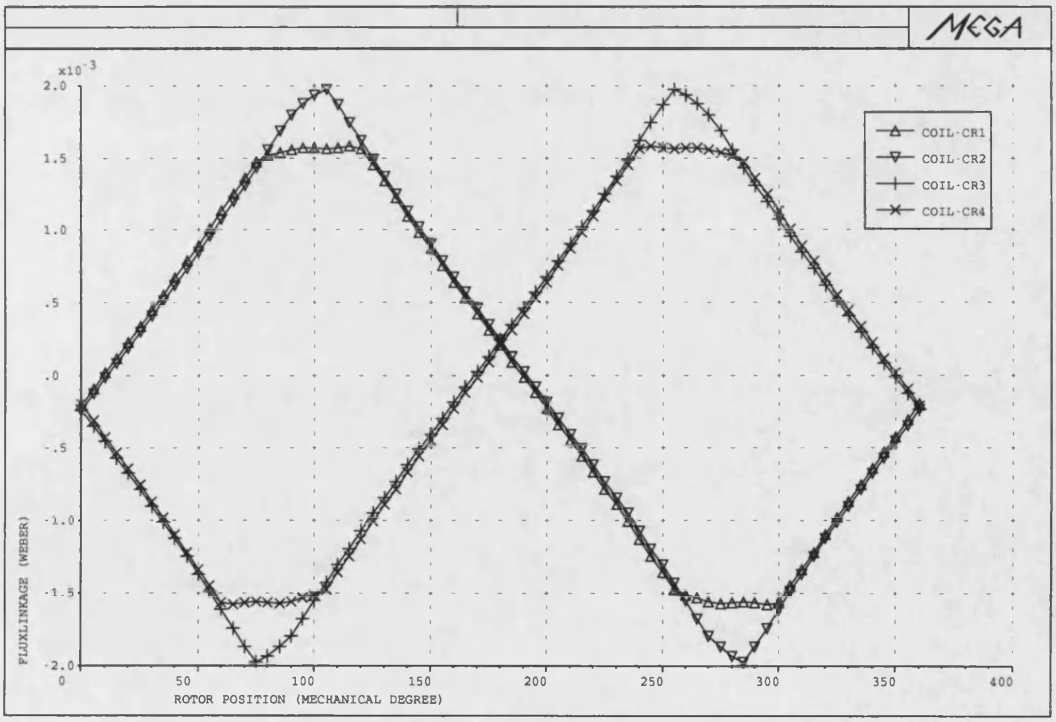

Figure 6.13: Phase-R coil group flux-linkage in homopolar machine

Harmonic order	Original Rotor	Modified Rotor
1	100	100
3	-10.5	-2.4
5	2.2	0.06
7	-0.11	0.04
9	-0.35	-0.09
11	0.47	-0.014
13	-0.29	5E-3
15	0.17	-0.04
17	0.06	-0.04

Table 6.1: Harmonic content of phase R, original and modified rotor

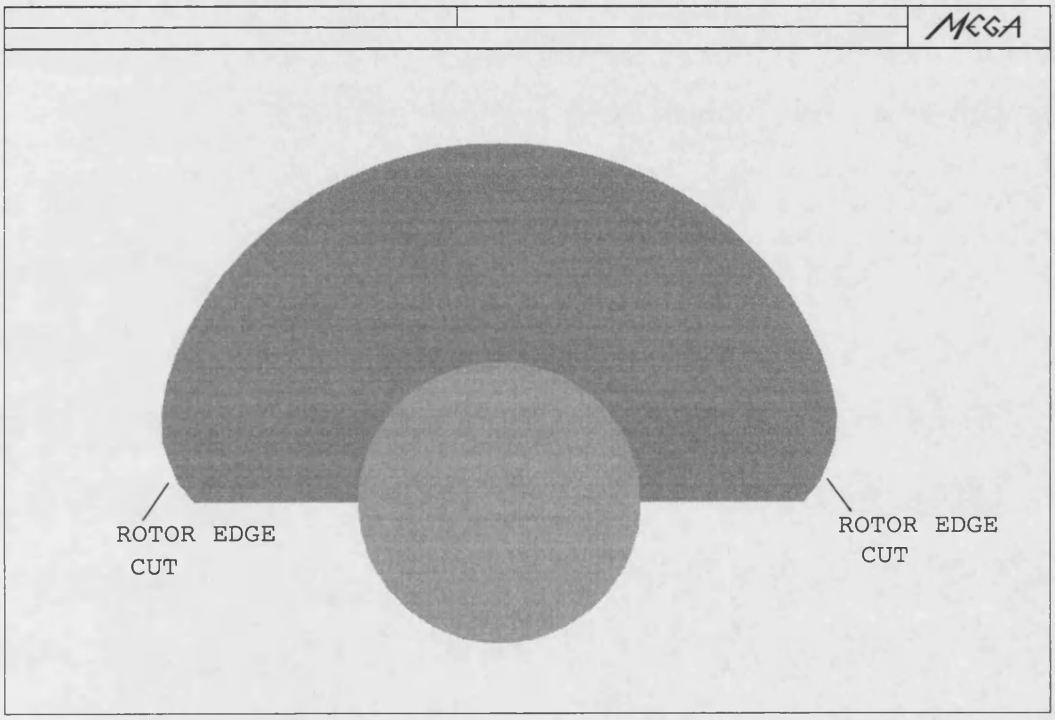

Figure 6.14: Rotor edge cut in Finite Element slice

6.4 Phase flux linkages

The phase flux linkages were calculated using the individual coil linkages which

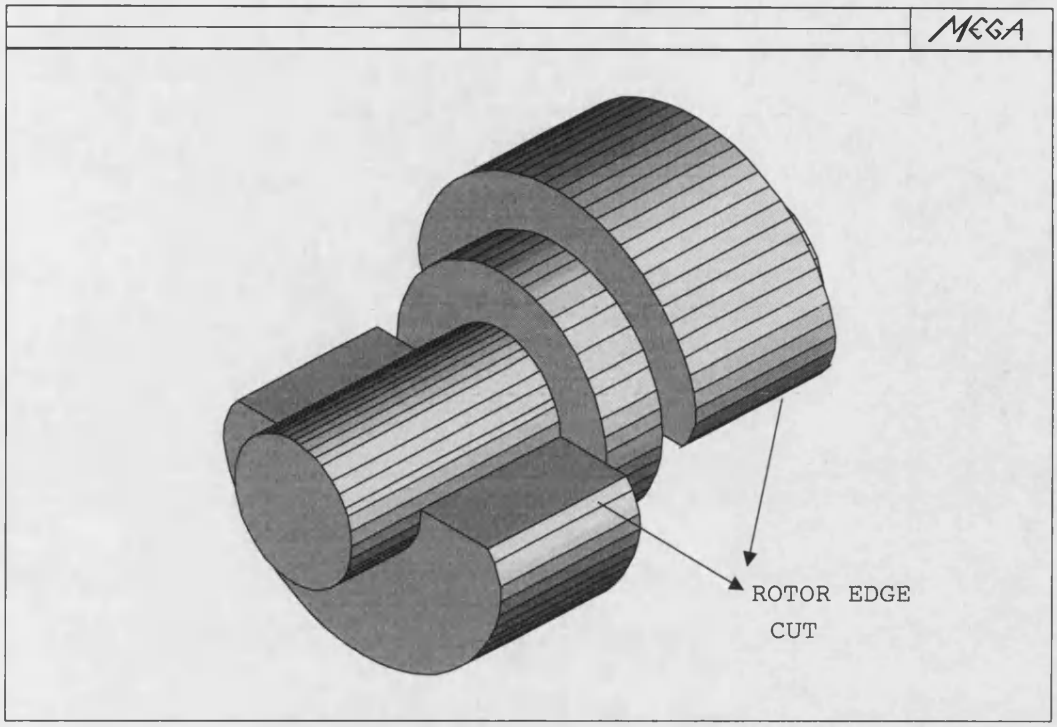

Figure 6.15: Modified rotor in 3D

have been calculated above. The armature winding configuration and coil flux linkages for each phase can be used to calculate the phase flux linkages for any armature winding however complex it may be. The phase flux linkages for the heteropolar machine are given in Fig. 6.17. Fig. 6.18 shows the phase flux linkage in the homopolar machine with the original rotor whilst Fig. 6.19 shows for comparison the flux linkage with the modified rotor. It will be observed that the modified profile produces a wave shape closer to sinusoidal and thus is confirmed by the results of a harmonic analysis shown in table 6.1.

6.5 Calculation of no-load phase emfs

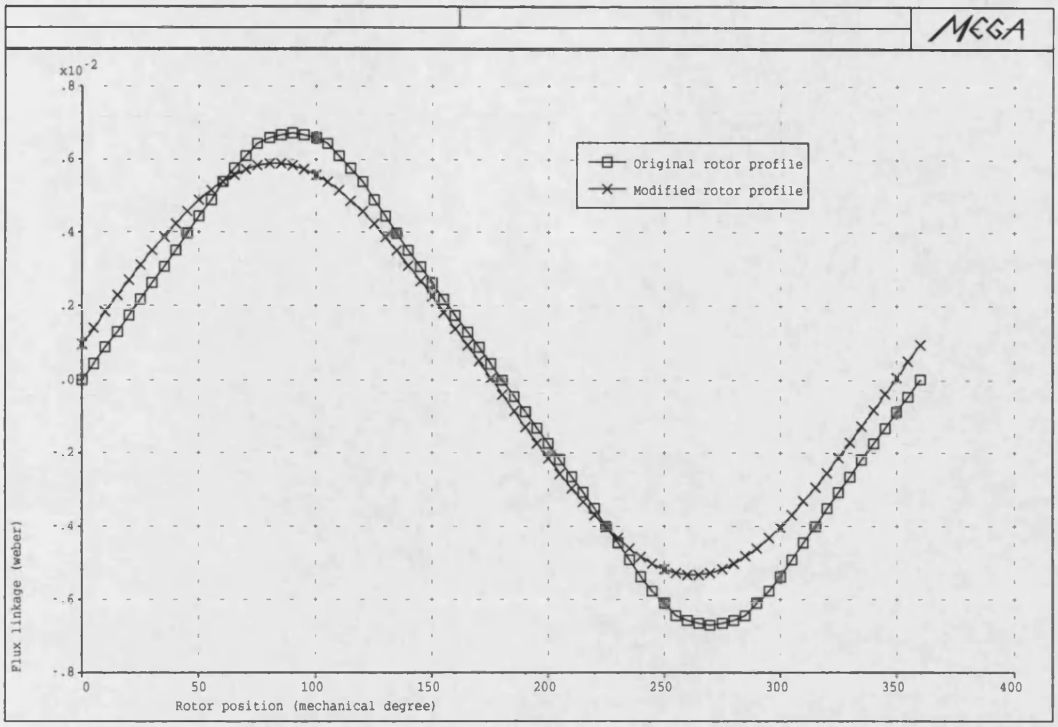

Figure 6.16: Flux linkage in original and modified rotor, $phase - R$

Phase emfs are given by the rate of change of flux linkages as shown in equation (6.1). The phase flux linkage due to the excitation field current varies within rotor position. Equation (6.1) can be re-expressed as:

$$\frac{d\lambda}{dt} = \frac{d\lambda}{d\theta} \times \frac{d\theta}{dt} = \frac{d\lambda}{d\theta} \times \omega \tag{6.7}$$

Therefore the phase emfs can be calculated by multiplying the space rate of change of phase flux linkages by ω.

Fig. 6.20 and Fig. 6.21 show the three phase voltages calculated for the heteropolar and homopolar machines respectively. Fig. 6.22 shows $phase - R$ only of the homopolar machine with and without the re-profiled poles.

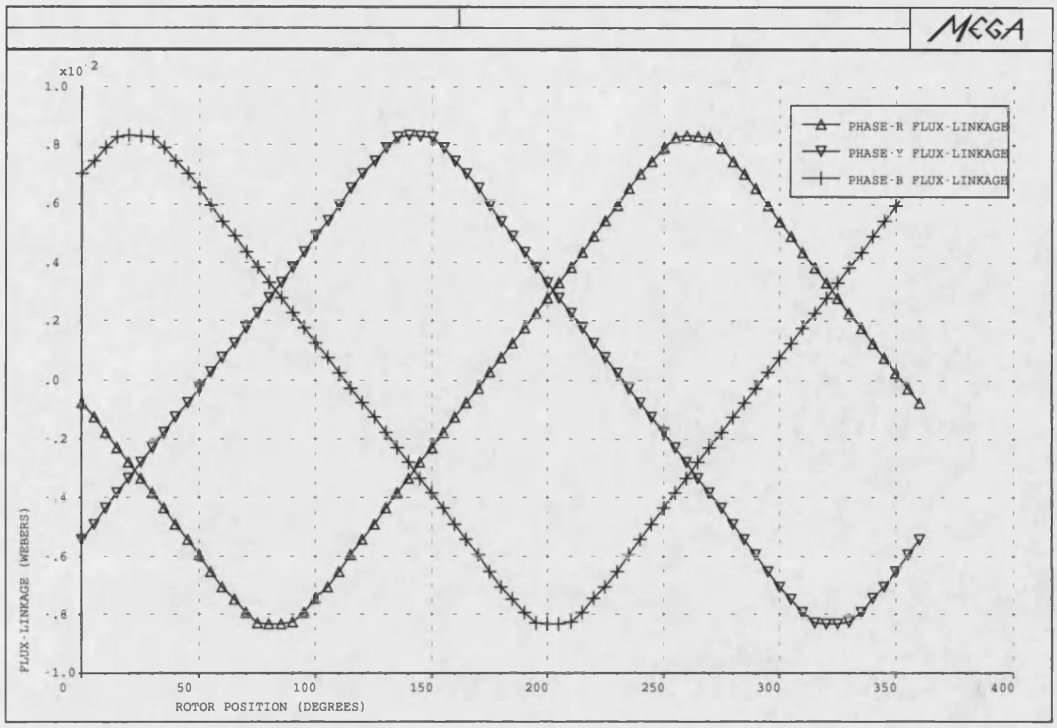

Figure 6.17: Phase flux-linkage in the heteropolar machine

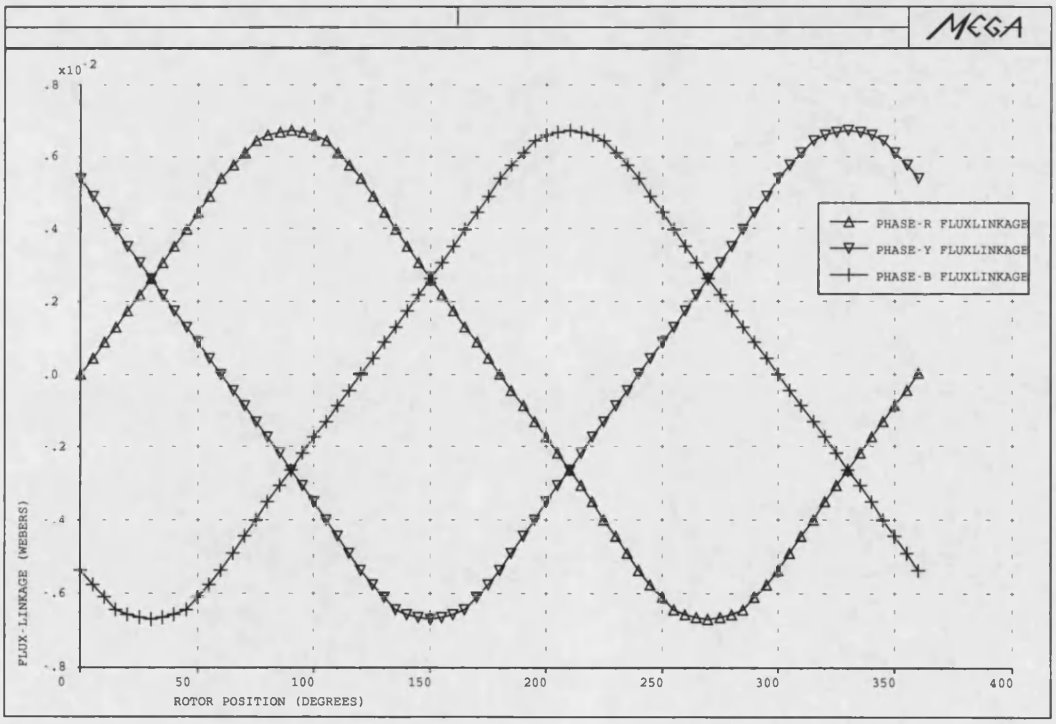

Figure 6.18: Phase flux-linkage in the homopolar machine

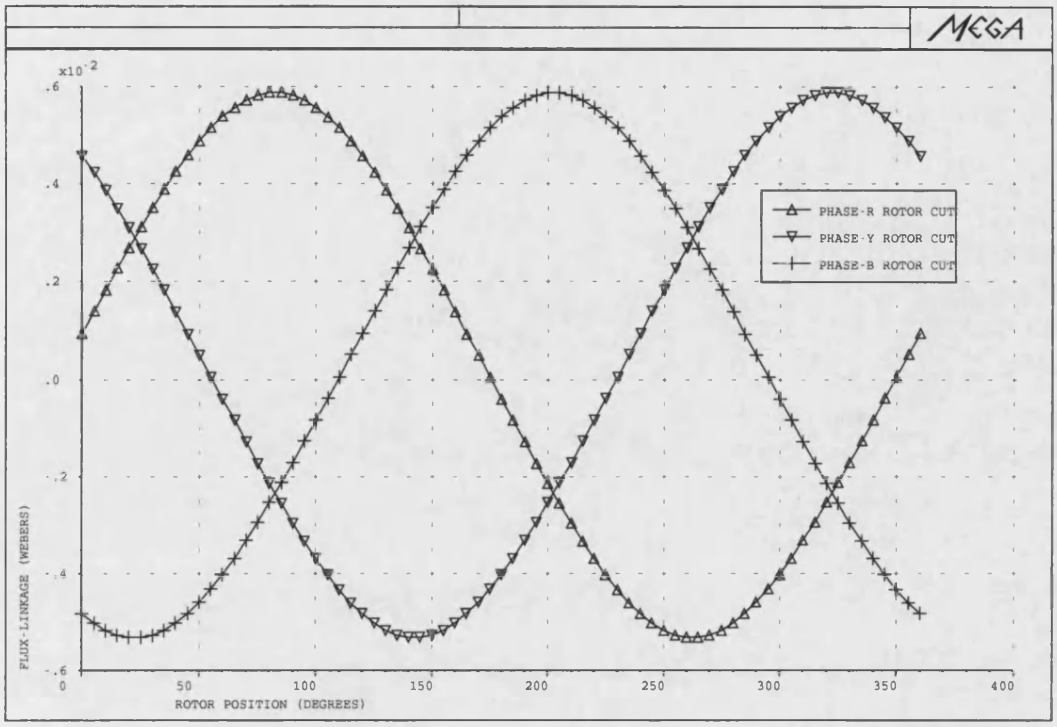

Figure 6.19: Phase flux-linkage in the homopolar machine with modified rotor

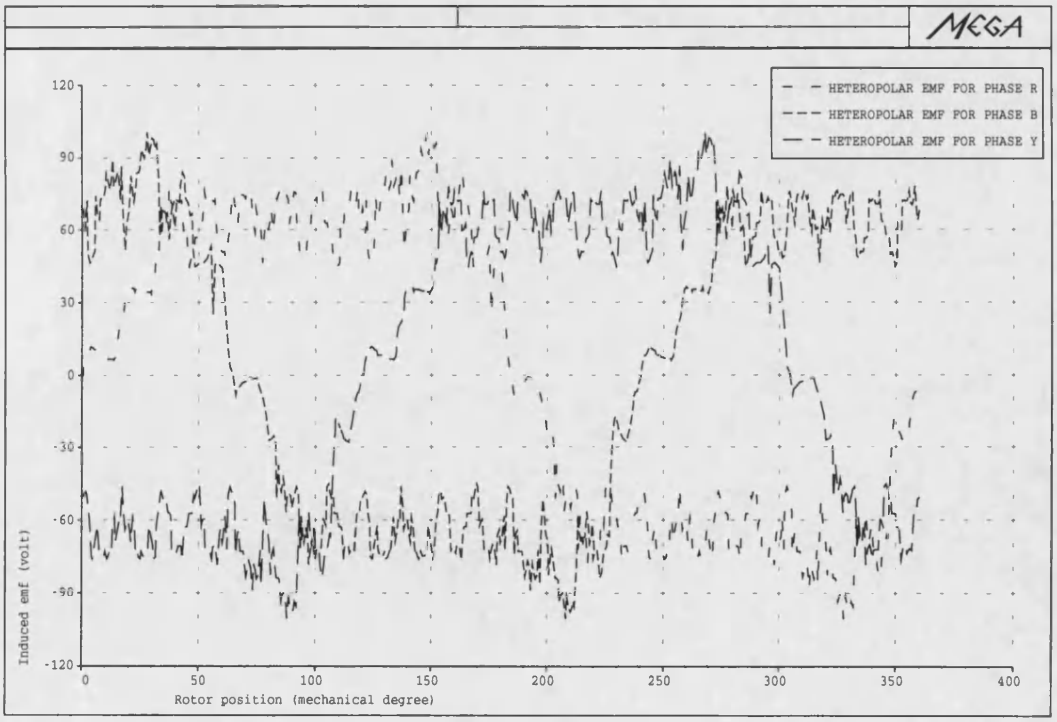

Figure 6.20: Calculated three phase voltages in the heteropolar machine

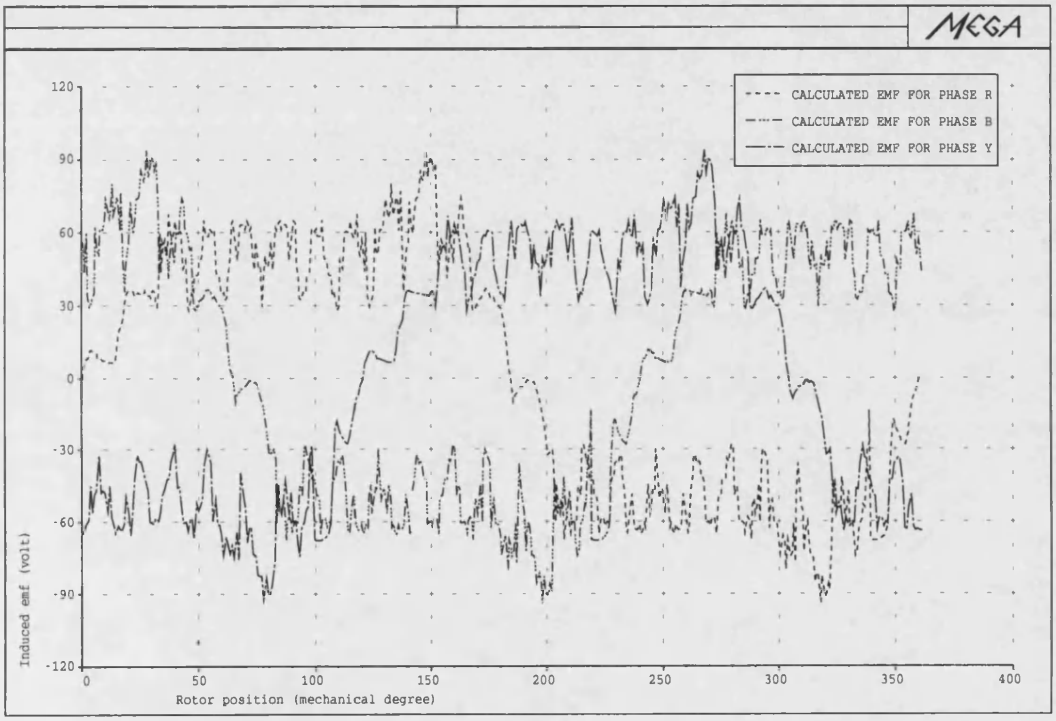

Figure 6.21: Calculated three phase voltages in the homopolar machine

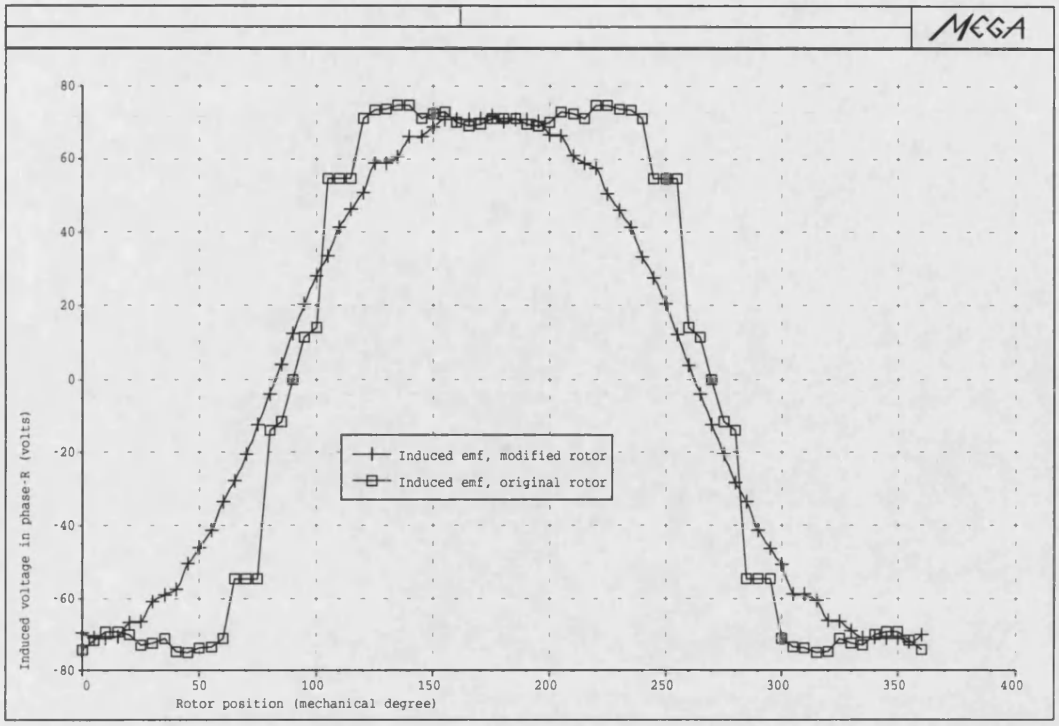

Figure 6.22: Phase R only of homopolar machine

6.6 3D modelling and computer time consumed

In the 3D modelling, the heteropolar machine has 17 levels and the total number of nodes and element are 50847 and 52704 respectively. This model as a magnetostatic problem needs at least 30 minutes to solve for a particular rotor position.

In case of the homopolar machine, the model has only 15 levels and the total number of nodes and element are 44925 and 46228 respectively. This model needs only 20 minutes to solve for a particular rotor position.

6.7 Machine load performance in comparison with FEM

In this section the results of the tests performed on the prototype machine together with the equivalent finite element values are presented. The tests that were carried out on the prototype machine were also performed on the FE models by using the combined external circuit and FE method as described in the following section.

6.7.1 Finite element model connected to an external circuit

The machine is complex and the flux distribution in it is difficult to calculate except by a full 3D finite element model. To facilitate this the rotor and stator were meshed separately and joined together by a sliding Lagrange interface placed in the middle of the air gap as it has been described in the previous chapters.

The currents in the laminated iron regions were ignored and the regions were considered to be isotropic. The field solution for a known current is then a magnetostatic problem. However for a simulation involving an external excitation circuit and load, the currents are unknown; and additional complexity in this case is the induced voltage due to the motion of the rotor. The easiest solution to this sort of problems to solve the circuit equations as a single system [40].

$$[K]\mathbf{x} + [C]\frac{\partial \mathbf{x}}{\partial t} = \mathbf{f} \tag{6.8}$$

The unknown vector x comprises the magnetic scalar unknowns of the field model, the Lagrange multipliers that enforce the sliding interface and the circuit voltages. The forcing function $\mathbf{f}$ represents the specified voltages in the circuit. The stiffness and damping matrices, $[K]$ and $[C]$ include both the field model and a nodal circuit model. The motional effects are modelled by the Lagrange multiplier terms in the stiffness matrix. These terms are calculated at each

time step. Because of the stiff nature of the electromagnetic system an implicit backward difference scheme was used to implement the time stepping of these equations. The finite element method used the system explained earlier where equation (6.7) is represented by the circuit shown in Fig. 6.23.

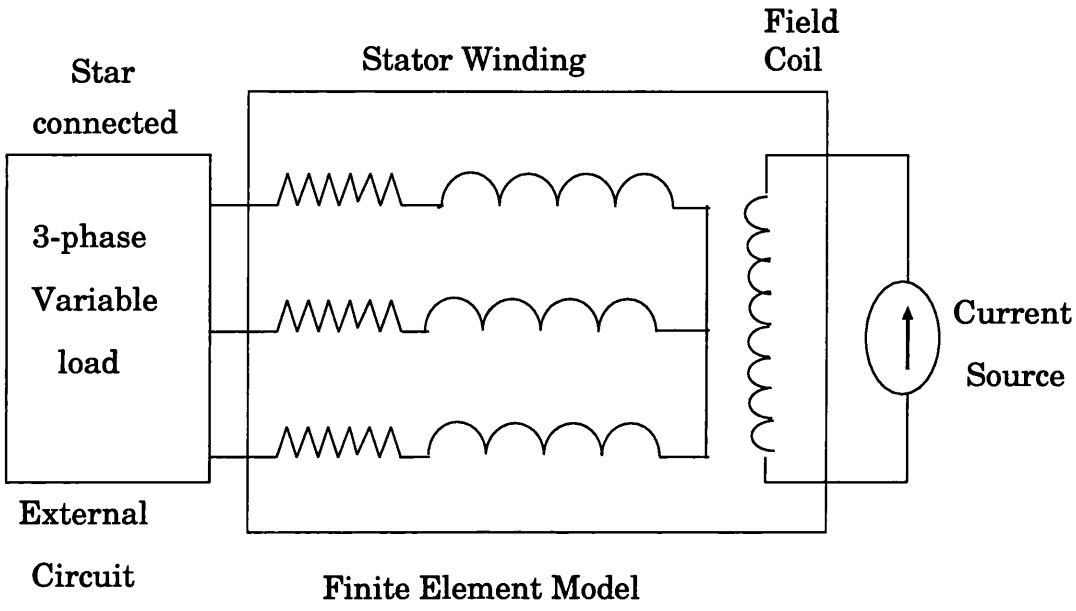

Figure 6.23: FE Model connected to an external circuit

6.7.2 Determination of equivalent circuit parameters

Two basic sets of characteristic curves for a synchronous machine are involved in the determination of the appropriate machine constants. The first of these are experimental, taken from the machine, and the second are obtained from FEM.

6.7.3 Air-gap magnetic flux

The flux in the air-gap was measured using a search coil which is inserted on the stator side. The search coil has an area equal to:

$$A_{search} = \pi D_{search} L_{search} = \pi \times 179.8 \times 10^{-3} \times 50 \times 10^{-3} = 0.0088\ m^2$$

From this search coil, a flux waveform was recorded and it is shown together with the FEM calculated value on Fig. 6.24, the results are also separately shown on Fig. 6.25 and Fig. 6.26, for clarity.

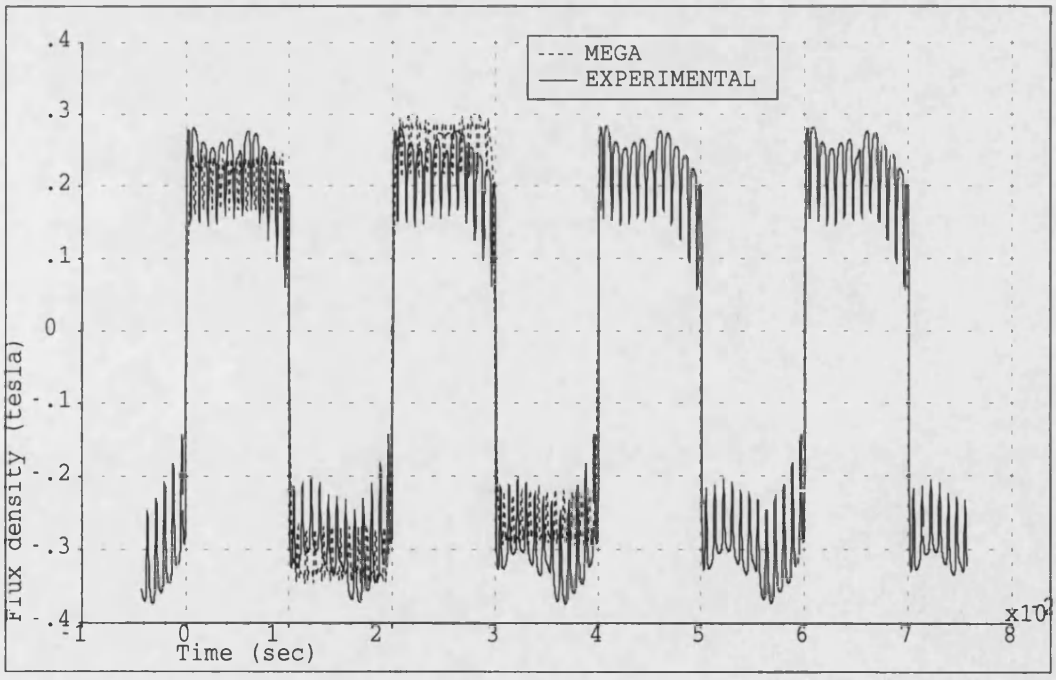

Figure 6.24: Air-gap flux density experimentally and FEM

The waveform, that was taken from the search coil can be explained in levels

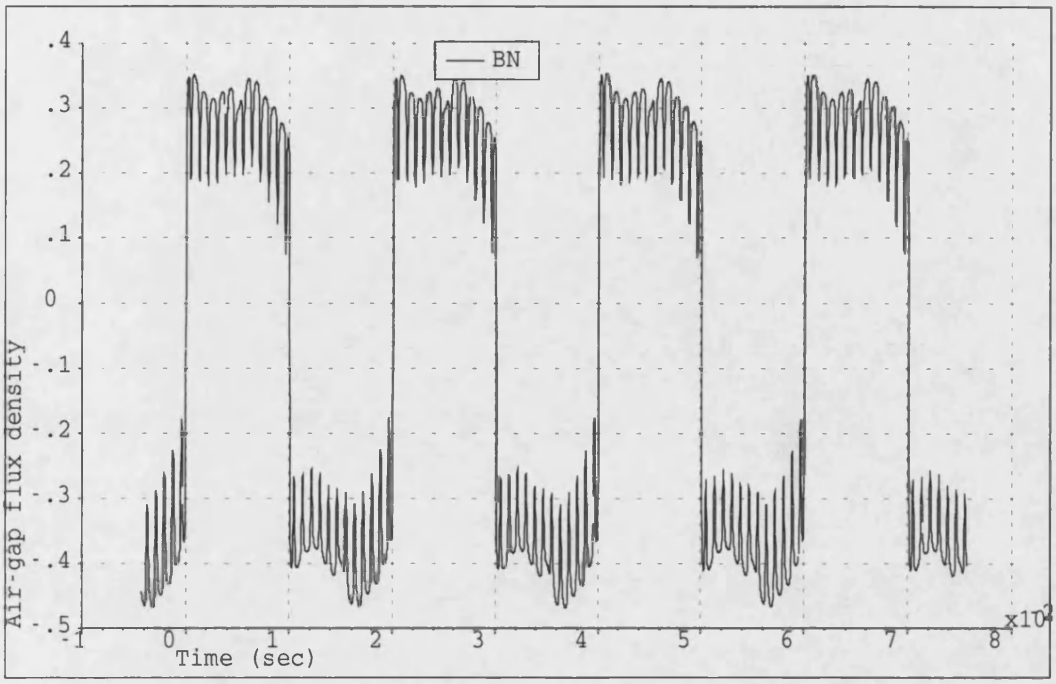

Figure 6.25: Experimental Air-gap flux density

term by using FEM(the levels here have the same meaning as explained in chapter 4), thus the air gap flux can be shown individually from FEM at each level and it will be noticed that the flux has the half cycle shape for the first rotor end, whilst at the other end the flux has the shape of the negative half cycle. Hence when they are added together, the total waveform has the shape of a complete cycle as shown in Fig. 6.24.

In order to prevent repetition of presenting all fluxes in all the levels only one shape of flux from each side will be seen, for example, from level 4 through to level 6 the shape of the flux is the same, as it is the case from level 9 through to level 11, however all flux levels have different values.

Fig. 6.27, and Fig. 6.28, represent the flux in levels 4 and 11 respectively.

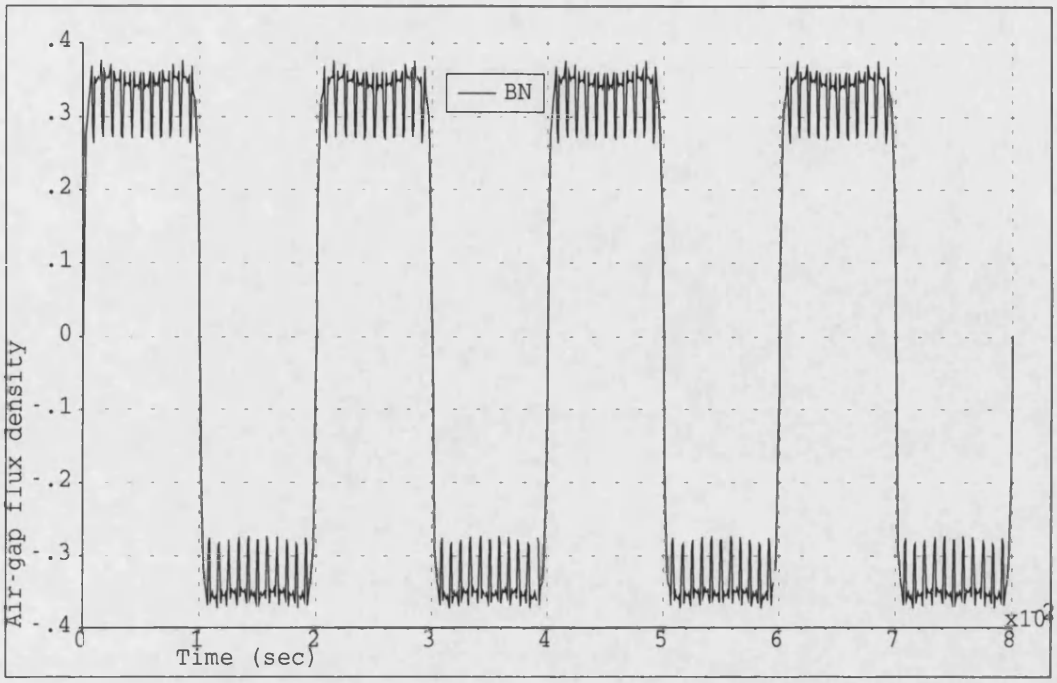

Figure 6.26: FEM Air-gap flux density

6.7.4 Opencircuit test

The open circuit characteristic is determined experimentally by driving the machine mechanically at synchronous speed with its armature terminal on open circuit and by reading the terminal voltage corresponding to a series of values of field current. In Fig. 6.29 the results are shown compared with FEM, the amount of the residual flux in the prototype machine has been assumed to be the same in the 3D FEM. The terminal voltages are shown in Fig. 6.30 at a field current of 4.5 *amperes*, and in table (6.2) the harmonic content of both experimental and FEM voltage waveforms for phase R are given.

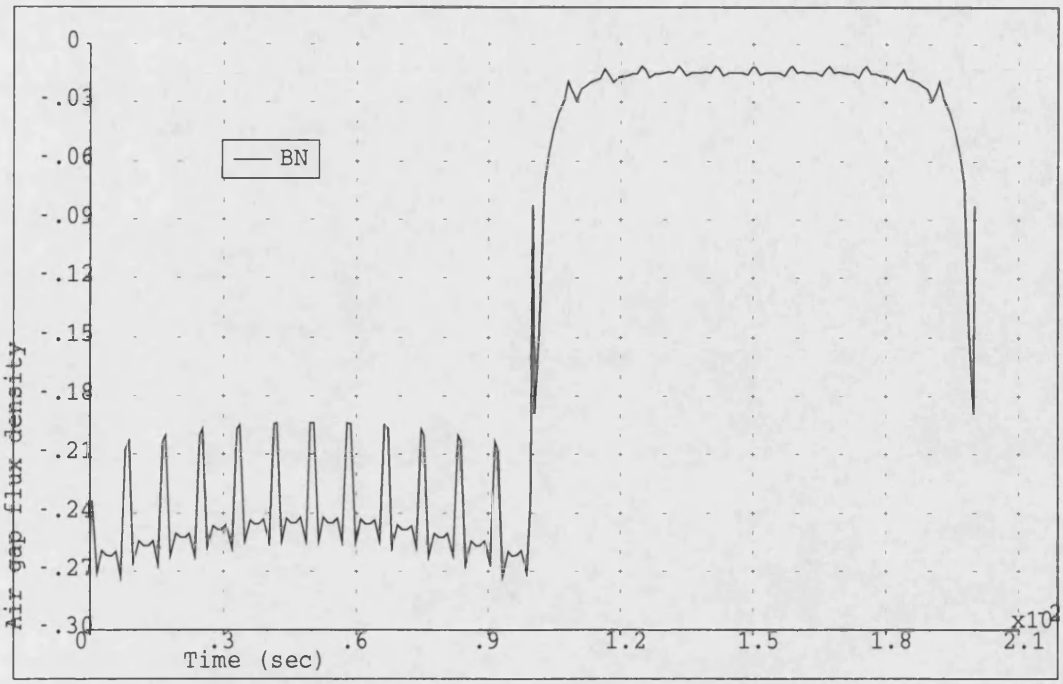

Figure 6.27: Air-gap flux level 4

6.7.5 Short circuit test

In the short circuit test, the terminals of the synchronous machine which is being driven at synchronous speed (3000 *rpm*) are short circuited through suitable ammeters and the field current is gradually increased until the armature current has reached its full load value. The data can be plotted against the field current. This relation is known as the short circuit characteristic and is shown in Fig. 6.31

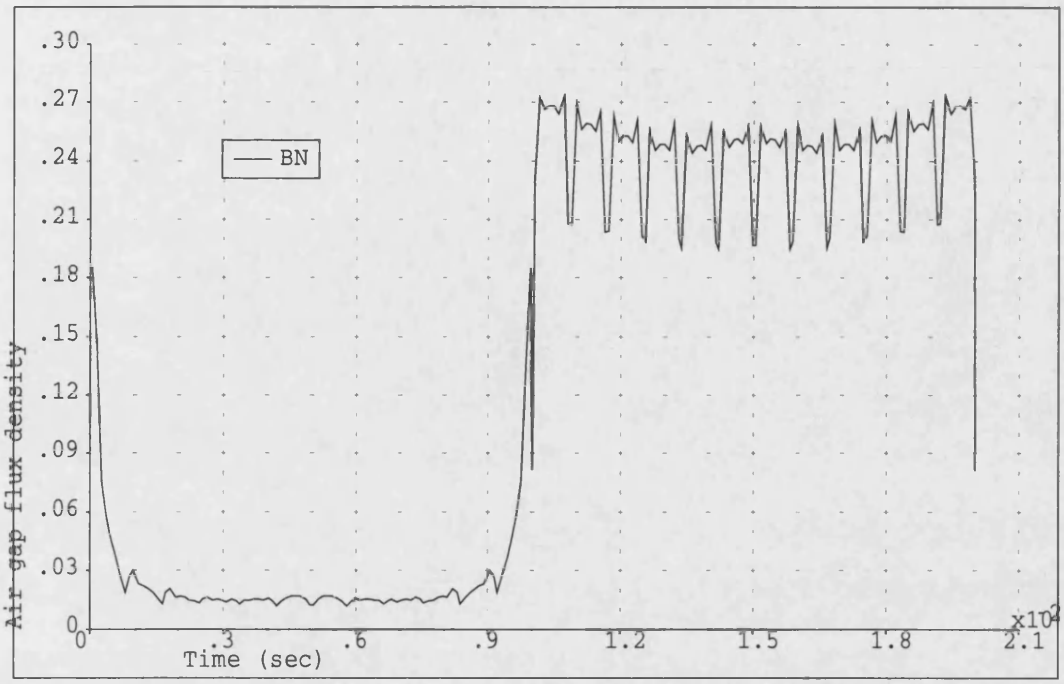

Figure 6.28: Air-gap flux level 11

6.7.6 The saturated and unsaturated synchronous reactances

Corresponding to unsaturated operating conditions within the machine, this reactance can be found from the open and short circuit data.

$$X_{un} = \frac{E_{oc}}{\sqrt{3} I_{sc}} \tag{6.9}$$

where E_{oc} is the Line to Line open circuit voltage taken from the air gap line in Fig. 6.29 for a given excitation field current I_f and I_{sc} is the short circuit armature current obtained at the same field excitation in Fig. 6.31. This reactance is 58Ω experimentally and 51Ω calculated from FEM.

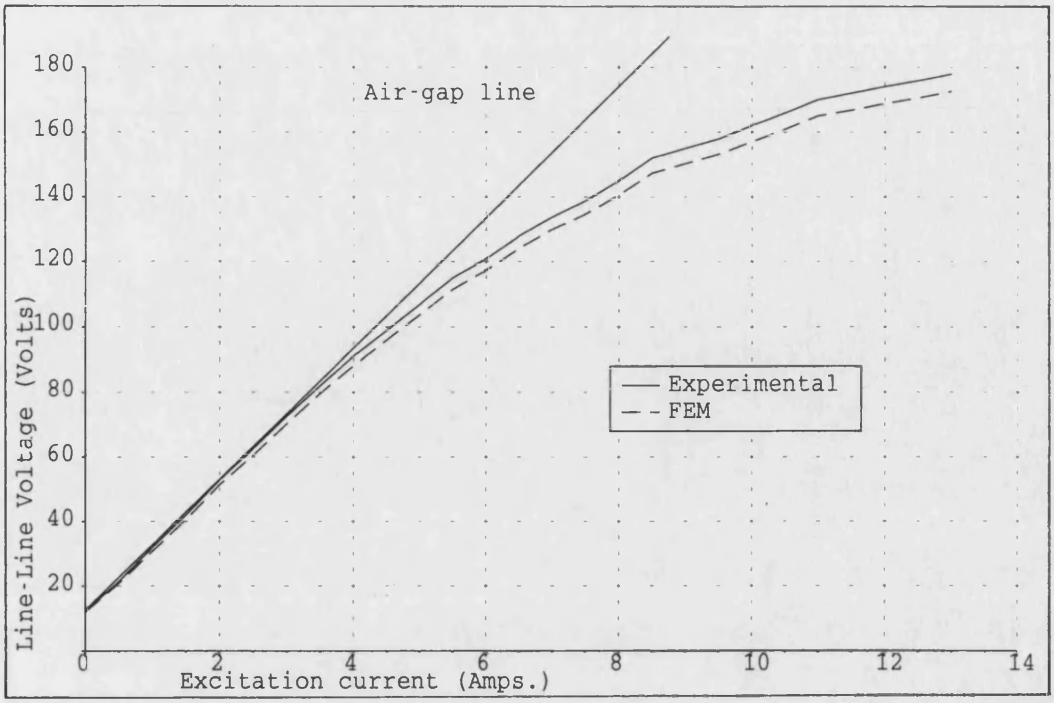

Figure 6.29: Open circuit characteristic

In the same way, the saturated reactance also has been calculated from the open and short circuit data and using the above equation but E_{oc} in this case is the Line to Line open circuit voltage taken from the open circuit line in Fig. 6.29 for a given excitation field current I_f and I_{sc} is the short circuit armature current obtained at the same field excitation in Fig. 6.31. This reactance is 45.2Ω experimentally and 37.4Ω calculated from FEM.

6.7.7 Slip test

A slip test has been performed to determine X_d and X_q. In this test three phase voltages were applied at a speed slightly below synchronous speed without field excitation. Oscillograms were taken of the armature terminal voltage, and the

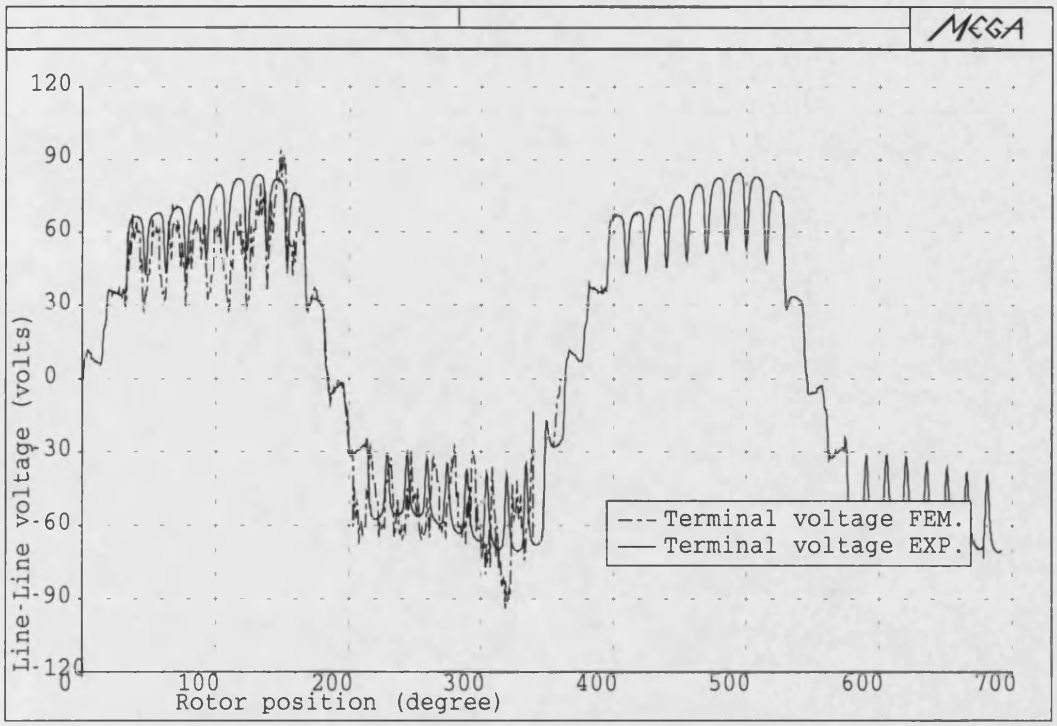

Figure 6.30: Terminal voltages at $I_f = 4.5 amperes$

armature current. The direct-axis and quadrature-axis reactance are found as follows:

$$X_d = \frac{V_{max}}{I_{min}} \quad and \quad X_q = \frac{V_{min}}{I_{max}} \tag{6.10}$$

The experimental X_d and X_q are 77.6Ω and 72.5Ω, while the calculated values from FE are 66.2Ω and 57.6Ω respectively.

6.7.8 Load test

In this test the 3 phase armature windings are connected to a load and the machine is driven at the synchronous speed. Fig. 6.32, shows the calculated

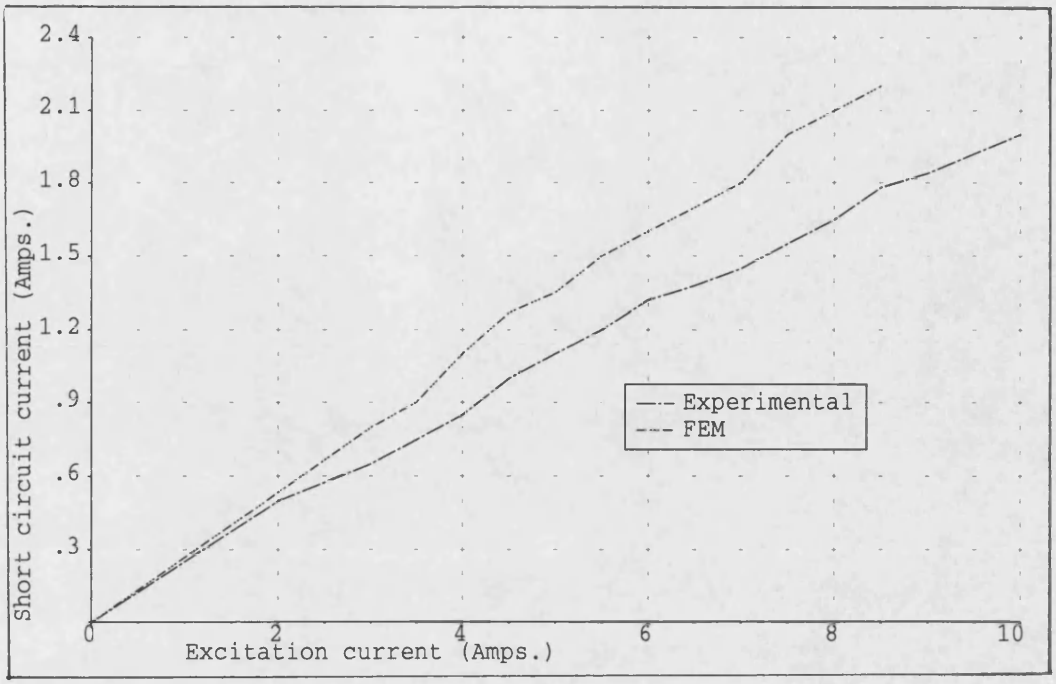

Figure 6.31: Short circuit characteristic

and measured load voltages for various values of armature current at inductive and resistive loads. The waveforms of load voltage and current (at inductive load) are illustrated in Fig. 6.33 and Fig. 6.34 respectively.

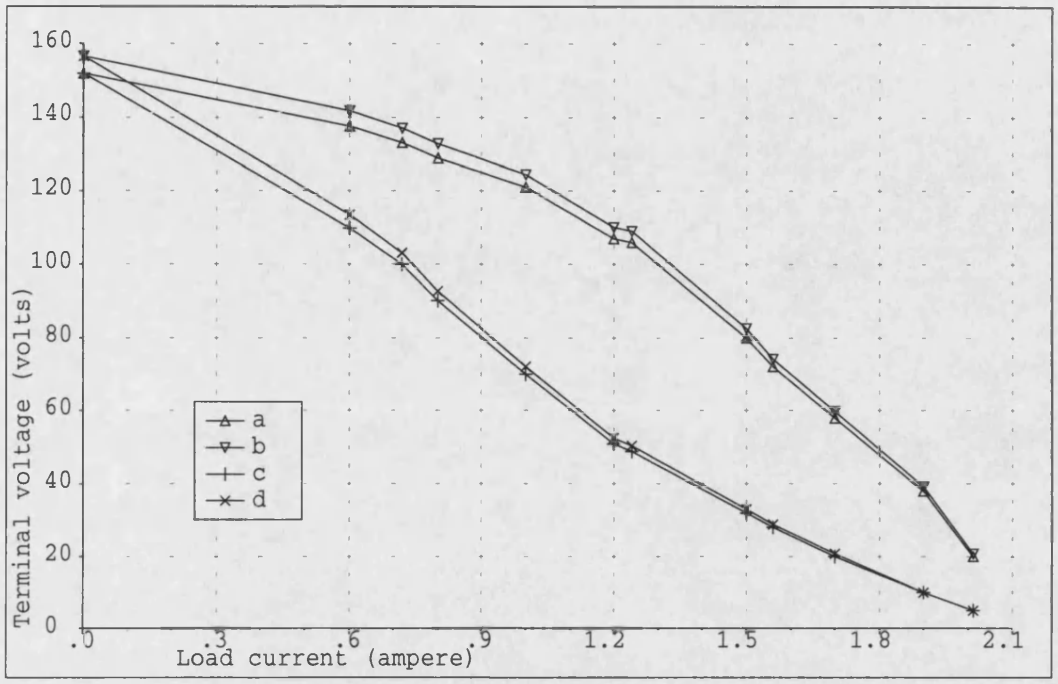

Figure 6.32: Load test, (a)Experimental resistive load, (b)FEM resistive load, (c)Experimental inductive load, (d)FEM inductive load

Harmonic order	**FEM**	**EXP.**
1	100	100
3	-1.6	-2.6
5	2.3	3.2
7	0.3	0.5

Table 6.2: Harmonic content of phase R, Experimental and FEM

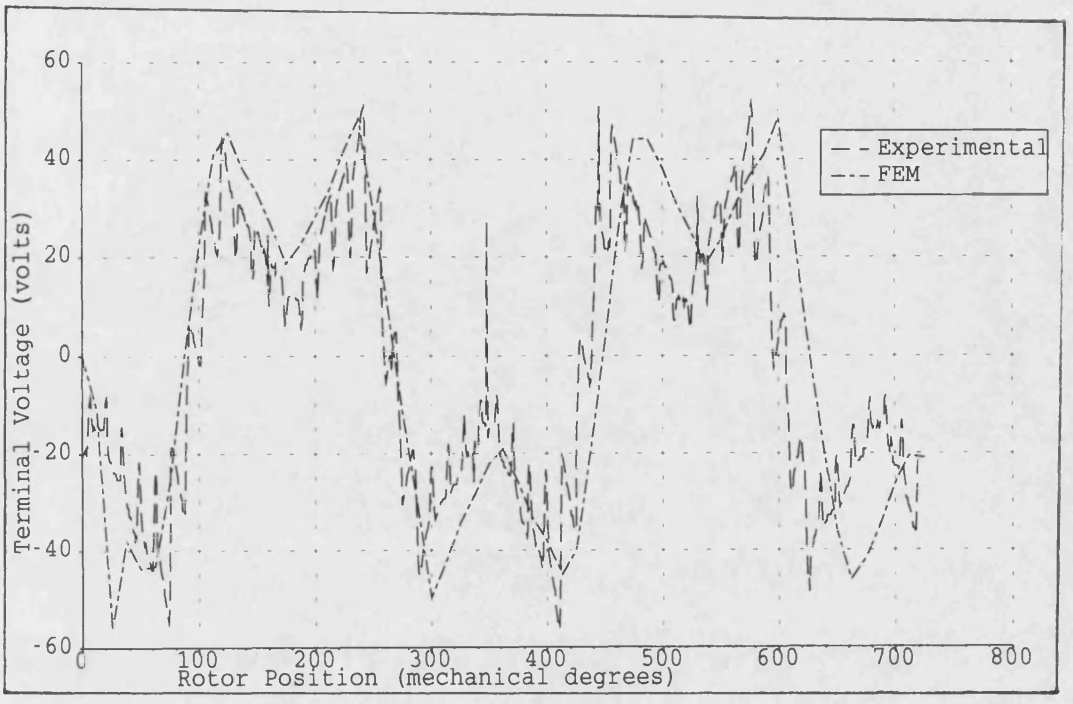

Figure 6.33: Load Voltage Waveform

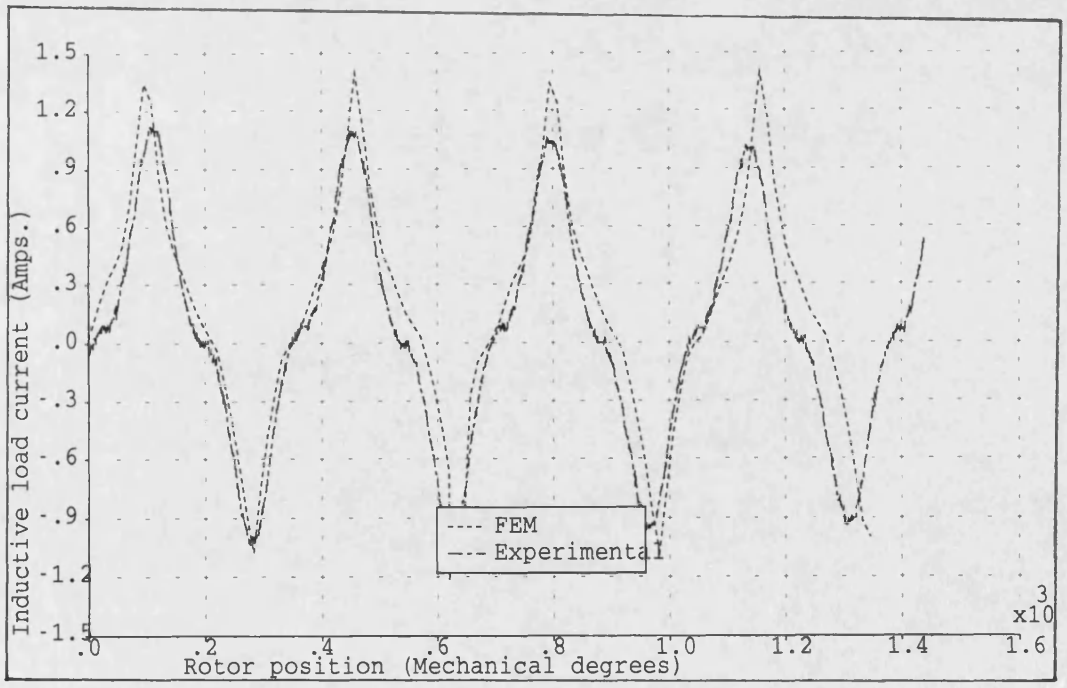

Figure 6.34: Load Current Waveform

6.8 Loss measurement and Output Characteristic

Conventional copper and iron losses, can be obtained from the open and short circuit tests. If the mechanical power required to drive the synchronous machine during the open circuit test is measured, the no-load rotational losses can be obtained. These losses comprise friction, windage and core loss corresponding to the flux in the machine at no-load. The friction and windage losses at synchronous speed are constant, while the open circuit core loss is a function of the flux, which in turn is proportional to the open circuit voltage. The mechanical power required to drive the machine at synchronous speed and unexcited is its friction and windage loss. When the field is excited, the mechanical power equals the sum of the friction, windage, and open circuit core loss. The open circuit core loss therefore can be found from the difference between these two values of mechanical power. Appendix [C] explains the measurement of the friction loss which was found equal to 11.3 *watts*. A curve of open circuit core loss as a function of open circuit voltage is shown in Fig. 6.35, also plotted on this figure are the FEM results obtained as explained in chapter 5, section5.4.

In addition to the conventional losses there are other losses generally termed the stray losses. The magnitude of stray losses can be found from a short circuit test if the $D.C$ resistance loss plus the friction and windage loss are subtracted from the mechanical input power on short circuit, then the difference is the loss due to skin effect and eddy currents in the armature conductors plus the local

core losses caused by the armature leakage flux, i.e the stray loss. This stray load loss is commonly considered to have the same value under normal load conditions as on short circuit. It is a function of the armature current as shown in Fig. 6.36. The formulation used in the FEM calculations is magnetostatic and therefore this loss was not calculated.

Fig. 6.37 compares measured and FEM calculated efficiencies. The experimental result was obtained by adding the measured stray, field resistance, armature resistance and core losses to the output power to find the input power. The FEM input power was obtained by adding the calculated field resistance, armature resistance and core losses to the calculated output power (i.e ignoring the stray losses). The same constant field current was assumed in both cases.

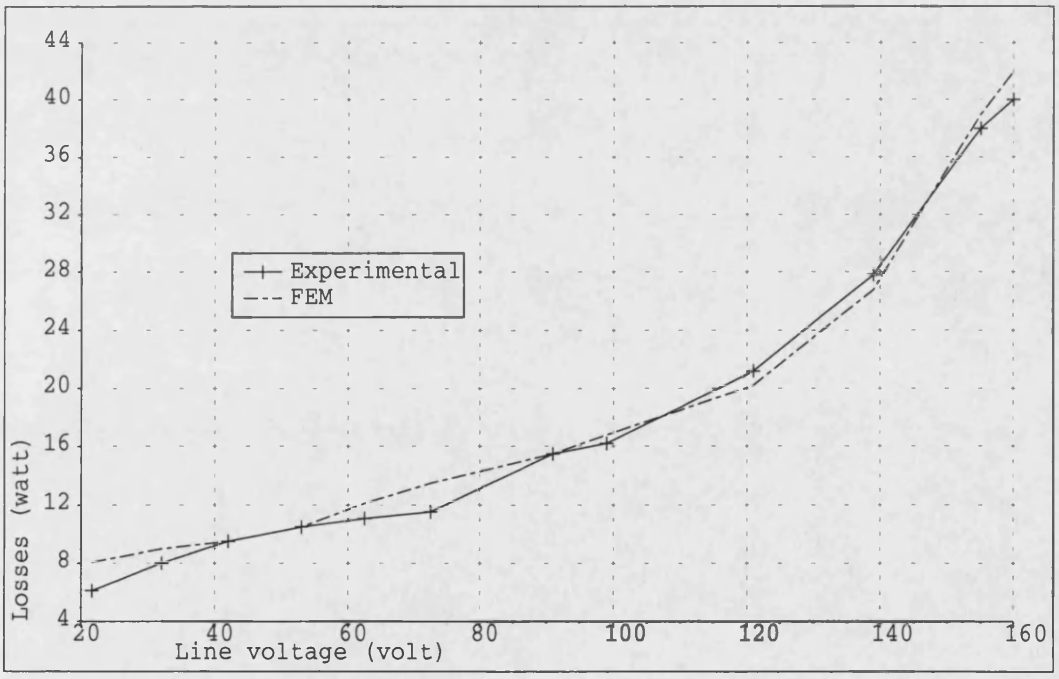

Figure 6.35: Core loss characteristic

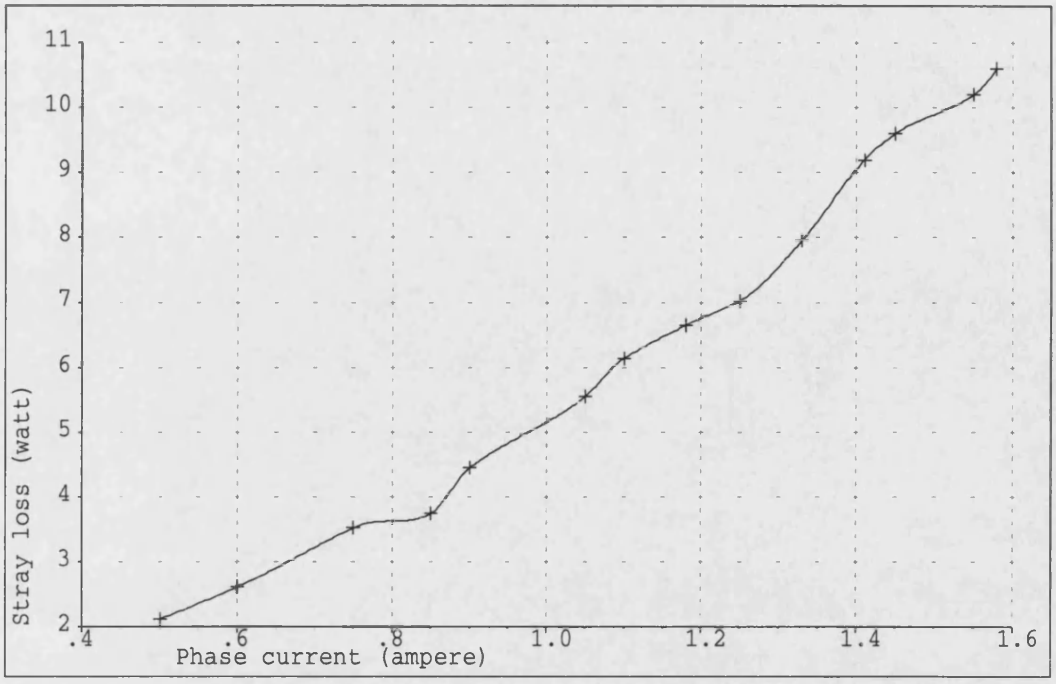

Figure 6.36: Machine stray loss

6.9 Comparison of the phasor diagram method with FEM and measured results

The load performance of the machine can be calculated using the FEM calculated results for X_d and X_q (please see section 6.7.7) use is made of the phasor diagram shown in Fig. 6.38(a) and expanded in Fig. 6.38(b). From this diagram it can be deduced that:

$$E_{aff} = V + jIX_q \tag{6.11}$$

and

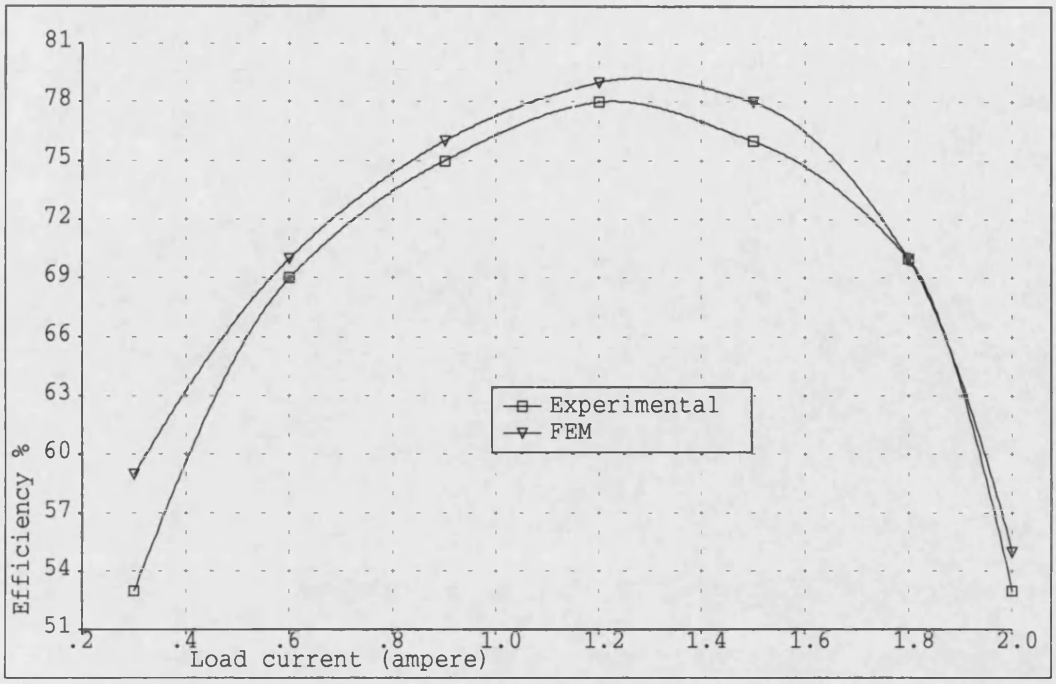

Figure 6.37: Output efficiency characteristic

$$E_{af} = \mid E_{aff} \mid + \mid I_d(X_d - X_q) \mid \tag{6.12}$$

Where $I_d = I \sin \Psi$, and $\psi = \delta + \theta$.

The calculated values from FEM for X_d and X_q are 66.2Ω and 57.6Ω respectively. These values have been used in the above equations (please see the following chapter section (7.5) for more details of calculation of machine load performance using the two-axis reactance theory) to predict the load performance for both resistive and inductive load at 0.8 lagging power factor. The characteristics are shown in Fig. 6.39, it will be observed that a reasonable fit to experimental values is obtained by this technique.

6.10 Discussion

The results presented in this chapter have been obtained from both FEM results and from experimental tests. These results included machine parameters, machine load performance and the efficiency of the machine. These results show the calculated emf from FEM on open circuit to be about 3.5% more than that of the experimental, the unsaturated reactance results from FEM are about 12% less than the experimental values whilst the saturated values of the latter are about 17% more than the calculated. The X_d and X_q reactances from the experimental test were about 12% more than those from FEM and the predicted machine efficiency from FEM is about 3% more than that from experimental.

This agreement validates the full FE model and it can clearly be used for design purposes. In addition the quicker method using the parameters from the FE calculation in the phasor diagram also gives a reasonable fit to the experimental results and can be used to give an indication of the machine performance. This is not as good as the full FE solution but nevertheless is sufficient for initial design purposes.

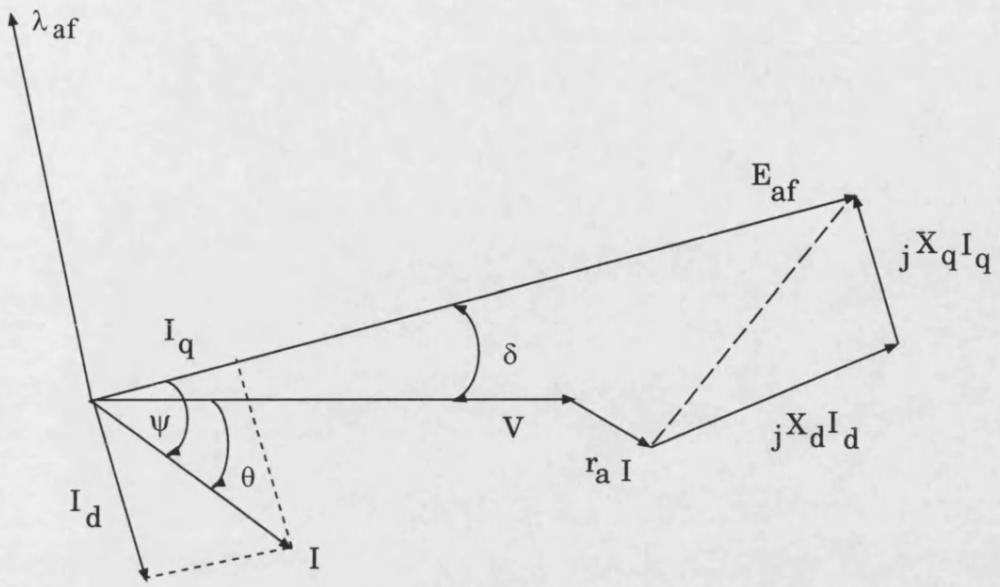

a) Phasor diagram of terminal voltage and impedance drops

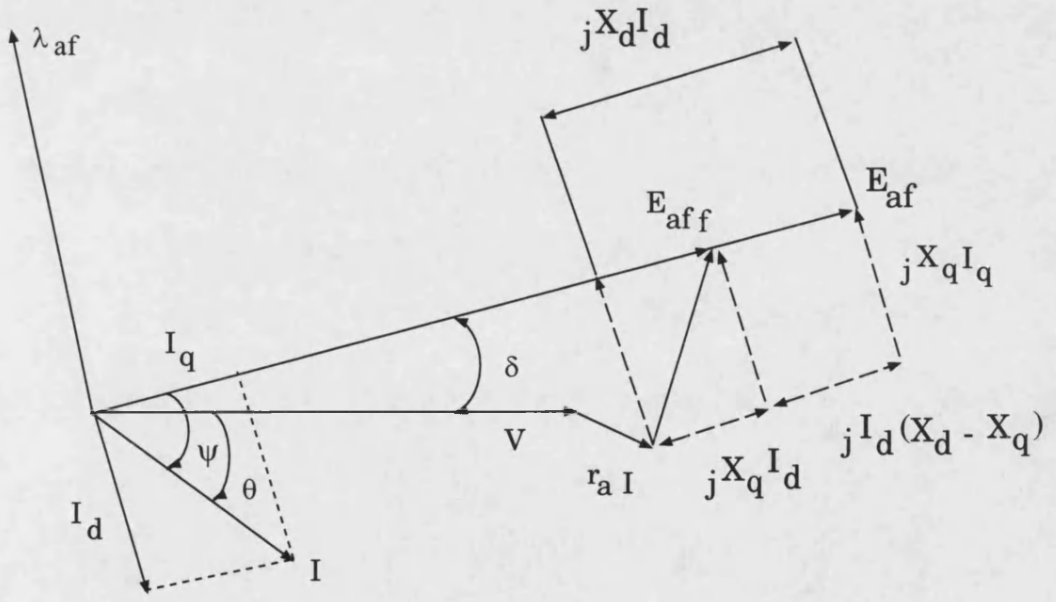

b) Phasor diagram as a basis for determining δ

Figure 6.38: Phasor diagram used to recalculate the load performance

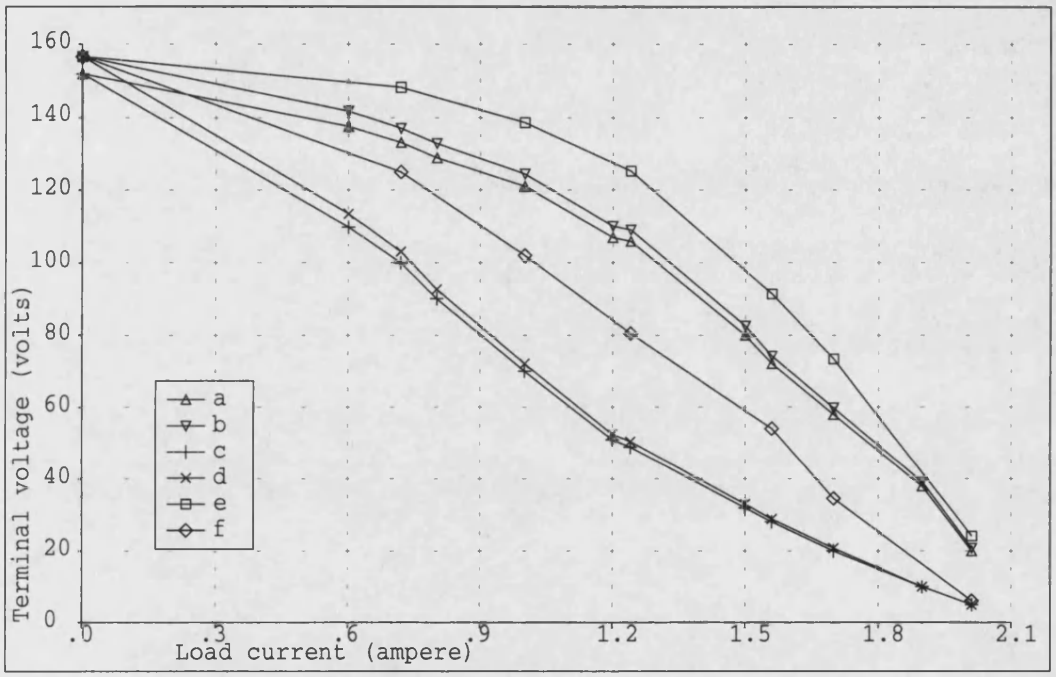

Figure 6.39: Machine load performance, (a)Experimental resistive load, (b)FEM resistive load, (c)Experimental inductive load, (d)FEM inductive load, (e)Calculated resistive load using phasor diagram with FEM calculated parameters, (f)Calculated inductive load using phasor diagram with FEM calculated parameter

Chapter 7

Analytical design approach

7.1 Introduction

In this chapter, the principle of operation and governing equations of a three phase synchronous generator are given. Conventional methods are used to calculate the open circuit voltage, air gap flux density and the synchronous reactance by assuming the homopolar machine is a cylindrical rotor machine when both rotor ends are brought together. FEM results are also employed here and only the fundamental components are considered.

7.2 Induced armature voltage

In order to relate the phase of flux linkage to the voltage that results from its time variation, it is necessary to establish conventions regarding the sign of the induced voltage in the generator. Therefore, consider the magnetic circuit and resistance r_a in series with an independent voltage source e_s and load voltage V_{an}, according to Kirchhoff's voltage law,

$$e_s = r_a i_a + p\lambda_a + V_{an} \tag{7.1}$$

Where the flux linkage λ_a may be produced by i_a alone or in combination with currents in other circuit coupled inductively with the magnetic circuit. The time derivative $p\lambda_a$ may result from single or combined time variations of current, magnetic permeance and inductive coupling. When the source e_s is removed, the magnetic circuit and the resistance r_a can represent one phase of synchronous generator which reduce equation (7.1) to :

$$V_{an} = -r_a i_a - p\lambda_a \tag{7.2}$$

However, λ_a results from both the mmf of the armature current and that of the field current.

If we take the fundamental component of the calculated flux density from the FE which is shown in Fig. 7.1(a), this flux density at θ which shows an armature

coil of N_{coil} turns and of pitch P linking a sinusoidally distributed magnetic flux(the flux in the air-gap is not a sinusoidall, but the flux linking the armature coil sides from both ends is a sinusoidally distributed), and expressed by :

$$B_\theta = B_{amp} \sin\theta \tag{7.3}$$

Where B_{amp} is the amplitude of the flux density space wave and assumed constant.

The flux in the strip subtended by $d\theta$ is :

$$d\phi_{coil} = B_\theta dA \tag{7.4}$$

When $dA = \frac{1}{2} LDd\theta_m$, in which L is the axial length of the stator iron and D the diameter of the inner surface of the armature iron as indicated in Fig. 7.1(b).

The flux is assumed to be confined to the axial length L , and $\theta_m = \frac{2\theta}{P}$, equation (7.4) can rewritten as:

$$d\phi_{coil} = \frac{LD}{P} B_{amp} \sin(\theta) d\theta$$

The flux that links the coil is :

$$\phi_{coil} = \frac{LD}{P} B_{amp} \int_{\alpha}^{\alpha+P\pi} \sin(\theta) d\theta$$

$$= \frac{LD}{P} B_{amp} [\cos(\alpha) - \cos(\alpha + P\pi)]$$

$$= \frac{2LD}{P} B_{amp} \sin(P\frac{\pi}{2}) \sin(\alpha + P\frac{\pi}{2})$$

which results in the flux linkage

$$\lambda_{coil} = N_{coil}\phi_{coil} = \frac{2LD}{P} N_{coil} B_{amp} \sin(P\frac{\pi}{2}) \sin(\alpha + P\frac{\pi}{2})$$

$$= \lambda_{coil} M \sin(\alpha + P\frac{\pi}{2}) \tag{7.5}$$

Where

$$\lambda_{coil} M = \frac{2LD}{P} N_{coil} B_{amp} \sin(P\frac{\pi}{2}) \tag{7.6}$$

If the generator is driven at a constant angular velocity ω in electrical measure and in the direction indicated in Fig. 7.1(a).

$$\alpha = -\omega t$$

and the flux linkage is then expressed as a function of time by

$$\lambda_{coil} = -\lambda_{coil} M \sin(\omega t - P\frac{\pi}{2}) \tag{7.7}$$

which induces a coil voltage of

$$e_{coil} = -p\lambda_{coil} = \omega \lambda_{coil} M \cos(\omega t - P\frac{\pi}{2}) \tag{7.8}$$

Equation (7.7) expresses the maximum flux linkage, it could then link the entire flux per pole ϕ at the armature surface of the air-gap. It follows that

$\phi = \frac{2LD}{P} B_{amp}$, and the induced voltage is:

$$e_{coil} = \omega N_{coil} K_p \phi \cos(\omega t - P\frac{\pi}{2}) \tag{7.9}$$

Where $K_p = \sin(P\frac{\pi}{2})$ (pitch factor). $K_p = 0.97$, since $P = 5/6$. The winding distribution factor $K_d = 0.957$, (for more information please see appendix [D]).

since $\omega = 2\pi f$, the $r.m.s$ value of the coil voltage is

$$E_{coil} = \frac{2\pi N_{coil} K_p \phi}{\sqrt{2}} = 4.44 f N_{coil} K_p \phi \tag{7.10}$$

Substituting the dimensions of experimental homopolar machine yields, $E_{coil} = 15.35\ volts$ where $E_{phase} = 61.4\ rms\ volts$, this compares with the experimental and $MEGA$ calculations which are 54 and 58 respectively.

The flux linkage leads the resulting voltage induced in a generator coil by 90° in time phase as shown by a comparison of equation (7.7) and (7.9) and illustrated from FE calculation graphically in Fig. 7.2.

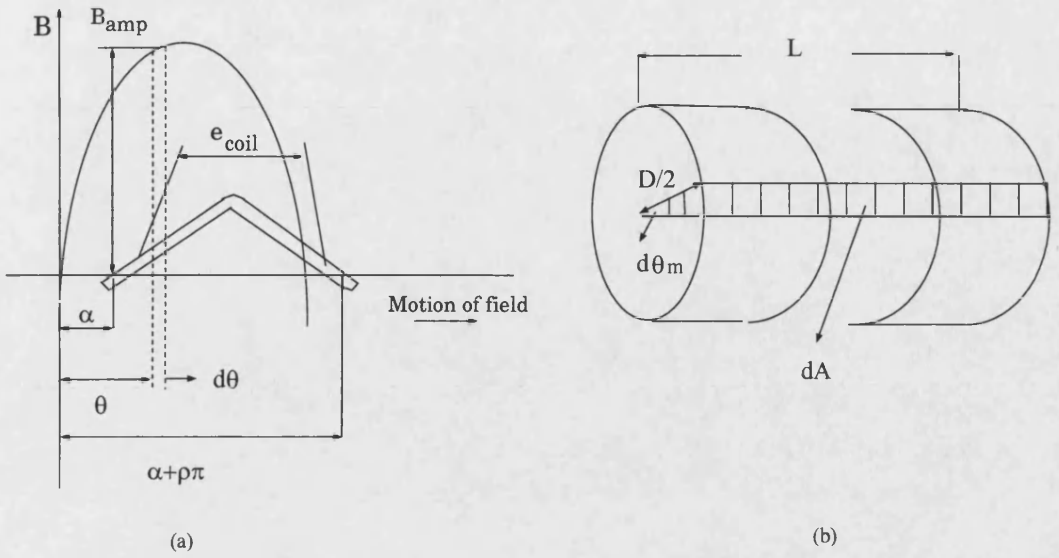

Figure 7.1: N-turn armature coil in a sinusoidally distributed magnetic field

7.3 Armature $M.M.F$:

The armature current in a synchronous machine produces an mmf which is stationary with respect to the mmf of the field winding under steady balanced conditions. The phase angle between the current and the voltage of the armature fixes the position of the armature mmf with respect to the poles. For example if the phase angle θi between the armature current and the voltage induced in the armature is zero, as indicated by the phasor diagram in Fig. 7.3(b), the armature mmf is in the $q-axis$, as illustrated in Fig. 7.3(a).

The $d-axis$ is shown passing through the field poles N_F and S_F. If the voltage in phase a is generated by the field flux is expressed by:

$$e_{af} = \sqrt{2}E_{af}\sin(\omega t)$$

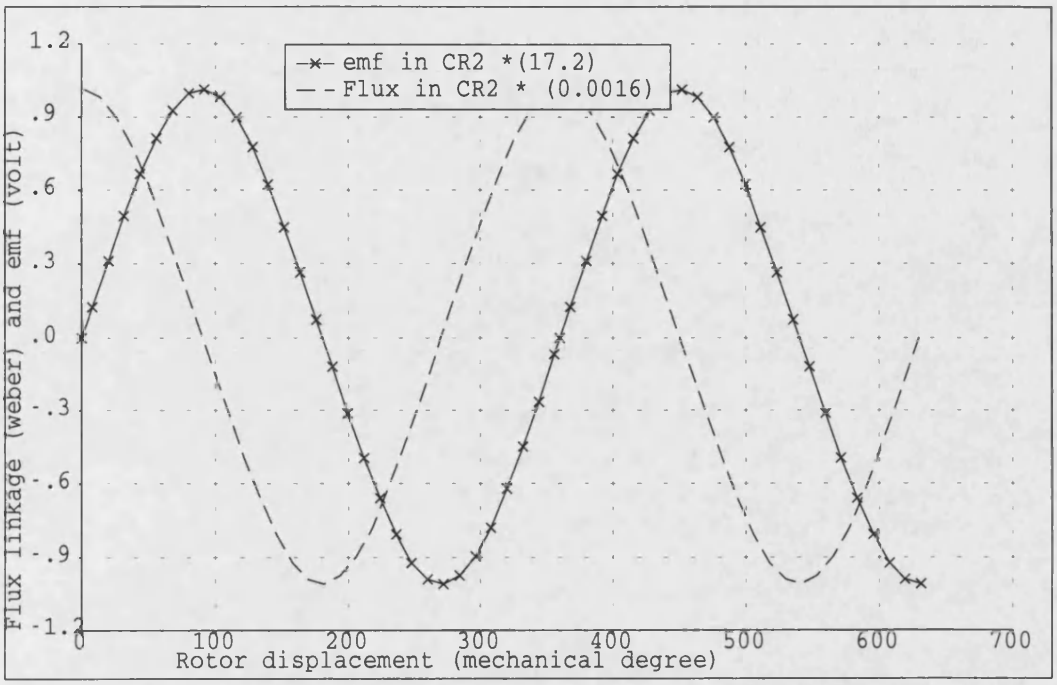

Figure 7.2: FE Flux linkage and induced emf in coil $CR2$ phase R

Then, the current in phase a is , for $\theta_i = 0$

$$i_a = \sqrt{2} I_a \sin(\omega t)$$

At $\omega t = \frac{\pi}{2}$, the instantaneous voltage and current in phase a are both a positive maximum, while those in b and c phases are negative and one-half of their maximum values. The armature mmf then produces an mmf along the path indicated by the dashed lines in Fig. 7.3(a) with the armature poles indicated by N_A and S_A. This mmf pattern rotates at synchronous speed in the same direction as the rotor and is therefore stationary relative to the field poles and in its reaction upon the field poles, producing torque opposite to the direction of

rotation. When the direction of the armature mmf is along the $q-axis$ (since the current and voltage are in phase), it has no magnetizing or demagnetizing effect upon the field. This can be noticed in Fig. 7.4 from the FEM analysis where the armature currents case described above were employed. It is assumed that both rotor ends (left and right in Fig. 7.4) are considered together to represents the case of a uniform air-gap.

In the condition when ωt has increased from $\frac{\pi}{2}$ to $\frac{5\pi}{6}$ (i.e by an angle of $\frac{\pi}{3}$ $rad.$), the negative value of i_c is maximum while at the same instant i_a and i_b are at one-half the positive maximum values, practically and under operating conditions the current lags the induced voltage by $\theta_i = \frac{\pi}{3}$ Fig. 7.3(d). The armature mmf now lags the $d-axis$ by $\frac{\pi}{3}$ rad and has components in both the direct and quadrature axis and is exerting a demagnetizing effect on the field. This also has been simulated in the FEM and shown in Fig. 7.5, for the same assumption that both rotor ends (left and right in Fig. 7.5) have been considered together to represent the case of a uniform air-gap.

By the same token, when the armature current leads the generated voltage it strengthens the field.

7.4 Unsaturated Inductance:

The effect of slots in the stator on the reluctance of the air-gap may be taken into account by increasing the length of the air gap from the actual clearance

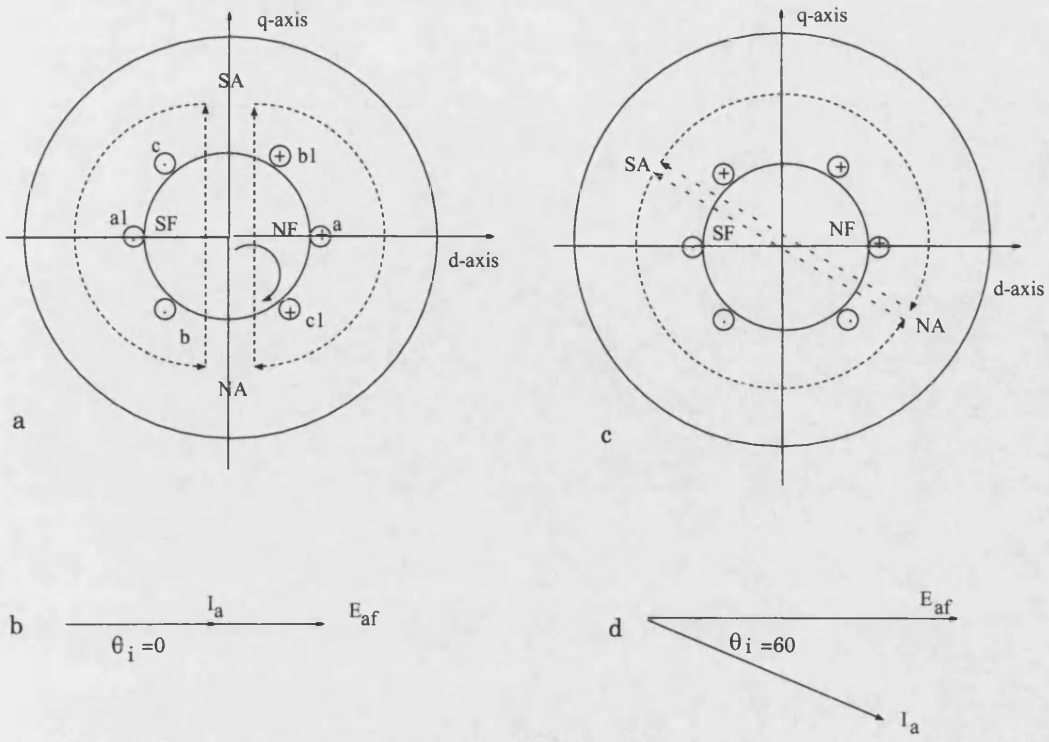

Figure 7.3: (a)Current in phase with generated voltage, (b)Flux path due armature mmf, (c) and (d) Armature flux path and currents lagging 60^o

g between stator to an effective length g_e. Generally the ratio $\frac{g_e}{g}$ for small machine in which g ranges from $0.025cm$ to $0.076cm$, usually between 1.1 and 1.25 (Carter's coefficient).

7.4.1 Inductance of the field:

If we assume H is normal to the iron surface (and curvature of the air-gap is neglected), the amplitude of H due to the mmf field is:

$$H_{amp.(field)} = \frac{MMF_{field}}{g_e} \tag{7.11}$$

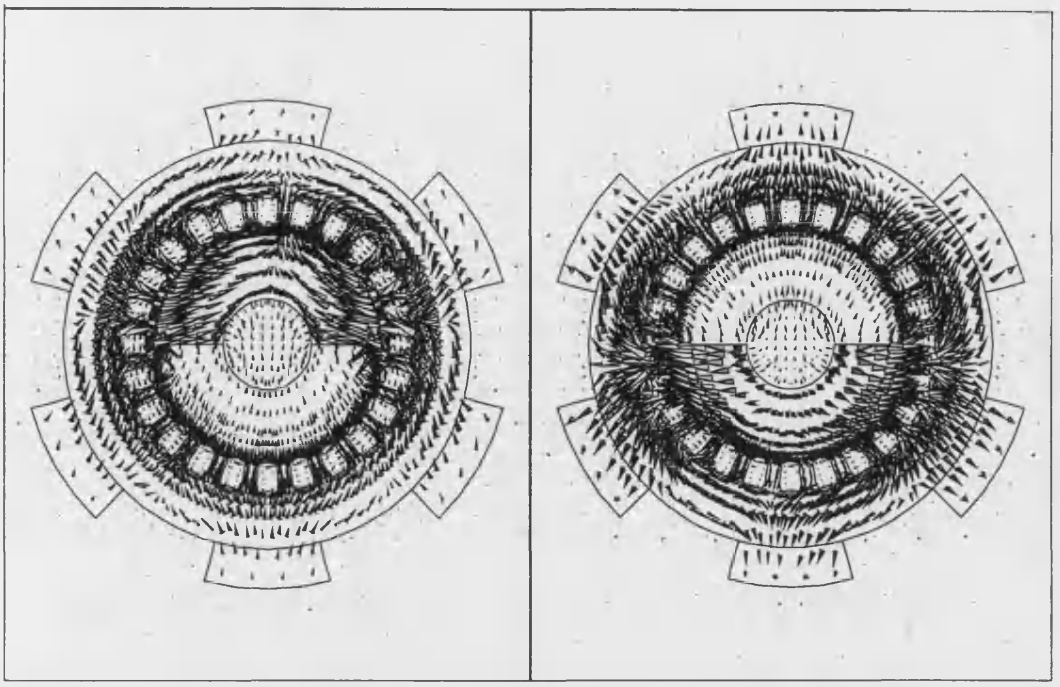

Figure 7.4: Armature field in FEM, the case above in Fig.7.3(a)

(Assuming that the iron is infinitely permeable).

The amplitude of the fundamental in the field mmf is:

$$MMF_{field} = \frac{4}{\pi} \times \frac{N_f i_f}{P} \qquad \text{ampere.turns/pole} \qquad (7.12)$$

Where N_f is the number of turns in series in the field winding and i_f is the field current.

The amplitude of the B wave due to i_f is:

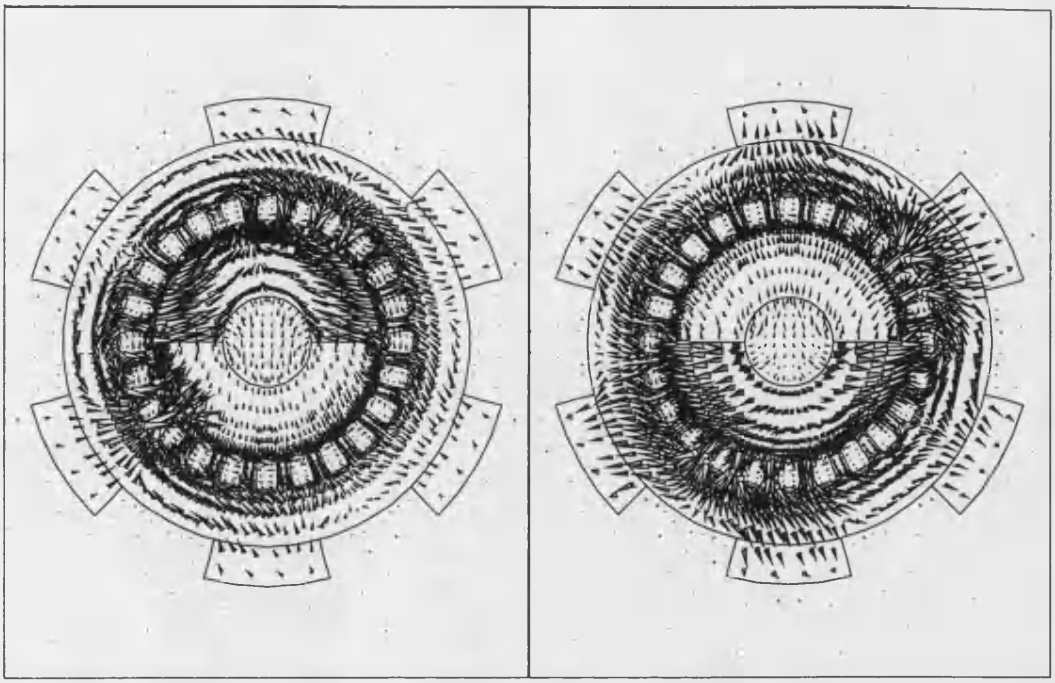

Figure 7.5: Armature field in FEM, the case above in Fig.7.3(d)

$$B_{amp.(field)} = \mu_o H_{amp.(field)} = \frac{4\mu_o N_f i_f}{\pi P g_e} \tag{7.13}$$

This peak air gap flux density has been calculated and found to be equal to 0.38 $Tesla$. However this takes no account of the mmf drop in the iron when this is included (please see appendix[D] for more details), the result was 0.308 $Tesla$. The experimental air-gap flux density was measured using a search coil and was found equal to 0.32 $Tesla$.

The average value of a sinusoid is $\frac{2}{\pi}$ times its amplitude, the flux per pole must be:

$$\phi_{field} = \frac{2}{\pi} B_{amp.(field)} \times area/pole \qquad \text{weber}$$

area per pole is $\pi D_g L/P$ where L is the effective axial length and D_g is the mean diameter at the air-gap, then:

$$\phi_{field} = \frac{2}{\pi} \times \frac{4\mu_o N_f i_f}{\pi P g_e} \times \pi D_g L/P$$

$$= \frac{8\mu_o N_f i_f D_g L}{\pi P^2 g_e} \tag{7.14}$$

The field flux linkage of:

$$\lambda_{field} = N_f \phi_{field} = \frac{8\mu_o D_g L N_f^2 i_f}{\pi P^2 g_e} \tag{7.15}$$

If the field leakage flux is not taken into account, then the self-inductance of the field winding is expressed by:

$$L_{field} = \frac{\lambda_{field}}{i_f} = \frac{8\mu_o D_g L}{\pi g_e} \times (\frac{N_f}{P})^2 \qquad (7.16)$$

7.4.2 Inductance due to the armature reaction:

The armature flux $\phi_{arm.}$ due to the armature $MMF_{arm.}$ can be determined on the same basis as ϕ_{field}.

$$\phi_{arm.} = \frac{2\mu_o A D_g L}{P g_e}$$

Where A is the amplitude of the fundamental in the armature mmf

$$A = \frac{0.9 m N_{ph} I}{Pa} \qquad \text{ampere.turns/pole}$$

Therefore:

$$\phi_{arm.} = \frac{1.8\mu_o m D_g L N_{ph} I}{P^2 a g_e} \qquad (7.17)$$

This flux in rotating at synchronous speed induces a voltage in each armature phase expressed by:

$$E_{phase} = \frac{4.44 f N_{ph} \phi}{a} \tag{7.18}$$

Where a is armature circuit in group of phase may be connected in series, in parallel or in series-parallel.

Substitution of equation 7.17 in equation 7.18 yields:

$$E_{arm.} = \frac{8 f \mu_o D_g L}{g_e} (\frac{N_{ph}}{Pa})^2 I \tag{7.19}$$

Then the reactance due to the armature reaction is defined by:

$$X_{ad} = \frac{E_{arm.}}{I} = \frac{8 \mu_o m D_g L}{g_e} (\frac{N_p h}{Pa})^2 \tag{7.20}$$

it follows that the magnetizing inductance is

$$L_{ad} = \frac{X_{ad}}{2\pi f} = \frac{4 \mu_o m D_g L}{\pi g_e} (\frac{N_{ph}}{Pa})^2 = 1.6 \times \frac{m D_g L}{g_e} (\frac{N_{ph}}{Pa})^2 \times 10^{-6}$$

where for a three phase winding, $m = 3$

$$L_{ad} = \frac{4.8 D_g L}{g_e} (\frac{N_{ph}}{Pa})^2 \times 10^{-6} \qquad \text{Henry/phase} \tag{7.21}$$

7.4.3 Machine synchronous reactance:

The fundamental component fluxes ϕ_{field} and $\phi_{arm.}$ produce flux linkages with the armature which induce corresponding components of armature voltage.The flux linkage with the armature winding due to the field current is:

$$\lambda_{af} = \frac{N_{ph}}{a} \phi_{field} \tag{7.22}$$

and that due to the balanced armature current is:

$$\lambda_a = \frac{N_{ph}}{a} \phi_{arm.} \tag{7.23}$$

The resultant of the field and the armature $mmfs$ produce the net air-gap flux:

$$\phi_{res.} = \phi_{field} + \phi_{arm.} \tag{7.24}$$

which results in the net armature flux linkage

$$\lambda_{ag} = \lambda_{af} + \lambda_a \tag{7.25}$$

all quantities in the equations above are phasors, and generates the corresponding components of armature voltage:

$$E_{ag} = E_{af} + E_A \tag{7.26}$$

The equivalent leakage flux ϕ_l and the flux $\phi_{arm.}$ of armature reaction are both in phase with the current. This magnetizing inductance and leakage inductance may therefore be added to yield the synchronous inductance:

$$L_s = L_{ad} + L_l \qquad \text{Henry/phase} \tag{7.27}$$

with the corresponding synchronous reactance

$$X_s = X_{ad} + X_l \qquad \Omega/\text{phase} \tag{7.28}$$

X_{ad} was calculated from equation(7.20) and equal to 38.7Ω. X_l can be calculated using the equation below [41]:

$$X_l = X_{ls} + X_{le} \tag{7.29}$$

Where X_{ls} and X_{le} are both slot and end winding components.

$$X_{ls} = 4\pi\mu_o f T_c^2 N_c W d_s \tag{7.30}$$

$$X_{le} = \frac{3}{2}\mu_o f (T_c N_c K_w)^2 D_m W^- \frac{1}{g_q^-} \tag{7.31}$$

Substituting in the above equations yield $X_{ls} = 1.15 \times 10^{-2}$, and $X_{le} = 36.724$, both in *ohm*. Therefore $X_l = 36.7355\ \Omega$. The total unsaturated armature

reactance is 74.7Ω

The air-gap voltage E_{ag} can be written as:

$$E_{ag} = V + (r_a + jX_l)I \tag{7.32}$$

and the open circuit voltage E_{af} as:

$$E_{af} = V + (r_a + jX_s)I \tag{7.33}$$

In performing the above work it was assumed that considering the effects of the two ends of the machine simultaneously would result in an effective cylindrical structure which could be described by the simple machine equivalent circuit which is implied by the equation above. However the slip test performed on the machine showed that a minor effective saliency is present. Therefore more accurate results should be obtained from a two-axis treatment.

7.5 Machine two-axis phasor diagram

From the phasor diagram of Fig. 6.38(This phasor diagram has been already used to recalculate the load performance in the previous chapter in section 6.9

when X_d and X_q were calculated from FEM and used in the two-axis phasor diagram), the open circuit voltage E_f can be found from the equation below:

$$\mid E_{af} \mid = \mid E_{aff} \mid + \mid I_d(X_d - X_q) \mid \tag{7.34}$$

$$E_{aff} = V + jIX_q \tag{7.35}$$

Where $I_d = I \sin \Psi$, and $\Psi = \delta + \theta$.

The direct and quadrature-axis components of the air-gap reactance, X_{dm} and X_{qm}, respectively, combine with the leakage reactance X_l in the usual way to provide the total synchronous reactance components of the machine X_d and X_q [41], i.e :

$$X_d = X_{dm} + X_l \tag{7.36}$$

$$X_q = X_{qm} + X_l \tag{7.37}$$

$$X_{dm} = \frac{3}{2}\mu_o f(T_c N_c K_w)^2 D_m W^- \frac{1}{g_d^-}(\sin\frac{\beta^-\pi}{2}) \qquad (7.38)$$

$$X_{qm} = \frac{3}{2}\mu_o f(T_c N_c K_w)^2 D_m W^- \frac{1}{g_q^-}(1 - \cos\frac{\beta^-\pi}{2}) \qquad (7.39)$$

Substituting in the above equations yield $X_{dm} = 35.3\Omega$, and $X_{qm} = 26.5\Omega$. Therefore the values for X_d and X_q are 72Ω and 63.2Ω respectively.

These reactances can be used in the two axis-phasor diagram equations to calculate the machine load performance for the resistive and inductive cases.

- *Resistive load*: The initial terminal voltage can be taken from the experimental resistive load test results say $V = 109.2$ *volts*, and the load current is $I = 1.24$ *ampere*. Then calculate E_{aff} as:

$$E_{aff} = 109.2 + j(1.24)(63.2) = 109 + j78.4 = 134.4\angle 35.7^o \qquad \text{(volts)}$$

Then to calculate the value of I_d as:

$$I_d = I \sin \Psi = 1.74 \times 0.58 = 0.72 \qquad \text{(amperes)}$$

Where $\Psi = \theta + \delta$, and since a resistive load case, $\theta = 0$.

Therefore the open circuit voltage E_{af} can be calculated as:

$$\mid E_f \mid = \mid 134.4 \mid + \mid 0.72 \times 8.8 \mid = 138.3 \qquad \text{(volts)} \qquad (7.40)$$

Where $\mid X_d - X_q \mid = 8.8\ \Omega$

As the machine experimental open circuit voltage is 155.6 *volts*, therefore the terminal voltage would be $= \frac{155.6}{138.3} \times 109.2 = 67.2$ *volts* (we assume a linear relation). However many values for the terminal voltages can be calculated to obtain the resistive load curve.

-*Inductive load*: The terminal voltages for the inductive load also can be calculated in the same way described above, but the load current I at 0.8 $p.f$ lagging ($\theta = 36.6$).

Fig. 7.6 shows the machine load performance for both, when X_d and X_q were calculated from FEM and from the simple machine theory. It will be observed a good agreement has been achieved between them.

In Fig. 7.7 the experimental machine load performance is shown in comparison with the calculated load performance from the two-axis phasor diagram (X_d and X_q were calculated from the simple machine theory). Fig. 7.8 is the experimental machine load performance in comparison with the calculated load performance from the two-axis phasor diagram (X_d and X_q were calculated from the FEM). In general the results from the FEM is closer to the experimental, than the results in Fig. 7.7 obtained from calculations.

7.6 Conclusions

The calculated open circuit voltage, air-gap flux density and the synchronous reactance components X_d and X_q are shown in the table below compared with those from experimental measurements and from the results obtained from FEM.

Parameters	**Calculated from simple theory**	**Measured**	**FEM**
E_{af}	61.4	54.9	56.4
B_g	0.308	0.32	0.34
X_{un}	74.7	58	51
X_s		45.2	37.4
X_d	72	77.6	66.2
X_q	63.2	72.5	57.6

Table 7.1: Calculated parameters compared with measurement and FEM

It can be seen from above a close agreement has been achieved for the parameters from calculation, measurements and from FEM results.

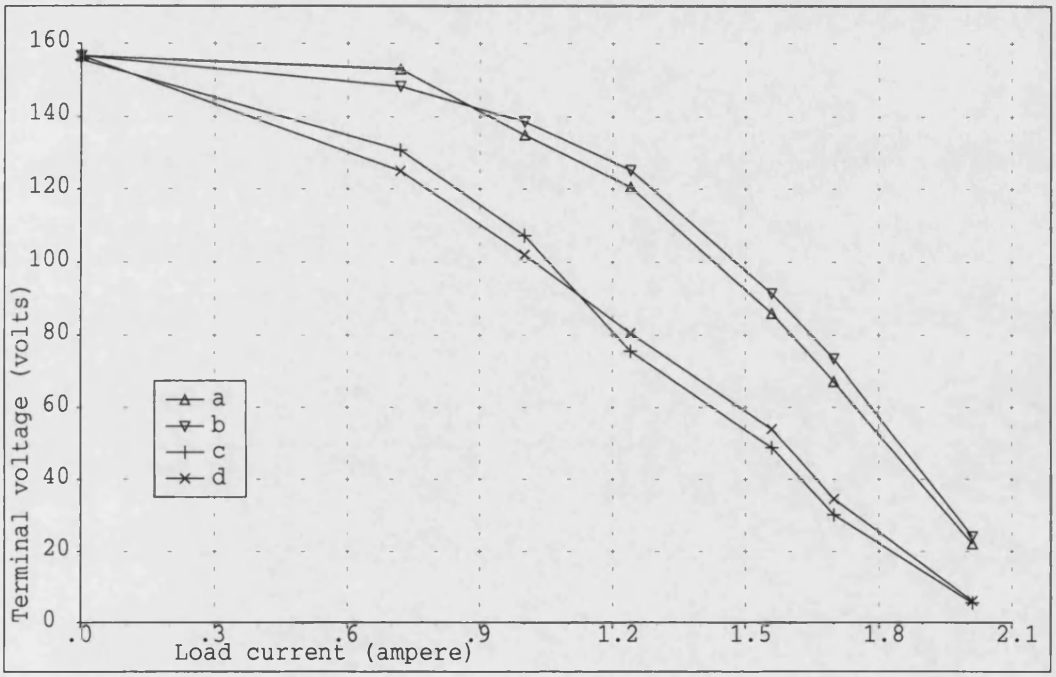

Figure 7.6: Machine load performance, (a)Resistive load X_d and X_q calculated from simple machine theory, (b)Resistive load X_d and X_q calculated from FEM, (c)Inductive load X_d and X_q calculated from simple machine theory, (d)Inductive load X_d and X_q calculated from FEM.

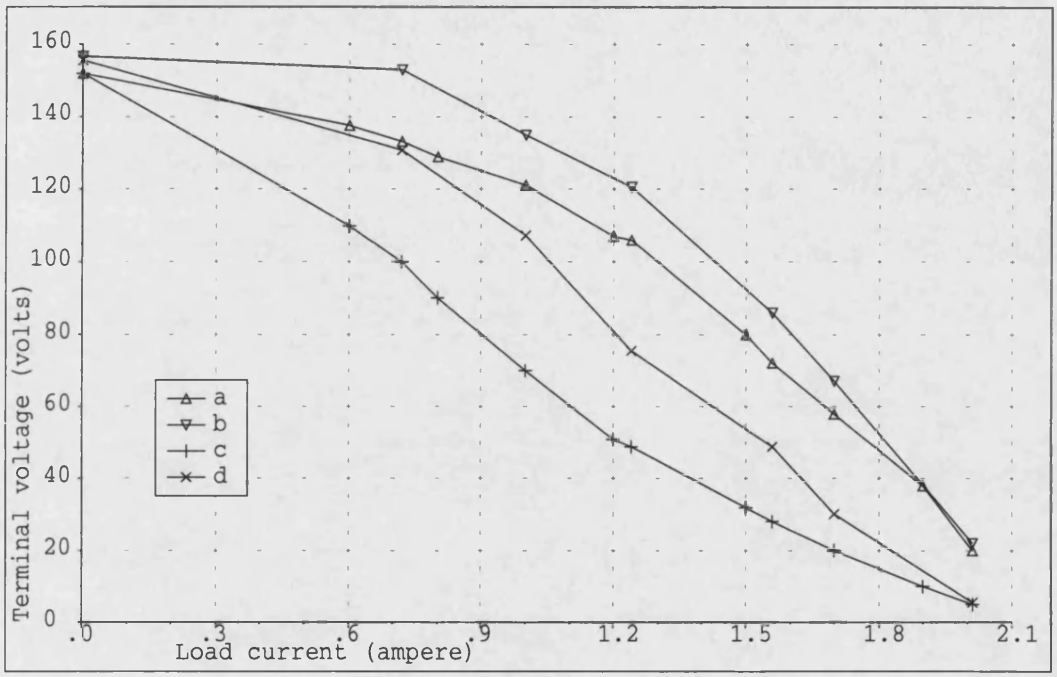

Figure 7.7: Machine load performance, (a)Experimental resistive load, (b)Resistive load X_d and X_q calculated from simple machine theory, (c)Experimental inductive load, (d)Inductive load X_d and X_q calculated from simple machine theory

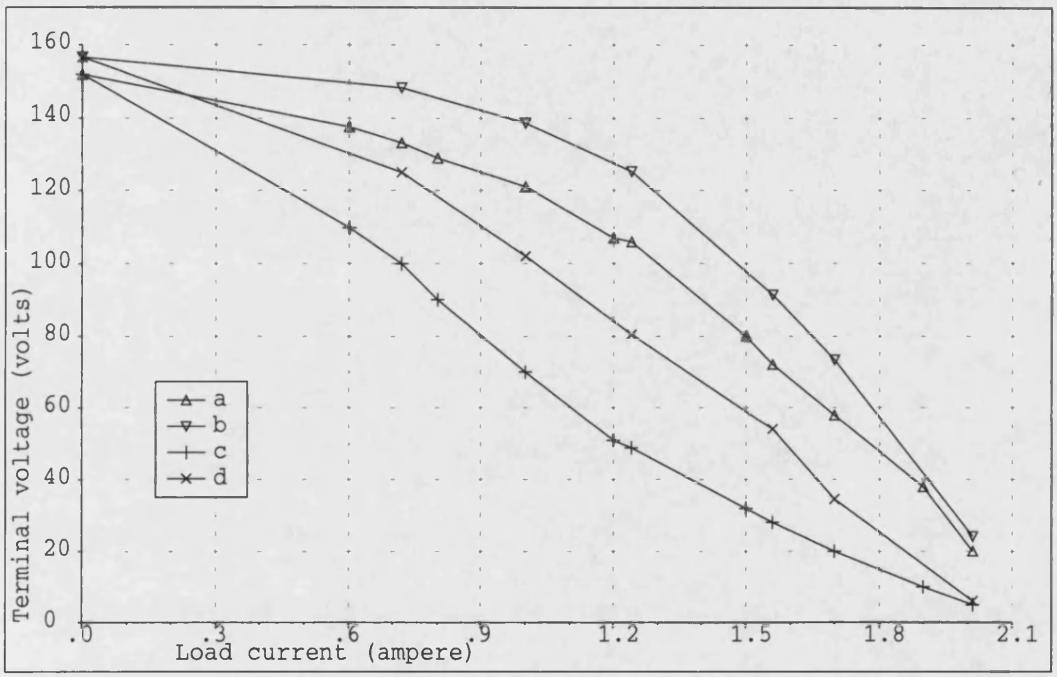

Figure 7.8: Machine load performance, (a)Experimental resistive load, (b)Resistive load X_d and X_q calculated from FEM, (c)Experimental inductive load, (d)Inductive load X_d and X_q calculated from FEM

Chapter 8

Improved Machine design

8.1 Introduction

The experimental machine design was not optimized. However the current design dimensions which have been obtained from FEM results were used to construct the prototype machine. These parameters related to the machine magnetic circuit dimensions and can be improved to achieve better design. For example it has been shown in the previous chapter that the machine magnetic circuit is saturated, the reactance is high and the output power is low. This chapter seeks to redesign the machine so that some of these disadvantages are suppressed.

8.2 Machine improved design magnetic circuit

In order to reduce the reactance of the machine the air-gap must be increased as an example Fig. 8.1, shows a machine within 3 times the air-gap of the original design to produce the same induce voltage on open circuit (155 *volts*), in this design the field coil mmf must also be increased 3 times $i.e$ to (3×562.5 $ampere - turn$). If the same coil design is used the field circuit losses will be increased 9 times $i.e$ (729) *watts*, this is a high value but can be reduced by employing a field coil with greater cross section. If the sectional dimensions are 25×22 cm^2, then the field loss is 208 *watts* compared with 81 *watts* from the original design.

8.3 Machine saturation

There are different levels of saturation in this machine. The saturation is highest in the middle of the machine. In particular the rotor centre shows the highest level of saturation where the laminations are circular.

This saturation can be avoided if the rotor shaft is made from a magnetic material such as mild steal (please see appendix [A] for details) instead of the non-magnetic material which is used in the original design[42]. This reduces the saturation by 54% in the $3D$ FEM. The non-magnetic shaft was adopted in

the original design to help to prevent bearing fluxes and high external fields. A comparison between the flux conditions with and without a magnet shaft are shown in Fig. 8.2 and Fig. 8.3, respectively. In Fig. 8.4 and Fig. 8.5, the flux distribution with and without magnetic shaft are compared. It is clear the flux has made a path through the axial shaft and produces high external fields in magnetic shaft case (Fig. 8.2).

8.4 Rotor laminated poles

The rotor was laminated in the original design. However it could have been solid since the flux in the rotor does not alternate as was explained in chapter 3. The rotor carries a constant flux within an induced a north pole on one end and a south pole on the other end of the rotor.

The only alternating flux in the rotor is due to the stator slotting. The flux in the tooth area is illustrated in Fig. 8.6, it will be observed that as the rotor moves a point near the surface experiences flux changes. These changes cause local iron losses which are one component of the stray losses. In solid pole rotors used for high speed machines the stray loss will always remain a disadvantage which can not be avoided [43].

8.5 Machine output power

It has been shown in section 5.4 chapter 5, that the iron losses may be found from the FEM calculations and hence the method is used to calculate the iron losses in the improved design. This was found to be 47.1 *watts* as detailed in appendix [F].

The copper loss in the stator is equal to $3 \times I_a^2 \times R_{arm.}$ and $R_{arm.}$ is the armature phase resistance and is equal to $\frac{130}{120} \times 1.55 = 1.68\Omega$. Since the length of the winding in this improved design is increased. The resistance was scaled from the original using the ratio of the two mean turn lengths.

The efficiency is shown in Fig. 8.7 against output power for resistive load in comparison with the efficiency of the old design. It will be observed that the efficiency has been increased from about 55% in the old design at full load to about 75% in the improved design. Therefore the machine efficiency has been improved by more than 26%.

8.6 A comparison with a conventional machine

A conventional cylindrical machine has been modelled to compare with the improved design. The general 3D view of this machine is shown in Fig. 8.8, it has an axial stack length is half of the length of the improved design. This has

the same peak air-gap flux when the same mmf (562.5 $ampere-turn$) is used. Hence the flux linkage, taking both ends of the machine into account, is the same for the homopolar and cylindrical versions. A comparison between the induced emf in the stator coil of the two machines is shown in Fig. 8.9, this indicates that approximately the same emf is induced at the same field mmf. The weight of both improved and conventional machines have been calculated in the same way as in chapter 5 for comparison purposes.

In the Improved design machine the weight in the stator is $22.5kg$ (this total weight is the sum of the stator core weights $15kg$ and the longitudinal block weights $7.45kg$). The rotor weight is $4kg$. Thus the total weight is $26.5kg$. In the conventional machine the weight of the stator is about $8kg$ and the weight of the rotor is $3.3kg$. The total weight of the conventional machine is thus $11.3kg$. The conventional machine is only 42% of the weight of the improved machine. This disadvantage is however offset by the advantage of a passive rotor which can rotate at high speeds coupled within inexpensive voltage output regulation using a stationary winding.

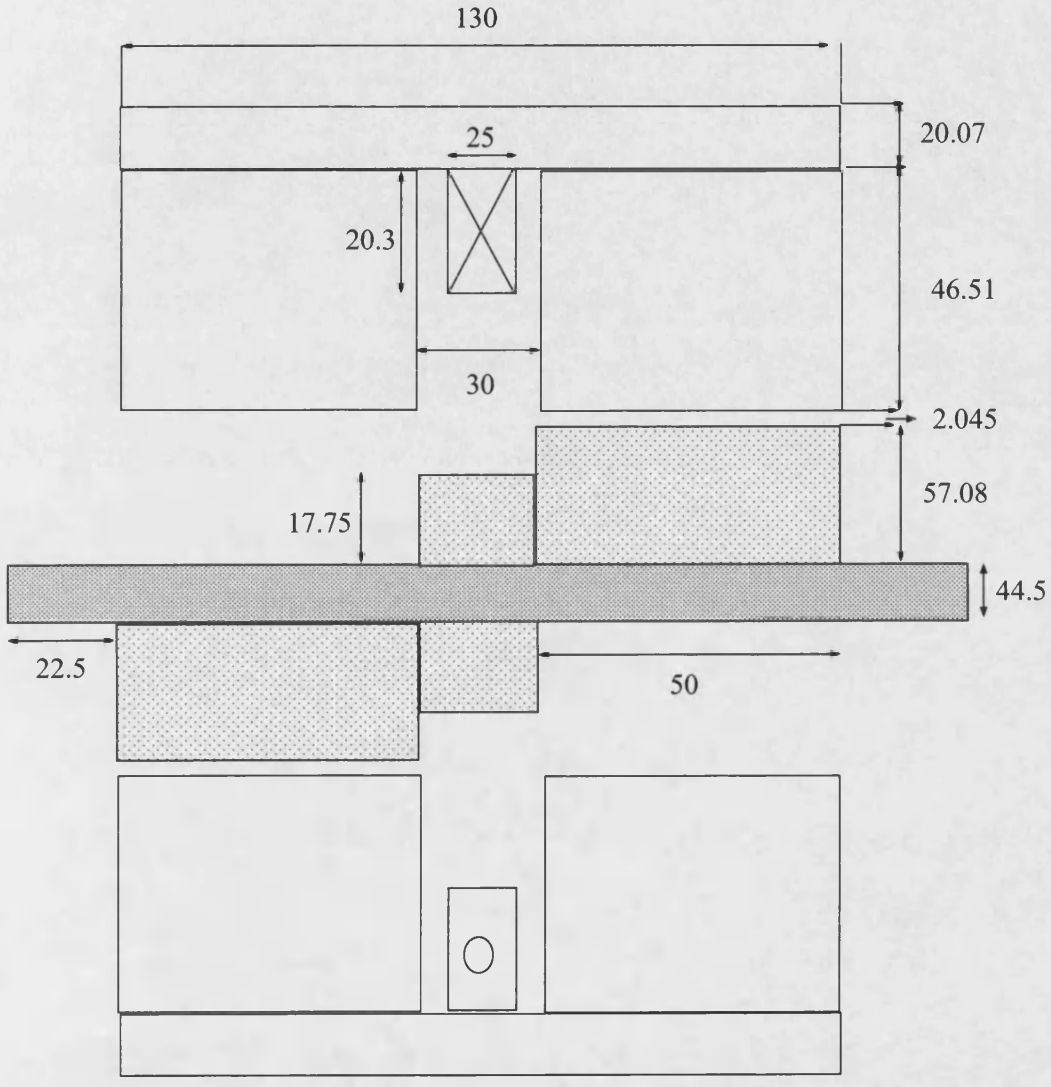

Figure 8.1: Improved machine dimensions

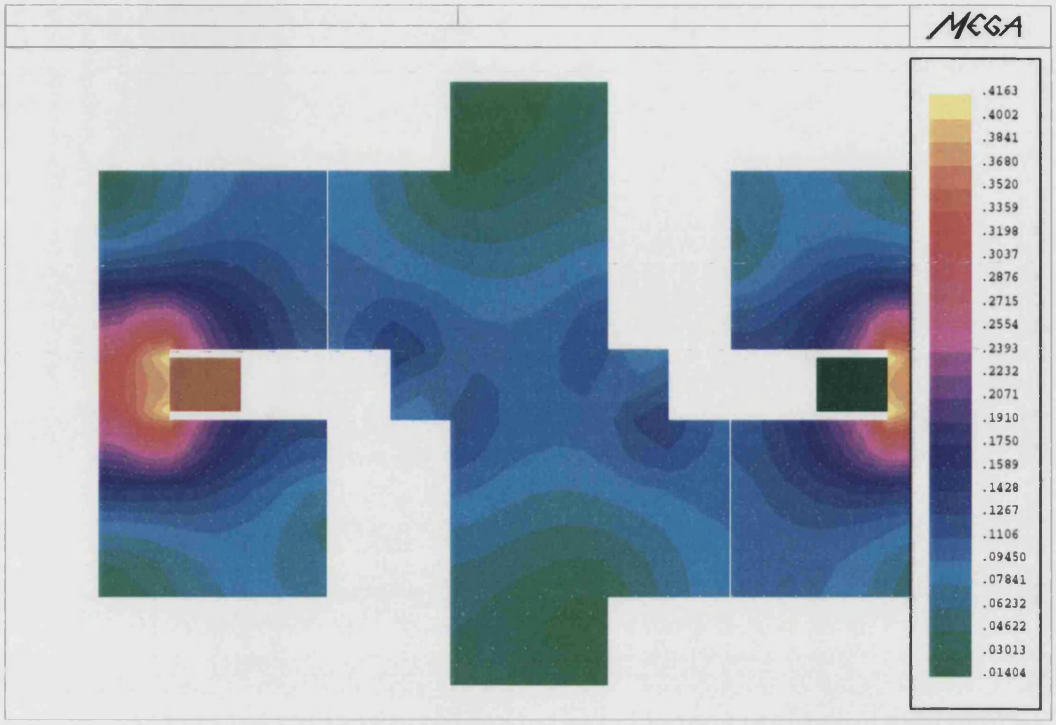

Figure 8.2: Saturation level with magnetic shaft

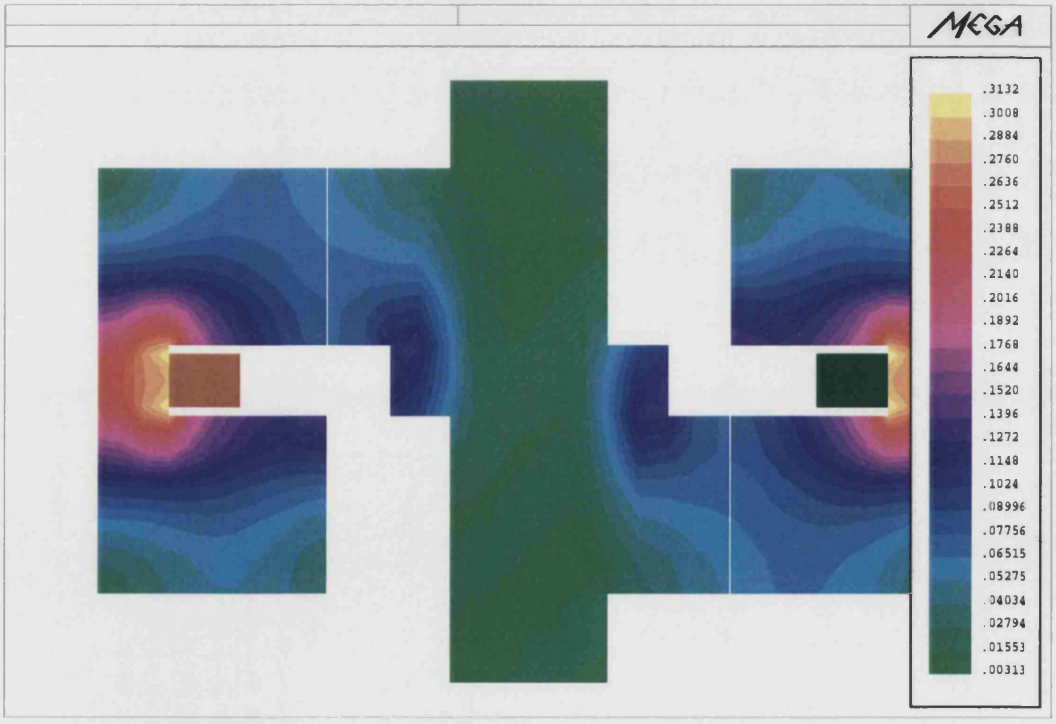

Figure 8.3: Saturation level without magnetic shaft

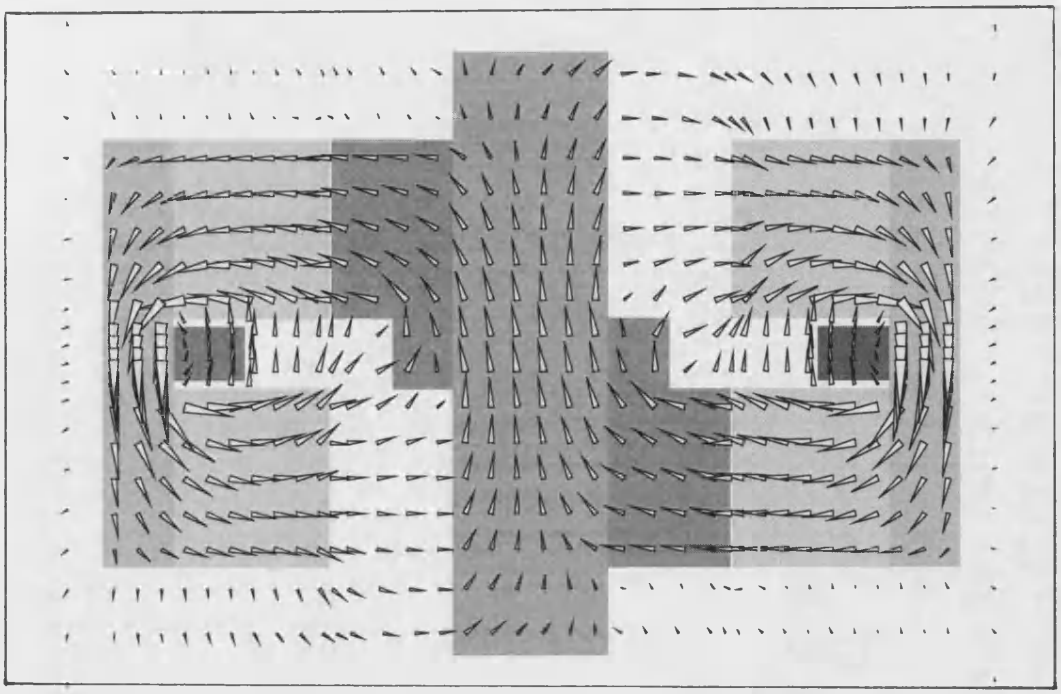

Figure 8.4: Vector flux with magnetic shaft

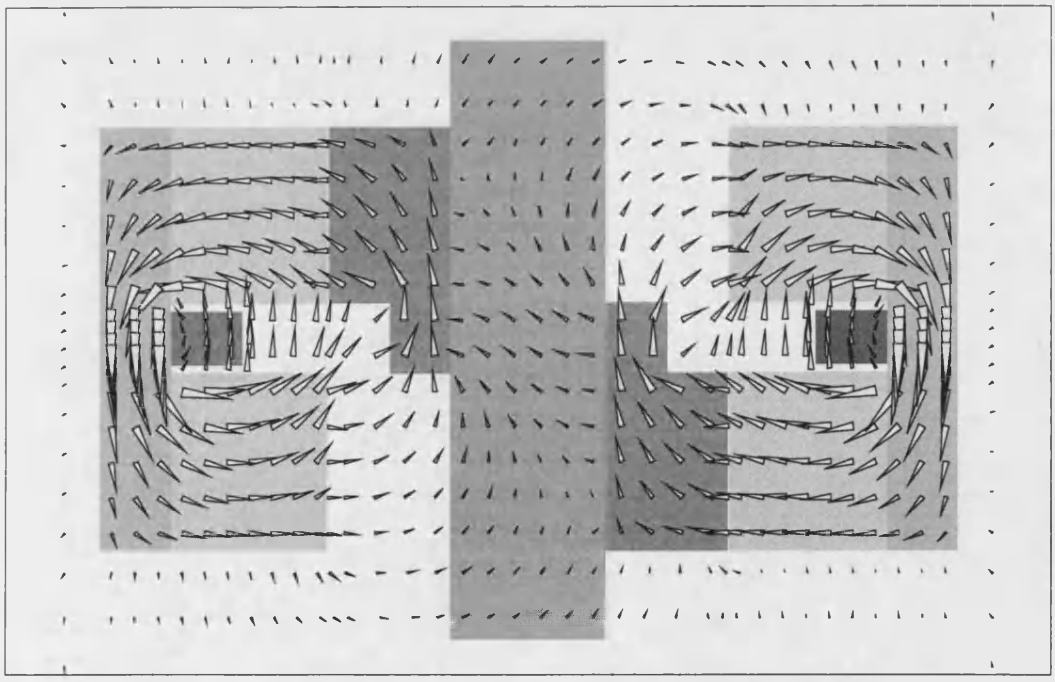

Figure 8.5: Vector flux without magnetic shaft

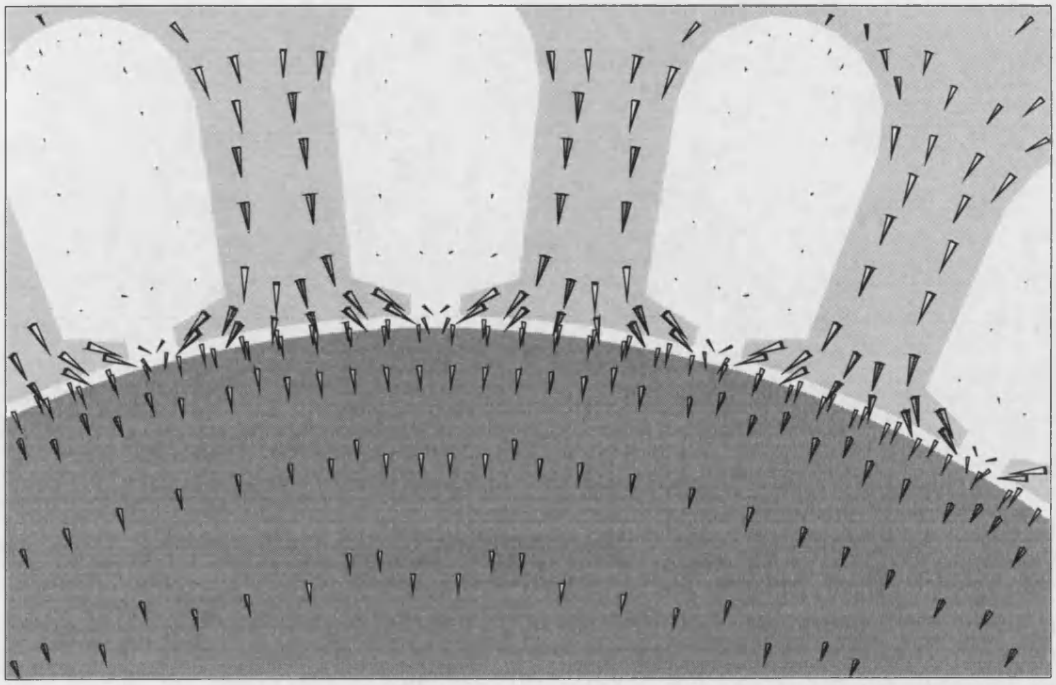

Figure 8.6: Rotor flux due to slotting

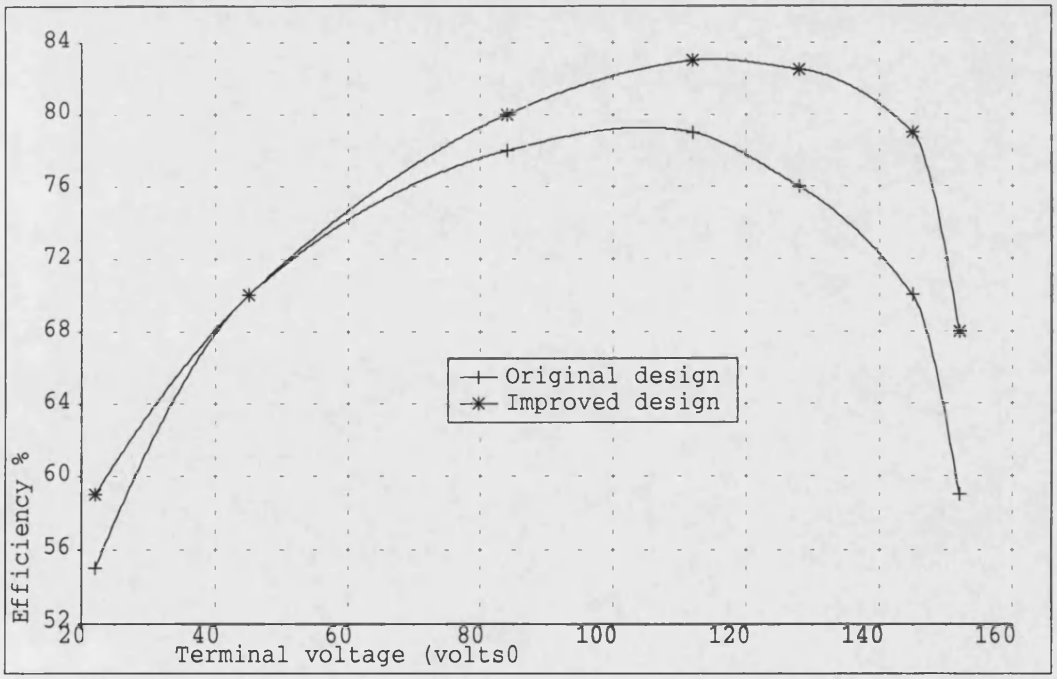

Figure 8.7: Efficiency of the Improved design in comparison with the efficiency of old design

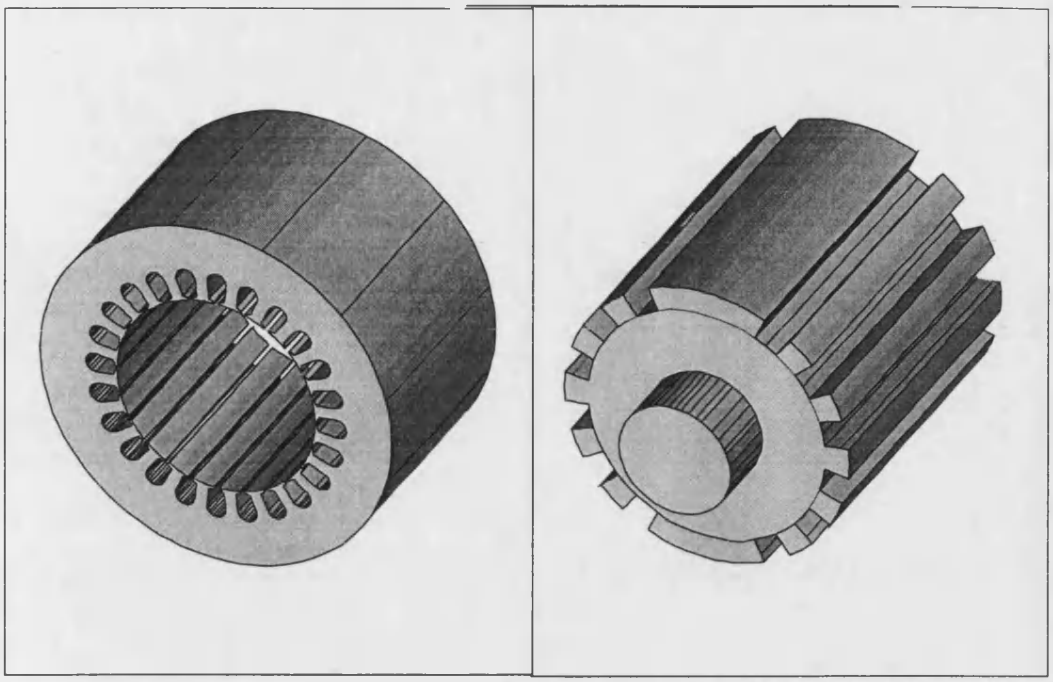

Figure 8.8: Conventional machine in 3D view

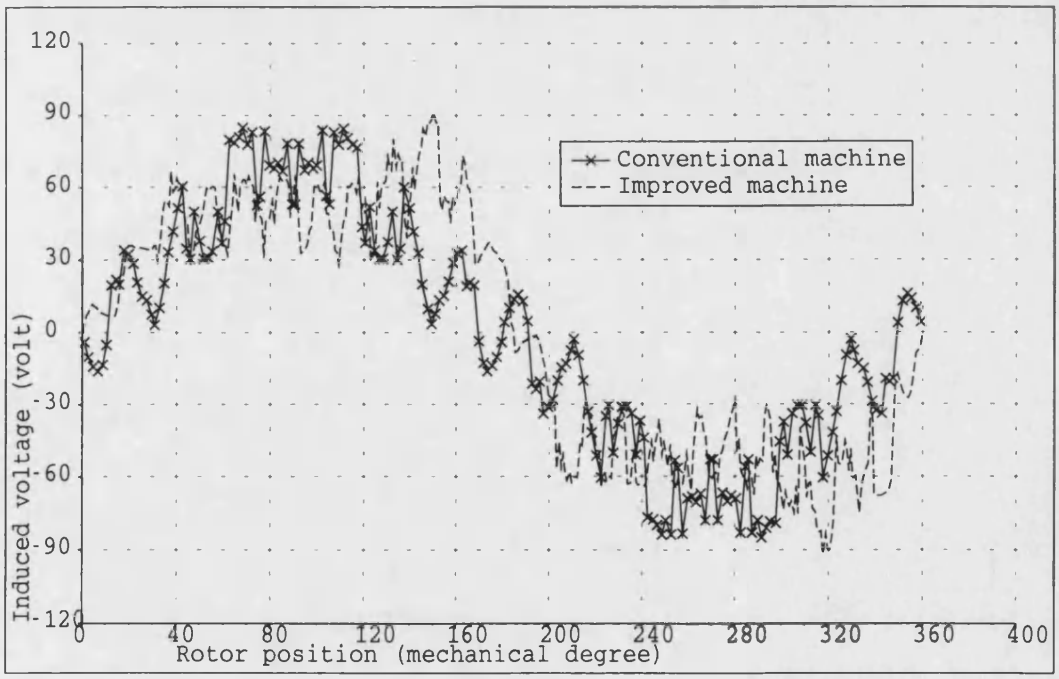

Figure 8.9: Induced emf in stator coil in both, improved and cylindrical machines

Chapter 9

Conclusion

The analysis design, and the construction of an $A.C$ side excited homopolar synchronous machine has been presented. This has involved the utilization of both $2D$ and $3D$ finite element methods to calculate the machine parameters and performance. A simple synchronous machine theory has also been employed for calculation purposes. All the calculations were validation by results from a prototype.

The principle of operation of the homopolar and heteropolar machines was explained. It was shown that the flux crosses the air-gap in both directions in the case of the heteropolar machine, conversely in the homopolar case the flux has the same direction at all points round the periphery.

The machines were modelled by using FEM methods. A $2D$ FE was first used

in the early stage of the design to predict the flux pattern in the homopolar and heteropolar machines. However a full $3D$ FEM was considered later for both machines. $3D$ finite element modelling was used to predict the complex field path in the machines, also to calculate the coil, phase flux linkages, and the induced phase emf. A modified rotor profile was also studied, this improved the emf waveform.

The theoretical results obtained from the $3D$ FE analysis in the homopolar and heteropolar were used for comparison purposes. It was concluded that for equal induced emf and armature current the loss in the heteropolar machine is 10% greater than the loss in the homopolar machine. Also the mass of the heteropolar is about 19% greater than the homopolar machine. Therefore the homopolar machine has been selected to be constructed as a prototype machine.

The construction of this homopolar machine was considered with care. Due account was taken of the nature of the magnetic field traversing each part of the machine in order to decide which sections should be laminated.

The test results from measurements on the prototype were verified with those from calculations in $3D$ FEM. The tests included open circuit test, short circuit test, slip test and so on. The test conditions were implemented in a $3D$ finite element model using FEM external circuit techniques. The results from this technique compared well with the results from the prototype.

The calculated parameters from FEM were used in a two-axis phasor diagram. Here the FEM, short circuit and slip tests were used within the FEM calcu-

lated open circuit voltage to obtain the two-axis synchronous reactances. The calculated load performance using these two-axis synchronous reactances also compared well with the experimental load performance.

The analytical machine approach was based on a simple magnetic circuit analysis. The calculated machine parameters were also compared with those both calculated from FEM and measured on the prototype machine. Excellent agreement was obtained.

Excellent agreement was also obtained between the FEM calculated and experimental load performance. The method using the two-axis phasor diagram with both calculated X_d and X_q from FEM and from the simple magnetic circuit analysis gave answers which whilst not as close as FEM are sufficiently accurate for many design purposes. The best design process therefore is to use the simple magnetic circuit theory in the initial design study to find the required machine dimensions, then to refine the calculated performance using the two-axis theory.

It has been observed that the machine has a high reactance value and the saturation level can not be ignored.

Improved machine design was investigated to reduce the machine reactance and saturation level, also by using 3D FEM. The improvement obtained increased the efficiency of the machine to 82% and the saturation conditions improved by 54%. This allowed comparison with a conventional machine to be made. This showed as might be expected of a homopolar machine that the machine mass

is about twice that of a conventional arrangement. However the conventional machine with a wound rotor can not be used for high speed working.

In these circumstances the comparison is between an unregulated permanent magnet construction with an expensive full power electronic regulator and a heavier machine with a passive rotor which can be regulated by adjusting the current in a simple stationary winding. Clearly there are niche markets where the homopolar machine can be used.

Appendix A

Stator and rotor BH-curves

In this appendix Fig. A.1, and Fig. A.2, are the characteristic material $BH-$ *curve* of the rotor and stator respectively.

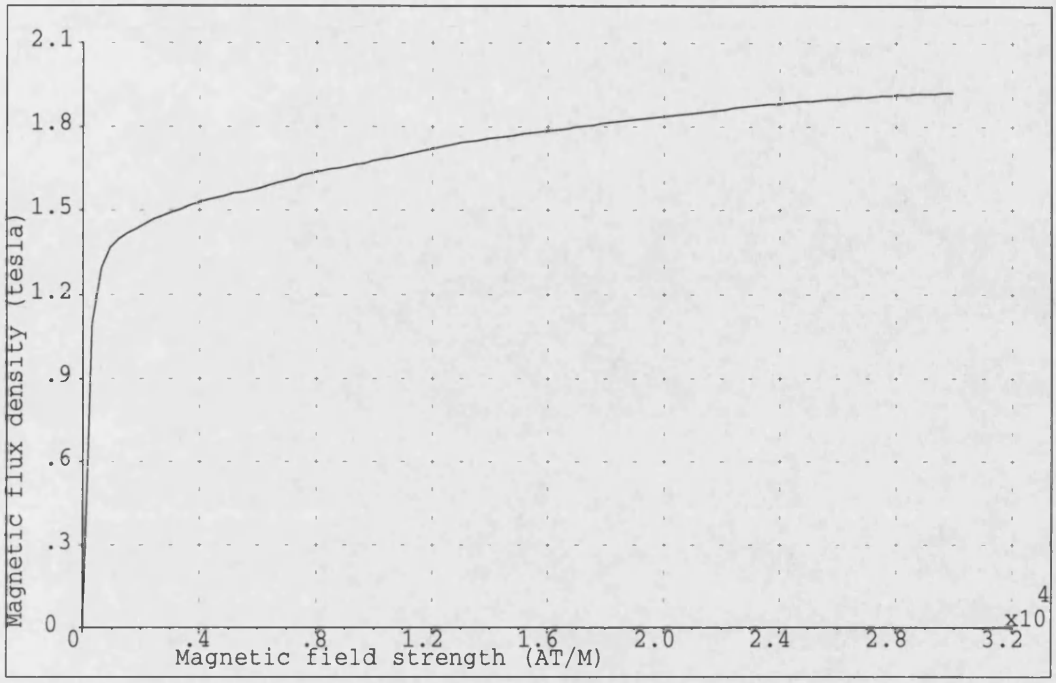

Figure A.1: Rotor BH-curve

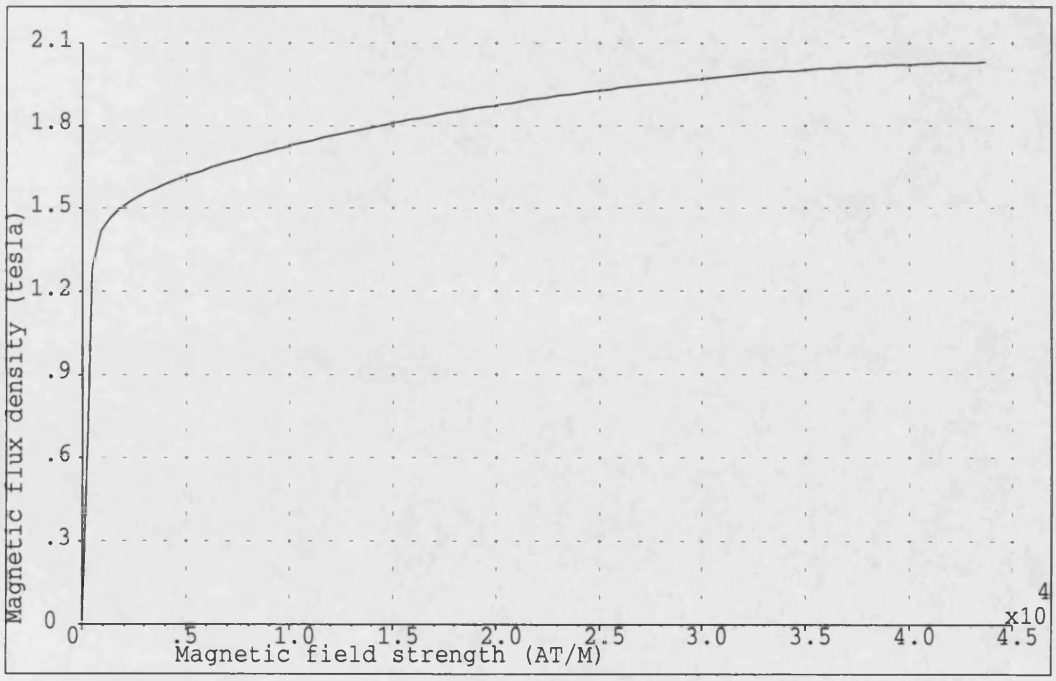

Figure A.2: Stator BH-curve

Appendix B

Rotor dynamic balance

B.1 Introduction

The rotor has to be dynamically balanced since the shaft carries rotating masses not in the same plane, it may be in static balance but due to inertia forces when rotating may be subject to an unbalanced couple. Whether the masses are in the same plane or not, the inertia forces act radially outwards and may therefore balance, but since the lines of action of the inertia forces act in different planes, each force produces a different moment about any given plane of the shaft. Thus an unbalanced moment may arise[44]. For a shaft to be in complete dynamic balance there must be no unbalanced force or couple. This couple must be resisted by the reactions at the bearings. When the shaft rotates so does

the direction of the unbalanced couple and bearings are therefore subject to rotating radial forces. This condition, if allowed to persist, sets up undesirable vibrations.

B.2 Calculation of centre laminations

In Fig. B.1, the shaded area A represents the rotor lamination area, and b is the centre of lamination slice to the centre shaft, this has to be calculated in order to find out the inertia force as follows:

$$A = \frac{\pi(r^2)}{2} - \frac{\pi r_1^2}{2} \tag{B.1}$$

$$(b)(A) = (\frac{4r}{3\pi})(\frac{\pi r^2}{2}) - (\frac{4r_1}{3\pi})(\frac{\pi r_1^2}{2}) \tag{B.2}$$

From these above equations, $A = 4252.4 \times 10^{-6}$, and $(b)(A) = 170.1368 \times 10^{-6}$, where $b = 0.04$ *metre*.

B.3 Dynamic forces at bearings

The shaft shown in Fig. B.2(a), carries two masses in the same axial plane but diametrically opposite to one another. To calculate the dynamic loads on the bearings when the shaft rotates at 3000 rpm, each mass is almost 2 k_g at 40 mm radius. In this Fig. B.2(b), also shows the end view when the masses are in the vertical plane; the shaft is evidently in static balance since mb values are equal and opposite(m is mass, and b is radius of mass). When rotating, therefore, the inertia forces are in balance. Nevertheless the two rotating masses exert a pure couple anti-clockwise due to the two equal inertia forces acting at distance d apart as shown in Fig. B.3.

$$Moment\ of\ couple = m\omega^2 b \times d$$

This couple is in equilibrium with reactions at bearing A and B, respectively, acting as shown in Fig. B.2(c), to produce a clockwise couple. For each rotating mass:

$$inertia\ force\ F_1 = F_2 = m\omega^2 b$$

$$moment\ of\ couple = F_1 \times d = F_2 \times d = 552.84\ N.m$$

To remove these reactions from the bearings other masses have to be added on both sides of rotor ends and as shown in Fig. B.4.

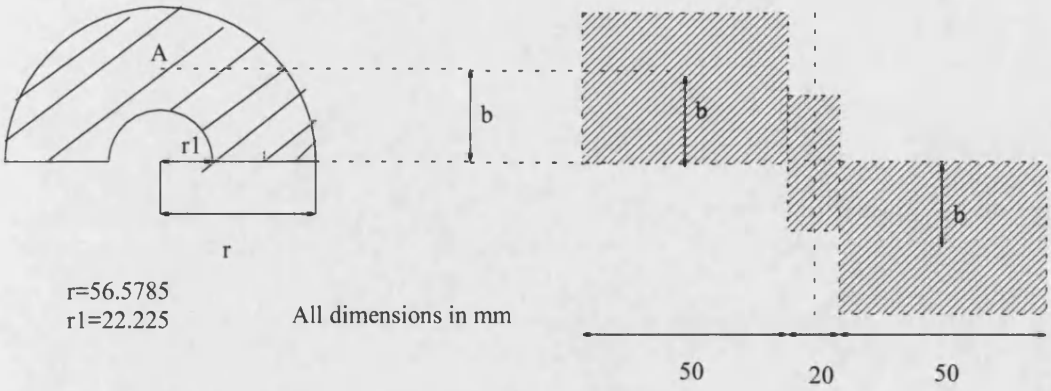

Figure B.1: Lamination centre area

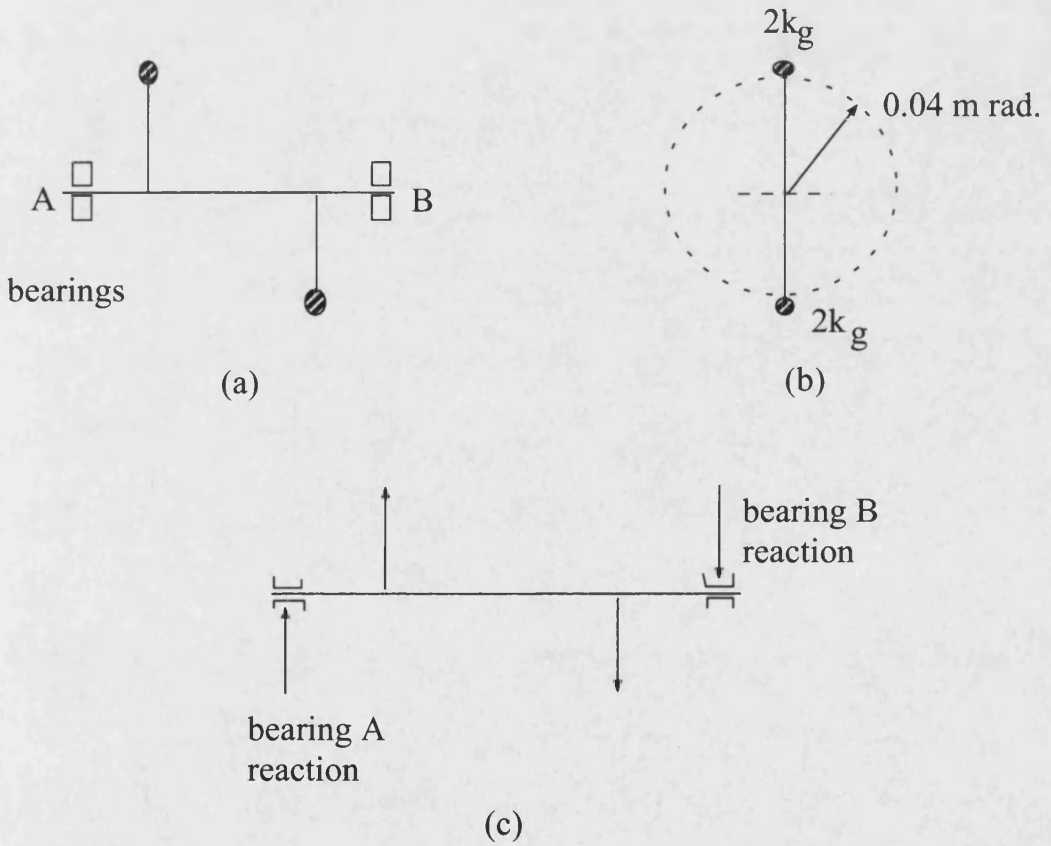

Figure B.2: Bearings load reactions

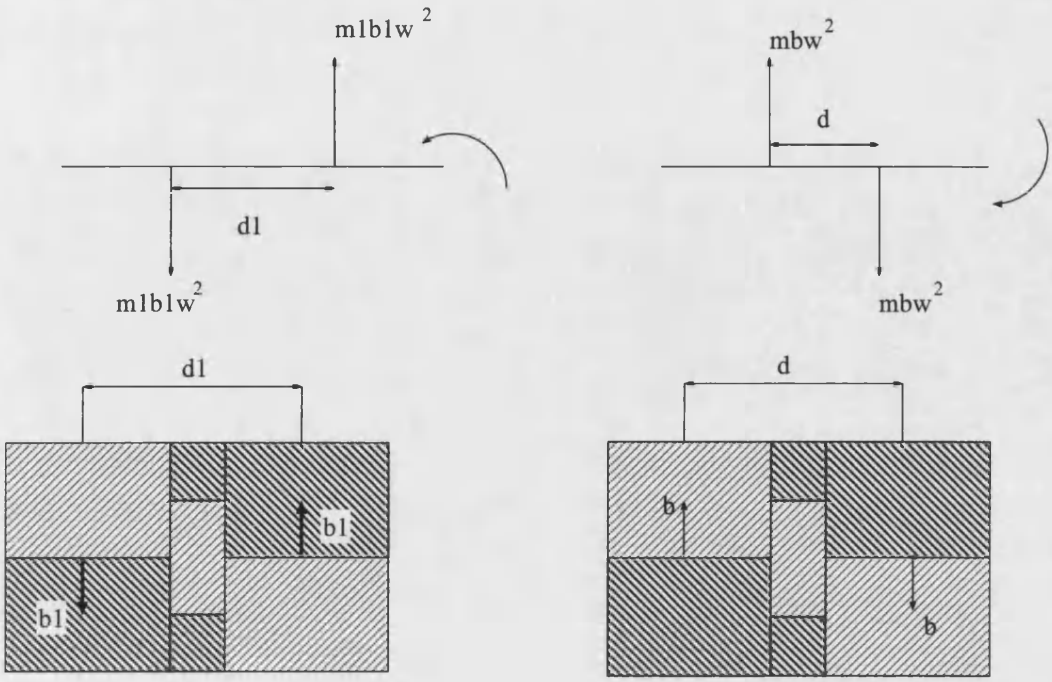

Figure B.3: Couple exertion

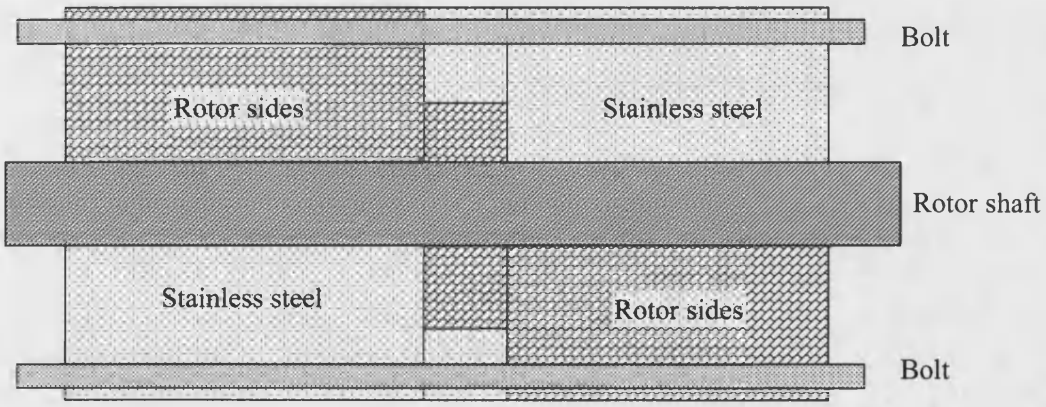

Rotor after balance

Figure B.4: Rotor shape after balance

Appendix C

Input torque measurement

C.1 Power and torque in synchronous generator

Not all the mechanical power going into a synchronous generator becomes electric power out of the machine. The difference between output power and input power represents the losses of the machine. A power flow diagram for a synchronous generator is shown in Fig. C.1.

The input mechanical power is the shaft power in the generator is :

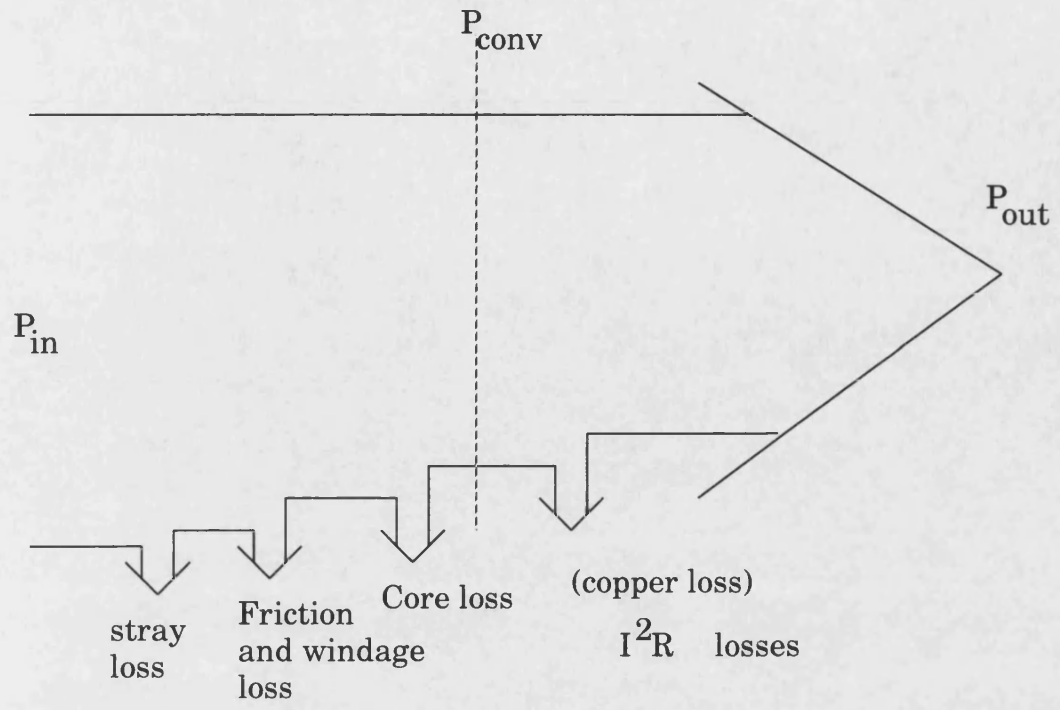

Figure C.1: The power flow diagram

$$P_{in} = T_{app}\omega_m \tag{C.1}$$

While the power converted from mechanical to electrical form internally is given by:

$$P_{conv} = T_{ind}\omega_m \tag{C.2}$$

or, can be rewritten as :

$$P_{conv} = 3E_A I_A \cos\delta \tag{C.3}$$

where δ is the angle between E_A and I_A. The difference between the input power to the generator and the power converted in the generator represents the mechanical , core and stray losses of the machine. The real electrical output power can be expressed in line quantities as :

$$P_{out} = \sqrt{3} V_T I_L \cos\theta \tag{C.4}$$

or in phase quantities as:

$$P_{out} = 3V_\phi I_A \cos\theta \tag{C.5}$$

The armature resistance R_a is ignored since X_s greater than R_a, notice that in Fig. C.2, when stator resistance is ignored, therefore,

$$I_A \cos\theta = \frac{E_A \sin\delta}{X_s} \tag{C.6}$$

The output power can then be written as :

$$P = \frac{3V_\phi E_A \sin\delta}{X_s} \tag{C.7}$$

and because $P_{conv} = T_{ind}\omega_m$, the induced torque can be expressed as:

$$T_{ind} = \frac{3V_\phi E_A \sin\delta}{\omega_m X_s} \tag{C.8}$$

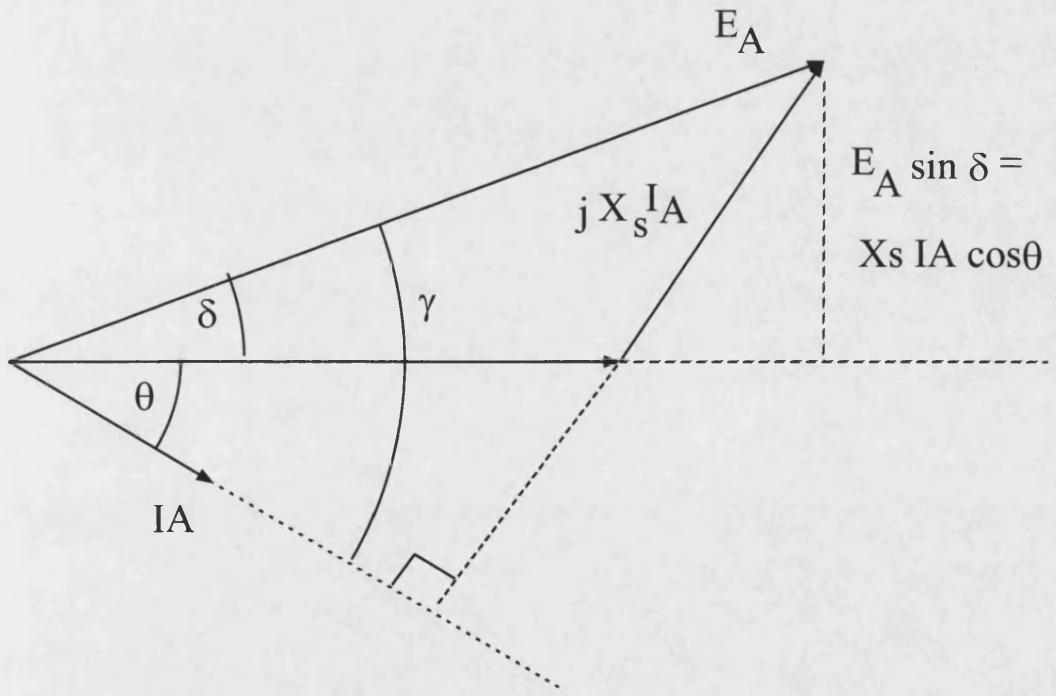

Figure C.2: Simplified phasor diagram

C.2 Torque measurement

Fig. C.3 shows the experimental set up to measure the input torque to the machine. When the machine is unexcited and runs at synchronous speed, the input power represents the friction and windage loss, and when the machine is excited the input power represents the total friction, windage and core loss.

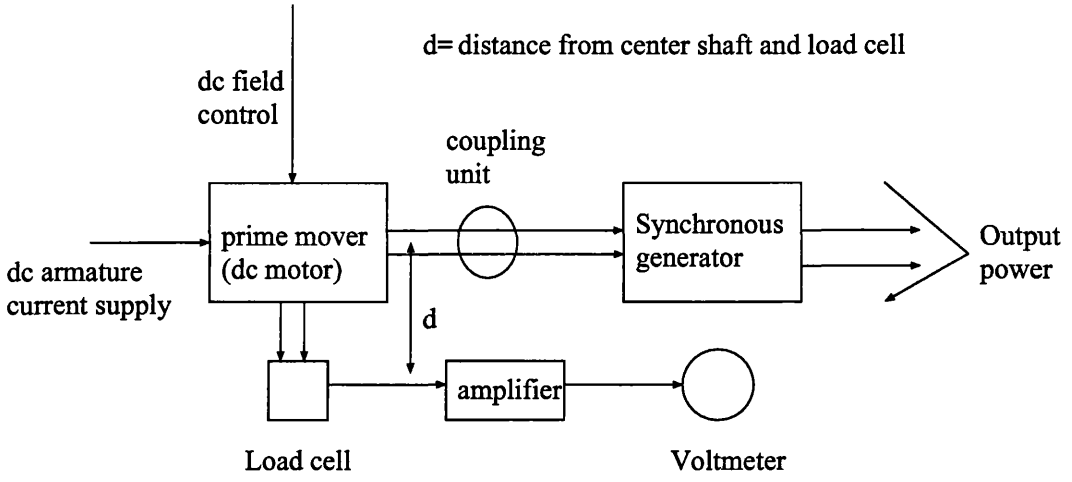

Figure C.3: Torque measurement set-up

C.3 Load cell calibration

Three different weights have been used, these weights (in kg) are, 2.266, 4.532, and 8.547. The corresponding voltages (in $volts$) are, 0.7, 0.94, and 1.36 respectively, and for no weight the voltmeter shows 0.48 $volts$. From the information available above, a calibration factor can be developed of 97.6 $Newton/volts$

C.4 Loss calculation

At zero speed the voltmeter reading is 0.465 *volts*, and when the machine was driven at 3000 *rpm* the voltmeter reading is 0.45 *volts*. The difference between the voltmeter readings is 0.015 *volts*. The force is:

$$F = 0.015\ (volts) \times 97.6\ (Newton/volts) = 1.464\ (Newton)$$

The applied torque is :

$$T_{app} = F \times d = 1.464 \times 0.25 = 0.366\ (N.m)$$

where d was measured from center rotor shaft and load cell and equal to 0.25 *meter* .

The input mechanical power is:

$P_{in} = T_{ind} \times \omega_m = 0.366 \times 314.159 = 115\ watts.$

When the machine was excited, the loss was the sum of friction, windage and core loss and equal to 115 *watts*. When the machine was not excited the loss was friction and windage only and equal to 77 *watts*, hence the core loss was found equal to 38 *watts*. This is to compare with 31 *watts* which was calculated from FEM.

Appendix D

Machine magnetic circuit

D.1 Machine parts cross sectional area

A section of the homopolar machine is shown in Fig. D.1. This was used to identify the magnetic circuit and hence to calculate the total mmf required to produce the 0.5 *tesla* in the air gap. The BH-curves of the stator and rotor are shown in appendix[A]. In this calculation, a four different cross sectional areas have been considered, the stator cross sectional area A_s, the longitudinal block path A_p, the rotor A_r, and the air-gap A_g.

The magnetic flux density in each section is calculated by assuming a certain value in the air gap until the required total mmf is found as follows:

1- The air-gap cross sectional area $A_g = \pi D_g L$, where D_g is the mean diameter

at the air-gap, and L is the effective axial length of the iron.

$$D_g = \frac{114.5 + 113.156}{2} = 113.828$$

This would give $A_g = 0.036\ m^2$.

2- Area of stator $A_s = \pi D_s L$, where D_s is the mean diameter at the stator.

$$D_s = \frac{203 + 114.5}{2} = 158.75\ mm$$

This would give $A_s = 0.05\ m^2$

3- Area of longitudinal path $A_p = \pi D_P L$, where D_p is the mean diameter at the path.

$$D_P = \frac{203 + 223}{2} = 213\ mm \tag{D.1}$$

This would give $A_p = 0.08\ m^2$

4- Area of rotor $A_r = A_{r1} + A_{r2}$, where A_{r1} is the area of the half laminations, and A_{r2} is the area of the centre rotor (full circle lamination).

$A_{r1} = \frac{\pi D_{r1} L}{2}$, where D_{r1} is the mean diameter at rotor half laminations.

$$D_{r1} = \frac{113.156 + 44.45}{2} = 78.803 \tag{D.2}$$

This would give $A_{r1} = 0.0124\ m^2$

Now, $A_{r2} = \pi D_{r2} L$, where D_{r2} is the mean diameter at rotor center full lamination.

$$D_{r2} = \frac{80 + 44.45}{2} = 62.225\ mm \tag{D.3}$$

This would give $A_{r2} = 0.004\ m^2$, and then $A_r = 0.0164\ m^2$.

If we, assume the magnetic flux in these areas is the same and neglect the leakage flux, then:

$$B_s A_s = B_r A_r = B_p A_p = B_g A_g \tag{D.4}$$

The above equation can rewritten as :

$$B_r = 4.878 \times B_p \tag{D.5}$$

$$B_p = 0.625 \times B_s \tag{D.6}$$

$$B_s = 0.9 \times B_g \tag{D.7}$$

Directly, we can find $B_r = 2.736 \times B_g$. It follows that 0.57 *tesla* in the air-gap would give 1.56 *tesla* in the rotor and from the rotor BH-curve this amount of flux density would be achieved when a magnetic field strength of 4687.5 AT/m has to be provided, therefore :

$$mmf_t = H_t \times l_t = 4687.5 \times 120 \times 10^{-3} = 562.5\ AT. \tag{D.8}$$

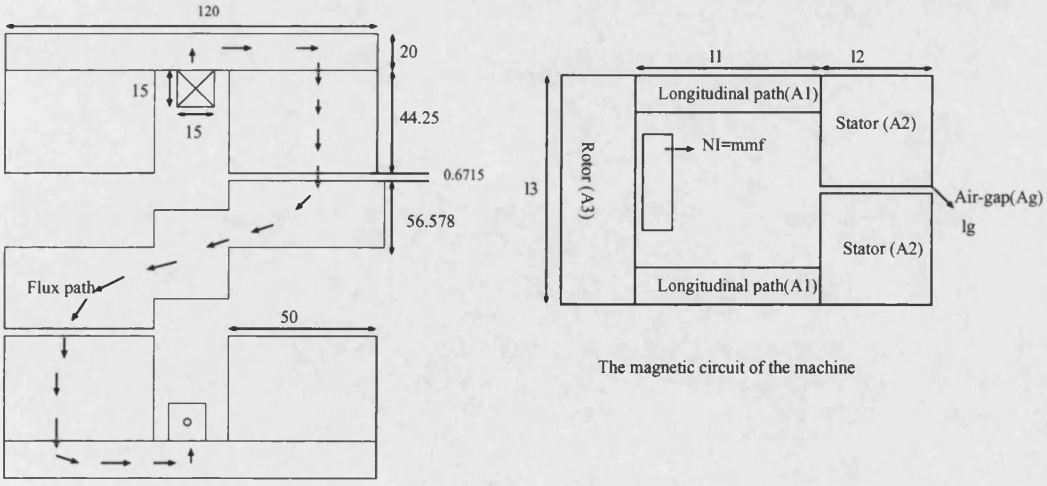

Figure D.1: Machine magnetic circuit

D.2 Slot area calculation

The area of slot can be divided into two halfs, each half has an area of $a+b+c$, and each can be calculated individually as shown in Fig. D.2, hence:

$$Area\ a = \frac{2 \times 12}{2} = 12\ mm^2 \tag{D.9}$$

$$Area\ b = 4 \times 12 = 48\ mm^2 \tag{D.10}$$

$$Area\ c = \frac{6^2\pi}{4} = 28.274\ mm^2 \tag{D.11}$$

Area $= a + b + c = 88.274\ mm^2$, and total area is $176.548\ mm^2$.

D.3 Copper area

Wire diameter (used in stator winding) $= 0.8\ mm^2$, number of wires per coil $= 135$, since 3 strand/conductor, therefore number of turns/coil $= 45$ turns

Cross sectional area of wire =

$$\frac{0.8^2\pi}{4} = 0.5\,mm^2 \tag{D.12}$$

area of conductor =

$$3 \times 0.5 = 1.5\,mm^2 \tag{D.13}$$

Coil cross sectional area = $1.5 \times 45 = 67.5\ mm^2$, this is the net copper area in the slot, packing factor can then be found as follows :

$$packing\ factor = \frac{67.5}{176.548} = 0.4$$

Now, this value can be used to calculate the *ampere.turns* I_s as it is shown in Fig. D.3 in the slot, using equation below[45]:

$$I_s = J \times P_f \times (S_w - 2t_i)[S_d - (S_h + 2t_i)] \tag{D.14}$$

When a current density J is $5A/mm^2$, then:

$$I_s = 248.4\ AT$$

this would give a current of a peak value 5.52 *ampers* when number of turns is 45. The *rms* value is $5.52 \times 0.707 = 4$ *ampers*.

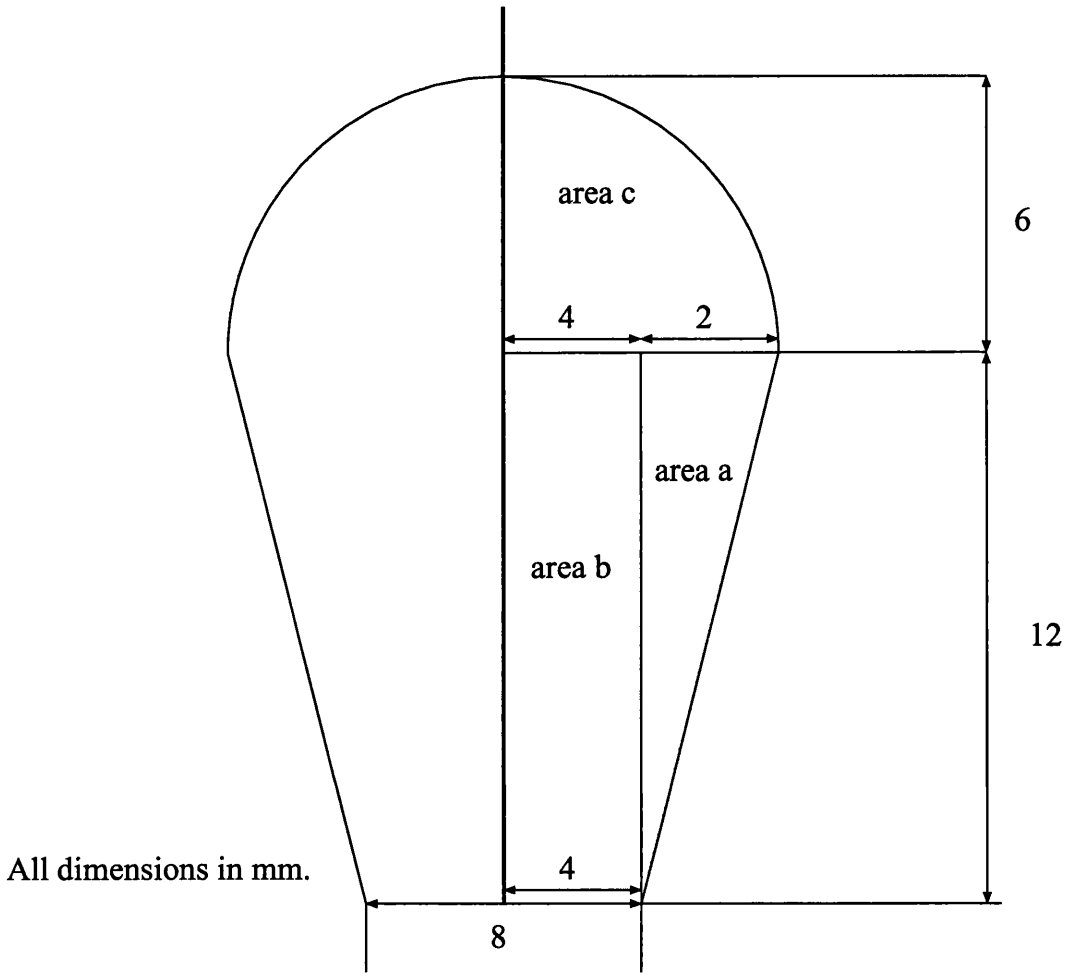

Figure D.2: Slot area calculation

D.4 Effective air-gap

Effective air-gap length can be calculated using Carters coefficient:

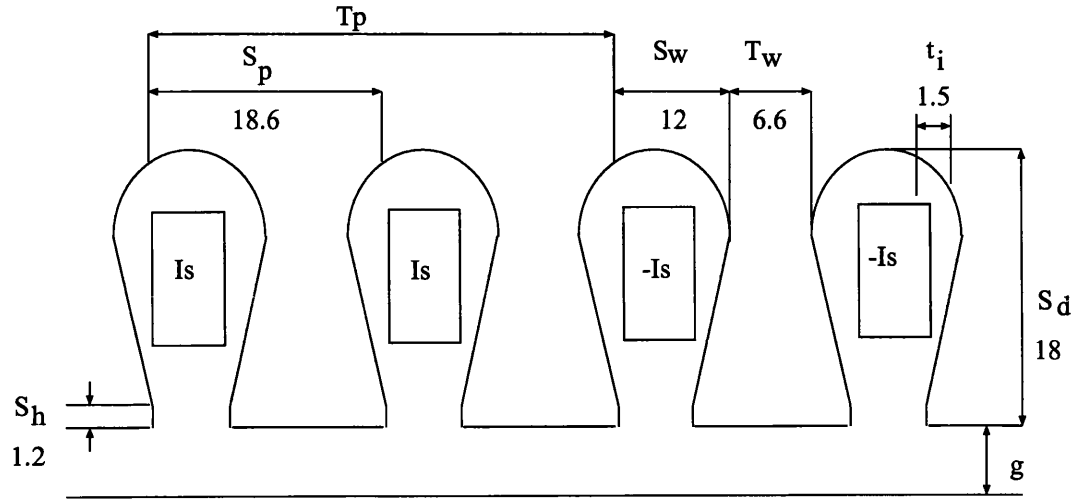

Figure D.3: Current density calculation

$$g_{eff} = g\frac{5g + 1(1-\alpha)t_s}{5g + (1-\alpha)t_s - (1-\alpha)^2 t_s} \tag{D.15}$$

where g is the air gap length, t_s is the slot pitch, $\alpha = \frac{t_t}{t_s}$ and t_t is the tooth width. Referring to Fig. D.4, $g_{eff} = 1.32\ mm$

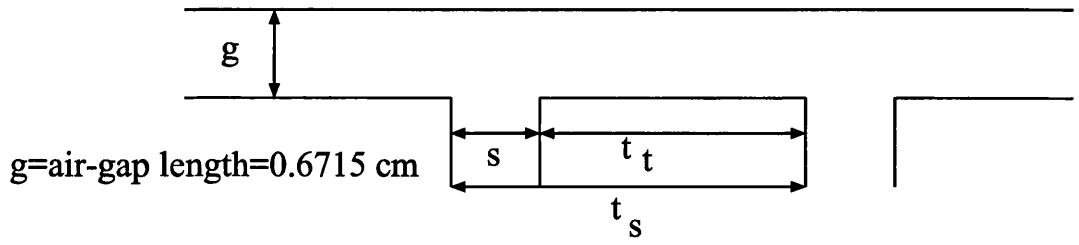

g=air-gap length=0.6715 cm

t_t =tooth width=0.66cm

ts=slot pitch=1.81 cm

Figure D.4: Effective air-gap

D.5 Winding factor

Since, it is a simple 3- phase Y-connected synchronous machine. It has a single layer coil construction with 4- stator coils per phase distributed as shown in winding arrangement in Fig. D.5.

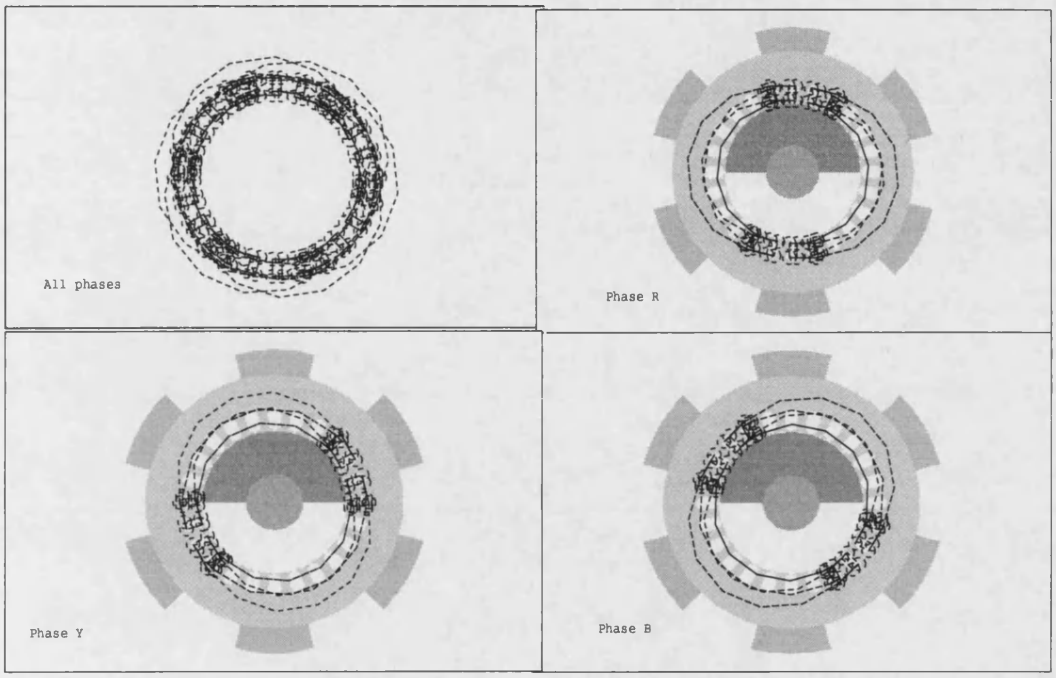

Figure D.5: Winding arrangement in $3D\ FEM$

Each coil consists of 45 turns, the windings have an electrical pitch of $\frac{5}{6} \times 180°$. The stator has 6 phase belts with 4 slots per belt, so it has 24 slots. The entire spans is 360°, the slot pith of this stator is $\alpha = \frac{360}{24} = 15°$.

Since there are 24 slots and 2 poles on this stator, there are 12 slots per pole, but a coil pitch of 180° electrical degrees is $\frac{5}{6} \times 180°/180° = 0.833$, so that the pitch factor is :

$$K_p = \sin(P\frac{\pi}{2}) = \sin(\frac{5}{6} \times \frac{\pi}{2}) = 0.97$$

The winding distribution factor is :

$$K_d = \frac{\sin(\frac{n\alpha}{2})}{n \sin(\frac{\alpha}{2})}$$

Where, n is the number of $slots/phase/pole = 4$, therefore $K_d = 0.957$

Appendix E

Steel manufacturers curves

The specific weight loss can be calculated from these two curves in Fig. E.1 and Fig. E.2 as shown below:

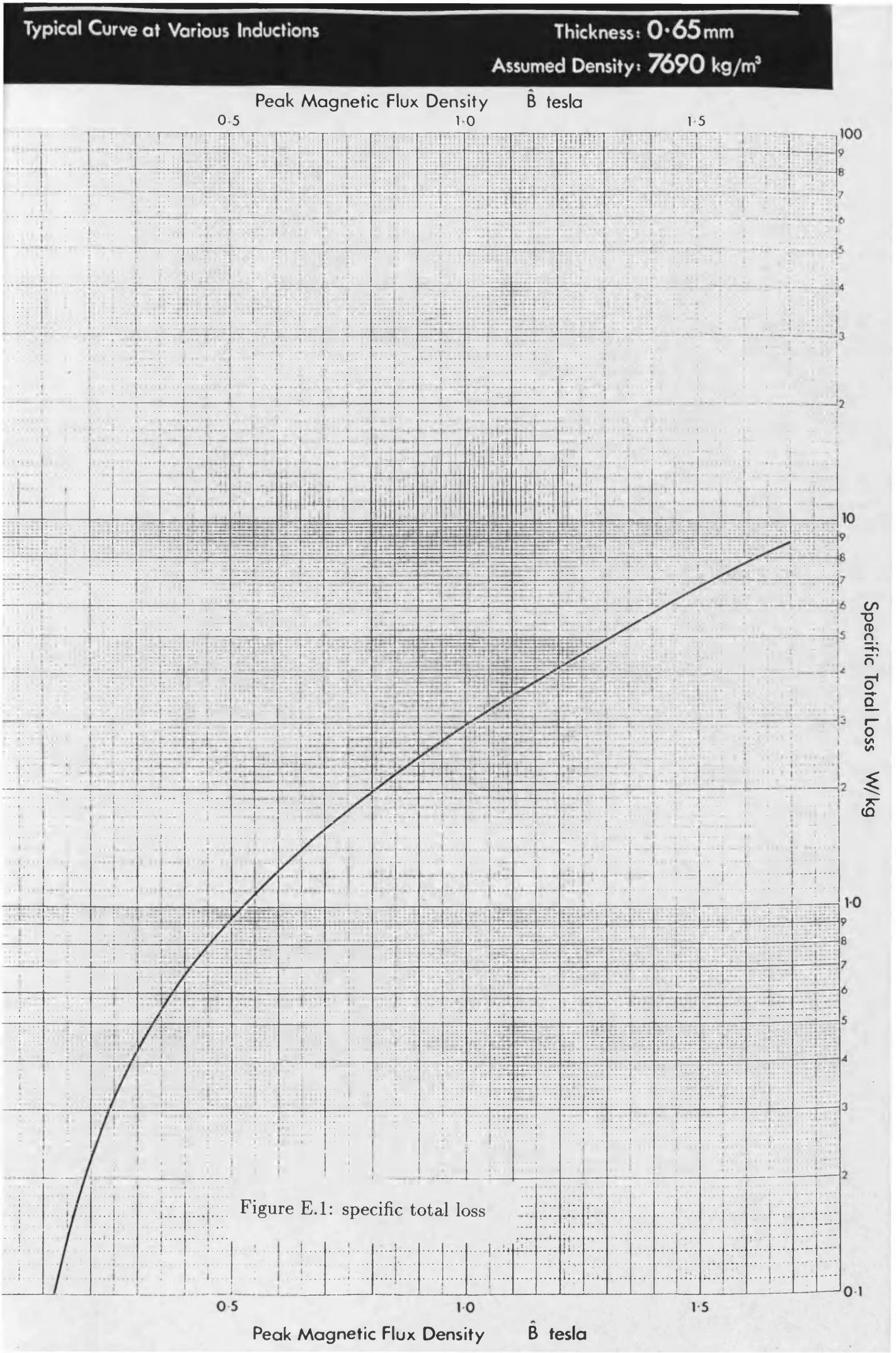

Figure E.1: specific total loss

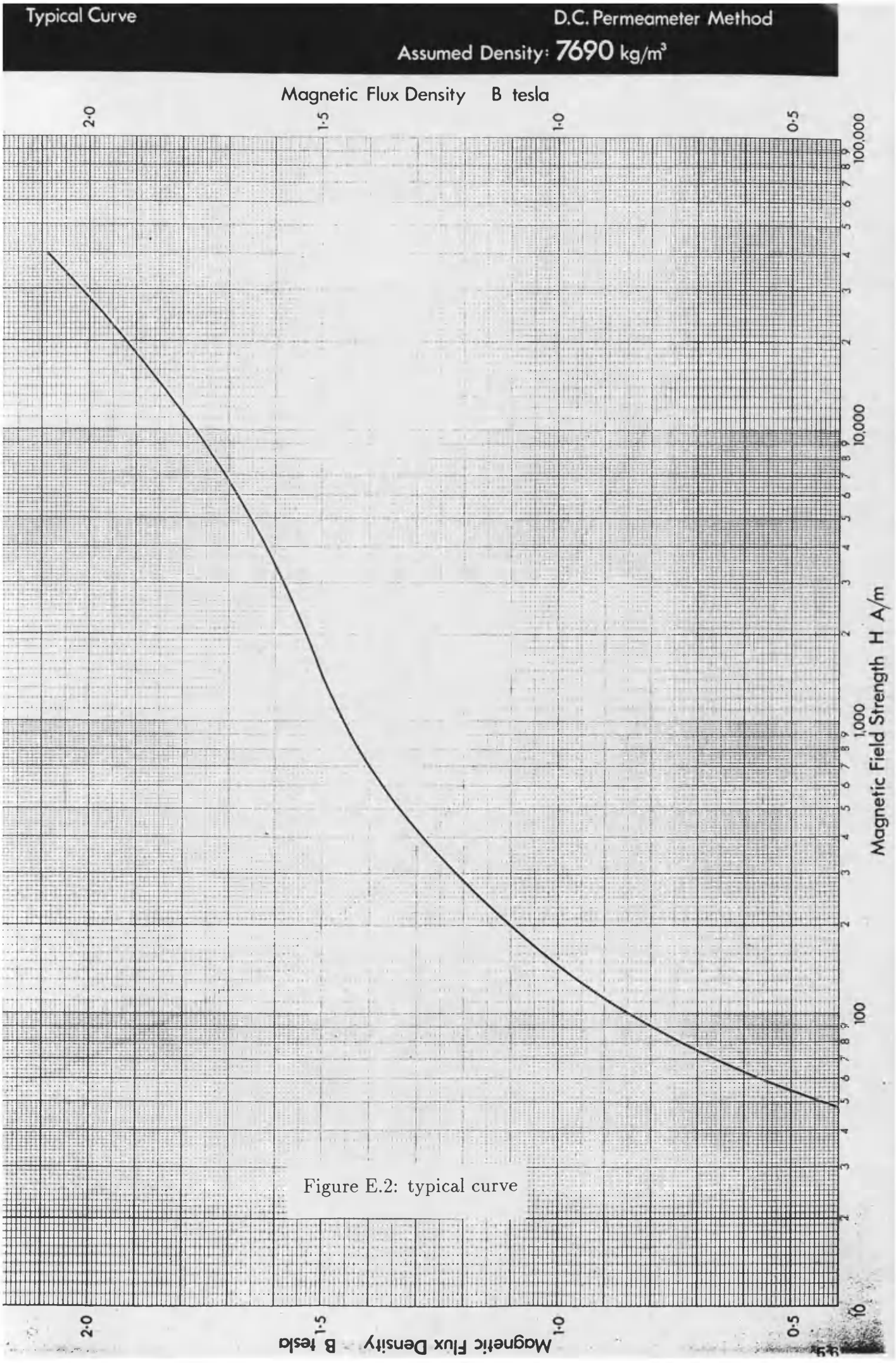

Figure E.2: typical curve

Appendix F

Improved design iron losses calculation

The total iron loss has been calculated in each part of the stator, in the teeth, back iron, and in the longitudinal blocks.

Using the technique given in chapter 5 section 5.4 for iron loss calculations from FEM.

The peak flux density in the teeth is 0.86 $tesla$, and from the curve in appendix[E] the specific total loss is 1.8 $watt/k_g$. The peak flux density in the back iron is 0.54 $tesla$ and the corresponding specific total loss value is 0.82 $watt/k_g$. The total specific losses in both teeth and back iron are 2.62 $watt/k_g$. In the longitudinal blocks the peak flux density is 0.44 $tesla$, and the specific

loss for this value is 0.74 $watt/k_g$. The volume of the stator is 0.1974×10^{-2} and the volume density is 7690 k_g/m^3 and this gives total weight of 15.1 k_g. Therefore the total loss in the teeth and back iron is $2.62 \times 15.1 = 39.6$ *watts*. The volume of the longitudinal blocks is 0.9690×10^{-3}. For the same volume density 7690 k_g/m^3, the losses are 7.5 *watts*. Therefore the total iron loss in the stator is $39.6 + 7.5 = 47.1$ *watts*.

References

[1] Wang R and Demerdash NA. "Computation of load performance and other parameters of extra high speed modified Lundell alternators from 3D FE magnetic field solutions". *IEEE Trans. on Energy Conversion*, 7(2):pp342–352, June 1992.

[2] Nair R. "Generators for alternative energy scheme". *IEE conference proceeding, Oxford, England*, pages pp499–504, September 1993.

[3] Wharton E. "Unusal machine configurations". *IEE conference publication*, 136:pp51–54, 1976.

[4] Repas D.S and Edkin R.A. "Performance characteristcs of 14.3 KVA modified Lundell alternator for 1200 Hz brayton-cycle space-power system". *Nasa Report, Nasa TN D-5404*, 1969.

[5] Demerdash N.A, Wang R, and Secunde R. "Three dimentional magnetic field in extra high speed modified Lundell alternator computed by a combined vector-scalar magnetic potential FE method". *IEEE Trans. on Energy Conversion*, 7(2):pp353–363, June 1992.

[6] Wang R and Demerdash N.A. "Extra high speed modified Lundell alternator parameters and open/short-circuit characteristics from gobal 3D-FE megnetic field solutions". *IEEE Trans. on Energy Conversion*, 7(2), June 1992.

[7] Martin N. Wilson. *"Superconducting Magnets"*. Oxford University press, New York, 3rd edition, 1983. ISBN:0-19-854810-9.

[8] J R Bumby. *"Superconducting rotating electrical machines"*. Oxford University press, New York, 3rd edition, 1983. ISBN:0-19-859327-9.

[9] Thullen P, Dudley J C, Greene D L, Smith J L, and Woodson H H. "An experimental alternator with a superconducting rotating field winding". *IEEE Trans. on Power Apparatus and Systems*, PAS-90(2):pp611–619, March 1971.

[10] Kirtley J L and Furuyama M. "A design concept for large superconducting alternators". *IEEE Trans. on Power Apparatus and Systems*, PAS-94(4):pp1264–1269, July 1975.

[11] Kingsley C, Wilson G L, Kirtley J L, Keim T A, Smith J L, and Thullen P. "Steady state electrical tests on the MIT-EPRI 3 MVA superconducting generator". *IEEE Trans on Power Apparatus and Systems*, PAS-95(3):pp887–893, May 1976.

[12] Smith J L and Liepert A G. "Construction of MIT-DOE 10 MVA superconducting generator". *IEEE Trans on Magnetics*, MAG-21(2):pp791–794, March 1985.

[13] Southall H L and Oberly C E. "System considerations for airborne, high power superconducting generators". *IEEE Trans. on Magnetics*, MAG-15(1):pp711–714, March 1979.

[14] Fealey J A, Jones W D, Keim T A, and Laskaris T E. "Comprehensive test and evaluation of a 20 MVA superconducting gnerator". *IEEE Trans. on Power Apparatus and Systems*, PAS-104(6):pp1484–1491, June 1985.

[15] Nakamura S and Shindo Y. "A 30 MVA superconducting synchronous condenser: Design and it's performance test results". *IEEE Trans. on Magnetics*, MAG-21(2):pp783–790, March 1985.

[16] Maki N, Yamaguchi K, Takahashi M, and Sanematsu T. "Test results of 50 MVA superconducting generator". *IEEE Trans. on Magnetics*, MAG-23(5):pp3536–3538, September 1987.

[17] Singh S K and Mole C J. "Future development of large superconducting generators". *IEEE Trans. on Magnetics*, 25(2):pp1783–1786, March 1989.

[18] Smith J L. "Development of superconducting synchronous machines in the USA". *IEEE Trans. on Magnetics*, MAG-23(5):pp3529–3532, September 1987.

[19] Richardson K, Evans P D, Eastham J F, Appleton A D, and Alford N McN. "An alternator using a high temperature superconductor for field excitation". *IEE, 4th International conference on electrical machines and drives conference publication*, 2(310):pp202–204, September 1989.

[20] Laquer H L. "High temperature superconductivity: What, why, where and how". *Proceeding of the 23rd Intersociety Energy Conference Version Engineering Denver Conference USA*, pages pp493–499, July 1991.

[21] Eastham J F. "Novel synchronous machines:Linear and Disc". *IEE Proceding Part B*, 137(1):pp49–58, January 1990.

[22] Teruo Azukizawa. "Optimum linear synchronous motor design for high speed ground transportation". *IEEE Trans. on Power Apparatus and Systems*, PAS-102(10):pp3306–3314, October 1983.

[23] Eastham J F, Balchin M J, and Coles P C. "Full-Scale Testing of a high speed linear synchronous motor and calculation of end-effect". *IEEE Transaction on Magnetics*, 24(6):pp2892–2894, November 1988.

[24] Balchin M J and Eastham J F. "Characteristics of a homopolar linear synchronous machine with passive secondary". *Electric Power Applications*, 2(6):pp213–218, December 1979.

[25] Dawson G E, Eastham A.R, and Ong R. "Computer-aided design studies of the homopolar linear synchronous motor". *IEEE Transactions on Magnetics*, Mag-20(5):pp1927–1929, September 1984.

[26] Lorenzen H W, Nuscheler R, and Meyer A. "Experimental investigation of the operating behaviour of linear synchronous motors". *IEEE Trans. on Energy Conversion*, EC-1(4):pp73–82, December 1984.

[27] MEGA GROUP. "Mega V6.00 user manual". *Applied Electromagnetic Research Centre Bath University*, 1995.

[28] Q.H Al-Akayshee and J.F.Eastham. "A comparison between AC Side Excited Heteropolar and Homopolar Synchronous Machines". *International Confrence on Power Electronics*, January 1996. Drives and Energy Systems for Industrial Growth, PEDES 96, New Delhi, INDIA.

[29] Nonaka S, Kesamaru K, and Horita K. "Analysis of brushless 4 pole 3 phase synchronous generator without exciter by FE method". *IEEE Industry Application Society Annual Meeting*, pages pp218–223, 1992.

[30] Nonaka S and Kesamaru K. "Magnetic field analysis of Brushless 2 pole synchronous generator without exciter by FE method". *IEEE industry applications society*, pages pp308–313, 1989. Conference record-IAS annual meeting.

[31] Eastham J F, Rodger D, Lai H C, and Nouri H. "Finite element calculation of fields around the end region of a turbine generator test ring". *IEEE Trans. on Magnetics*, 29(2):pp1415–1418, 1993.

[32] Chari M V K and Silvester P. "Analysis of turboalternator magnetic field by finite element". *IEEE Trans. on Power Apparatus and Systems*, PAS-90(2):pp454–464, March 1971.

[33] Demerdash N A, Hijazi T M, and Arkadan A A. "Computation of winding inductance of PM brushless DC motors with damper windings by en-

ergy perturbation". *IEEE Trans. on Energy Conversion*, 3(3):pp705–713, September 1988.

[34] Alhamadi M A and Demerdash N A. "Modeling of effects of skewing of rotor mounted PMs on the performance of brushless DC motors". *IEEE Trans. on Energy Conversion*, 6(4):pp721–729, December 1991.

[35] Jamil M K and Demerdash N A. "Harmonics and core losses of PM DC motors controlled by chopper circuits". *IEEE Trans. on Energy Conversion*, 5(2):408–414, June 1990.

[36] Recep Akmese. *Design, operation and dynamic performance of a brushless DC tubular drive system.* PhD thesis, School of Electronics and Electrical Engineering, 1989. Bath University.

[37] K.J.Binns, P.J.Lawrenson, and C.W.Trowbridge. *"The analytical and numerical solution of electric and magnetic fields".* John Wiley and sons Ltd, 2^{nd} edition, 1994.

[38] P.J.Leonard, H.C.Lai and. J.F.Eastham, and Q.H.Al-Akayshee. "Automatic treatment of multiple wound coils in 3D finite element problems including multiply connected regions". *IEEE Trans. on Magnetics part 1 IEMGAQ*, 32(3):796–799, 1996. Compumag Berlin, Germany.

[39] Lai H C, Rodger D, and Leonard P J. "Coupling meshes in 3D problems involving movements". *IEEE Trans. on Magnetics*, 28(2):pp1732–1734, March 1992.

[40] P.J.Leonard Q.H.AL-Akayshee, J.F.Eastham. "Calculation of the parameters and load performance of a homopolar machine". *INTERMAG 96, International Magnetics Conference, Seattle, Washington*, April 1996.

[41] Evans P D and Eastham J F. "Double disc alternator with AC side excitation. *Proc IEE Part B*, 130(2):pp95–119, March 1983.

[42] Q.H.Al-Akayshee and J.F.Eastham. "3D finite element modelling of an AC side excited machine". *Accepted in the international second scientific engineering conference*, April 1997. To be held on the 8-11 April 1997, Mansoura University, Egypt.

[43] Ouden W Den and Hamels D. "Efficiency of small homopolar synchronous motors at high speeds". *Electric Machines and Power Systems*, 13(1):pp29–40, 1987.

[44] J.HANNAH and M.J.HILLIER. *"Applied mechanics"*. Longman Scientific and Technical, 3rd edition, 1995. ISBN:0-582-24453-6.

[45] Eastham J F, Akmese R, and Hill Cottingham R J. "Prediction of thrust force in tubular induction machines. *IEEE Trans. on Magnetics*, 28(2):pp1375–1377, March 1992.

RELATED PAPERS

1) Q.H.AL-Akayshee, J.F.Eastham, P.J.Leonard

Calculation of the parameters and load performance of a homopolar machine.

INTERMAG 96, International Magnetics Conference, Seattle, Washington, April, 1996.

2) Q.H Al-Akayshee and J.F.Eastham

A Comparison between *A.C* Side Excited Heteropolar and Homopolar Synchronous Machines.

International Confrence on Power Electronic Drives and Energy Systems for Industrial Growth, PEDES 96, New Delhi, INDIA, Jan, 1996.

3) P.J.Leonard and H.C.Lai and. J.F.Eastham and Q.H.Al-Akayshee

Automatic treatment of multiple wound coils in $3D$ finite element problems including multiply connected regions.

IEEE Trans. on Magnetics part 1 IEMGAQ, Volume, 32, number=3, Compumag Berlin, Germany, Jul, 1995, pages 796-799.

4) Q.H.Al-Akayshee and J.F.Eastham

3*D* Finite Element Modelling of an *A.C* Side Excited Machine.

Accepted for the Second Scientific Engineering Conference to be held on the $1-3$ *April* 1997 in Mansoura, Egypt.

Calculation of the parameters and load performance of a homopolar machine.

Q.H. Al-Akayshee ,J.F.Eastham, P.J.Leonard
School of Electrical & Electronic Engineering, Bath University, Bath. U.K.

Abstract— **A homopolar synchronous machine has been designed with excitation and armature winding on the stator (stationary) side of the air-gap. The purpose of this work is to use 3D finite element modelling techniques to calculate the synchronous reactance components in $d-q$ axis and secondly to model all the fields on load. The computational work is validated by the results from a prototype machine.**

I. Introduction

A.C side excited synchronous machines have both excitation and armature winding on the stationary member (stator). The rotors carry no windings but the generated voltage can be regulated by varying the stator-side excitation. Since the rotors are passive and robust the machines have been used for high speed application[1]. They have also been suggested for the use in alternative energy schemes[2], especially small hydro applications where advantage can be taken of their easy and comparatively low skilled maintenance requirements.

One form of the machine has a homopolar action. The flux from the exciting coil is modulated by the shape of the passive rotor in such a way that induced emf is generated in the coils of the stator windings. A previous paper[3] describes the homopolar topology.

II. F.E Modelling

Fig. 1 shows the machine investigated, only the bottom half of the stator is shown for clarity. The positions of the armature and excitation windings will be observed.

The topology of the machine is complex and the flux distribution in it is difficult to calculate except by a full 3D finite element model. To facilitate this the rotor and stator were meshed separately and joined together by a sliding Lagrange interface placed in the middle of the air gap[4], Fig. 2 shows a close-up view of the joined meshes. The currents in the laminated iron regions were ignored and the regions were considered to be isotropic.

The field solution for a known current is then a magnetostatic problem[5]. However for a simulation involving an external excitation circuit and load currents are unknown,

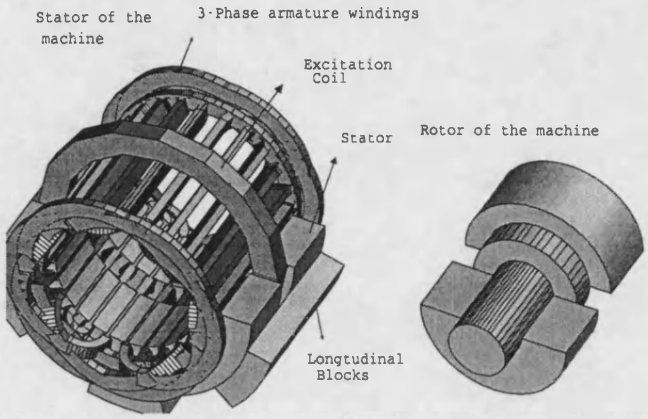

Fig. 1. Homopolar Machine

and additional complexity in this case is the induced voltage due to the motion of the rotor. The easiest solution to this sort of problems to solve the circuit equations as a single system[6].

$$[K]\mathbf{x} + [C]\frac{\partial \mathbf{x}}{\partial t} = \mathbf{f} \tag{1}$$

The unknown vector x comprises the magnetic scalar unknowns of the field model, the Lagrange multipliers that enforce the sliding interface and the circuit voltages. The forcing function $\mathbf{f}$ represents the specified voltages in the circuit. The stiffness and damping matrices, $[K]$ and $[C]$ include both the field model and a nodal circuit model. The motional effects are modelled by the Lagrange multiplier terms in the stiffness matrix. These terms are calculated at each time step. Because of the stiff nature of the electromagnetic system an implicit backward difference scheme was used to implement the time stepping of these equations.

III. Finite element and experimental results

A practical machine was constructed and tested, to verify the Finite Element Modelling (FEM). The finite element method used the system explained earlier where equation (1) is represented by the circuit shown in Fig. 3.

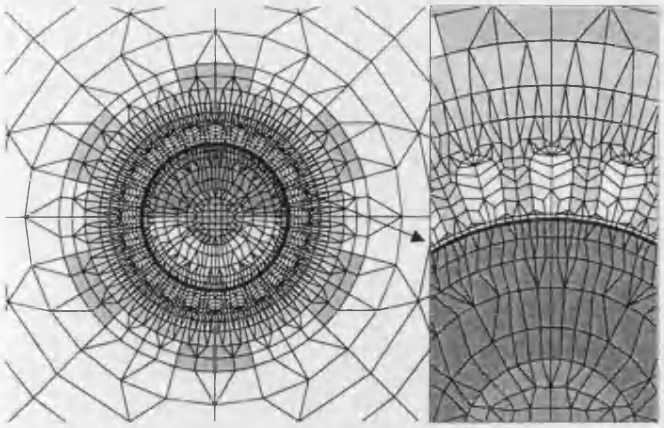

Fig. 2. Close-up mesh

The following tests were performed on the machine and equivalent finite element results were obtained for comparison.

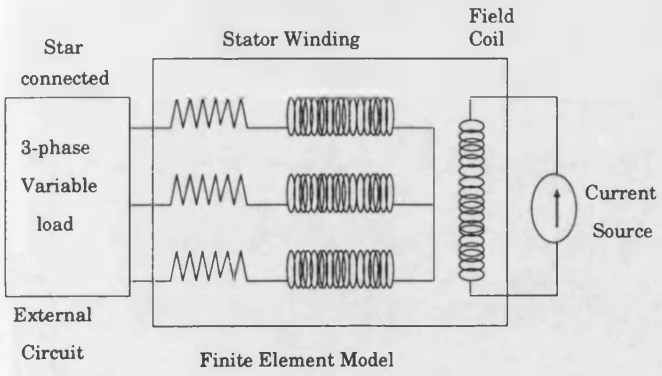

Fig. 3. FE Model connected to an external circuit

A. Open-circuit test: In which the open circuit voltage E_{oc} was measured as the field current is varied. The results are shown compared with FEM in Fig. 4.

B. Short-circuit test: In which the machine is short circuited at the terminals and results of short circuit current I_{sc} against field current I_f are obtained and compared with FEM in Fig. 5.

C. Unsaturated Synchronous Impedance: Direct axis synchronous reactance, $X_{d(un)}$ was calculated as follows:

$$X_{d(un)} = \frac{E_{oc}}{\sqrt{3} I_{sc}} \tag{2}$$

where E_{oc} is the Line to Line open circuit voltage taken from the air gap line for a given excitation field current I_f and I_{sc} is the short circuit armature current obtained at the same field excitation. This reactance is 68Ω experimentally and 61Ω calculated from FEM.

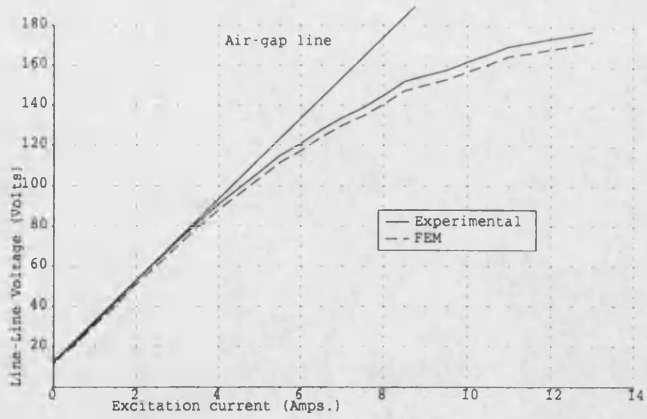

Fig. 4. Open circuit test

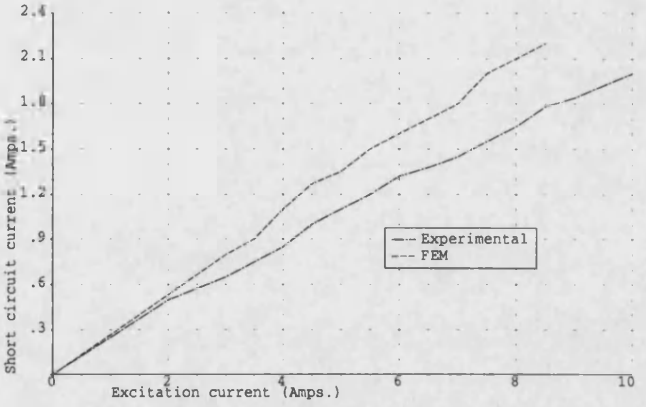

Fig. 5. Short circuit test

IV. Slip test

A slip test has been performed to determine X_d and X_q. In this test three phase voltage were applied at a speed slightly below synchronous speed without field excitation. Oscillograms were taken of the armature terminal voltage, and the armature current. The direct-axis and quadrature-axis reactances are found as follows:

$$X_d = \frac{V_{max}}{I_{min}} \quad and \quad X_q = \frac{V_{min}}{I_{max}} \tag{3}$$

The experimental X_d and X_q are 77.6Ω and 72.5Ω, while the calculated values from FE are 66.2Ω and 57.6Ω respectively.

V. Load test

In this test the 3 phase armature winding are connected to a load and the machine is driven at the synchronous speed. Fig. 6, shows the calculated and measured load

voltages for various values of armature current at inductive and resistive loads. The waveforms of load voltage and current (at inductive load) are illustrated in Fig. 7 and Fig. 8 respectively.

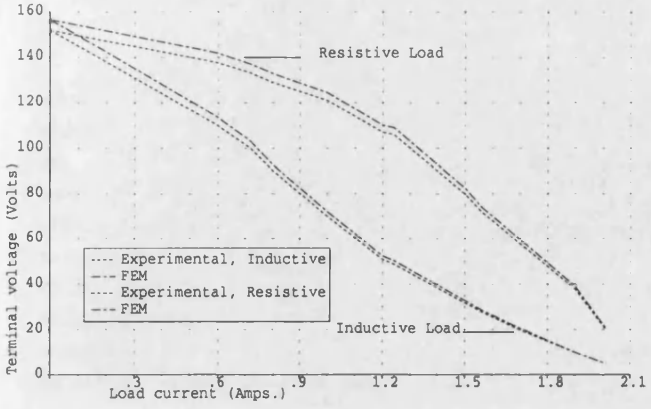

Fig. 6. Load test

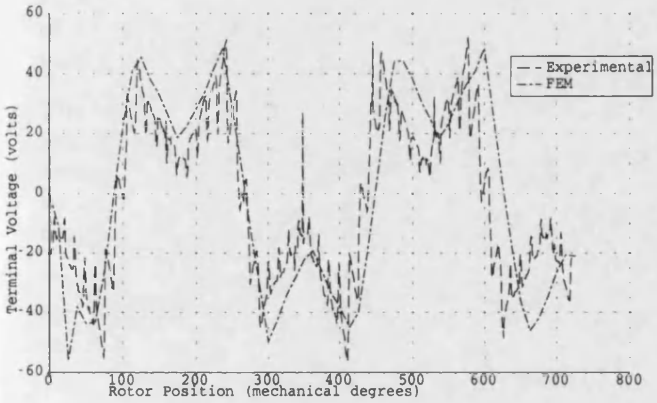

Fig. 7. Load Voltage Waveform

VI. Conclusion

In general the agreement between the finite element and measured results is reasonable for this complex geometry. The laminated regions were considered to be isotropic and the eddy currents driven in them were ignored. This may be the cause of the approximate results since the flux in the practical machine will to some extent be *'steered'* along the plane of the lamination. However the results are sufficient for future comparative design purpose.

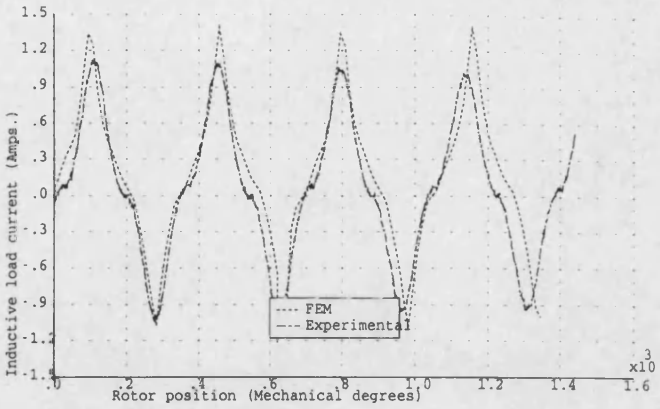

Fig. 8. Load Current Waveform

References

[1] R.Wang "Computation of Load Performance and Other Parameters of Extra High Speed Modified Lundell Alternators from 3D-FE Magnetic Field Solutions." IEEE Transaction on Energy Conversion, Vol. 7, No. 2, June 1992.

[2] R.Nair, "Inductor Generators for Alternative Energy Schemes." IEE Conference Proceedings, Sept. 1993, Oxford, England.

[3] Q.H. Al-Akayshee ,J.F.Eastham "A comparison Between A.C Side Exited Heteropolar and Homopolar Synchronous Machines." IEEE International conference for industrial growth (PEDES'96), New Delhi, INDIA, January 1996, pp. 530-34.

[4] H.C.Lai, D.Rogder, and P.L.Leonard, "Coupling Meshes in 3D Problems Involving Movements," IEEE Transactions on Magnetics, Vol.28, No.2, March 1992.

[5] P.L.Leonard, H.C.Lai, J.F.Eastham and Q.H.Al-Akayshee, "Automatic treatment of wound coils in 3D finite element problems including multiply connected regions," Conference record COMPUMAG 95, July 1995, pp.329-330.

[6] J.F.Eastham, M.J.Balchin, R.J.Hill-Cottingham, P.J.Leonard,"Numerical Analysis Techniques Applied to a Model Iron-Cored Compulsator, IEEE Transactions on Magnetics, Vol. 31, No. 1, Year 1995, pp. 587-792.

A Comparison between A.C Side Excited Heteropolar and Homopolar Synchronous Machines.

Q.H Al-Akayshee ,J.F.Eastham
School of Electrical & Electronic Engineering, Bath University, Bath. U.K.

Abstract—**Two forms of stator-side excited machines are considered in the paper, homopolar and heteropolar.They are compared by the use of 3D magnetostatic finite element modelling.The results from a prototype homopolar machine are also presented to validate the modelling method.It is found that the homopolar machine has some advantages over the heteropolar in weight and volume but there are some penalties in efficiency.**

I. Introduction

A.C side excited synchronous machines have both excitation and armature windings on the stator side of the air-gap, the machines are robust and have been used for high speed applications[1].

The machine has also been suggested for use in alternative energy schemes[2], especially in small hydro and wind power applications where advantage can be taken of their easy and comparatively low-skilled maintenance requirements.

The rotors carry no windings and are brushless but the generated voltage can be regulated by varying the stator-side excitation.

II. The topology of the machines

Two different topologies of machine will be contrasted in this paper namely homopolar and heteropolar.

The rotor and the stator of a 2 pole heteropolar machine are shown in Fig. ??, and Fig. 2, respectively.

The two oppositely connected excitation coils are shown in the stator figure but the a.c winding, carried in the slots of the centre core, is omitted for clarity (only one coil is shown). Fig. 3, is a longitudinal section of the machine shown at a particular

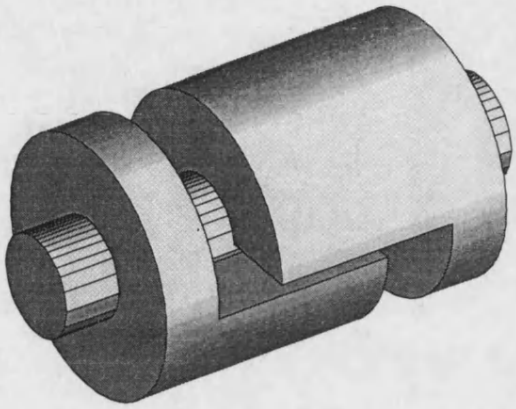

Fig. 1. Heteropolar Machine Rotor

position, it will be observed that the excitation coils drive flux so that a pair of poles are induced in the rotor a 'north' pole at the left of the diagram and a south at the right.If the rotor is turned by 180° as shown in Fig. 4, again two poles are induced but of opposite polarity.

It follows therefore, that a 3 phase emf will be induced in a two pole winding inserted in the slots of the centre core .This form of machine is called heteropolar because of the formation of the north-south pattern on the rotor.

The rotor and the stator of a homopolar machine are shown in Fig. 5, and Fig. 6, respectively.

Only one excitation coil is used in this machine. The a.c winding passes through the slots of both cores (only one coil of this winding is shown on Fig. 6). Fig. 7, is a longitudinal section of the machine shown at one particular position, if the left hand stator is considered as in Fig. 8, it will be seen that the rotor presents a 'north' pole at the top since flux passes from the rotor to the stator and then through the longitudinal blocks to carry on the other end of the rotor as shown in Fig. 9. It will be seen that there is no flux driven from the rotor to the other half circumference. If now the rotor is turned by 180° as shown in the longitudinal section in Fig. 10, then it

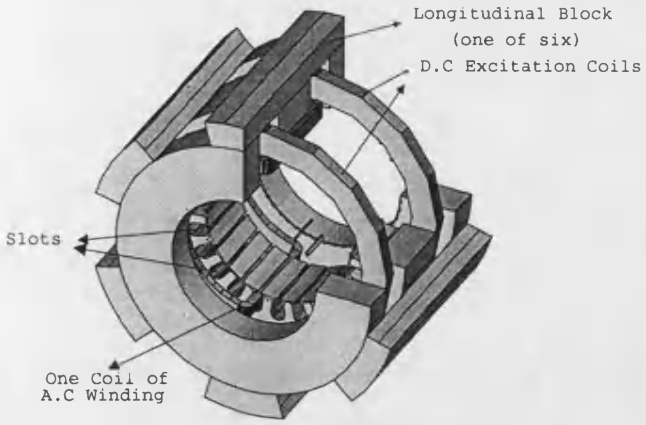

Fig. 2. Heteropolar Machine Stator

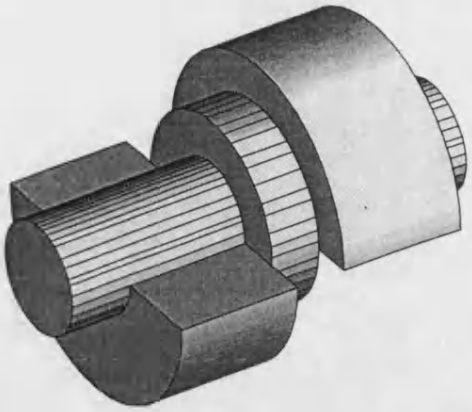

Fig. 5. Homopolar Machine Rotor

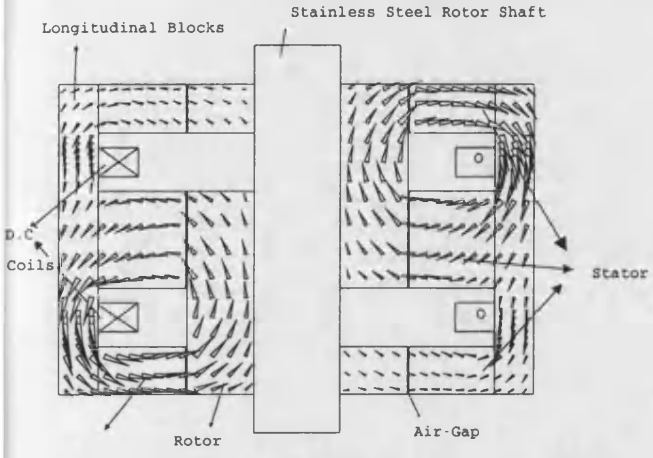

Fig. 3. Longitudinal Section at 0° Position

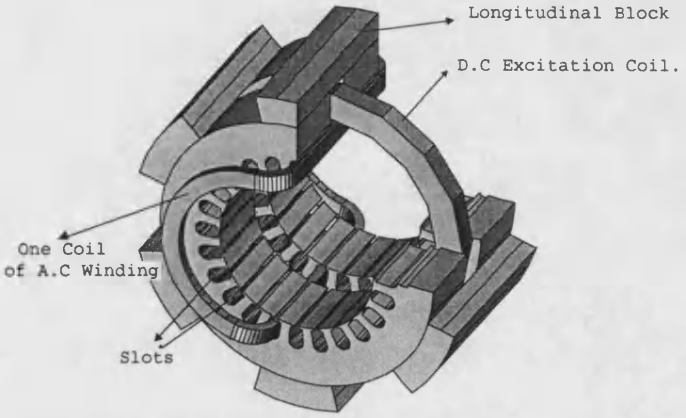

Fig. 6. Homopolar Machine Stator

will be seen that flux still passes from the rotor to the stator at the left hand core with the rotor still presenting a 'north' pole.

Consideration of the figures shows that a similar situation occurs on the right hand side core but this time a 'south' pole is always presented by the stator.

Since the flux is only modulated from one direction to zero in one core the machine is termed homopolar. However because of the two cores the flux linking a stator coil is first in one direction from one core and then in the reversed direction from the other. Views of the flux direction at each end of the machine are

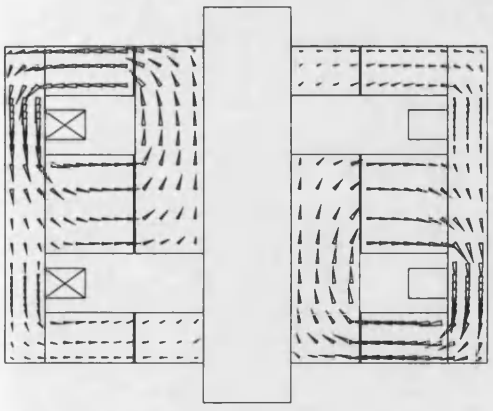

Fig. 4. Longitudinal Section at 180° Position

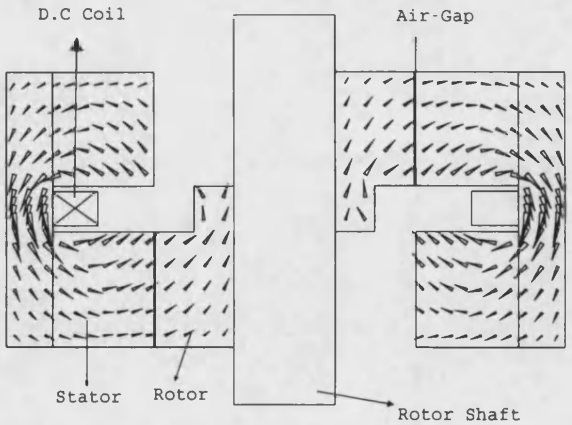

Fig. 7. Longitudinal Section at 0° Position

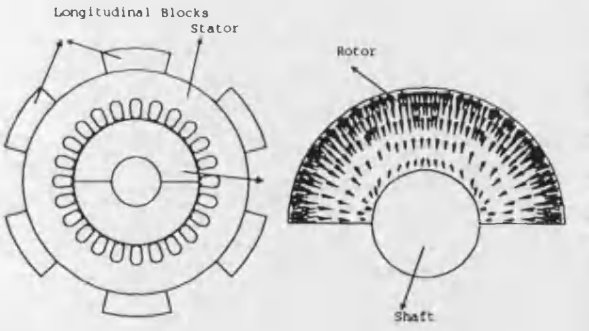

Fig. 8. Machine end 1 at 0° Position

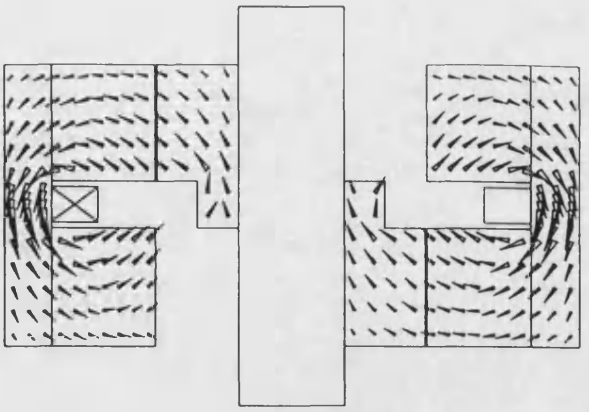

Fig. 10. Longitudinal Section at 180° Position

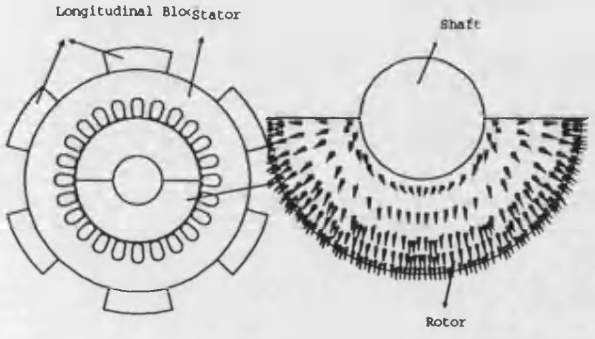

Fig. 9. Machine end 2 at 0° Position

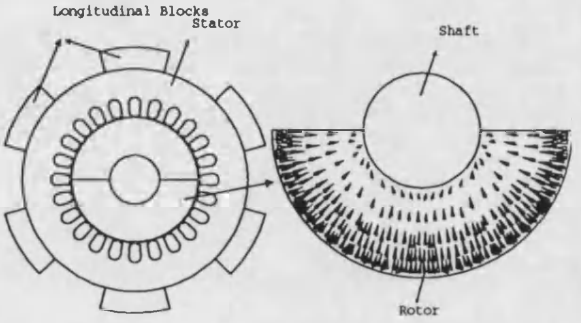

Fig. 11. Machine end 1 at 180° Position

shown in Fig. 11, and Fig. 12, respectively, while Fig. 13, and Fig. 14, show the direction of this flux in the middle of the machine at 0° and 180° Positions respectively.

III. 3D Finite Element Modelling

3D Finite Element representation[3] has been used to model the two forms mentioned above. In modelling electrical machines it is necessary to consider the rotor at all positions within the stator.In the method used in this work the rotor and stator are independently meshed with the two meshes coupled using 'Lagrange Multipliers'[4]. This enables the rotor to be rotated and snap shots taken of the field at a set of positions.

IV. Experimental Results

The homopolar machine has been constructed and tested. Fig. 15, shows the measured induced emf together with calculated. It will be observed that the

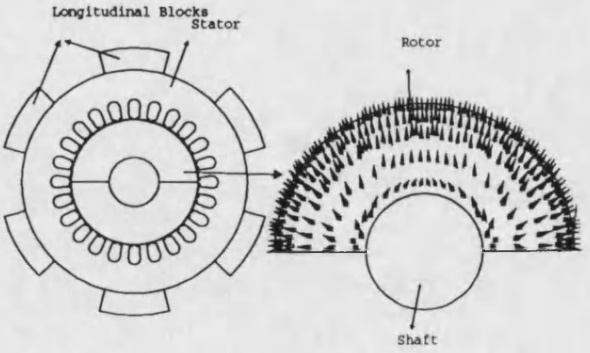

Fig. 12. Machine end 2 at 180° Position

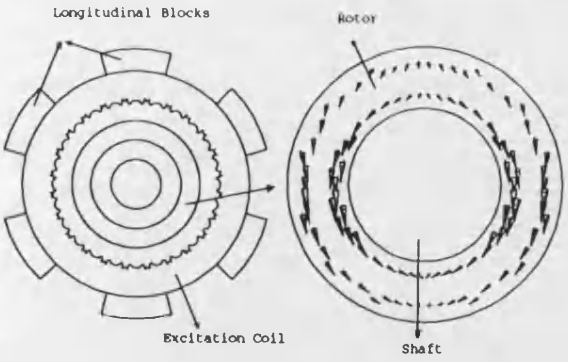

Fig. 13. Middle of the machine at 0° Position

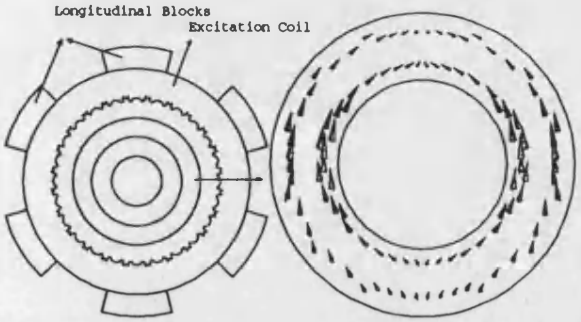

Fig. 14. Middle of the machine at 180° Position

agreement is reasonable. The rms value of the voltages were 54.9 and 56.4 volts for the computed and measured respectively. The induced emf of the heteropolar case was calculated, the rms value was 67.2 volts. This calculation was performed at the same field current and the 20% increase over the homopolar machine will be noted.

V. Details of Designs and Comparison

Both machines have been designed with the same armature currents and current densities and the same field currents and current densities.

The homopolar machine was first designed in 3D FE with dimensions as shown in Fig. 16. To meet the requirements of the induced voltage in the 3 phase A.C windings, the specifications of this machine are:

-Series conductors per armature slot (45),

-Series conductors in the field coil (125),

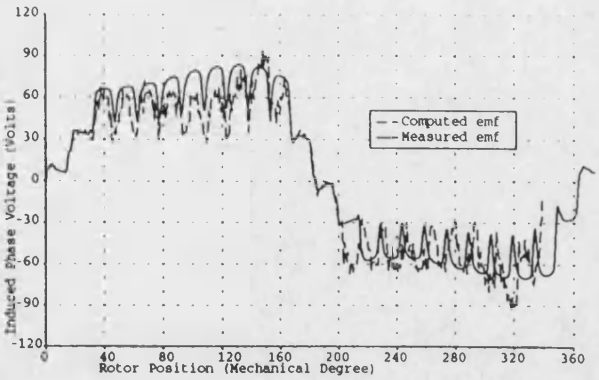

Fig. 15. Induced emf's

-Slots per pole and phase (4),

-Coil pitch (slots)(12),

-Slot depth (18 mm),

-Total armature slots (24),

-Number of poles (2),

-Total stator iron weight (20.42 kg),

-Rotor iron weight (under stator) (5.8 kg).

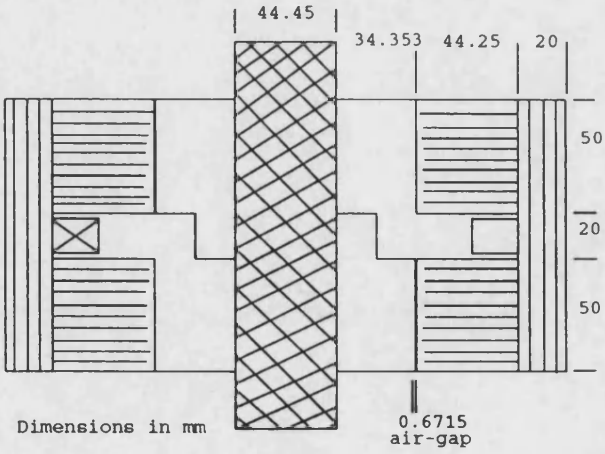

Fig. 16. Homopolar Machine Dimensions

In Fig. 17, the magnetic circuit of the heteropolar machine is shown the dimensions of the middle stator is the same as that of one side of the homopolar stator. The other two outside cores are each one half of the width of the centre core.The 30mm space between the middle stator and the side cores has been left for the end turns of the A.C winding. This is the same distance that has been used for the A.C winding of the homopolar machine. The specifications of this machine are:

-Series conductors per armature slot (45),

-Series conductors in the field coil (125),

-Slots per pole and phase (4),

-Coil pitch (slots) (12),

-Slot depth (18 mm),

-Total armature slots (24),

-Number of poles (2),

-Total stator iron weight (24.05 kg),

-Rotor iron weight (under stator) (8.3 kg).

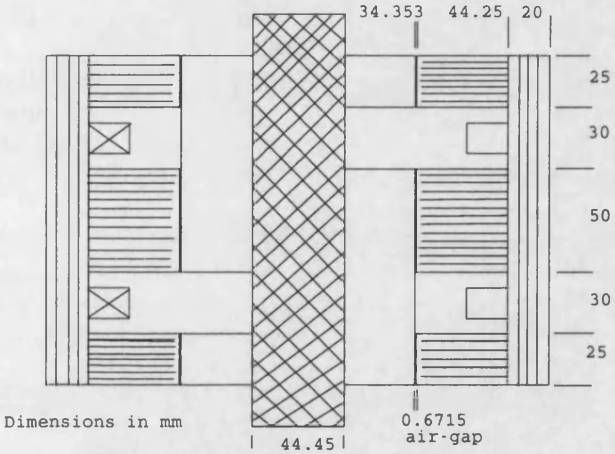

Fig. 17. Heteropolar Machine Dimensions

Now, to compare the two machines :

Given the same excitation current in both machines, the heteropolar machine has double excitation losses ($2I^2R$) while in the homopolar machine only half of that loss occurs (I^2R), for the reason that the heteropolar machine has two excitation coils compared with one excitation coil in the homopolar case.However for the same induced voltage only 90% of the current is needed in the heteropolar case hence the copper loss is ($1.62I^2R$) and therefore the loss is only 38.27% more than the loss in the homopolar machine.

In the homopolar machine, the length of the A.C winding is about 70mm longer than that in the heteropolar machine, therefore the A.C winding losses in the heteropolar machine are about 39% less than the losses in the homopolar machine.Hence the total copper loss in the heteropolar machine is 11% more than that in homopolar machine in the case of same excitation currents, but for the same voltage the total copper loss are nearly the same in both machines (1% more in the homopolar).

The total iron losses have been calculated in each part of the stator of each machine, teeth, back iron, and longitudinal blocks.The method used was to first find value of the peak flux density and then the corresponding value of specific loss in w/kg was found from steel manufacturers curves.From this the total loss can be found by integration.For the same excitation currents in both machines, the total iron losses in the stator of the heteropolar machine are 19.4% more than the losses in the homopolar machine, but for the same voltages this loss is 3% more than the losses in the stator of the homopolar machine.

The total weight of the heteropolar machine is about 19% greater than the homopolar machine.

VI. Discussion

It has been found that the homopolar machine is lighter than the heteropolar by 19%.The total loss in the heteropolar case is virtually the same (3% more) that in the homopolar case.

References

[1] Wang, R., Demerdash, N.A., "Computation of Load Performance and Other Parameters of Extra High Speed Modified Lundell Alternators from 3D-FE Magnetic Field Solutions."IEEE Transactions on Energy Conversion, Vol.7, No.2, June 1992.

[2] Nair, R., "Inductor Generators for Alternative Energy Schemes". IEE Conference proceeding, Sept.1993, Oxford, England.

[3] "MEGA" User Manual Version V5.32, School of Electronic and Electrical Engineering, Bath University, U.K .

[4] Lai, H.C., Rodger, D., Leonard, P.J., "Coupling Meshes in 3D Problems Involving Movements". IEEE Transactions on Magnetics, Vol.28, No.2, March 1992.

Automatic Treatment of Multiple Wound Coils in 3D Finite Element Problems including Multiply Connected Regions

P.J.Leonard H.C.Lai J.F.Eastham and Q.H.Al-Akayshee
University of Bath,
Claverton Down,
BATH BA2 7AY, UK

Abstract— **This paper describes an efficient scheme for incorporating multiple wire wound coils into 3D finite element models. The scheme is based on the magnetic scalar representation with an additional basis for each coil. There are no restrictions on the topology of coils with respect to ferromagnetic and conductor regions. Reduced scalar regions and cuts are automatically generated.**

Introduction

Many electrical machines use wire wound coils as the source of a magnetic field. The machine used as an example in this paper is shown in Fig.1.

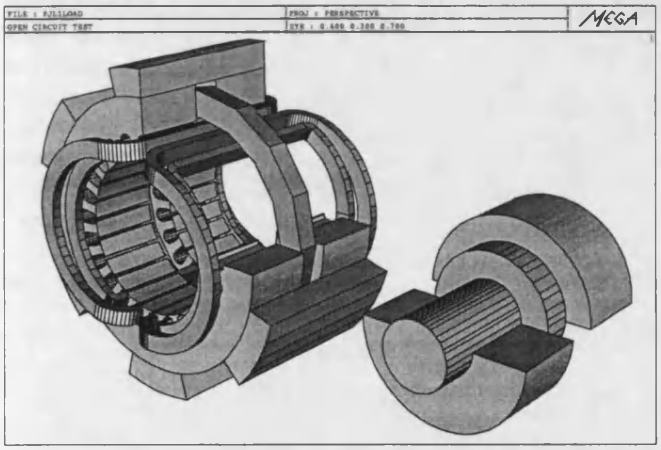

Fig. 1. Showing the finite element model.

In a previous publication we presented a scheme for modelling coils connected to external energy sources [1], based on a nodal magnetic scalar potential, with the use of a reduced scalar to contain the coil source field. One draw back of the scheme, for the casual user of an FE package, is mastering the concept of reduced scalar regions.

Our latest work has been to fully automate the definition of the reduced scalar region making the formulation transparent to the end user. We have also generalised the formulation to allow multiple coils. The program selects the elements needed to contain the coil within a reduced scalar region. This usually makes the scalar and reduced scalar regions multiply connected. Previous publications [2] have described the use of cuts in multiply connected eddy current problems. In this contribution we will show how these cuts can be introduced (automatically) into the reduced scalar scheme. Not only does this solve the problem of multiply connected regions but, the basis for the cuts is the same as the nodal magnetic scalar potential. This is important when the coil links a highly permeable magnetic circuit. Without the use of cuts we would be forced to take the reduced scalar region through the magnetic material. The well known cancellation problem that occurs when this is done is avoided by our scheme.

The user has only to define the coil geometry and specify it's connection to an external circuit. Care has been taken to keep the computational cost of coil integration to a minimum. This has been achieved by allowing each coil to have it's own reduced scalar region.

Theory

In this section we outline a general method for modelling wire wound coils.

Given a problem with a set of N independent windings. The field is represented by adding an additional vector basis function, $\mathbf{T}_i$ for each independent winding

$$\mathbf{H} = -\sum \nabla N_i \psi_i + \sum \mathbf{T}_i I_i \tag{1}$$

The only requirement is the curl of this vector is the turns density vector of the winding, that is, $\nabla \times \mathbf{T}_i I_i = \mathbf{J}_i$

We solve the usual non-divergence of flux equation

$$\nabla \cdot \mu \left(-\sum \nabla N_i \psi_i + \sum \mathbf{T}_i I_i \right) = 0 \tag{2}$$

If the F.E. scheme is to be connected to an external source then it is essential to have an equation relating the terminal voltage and the field. This is done by projecting the induced $\mathbf{E}$ onto the turns density vector ($\nabla \times \mathbf{T}_i$) and integrating [1]

$$V = \int_{\Omega} \mathbf{E} \cdot \nabla \times \mathbf{T}_i \, \mathrm{d}\Omega \tag{3}$$

Any resistance of the wire is easily added as an external resistor.

The integral in (3) requires a bit of development because $\mathbf{E}$ is not directly available within the magnetic scalar region.

Using the vector identity, $\mathbf{E}\cdot\nabla\times\mathbf{T}_i = \mathbf{T}_i\cdot\nabla\times\mathbf{E}+\nabla\cdot\mathbf{T}_i\times\mathbf{E}$, yields

$$\int_\Omega \mathbf{E}\cdot\nabla\times\mathbf{T}_i\,\mathrm{d}\Omega = \int_\Omega \mathbf{T}_i\cdot\nabla\times\mathbf{E}\,\mathrm{d}\Omega + \oint_\Gamma \mathbf{T}_i\times\mathbf{E}\cdot\hat{\mathbf{n}}\;\mathrm{d}\Gamma \tag{4}$$

The surface integral disappears if $\mathbf{T}\times\mathbf{E}\cdot\hat{\mathbf{n}} = 0$. In practice this means if $\mathbf{E}\times\hat{\mathbf{n}} \neq 0$ then we must ensure $\mathbf{T}\times\hat{\mathbf{n}} = 0$.

The curl of $\mathbf{E}$ is well known as $\dfrac{\partial\mathbf{B}}{\partial t}$ so

$$\int_\Omega \mathbf{E}\cdot\nabla\times\mathbf{T}_i\,\mathrm{d}\Omega = -\int_\Omega \mathbf{T}_i\cdot\frac{\partial\mathbf{B}}{\partial t}\,\mathrm{d}\Omega \tag{5}$$

After the usual Galerkin procedure these equations lead to a symmetric matrix.

Implementation

The scheme described above is quite general, given any suitable vector $\mathbf{T}$ we can always construct another vector by adding the gradient of a scalar. Two objectives have led us to our choice of $\mathbf{T}$ in this paper. Firstly $\mathbf{T}$ normally requires integrating the source field using Biot-Savart. This can be expensive so we attempt to minimize the volume within which $\mathbf{T}$ is non zero. Secondly if $\mathbf{T}$ exists within materials of high permeability (unavoidable if a coil links a magnetic circuit as shown in Fig.2) then cancellation problems can occur which can be kept to a minimum if $\mathbf{T}$ has the same basis as $\nabla\psi$ within the magnetic material.

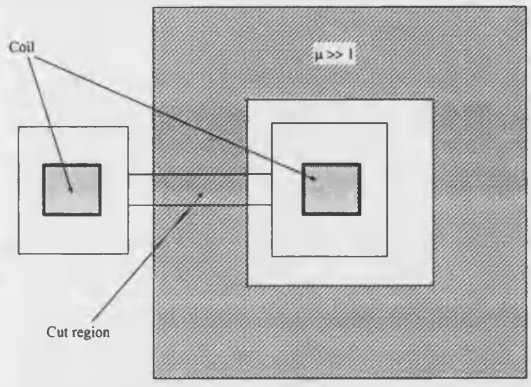

Fig. 2. Showing the cross section of a coil and a magnetic circuit

The reduced and total scalar method [3] can be used to minimize the extent of the $\mathbf{T}$ vector , however it requires the reduced scalar region to be simply connected. We have generalised the reduced scalar method by eliminating multiply connect regions using cuts. The vector $\mathbf{T}$ lives in two different types of region: the coil region is the set of elements which overlap the physical coil; the cut region is a region which spans any hole formed by the coil region, see Fig.3.

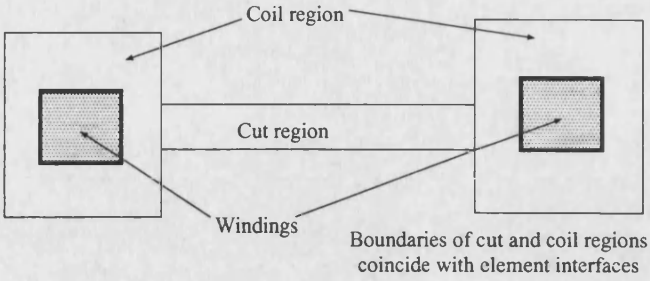

Fig. 3. Showing the different regions in which $\mathbf{T}$ lives.

Within the coil region the $\mathbf{T}$ vector is defined as

$$\mathbf{T} = \mathbf{H}_s - \nabla M \tag{6}$$

where, $\mathbf{H}_s$ is the source field due to $1Amp$, calculated using Biot-Savart. The ∇M is added to eliminate the tangential component of $\mathbf{T}$ on the interface between the coil region and the total scalar region. On this interface M is defined as line integral on the surface from some reference point

$$M(a) = \int_{ref}^{a} \mathbf{H}_s\cdot\mathrm{dl} \tag{7}$$

If the scalar potential has been set to zero at some point this is used as the reference. The line integral is not allowed to go through the cut region. The scalar M is interpolated using the element shape functions. On the internal nodes within the coil region M is taken to be zero.

In the cut region $\mathbf{T}$ is modelled by the gradient of the discontinuous auxiliary cutting potential, which uses the same basis as the scalar potential, ψ, so we avoid the cancellation problem. If the core in Fig.2 has a conductivity the cut naturally interfaces with the magnetic vector potential used to model the core [2].

The vector basis $\mathbf{T}$ for a simple race track coil is shown in Fig.4.

Automation

The windings are meshed separately to the F.E. mesh. Each winding comprises a set of coils connected in series. For complicated devices the manual definition of the coil region elements is a time consuming and error prone process. We have automated this process by finding the F.E. elements which overlap (in 3D) with the coil elements. In practice different windings may share the same coil elements as shown in Fig.5. This adds to the complexity

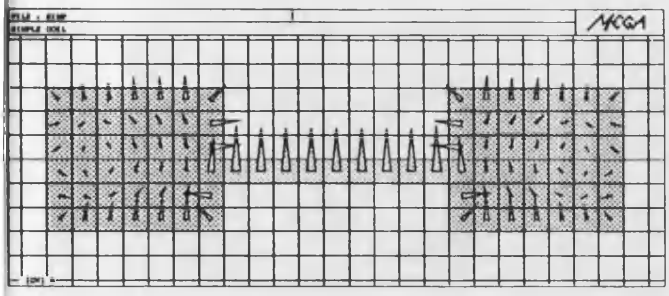

Fig. 4. Showing the T vector in the coil region and cut region.

of book keeping within the program but is unimportant from the users point of view.

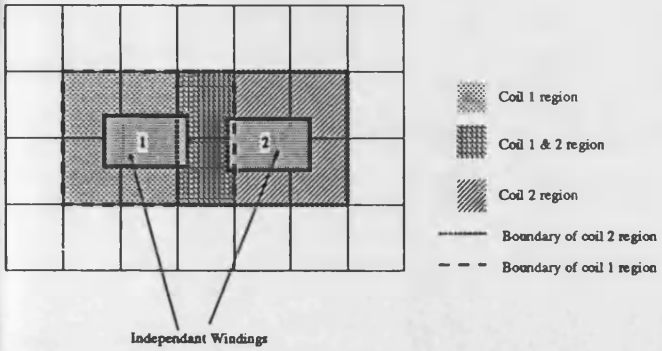

Fig. 5. Showing two coils, their regions and boundaries

In most cases this procedure produces a multiply connected coil region. Cuts are automatically generated [4] to render the complete T region simply connected. Note that it is possible that more than one cut be generated for each coil region depending on the topology of the winding. It is also possible for cuts to fold and intersect with themselves or any of the other cuts. For example Fig.6 shows a coil arrangement which could in reality be a single winding with different number of turns in each branch. In general 3 cuts are needed to make the regions simply connected.

Calculating the required jump across the cuts (per amp current) is done if possible whilst calculating the integral of M for each coil. The integration is not allowed to go through a cut. If both sides of the cut have been visited by the integration it may be possible to assign a basis (jump per amp in coil) for the cut. An interesting case arises when two cuts overlap on the surface of the reduced scalar. In this case assigning a value for the jump must be postponed until the values for the other cuts have been assigned.

Results

A novel homopolar generator has been designed and tested using the *MEGA* [5] package which uses the scheme outlined in this paper. The Machine comprises a 3 phase AC winding on the stator excited by a single coil also on the stator. The computer model of the motor was shown in Fig.1. For clarity one quarter of the stator is not displayed and only one phase of the stator winding is shown.

The machine has been modelled dynamically with the rotor speed fixed and the stator and rotor meshes coupled via a sliding Lagrange interface [6]. The 3 phase AC windings were connected to an external star load. A full time transient dynamic simulation was required to model the machine correctly. The flux path for one rotor position is shown in Fig.7

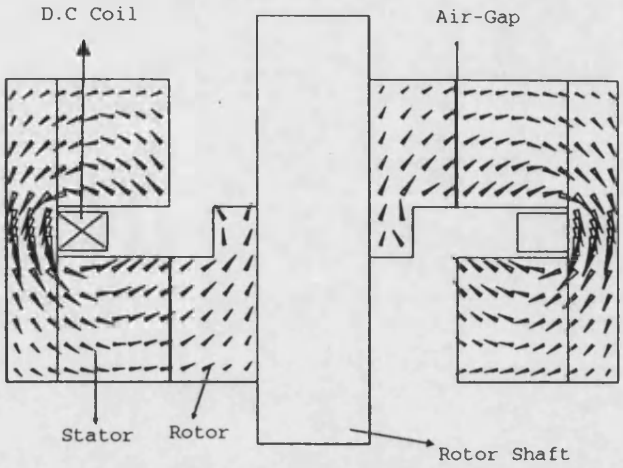

Fig. 7. Longitudinal Section of motor at 0° Position

The experimental verification of this scheme will be published elsewhere [7], in this contribution we shall describe some of the theoretical aspects of this problem.

Each stator phase comprises four coils connected in series. We have a choice: treat the sets of coils as a single winding or four separate coils and connect them via the external circuit feature of the package. Because the coil integration is done separately for each coil the later approach is about 16 times quicker than the former. The end region of the machine has a complex coil geometry that is very difficult to mesh exactly. We chose to approximate the coils by a set of physically intersecting windings. Reduced scalar elements are put into sets which are classified by the coils which intersect that element. For this problem 150 distinct sets were required. Each of the sixteen AC coils generated it's own cut.

The DC coil poses an interesting problem. Because the rotor section is meshed separately there is a hole within the stator region which is linked by this DC coil. However this coil requires a cut. Rather than trying to extend this cut through the Lagrange surface to the rotor we can make it go to one of the outer boundaries. This is done automatically by the program by making the cut avoid the sliding Lagrange surface and ensuring that the outer boundary of the problem has the correct boundary

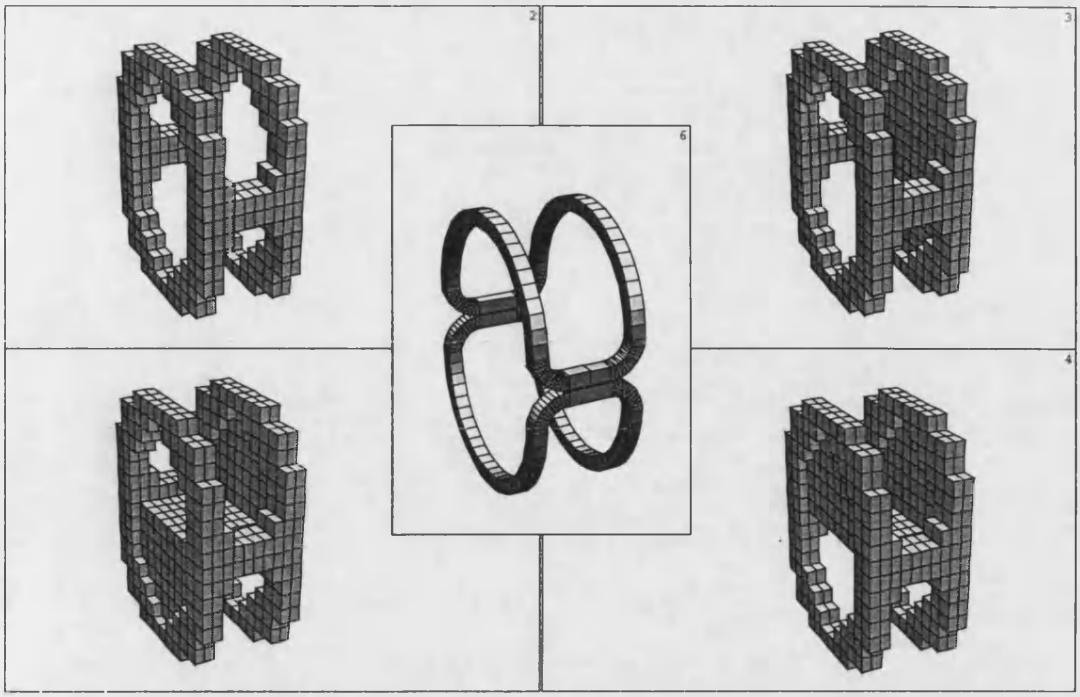

Fig. 6. Showing a winding, the coil region and the 3 cuts.

condition to allow the cut to span between the boundary and the coil region, shown in Fig.8.

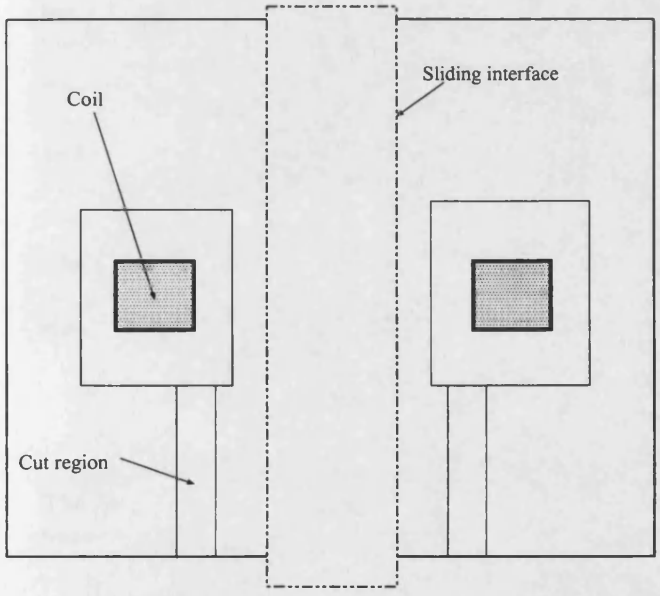

Fig. 8. Showing the sliding interface and the cut generated to the outer boundary of the problem

Conclusion

We have presented a general scheme for dealing with wire wound coils in 3D finite element problems. The scheme has been automated, hiding the difficult concepts such as reduced scalar regions and cuts from the user. The scheme is optimal, in the sense that, the coil integration is contained within the minimum possible region. The scheme has no topological restrictions.

References

[1] P.J.Leonard and D.Rodger. "Modelling voltage forced coils using the reduced scalar potential method". *IEEE Trans. Mag.*, MAG 28(2):1615–1617, March 1992.

[2] P.J.Leonard and D.Rodger. "A new method for cutting the magnetic scalar potential in multiply connected eddy current problems". *IEEE Trans. Mag.*, 25(5):4132–4134, September 1989.

[3] J.Simkin and C.W.Trowbridge. "On the use of the total scalar potential in the numerical solution of three dimensional magnetostatic problems". *IJNME*, 14:423–440, 1979.

[4] P.J.Leonard H.C.Lai R.J.Hill-Cottingham and D.Rodger. "Automatic implementation of cuts in multiply connected magnetic scalar regions for 3D eddy current models". *IEEE Trans Mag.*, 29(2):1368–1371, 1993.

[5] "MEGA Version 5 user manual ". *Applied Electromagnetic Research Centre, Bath University, UK.*

[6] H.C.Lai D.Rodger P.J.Leonard. "Coupling meshes in 3D problems involving movement". *IEEE Trans. Mag.*, MAG 28(2):1732–1734, March 1992.

[7] Q.H Al-Akayshee and J.F.Eastham. " A comparison between AC side excited heteropolar and homopolar synchronous machines". *submitted to: International Confrence on Power Electronics, Drives and Energy Systems for Industrial Growth, PEDES 96, New Delhi, INDIA*, January 1996.

3D Finite Element Modelling of an $A.C$ Side Excited Machine

Q.H Al-Akayshee ,J.F.Eastham
School of Electrical & Electronic Engineering, Bath University, Bath. U.K.

***Abstract*—One form of stator-side excited machines is considered in the paper, a homopolar machine. The machine has a complex field geometry and is difficult to analyse except by the use of 3D magnetostatic finite element modelling. The results from such modelling are compared with measurements taken from a prototype homopolar machine to validate the analysis. Comparisons are drawn between the use of magnetic and non magnetic shafts. It is concluded that the modelling methods are sufficiently accurate for design purposes.**

I. INTRODUCTION

A.C side excited synchronous machines have both excitation and armature windings on the stator side of the air-gap, the machines are robust and have been used for high speed applications[1].

The machine has also been suggested for use in alternative energy schemes[2], especially in small hydro and wind power applications where advantage can be taken of their easy and comparatively low-skilled maintenance requirements.

The rotors carry no windings and are brushless but the generated voltage can be regulated by varying the stator-side excitation.

II. 3D FE MODELLING

The 3D mesh can be created by extruding a 2D base plane built from quadrilateral and triangular elements. The process of creating a 2D mesh is subset of the full 3D program.

This modelling method means that the base plane must contain the whole network topology of the entire model. The 3D-FE Models[3] are outlined in Fig. 1 and Fig. 2 for the rotor and stator of the machine respectively.

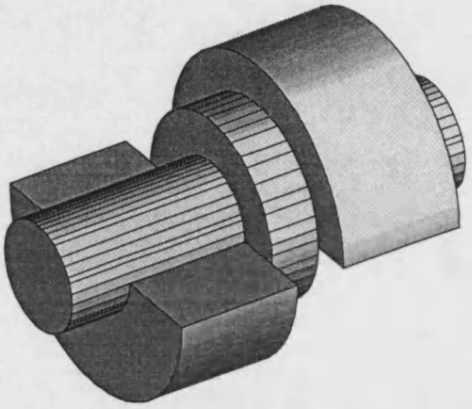

Fig. 1. Homopolar Machine Rotor

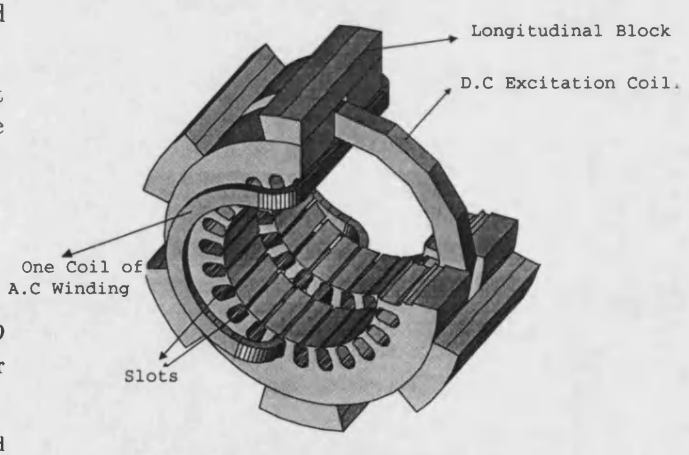

Fig. 2. Homopolar Machine Stator

In modelling electrical machines it is necessary to consider the rotor at all positions within the stator. In the method used in this work the rotor and

Professor J.F.Eastham FEng, School of Electronics and Electrical Engineering, University of Bath, Claverton Down, Bath BA2 7AY, UK. Telephone 44-1225-826056, Fax 44-1225-826305, Email: J.F.Eastham@bath.ac.uk, Mr. Q.H.Al-Akayshee MSc, School of Electronics and Electrical Engineering, University of Bath, Claverton Down, Bath BA2 7AY, UK. Telephone 44-1225-826610, Email: Q.Al-Akayshe@bath.ac.uk

stator are independently meshed with the two meshes coupled using 'Lagrange Multipliers'[4]. This enables the rotor to be rotated and snap shots taken of the field at a set of positions.

III. PRINCIPLE OF OPERATION

Only one excitation coil is used in this machine. The $A.C$ winding passes through the slots of both cores. Fig. 3 is a longitudinal section of the machine shown at one particular position, if the left hand stator is considered it will be seen that the rotor presents a *'north'* pole at the top since flux passes from the rotor to the stator. However there is no flux driven from the rotor at the bottom. If now the rotor is turned by 180° as shown in Fig. 4 then it will be seen that flux still passes from the rotor to the stator at the left hand core with the rotor still presenting a *'north'* pole.

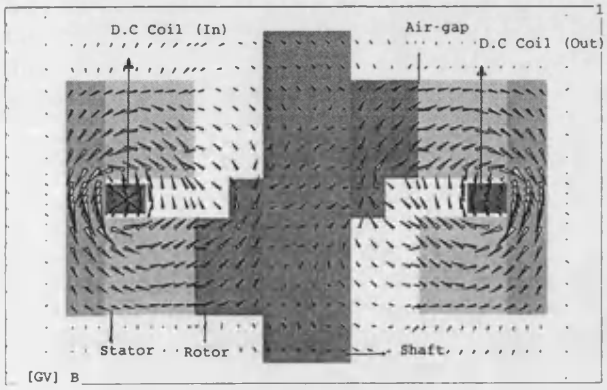

Fig. 3. Longitudinal Section at 0°

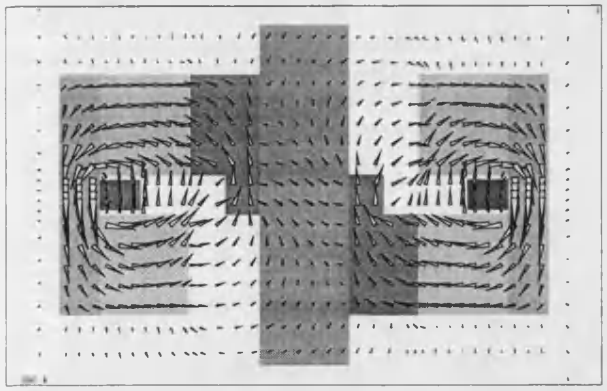

Fig. 4. Longitudinal Section at 180° Position

Consideration of the figures shows that a similar situation occurs on the right hand side core but this time a *'south'* pole is always presented by the stator. Since the flux is only modulated from one direction to zero in one core the machine is termed homopolar. However because of the two cores the flux linking a stator coil is first in one direction from one core and then in the reversed direction from the other[5].

IV. FINITE ELEMENT AND EXPERIMENTAL RESULTS

The following tests were performed on the machine and equivalent finite element results were obtained for comparison[6].

A. Open-circuit test: In which the open circuit voltage E_{oc} was measured as the field current I_f is varied. The results are shown compared with FEM in Fig. 5.

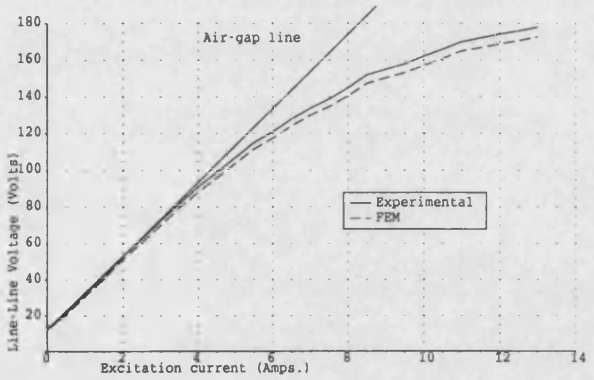

Fig. 5. Open circuit test

B. Short-circuit test: In which the machine is short circuited at the terminals and results of short circuit current I_{sc} against field current I_f are obtained and compared with FEM in Fig. 6.

C. Unsaturated Synchronous Impedance: Direct axis synchronous reactance, $X_{d(un)}$ was calculated as follows:

$$X_{d(un)} = \frac{E_{oc}}{\sqrt{3} I_{sc}} \tag{1}$$

where E_{oc} is the Line to Line open circuit voltage taken from the air gap line for a given excitation field current I_f and I_{sc} is the short circuit armature current obtained at the same field excitation. This reactance is 68Ω experimentally and 61Ω calculated from FEM.

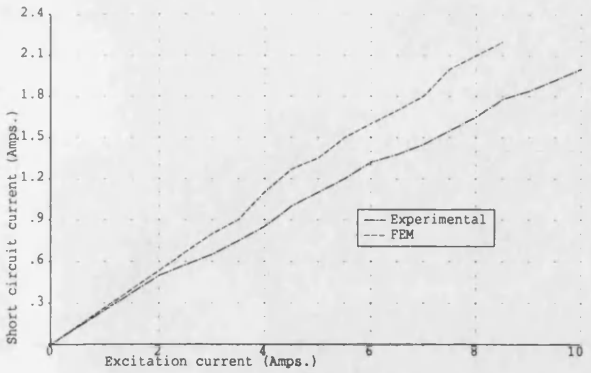

Fig. 6. Short circuit test

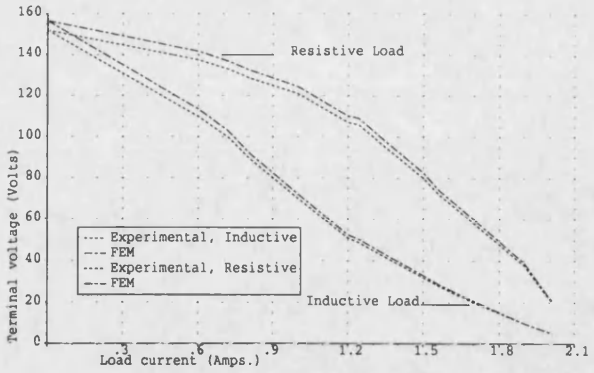

Fig. 7. Load test

V. Slip test

A slip test has been performed to determine X_d and X_q. In this test three phase voltage were applied at a speed slightly below synchronous speed without field excitation. Oscillograms were taken of the armature terminal voltage, and the armature current. The direct-axis and quadrature-axis reactances are found as follows:

$$X_d = \frac{V_{max}}{I_{min}} \quad and \quad X_q = \frac{V_{min}}{I_{max}} \tag{2}$$

The experimental X_d and X_q are 77.6Ω and 72.5Ω, while the calculated values from FE are 66.2Ω and 57.6Ω respectively.

VI. Load test

In this test the 3 phase armature windings are connected to a load and the machine is driven at the synchronous speed. Fig. 7, shows the calculated and measured load voltages for various values of armature current at inductive and resistive loads. The waveforms of load voltage and current (at inductive load) are illustrated in Fig. 8 and Fig. 9 respectively.

VII. MACHINE SATURATION

There are different levels of saturation in this machine. The saturation is highest in the middle of the machine. In particular the rotor center shows the highest level of saturation where the laminations are circular in the machine.

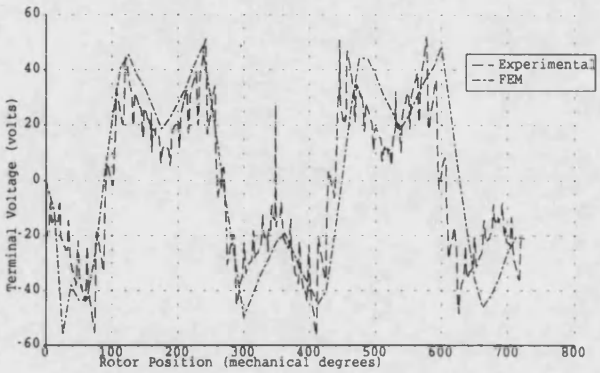

Fig. 8. Load Voltage Waveform

This saturation can be avoided if the rotor shaft is made from a magnetic material such as mild steal instead of the non-magnetic material which is used in the original design. The non-magnetic shaft was adopted in the original design to help to prevent bearing fluxes and high external field. Fig. 10 shows the condition of the flux when a magnet shaft is used.

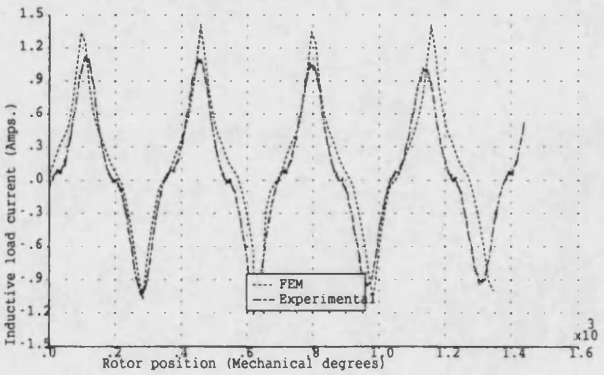

Fig. 9. Load Current Waveform

This is for comparison with Fig. 4 where the shaft is non-magnetic.

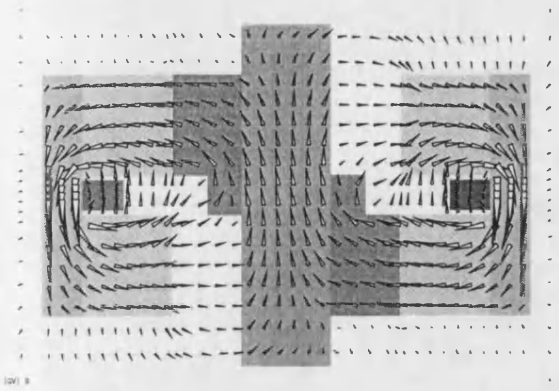

Fig. 10. Vector flux with a magnetic shaft

VIII. Rotor laminated poles

As explained in Section III., the main body of the rotor carries a constant flux with an induced north pole on one end and an induced south pole on the other. However, there are also local alternating flux components due to the stator slotting. The flux in the tooth area is illustrated in Fig. 11 and it will be observed that as the rotor moves a point near the surface experiences flux changes. These changes cause local iron losses which are one component of the stray losses. The experimental machine rotor was laminated to minimise these losses but this is not generally possible in high speed machines which require a solid pole construction for strength. In such machines the stray loss will always remain a disadvantage which can not be avoided[7].

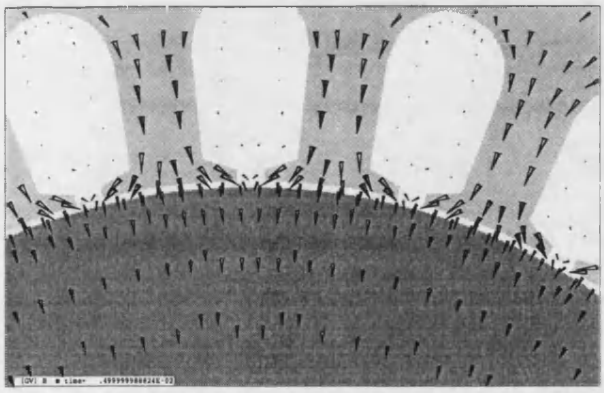

Fig. 11. Rotor flux due to slotting

IX. CONCLUSION

In general the agreement between the finite element and measured results is reasonable for this complex geometry. In particular the ability to calculate the out put current shape in saturated conditions is demonstrated. The laminated regions were considered to be isotropic and the eddy currents driven in them were ignored. This may be the cause of the approximate results since the flux in the practical machine will to some extent be '*steered*' along the plane of the lamination. However the results are sufficient for future comparative design purpose.

REFERENCES

[1] Wang, R., Demerdash, N.A., "Computation of Load Performance and Other Parameters of Extra High Speed Modified Lundell Alternators from 3D-FE Magnetic Field Solutions."IEEE Transactions on Energy Conversion, Vol.7, No.2, June 1992.

[2] Nair, R., "Inductor Generators for Alternative Energy Schemes". IEE Conference proceeding, Sept.1993, Oxford, England.

[3] "MEGA" User Manual Version V5.32, School of Electronic and Electrical Engineering, Bath University, U.K .

[4] Lai, H.C., Rodger, D., Leonard, P.J., "Coupling Meshes in 3D Problems Involving Movements". IEEE Transactions on Magnetics, Vol.28, No.2, March 1992.

[5] Q.H. Al-Akayshee ,J.F.Eastham "A comparison Between A.C Side Exited Heteropolar and Homopolar Synchronous Machines." IEEE International conference for industrial growth (PEDES'96), New Delhi, INDIA, January 1996, pp. 530-34.

[6] Q.H.Al-Akayshee, J.F.Eastham, and P.L.Leonard "Calculation of the parameters and load performance of a homopolar machine". INTERMAG 96, International Magnetics Conference, Seattle, Washington, April, 1996.

[7] W Den Ouden and D Hamels, "Efficiency of Small Homopolar Synchronous Motors at High Speeds", Electric Machines and Power Systems, Volume 13, Number 1, 1987, pp. 29-40 .